Modelling and Estimation of Spatiotemporal Cardiac Electrical Dynamics

A thesis submitted to the University of Sheffield for the degree of Doctor of Philosophy

Jinny Robson

Department of Automatic Control and Systems Engineering

April 2020

The
University
Of
Sheffield.

To my Father

Acknowledgements

First and Foremost, I would like to express my sincere gratitude to my supervisor Professor Visakan Kadirkamanathan for his unwavering support, untiring guidance and constant encouragement. I am also particularly grateful for all the research and teaching opportunities, which helped me to discover my career directions. Thanks for always being helpful and motivating me over these years.

I would like to thank Professor Richard. H. Clayton, for his valuable insights on computational electrophysiology and cardiac modelling. I am also grateful for his constant encouragement, advices and timely reviews throughout my PhD.

A special thanks to Dr. Anastasia Kadochnikova for all the valuable discussions on the estimation methods, invaluable comments on my thesis and for the all caffiene and sugar filled intense discussions. I also want to thank Dr. Parham Aram for the guidance and support during the course of my MSc and PhD studies.

Many thanks to Fodio for the friendship over these years, and to all my friends in ACSE, especially Rajintha, Harry, Zhenglin, Ke Sun, Miguel, Sachin, Waqas and Abidemi for all the general help, discussions and PhD adventures.

I am greatly indebted to my Appachan and my Amma, for their constant love, perseverance and support. Thanks to my sister Winny for always being the constant sunshine of my life. Thanks to my nephew Jadu for the much needed smiles.

A special thanks to my best-friend Sangeeth, for helping me to strive through the toughest times of my PhD. Thanks to all my cousins and friends in Kerala, especially Sanju, for the support and friendship.

I am grateful to Hari for constantly encouraging me throughout this journey, especially during the thesis writing phase.

A special thanks to Ukri for the warmest wishes towards the end of PhD.

Thank you GOD for everything.

Abstract

The heart is a complex biological system in which electrical activation signals initiate at the pacemaker cells, propagate through the heart tissue to both trigger and synchronise the mechanical contractions. Abnormalities in the cardiac electrical signals lead to dangerous cardiac arrhythmias. Therefore, understanding the functionalities of the cardiac electrical activity is essential for the development of novel techniques to facilitate advanced diagnosis and treatment for arrhythmia.

By combining experimental or clinical electrophysiology data with mathematical models, system theoretic approaches can be used to provide quantitative insights into the normal and pathological mechanisms of the cardiac electrical activity. This thesis proposes model-based estimation methods to reconstruct and quantify the underlying spatiotemporal cardiac electrical dynamics from the cardiac electrogram measurements.

Firstly, a statistical model-based estimation framework is proposed to reconstruct the tissue dynamics from the cardiac electrogram measurements. The reconstruction of the tissue dynamics is based on an integrated model of cardiac electrical activity, which incorporates the cardiac action potential dynamics at the cell-level, tissue-level and extracellular-level. The dynamics of the cardiac tissue is described using the monodomain tissue model, which is coupled with the continuous version of modified Mitchell-Schaeffer model. The resulting model equations are of infinite-dimensional form, which is converted into a finite-dimensional state-space representation via a model reduction method. In order to estimate the hidden state variables of the tissue dynamics from the cardiac electrogram measurements, a combined detection-estimation framework using a single filter unscented-transform based smoothing algorithm is proposed. The detection step in the proposed method enables the inclusion of localised stimulus events into the model-based estimation framework. The performance of the proposed algorithms are demonstrated using the modelled cardiac activation patterns of normal and reentrant conditions, in both one-dimensional and two-dimensional tissue field. The findings from this proposed study illustrate that the hidden state variables of the tissue model can be estimated from the electrogram measurements, simultaneously by detecting the stimulus events. Therefore, this method shows that the complex spatiotemporal cardiac activity can be reconstructed from the coarse electrograms using the state estimation methods.

Secondly, a complex network modelling approach is proposed to quantify the spatiotemporal organisation of electrical activation during human ventricular fibrillation. The proposed network modelling approach includes three different methods based on correlation analysis, graph theoretical measures and hierarchical clustering. Using the proposed approach, the level of spatiotemporal organisation is quantified during three episodes of VF in ten patients, recorded using multi-electrode epicardial recordings with 30 s coronary perfusion, 150 s global myocardial ischaemia and 30 s reflow. The findings show a steady decline in spatiotemporal organisation from the onset of VF with coronary perfusion. Following this, a transient increases in spatiotemporal organisation is observed during global myocardial ischaemia. However, the decline in spatiotemporal organisation continued during reflow. The results are consistent across all patients, and are consistent with the numbers of phase singularities. The findings show that the complex spatiotemporal patterns can be studied using complex network analysis.

Contents

List of Figures

List of Tables

List of Acronyms

AF atrial fibrillation

VF ventricular fibrillation

VT ventricular tachycardia

SCD sudden cardiac death

ICD implantable cardioverter defibrillator

APD action potential duration

CV conduction velocity

RP refractory period

ARP absolute refractory period

RRP relative refractory period

SA sinoatrial

AV atrioventricular

NSR normal sinus rhythm

PDE partial differential equations

ODE ordinary differential equations

SPDE stochastic partial differential equations

SDE stochastic differential equations

mMS modified Mitchell-Schaeffer

SNR signal to noise ratio

FHN FitzHugh-Nagumo

ECG electrocardiogram

AUC area under curve

UKF unscented Kalman filter

EKF extended Kalman filter

RTS extended Kalman filter

ERTS extended Rauch Tung Streibel

URTSS unscented Rauch Tung Streibel

ERTS extended Rauch Tung Streibel

MRMSE mean root mean squared error

RMSE root mean squared error

MSE mean squared error

TPR true positive rate

FPR false positive rate

TN true negative

TP true positive

FP false positive

RRUKF reduced rank unscented Kalman filter

Chapter 1

Introduction

Cardiac arrhythmias are a major public health problem in the world [10, 88, 114]. There are more than 2 million people affected by cardiac arrhythmia in the United Kingdom annually [146]. Cardiac arrhythmia can occur either in atria or ventricle chambers of the heart. Atrial fibrillation (AF) is the most common cardiac arrhythmia associated with cardiovascular diseases and increased risks of stroke [10]. On the other hand, the most critical cardiac arrhythmias are ventricular fibrillation (VF) and ventricular tachycardia (VT), which cause dangerous sudden cardiac death (SCD) [28, 123]. SCD resulting from ventricular arrhythmia is accounted for approximately 4-5 millions deaths per year in the world [10].

Cardiac rhythms are regulated by electrical activation waves of the heart. During each normal heartbeat, an electrical wave of activation is initiated by the heart's natural pacemaker and spreads through the entire heart to both trigger and synchronise mechanical contraction. Any disturbance to the normal pattern of generation and propagation of these electrical activation waves result in an abnormal cardiac rhythm or cardiac arrhythmia. During ventricular arrhythmia, the synchronised and regular contractions of the heart are suppressed by rapid and self-sustaining waves of electrical activation in the ventricles. As a consequence, the heart is not able to pump blood effectively, so VF and VT are quickly lethal unless halted by defibrillation [74].

The mechanisms underlying cardiac arrhythmias, in particular, ventricular arrhythmias are multiple and complex. Studies have demonstrated that both VT and VF are sustained by re-entrant activation patterns [122], where the activation wavefronts repeatedly propagate in a circular path, continuously spreading into the recovering tissue instead of following the normal pathways. Moreover, an unavoidable consequence of spontaneous VF is global myocardial ischaemia, resulting from ineffective mechanical function and reduced myocardial perfusion.

Several studies in both animal [24, 72] and human hearts [18, 86] have established that as a result of progressive global myocardial ischaemia, VF exhibits a series of stages where the frequency and the complexity of electrical activation waves vary. Understanding the dynamics of electrical activation waves during episodes of VF with global myocardial ischaemia is of great importance because this knowledge could be used to develop novel therapeutic strategies that could be optimised for each stage of VF [12, 125].

In clinical practice, the most effective treatment for patients at high-risk of ventricular arrhythmias is the implantable cardioverter defibrillator (ICD) [51], where external electrical signals are applied during abnormal conditions to regulate the cardiac electrical activity. Another preventative clinical method is to ablate the pathways of re-entrant activation patterns using radio-frequency energy [31, 122]. This treatment is especially effective for VT as it is driven by one re-entrant circuit [31]. On the other hand, VF is sustained by many re-entry circuits with complex patterns of electrical activation wavefronts [31]. Despite the extensive use of ICD and ablation therapies, mechanisms underlying the initiation and maintenance of ventricular arrhythmic conditions in the human heart are still a subject of extensive research.

Recent technological advances in recording techniques such as electrical and optical mapping of cardiac arrhythmia [57, 116] along with increasingly detailed models of cardiac electrophysiology [31], have greatly added to our knowledge of the mechanisms that initiate and sustain cardiac arrhythmias in the human heart. However, a detailed understanding of these mechanisms is important for further advancements in developing medical interventions. In recent years, researchers have been developing methods by combining cardiac modelling concepts with the electrophysiology data. Some of the important active research objectives in the cardiac modelling domain are the following [31, 135]:

- To predict the effects of anti-arrhythmic drugs on the cellular and tissue level cardiac activity [105, 113],
- To improve ablation procedures by using the personalised patient-specific models [17, 22],
- To improve the use of defibrillation shock level optimised for each stage of VF [12, 125],
- To develop patient-specific modelling with detailed electrical and mechanical cardiac dynamics [39, 60],
- To quantify the variability and uncertainty in the cardiac models [106],

- To reconstruct the underlying normal and abnormal tissue dynamics from the electrophysiology data such as surface measurements [66, 69].

The rest of this chapter is organised as follows: Section 1.1 provides the motivations of this thesis followed by the aims and objectives in Section 1.2. Finally, thesis structure and original contributions are summarised in Section 1.3 and Section 1.4, respectively.

1.1 Motivation

The development of quantitative techniques to provide better understanding of complex cardiac electrical activity is the key motivation of this thesis. In particular, this thesis aims to develop systems theoretic approaches to reconstruct and quantify the underlying cardiac electrical dynamics from cardiac electrograms.

A quantitative description of the system behaviour can be represented as a model through which the underlying system properties can be elucidated. Models are generally used to provide a better understanding of the underlying system behaviours, and also to make the best possible predictions of the dynamics. From the systems engineering perceptive, complex system behaviours are predominantly studied using model-based estimation problems, where the system dynamics is determined from the available measurements of the underlying process. The integral components in this approach are measurements, system model and the estimation method.

Data acquisition techniques for cardiac arrhythmia research enable patient-specific measurements of electrical activation from different spatial locations across the heart. By acquiring these observations over time, they can be treated as spatiotemporal data where the dynamics change over time and through space. Complex spatiotemporal patterns are thus formed from the spatial interactions with the dependency of temporal dynamics [15]. However, data acquisition techniques used to measure electrical activation sequences, especially during cardiac arrhythmia, are clinically challenging and are restricted to endocardium and epicardial measurements [31].

The limitations of experimental techniques are greatly mitigated by computational cardiac models, as they can provide quantitative descriptions of cardiac electrical dynamics at different spatial scales such as cell, tissue and surface [31]. As a result, cardiac-model based studies complemented with experimental measurements are considered as an effective tool to study the multi-scale characteristics and interactions of cardiac electrical activity through forward or inverse problems [130]. In particular, inverse problems of cardiac-electrophysiology aims to reconstruct the unobserved tissue dynamics from the observed electrogram measurements. The reconstruction of unobserved tissue field is important as it may elucidates the underlying spatiotemporal electrical dynamics during both normal and pathological conditions. Hence the motivation towards the work presented in this thesis.

Cardiac model equations are generally developed based on theoretical knowledge from different fields such as physiology, electrophysiology, numerical mathematics, etc. This stage is followed or generally combined with rigorous validation process using the data from clinical experiments and computational simulations. The cardiac models are generally nonlinear equations, which may take coupled partial differential equations and integral forms [32]. The key advantages of cardiac electrophysiological models are the following:

1. Cardiac models provide quantitative descriptions of state variables, which may not be directly measured using the experimental techniques,
2. Cardiac models consist of electrophysiologically meaningful parameters that provide better interpretation of the cardiac electrical activity.

In order to reconstruct the system dynamics from the surface measurements, systems engineering provides various estimation methods depending on the nature of the inverse problem. For instance, the above estimation problems can be solved using state estimation and parameter estimation methods, respectively. Spatiotemporal estimation methods are widely used in a range of disciplines such as neuroscience [53], cell chemotaxis [83], weather forecasting [71], epidemiology [8], and wind energy [103]. This provide an opportunity to develop a nonlinear estimation method based on computational cardiac models of electrophysiology, for reconstructing the underlying tissue dynamics from the surface measurements.

Another approach to study the cardiac electrical activity is by quantifying the organisation of spatiotemporal patterns and hence investigating the patterns of connectivity underlying electrical activation recorded at different spatial locations. This is particularly important for studying the heterogeneous system characteristics in the clinical recordings of VF. Moreover, one aspect that is poorly understood is whether the spatiotemporal patterns of electrical activation during VF arise from random or organised processes [85]. Early studies of VF emphasised the observation of turbulent electrical activation waves [110, 160]. In contrast, other studies have found spatial and temporal organisation in the pattern of electrical activation [30, 61, 151]. Spatial organisation is of particular interest because it could arise from an underlying connectivity structure that drives the complex activation patterns that are observed on the heart surface. The spatiotemporal interactions can be quantified by applying complex network modelling techniques to different clinical measurements.

The above described considerations in this section form the main research aims of the work presented in this thesis, and the following section highlights these and the respective objectives.

1.2 Research Aims and Objectives

The overall aim of this thesis is to develop model-based estimation methods for quantifying the cardiac electrical dynamics from cardiac electrograms. It includes the following:

- Develop a computational cardiac model-based estimation approach to reconstruct the dynamics at different spatial scales of heart.

  The key objectives of this part are summarised as follows:

  - Derive a generalised cardiac model by integrating existing models of cardiac electrophysiology.
  - Perform a simulation-based study using integrated cardiac models to study the initiation and propagation of complex activation patterns at different spatial levels.
  - Develop a detection-estimation methodology to reconstruct the tissue dynamics from the electrogram measurements in a one-dimensional and two-dimensional cardiac field.

- Develop a complex network modelling-based estimation approach to quantify the spatiotemporal organisation in the clinical recordings of VF.

  The key objectives of this part are summarised as follows:

  - Characterise the underlying network structures of electrical activation with functional association.
  - Quantify the level of spatiotemporal organisation during the different stages of VF.

1.3 Thesis Structure

The rest of the thesis is structured as follows:

- *Chapter 2*

  This chapter provides a foundation to the dominant concepts required for the modelling and estimation framework proposed in this thesis. This involves foundation to the cardiac electrophysiology concepts essential for developing the methods and interpreting the results. A literature review of existing cardiac models at the cell, tissue and the extracellular spatial fields is then provided. The review of different models contribute to a better understanding of the state variables and parameters at different spatial scales. This is followed by a brief description of different state estimation methods from systems theory. Finally, the state of art in the state estimation of cardiac models is provided. This review highlights the gaps in the literature, which forms the foundation for the proposed detection-estimation framework in this thesis.

- *Chapter 3*

  This chapter presents the derivation of an integrated cardiac model of electrophysiology that can be used for identification frameworks of cardiac activation patterns. The proposed model comprises of a novel continuous version of modified Mitchell-Schaeffer ionic model, coupled with the monodomain tissue model and an extracellular electrogram model. A simulation-based study on the proposed model is then presented to characterise the initiation and propagation of cardiac electrical activation waves during normal and abnormal cardiac conditions. Finally, qualitative and quantitative comparisons with the modified Mitchell-Schaeffer model are presented to validate the performance of the proposed model.

- *Chapter 4*

  This chapter introduces a novel methodology to reconstruct the tissue dynamics from the extracellular electrogram measurements. This chapter particularly focuses on estimating the state variables of the monodomain tissue equations in a one-dimensional cardiac field, by using the ionic model proposed in Chapter 3. After representing the model equations as a finite dimensional state space model, a state estimation methodology is applied using the Unscented Rauch-Tung-Striebel Smoother algorithm. The important contribution in this framework is the model-based detection and estimation of stimulus variables, which has not been reported before in the literature of cardiac modelling. This estimation of the stimulus variables is integrated into the framework via state-augmentation. The performance of the proposed methodology is demonstrated during normal and re-entrant activation patterns in a one-dimensional cable and ring field,respectively. Several experiments are then performed to illustrate the effectiveness of the proposed framework.

- *Chapter 5*

  The proposed detection-estimation framework presented in Chapter 4 is extended to the two-dimensional cardiac tissue field. By addressing the important challenges resulted from the high-dimensional state-space model, this chapter introduces a detection-estimation framework tailored for high-dimensional systems. The methodology involves Reduced Rank fixed-lag URTS smoother to obtain the smoothed estimates of the state variables. The performance of the proposed detection-estimation approach is evaluated using the complex spiral re-entrant activation patterns.

- *Chapter 6*

  This chapter presents a novel complex network modelling approach to quantify the spatiotemporal organisation in the clinical recordings of VF. The proposed network modelling approach comprises of correlation analysis, graph theoretical measures and hierarchical clustering method. Using the proposed approach, the level of spatiotemporal organisation was quantified during three episodes of VF in ten patients, recorded using multi-electrode epicardial recordings with 30 s coronary perfusion, 150 s global myocardial ischaemia and 30 s reflow. The results using the clinical data are presented, along with a detailed discussion on the proposed complexity measures and a comparison with the traditional methods.

- *Chapter 7*

  Finally, a summary of the work achieved in this thesis is presented, followed by a discussion on the potential future research areas.

1.4 Contributions

- **Published journal article based on the results from Chapter 6**

  Robson, J., Aram, P., Nash, M.P., Bradley, C.P., Hayward, M., Paterson, D.J., Taggart, P., Clayton, R.H. and Kadirkamanathan, V., 2018. Spatio-temporal organization during ventricular fibrillation in the human heart. Annals of biomedical engineering, 46(6), pp.864-876.

Chapter 2

Background to Model-based Estimation of Cardiac Electrophysiology

This chapter aims to introduce the key concepts that are essential for developing the model-based estimation methodology presented in later chapters. This chapter is focussed on the integral components of model-based estimation approaches, described in Section 1.1. They are : (1) Measurements. (2) System model. (3) Estimation method. For this purpose, this chapter is broadly classified into three sections. The first section, Section 2.1, provides a background to the cardiac electrical activation patterns at the different spatial scale of the heart. This section also highlights the limitations of the experimental techniques, which are mitigated by cardiac models of electrophysiology. As a result, Section 2.2 reviews the existing models in the literature of cardiac electrophysiology. Finally, Section 2.3 details the estimation methods for cardiac electrical dynamics, which include the stochastic state-space models and the state estimations methods.

2.1 Cardiac Electrical Dynamics

The heart is the primary organ of the cardiovascular system, situated between the lungs and surrounded by the pericardium membrane. It acts as an electromechanical pump to provide adequate blood flow throughout the body. A simplified anatomy shown in Figure 2.1 illustrates the four major pumping chambers in the heart. These chambers are separated into right and left halves by a muscular septum wall to prevent the blood flow between opposing chambers. Each side has an atrium (upper chamber) and a ventricle (lower chamber) that are connected by

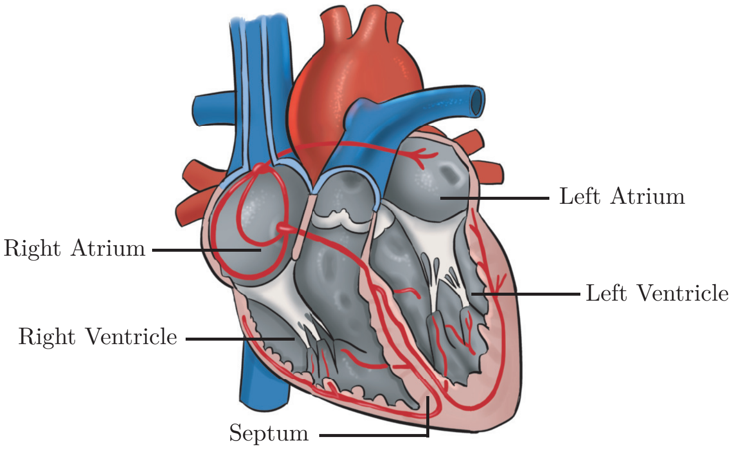

Figure 2.1. A simplified diagram of the human heart [131].

valves to direct the blood flow upon contraction. The mechanical contraction and relaxation of the pumping chambers is the cardiac rhythm, initiated and cordinated by the electrical activity in cardiac muscle cells.

The heart muscle can be considered as a composite tissue with various types of cells. The important type of cardiac cells that produce mechanical contraction is the excitable myocytes. Myocytes are encapsulated within a lipid membrane called sarcolemma, which separates the cell interior (intracellular space) from its exterior (extracellular space). Sarcolemma consists of ions such as Na^+, Ca^{2+}, K^+, which creates potential difference across its intracellular and extracellular spaces. This potential difference is also known as transmembrane potential given by

$$v = v^{in} - v^{ex}, \tag{2.1}$$

where v^{in} and v^{ex} are the potential in intracellular and extracellular space, respectively.

Cardiac myocytes are excitable above a threshold voltage to give an active response. Myocytes can respond to the external stimuli actively or passively. For instance, when an external electrical stimulus current from a stimulating electrode or an internal current from neighbouring myocytes, is above a threshold value, the cardiac myocytes respond actively. On the other hand, myocytes are at resting potentials without external stimulus, implying a passive response. The ability of cardiac myocytes to respond actively or passively to an electrical stimulus forms the basis of cardiac conduction system.

For a single cell membrane, the evolution of transmembrane potential over

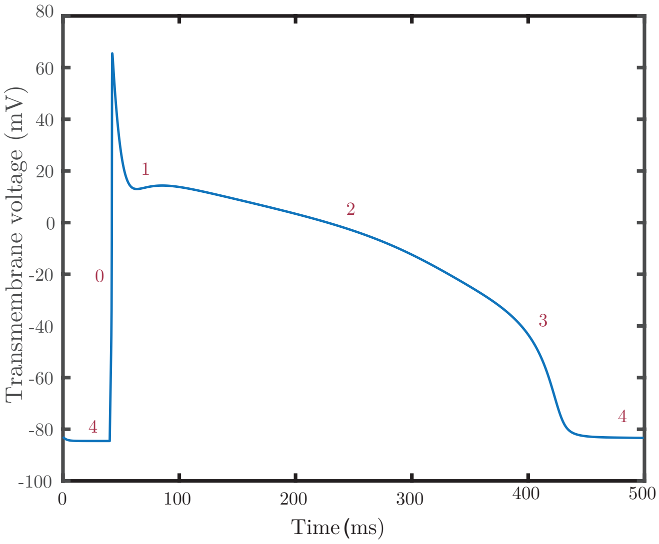

Figure 2.2. **An example of cardiac action potential from a heart muscle cell, simulated from Luo-Rudy cardiac cell model**. Each number indicates the phase within cardiac action potential.

time initiated by the stimulus is represented as action potential. Figure 2 shows a schematic representation of a cardiac action potential consisting of four major phases. When the transmembrane voltage is above a threshold potential, the rapid inward flow of Na^+ creates sodium current and depolarises the cell membrane at a very fast rate. This fast upstroke is Phase 0 of the action potential. Subsequently sodium current reaches the peak magnitude from where the transmembrane potential quickly decreases due to the outward flow of K^+. This is Phase 1 of the action potential as shown in Figure 2.2. However once the transmembrane potential reaches approximately -25 mV, the Ca^{2+} channels open and current flows to cell interior space. This reduced rate of repolarisation in Phase 2 causes a plateau state in the action potential against the outward flow of K^+ ions. Following this, the increased outward flow of K^+ causes repolarisation in Phase 3. Finally, cell membrane returns to its resting transmembrane potential in Phase 4 [126, 130]. This forms one cycle of action potential in a cell consisting of depolarisation, repolarisation stages followed by returning to resting potential condition.

The electrophysiological characteristics of the action potential are important aspects for studying the wavebreaks and dynamics during the initiation and evolution of arrhythmia [130]. Some of the key characteristics are illustrated in Figure 2.3 and detailed below.

- Action potential duration (APD): APD is defined as the amount of time when transmembrane voltage is higher than the threshold potential [23]. The mag-

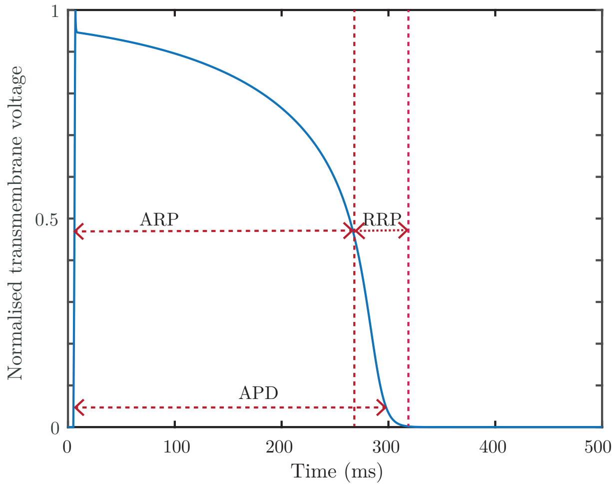

Figure 2.3. **Some of the key characteristics of cardiac action potential**. The abbreviations are detailed in the text. Here, the action potential is obtained from the Mitchell-Schaeffer model.

nitude of APD reduces when the cell is excited at a higher rate, and this condition is called as APD restitution. The slope of APD restitution curve is an important parameter used to predict the stability of electrical activation patterns [163].

- Conduction velocity (CV): It is defined as the speed at which the action potential propagates across the tissue. Together with APD the magnitude of CV decreases when the cell is excited at higher rate, and called as CV restitution. The slope of CV restitution curve is also considered to be influencing the initiation of wavebreak dynamics [107].
- Refractory Period (RP): After the initial excitation of cell membrane, the period in action potential during which the membrane cannot be re-excited by an external stimulus is called absolute refractory period (ARP). However after an interval, the cell membrane can be excited during the relative refractory period (RRP) with a higher stimulus magnitude [126]. These time measures also play an important role in initiation and dynamics of abnormal cardiac activation patterns [26].

The fast depolarisation of a myocyte in Phase 0 of the action potential triggers and opens the Na^+ channels of neighbouring myocytes connected through intercellular gap junctions. As a result, the action potential is propagated to the adjacent myocytes in the cardiac tissue.

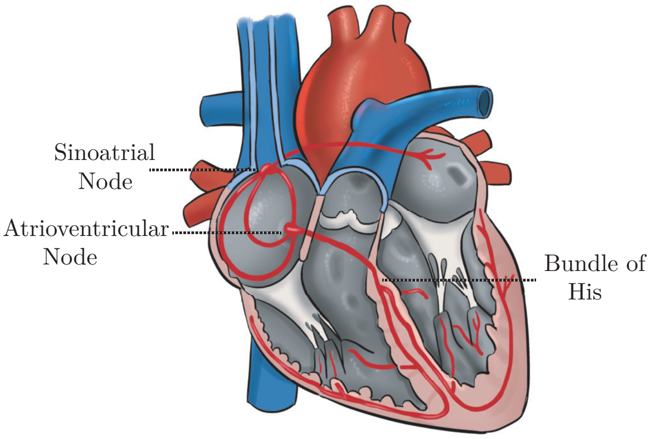

Figure 2.4. **Simplified representation of the cardiac electric conduction system [131].**

There are specialised myocytes located at various regions of heart that can produce the electrical impulses at a regular interval, which are collectively known as pacemaker cells. The action potentials generated at heart's major pacemaker cells known as sinoatrial (SA) node initiate and coordinate the heart rhythm. It should be noted that SA node is situated in the right atrium as shown in Figure 2.1(b), where the rate at which action potentials are generated ranges between 60 to 100 per minute[131]. The action potentials from SA node propagate through atrial myocytes causing the mechanical contraction of atria that results in blood flow to ventricles. These action potentials are then collected by atrioventricular (AV) node, which conducts the action potentials to the ventricles at a slower rate, approximately 40 to 55 beats per minute [131]. This ensures that the atria have adequate time to contract before the contraction of ventricles occurs. From the AV node, action potentials are then propagated to common Bundle of His located at the upper portion of the ventricle. The action potentials propagate along the left and right bundle branches and then subdivide into extensive networks of Purkinje fibers spreading throughout the ventricular muscles. This action potential propagation sequences through Purkinje allows the contraction of ventricles and pumping of the de-oxygenated blood to the lungs and oxygenated blood to the body tissues. This constitutes one complete cycle of cardiac heart rhythm [130]. Since normally, the heart is initially excited by the activation sequences at SA node, the normal heart rhythm is also known as normal sinus rhythm (NSR). The electrical activation sequences must be in an organised manner to synchronise the mechanical activity of heart and thereby to coordinate the blood flow to the rest of

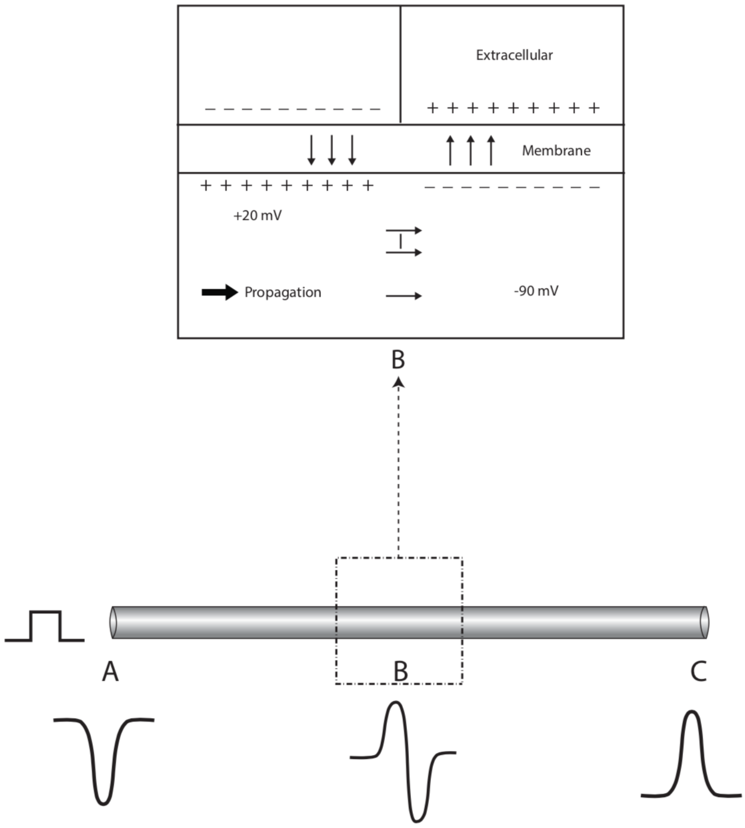

Figure 2.5. **Schematic representation of the extracellular potential field.** Here, a stimulus current is applied at the left end of the fibre, which propagates through the fibre. Each alphabet denotes a sensor location associated with electrogram measurements.

the body parts. However, unexpected interruptions in the excitation of electrical activation sequences at SA node or the during the propagation of electrical activation waves through the normal pathways, affect the NSR and result in dangerous abnormal heart rhythm or cardiac arrhythmia [90].

The depolarisation of cardiac cells also creates current flow into the extracellular medium [147]. The underlying electrophysiology of generation of extracellular potentials can be illustrated using the example in Figure 2.5. For this, cardiac tissue is considered to be a cylindrical fibre in which the cells are tightly arranged and located in an infinite volume conductor [126]. A stimulus current is then applied at the left end of the fibre, which causes the action potentials to propagate from the left side to right side. At any point along the propagation of activation wave, potential difference is created in axial direction between the active and inactive sites. This potential gradient is maximum at the front of activation wave and causes axial current flow from activated to inactivated sites. Moreover, to preserve the conservation of charges, some currents also propagate into extracellular and intracellular spaces at the front and back of activation wave front. This implies that the activation wave front acts as a current dipole as shown in Figure 2.5. The resulting extracellular potential created from current flow is positive in front of activation wave front and negative at the back of activation wave front [43]. At the sensor location denoted as A and C in Figure 2.5, the resulting electrograms are monophasic with negative and positive deflections. On the other hand, the resulting electrogram is biphasic at any sensor location in the middle of the fibre (see Figure 2.5, location B).

The extracellular potentials can be measured using electrodes placed at body surface [95] or directly at the surface of heart [57, 116]. These measurements enable to monitor the function of heart and are widely used for diagnosis and treatment of arrhythmia. The electrocardiogram (ECG) is an important example of body surface measurements of cardiac activity [95]. A cardiac cycle observed in ECG during NSR is shown in Figure 2.6.

It can be seen that ECG during NSR has important characteristics. The initial stage of cardiac cycle is represented as P wave. This stage corresponds to the atrial depolarisation, which is followed by QRS complex reflecting the depolarisation of ventricles. QRS complex also masks the repolarisation of atria. The final stage of cardiac cycle is ventricular repolarisation which is denoted as T wave in ECG. During ventricular arrhythmia, the rate of heart rhythm in ventricles is

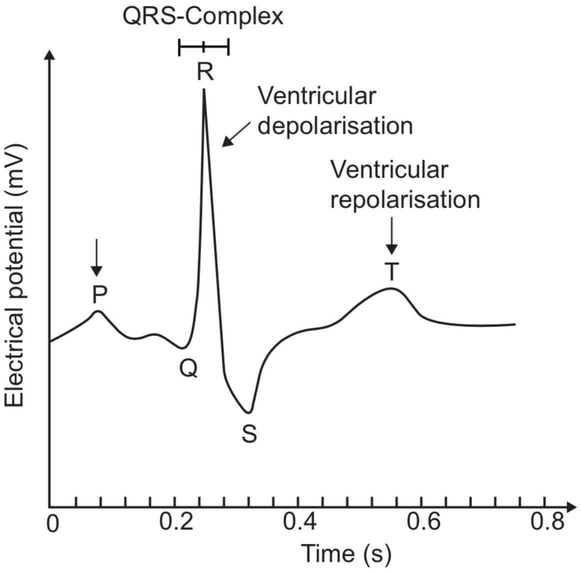

Figure 2.6. Example of one cardiac cycle in sinus rhythm represented by electrocardiogram.

higher compared to that of atrial rate. The heart rate during VT is typically 100 to 200 beats per minute and this is reflected in ECG with higher number of QRS complexes [89]. On the other hand, heart rate during VF is around 550 beats per minute [74] with zero cardiac output.

Electrical activation sequences that are recorded directly from cardiac muscle walls are known as intracardiac electrograms. Cardiac activity can be mapped from endocardium or epicardium surface of the heart using electrical or optical mapping techniques [31]. In electrical mapping method, electrograms are measured either as unipolar or bipolar electrograms. A bipolar electrogram is generated by connecting both cathode (positive) and anode (negative) electrodes to the cardiac tissue region. The resulting electrogram is obtained by subtracting the voltages in two electrograms. On the other hand, a unipolar electrogram is generated by connecting the cathode to tissue region whereas negative electrode is placed outside the heart. This is to ensure that the negative electrode gives zero potential and as a result, unipolar electrograms provide the information from one particular spatial location [44].

An example of electrical mapping during human VF is given in [116]. Intracardiac electrograms during human VF are measured from epicardial surface of heart using an elasticated sock consisting of an array with 256 unipolar electrodes. A complete mapping of both epicardium and endocardium during VF is detailed in [100]. The epicardial electrograms were acquired using 112 electrodes attached to elasticated sock. In order to map endocardial electrograms an extensible balloon catheter with an array of 112 electrodes is used. This balloons were then inflated after the insertion to endocardium for collecting the electrograms. Generally spatial resolution of the electrodes arrangement in electrical mapping is lower. On the other hand, optical mapping techniques generate transmembrane voltage measurements with high spatiotemporal resolution [57]. This mapping technique is based on fluorescence phenomenon, and uses voltage-sensitive dyes to capture the changes in transmembrane voltage across the cell membrane [93]. However, clinical practice of the optical mapping techniques is restricted as the voltage-sensitive dyes may be toxic, and potentially alter the underlying tissue properties [155].

As described in Section 1.1, all the experimental techniques described above acquire electrical activation sequences, especially during cardiac arrhythmia have following limitations: (1) Clinically challenging [18]. (2) Restricted to the surface of the heart [31]. (3) Unable to provide the electrophysiological interpretations at the tissue-level and cell-level [69]. Therefore, the underlying mechanisms of the cardiac electrical dynamics at the different spatial scales remain unidentified.

2.2 Models of Cardiac Electrophysiology

Mathematical models of cardiac electrophysiology provide a quantitative description of the cardiac activation and recovery patterns on spatial scale from cell level to the body surface [32, 33, 162]. In order to better understand the cardiac electrical dynamics at various spatial scales, an integrated model of electrophysiology is considered in this thesis. The integrated model equations are formulated to incorporate the action potential dynamics at the cell-level, tissue-level and extracellular-level. In order to identify a suitable cardiac model structure that can be employed for estimation methodology, this section reviews the existing models of the cell-level, tissue-level, and extracellular electrogram-level from the literature of cardiac electrophysiology.

2.2.1 Cell-level Modelling

Cell-level models aim to quantitatively describe the action potential in a single cell resulting from the ionic flow across the membrane. This ionic flow consequently creates the change in transmembrane potential. The mathematical description of this process can be derived by representing the small area of cell membrane as an equivalent electrical circuit. Figure 2.7 shows a schematic diagram of the electrical circuit. This model is often referred to as parallel conductance model since it consists of a capacitor connected in parallel with series of variable resistors and batteries [126]. Here, the membrane is represented as a capacitor whereas conductance and the Nernst potential of ion channels are represented using variable resistors and batteries [33].

In this model, the rate of change of transmembrane voltage from a single cell triggered by an external stimulus is given as

$$\frac{\partial v}{\partial t} = \frac{-(i^{ion} + i^{st})}{\kappa_m}, \tag{2.2}$$

where κ_m is the cell membrane capacitance per unit area (F m^{-2}), i^{st} is the external stimulus current per unit area (A m^{-2}). The negative sign is used to denote the inward flow of positive ions into the cell depolarises the transmembrane voltage. Also, i^{ion} is the total ionic current per unit area (A m^{-2}) given by

$$i^{ion} = \sum_n i_n, \tag{2.3}$$

where i_n is the current per unit area of an ion n. This is generally divided into inward and outward ionic currents depending on whether the ion depolarises or

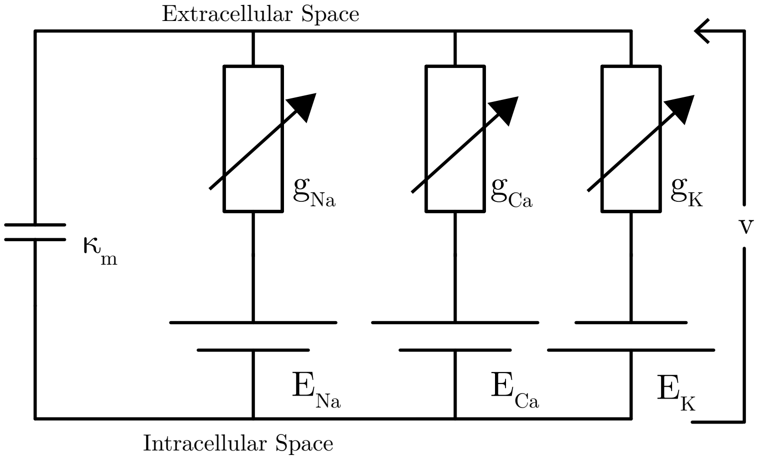

Figure 2.7. Simplified diagram of an equivalent electrical circuit that represents ionic flow across the cell membrane.

repolarises the cell membrane.

To reproduce the key characteristics of action potentials, the parameters in (2.2) should be incorporated accurately into the modelling framework. The stimulus current is generally modelled as pulses with a magnitude (v^{st}) and duration (T^{st}). The total ionic current is normally modified depending on the type of ions selected for the model. However, a general form of individual ionic current can be described using Ohm's law. By this, individual current component is proportional to the deviation of transmembrane potential from its equilibrium potential. This is mathematically described as

$$i_n = g_n(v - E_n), \tag{2.4}$$

where g_n is the proportionality constant representing the conductance of ion channel and E_n is the Nernst potential or equilibrium potential of an ion n.

An important example of parallel conductance model is Hodgkin and Huxley model of action potential generation of nerve cell [67]. Sir Alan Llyod Hodgkin and Sir Andrew Fielding Huxley formulated the quantitative description of ionic current mechanisms using the measurements collected from squid giant axon. The total ionic current in Hodgkin and Huxley model is separated into sodium, potassium and leakage currents. This can be rewritten using (2.4) to an alternate form as

$$i^{ion} = g_K(v - E_K) + g_{Na}(v - E_{Na}) + g_L(v - E_L), \tag{2.5}$$

where g_K, g_{Na} and g_L are the conductance associated with each ion. These are nonlinear functions and for an arbitrary ion, the formulation of conductance in

Hodgkin and Huxley model can be written as

$$g_n = \overline{g_n} h, \tag{2.6}$$

where $\overline{g_n}$ is the maximal conductance and h is the gating variable, which enables to characterise the opening and closing of ion channels, ranges between 0 and 1. The gating mechanism is an important property as it describes the probability that a specific ion channel is opened to allow the ionic flow into membrane. The time evolution of a gating variable is governed by first order differential equation

$$\frac{\partial h}{\partial t} = a_h(1-h) - b_h h, \tag{2.7}$$

where a_h and b_h are the rate constants of the gating variable h.

Hodgkin and Huxley model provides the basis to describe electrical properties of action potential from wide range of excitable cells. In the early 1960s, Denis Noble formulated the first electro-physiological model of a cardiac cell based on Hodgkin and Huxley model [118]. This model was developed based on the measurements from Purkinje fibre cells. This model is similar to Hodgkin and Huxley model consisting of sodium, potassium, and leakage currents. However, the cardiac action potential characteristics is obtained in Noble model by separating the conductance of potassium ions into inward and outward components, and identifying the model parameters from the experimental data. [119]. Since then, several cardiac cell models have been developed to study the underlying mechanisms of action potentials generation. Currently, over two hundred and fifty cardiac cell models exist differing in both level of complexity and the ability to describe the electrophysiological properties. The detailed description of these models is given in CellML physiome repository [1]. Briefly, the ventricular cell models are broadly classified into following groups:

First Generation Models

First generation models aim to reproduce the action potential characteristics using the underlying electrophysiological cell level dynamics. These models utilise the biophysically detailed description of ion channel, pump and exchanger currents [32]. The model formulation is similar to that of Hodgkin and Huxley model, where subset of relevant ionic currents is described as a function of maximal conductance and gating variables given in (2.6) and (2.7) respectively. Although these models are considered to be biophysically detailed, the level of complexity causes higher computational load for large-scale simulation studies [32]. Examples of first generation models include Beeler-Reuter model (8 variables) [13] and Luo-Rudy-1 model (8 variables) [96].

Second Generation Models

Similar to first generation models, second generation models are biophysically detailed and incorporate the ionic current properties in the model formulation [5]. In addition to this, these models also incorporate the intercellular concentration of each ion. As a result, second generation models contain more variables and higher level of complexity than the first generation models, which inherently increases the computational load [32]. Some of the examples are Luo-Rudy-2 model (15 variables) [97], Priebe-Beukelmann model (17 variables) [129] and Ten Tusscher-Noble-Noble-Panfilov model (17 variables) [150].

Simplified Two-Variable Models

Simplified models reproduce the macroscopic behaviour of cellular activity by mitigating the level of complexity in biophysically detailed models. This is achieved by replacing the large number of ionic currents as two state variables, which describe the depolarisation and repolarisation characteristics [130]. These models are computationally inexpensive to solve and are generally used for large-scale simulation of excitable systems [32]. An important example is FitzHugh-Nagumo (FHN) model with its two variables for excitation and recovery dynamics in a cell [48]. Several variants of FHN model equations exist in the literature [161]. However, a general model structure can be written as

$$\frac{da_e}{dt} = \psi_1(a_e, a_r), \tag{2.8}$$

$$\frac{da_r}{dt} = \psi_2(a_e, a_r), \tag{2.9}$$

where a_e and a_r are the excitation and recovery variables, $\psi_1(a_e, a_r)$ is a cubic polynomial function and $\psi_2(a_e, a_r)$ is a linear function of its variable. The behaviour of FHN model is typically studied using phase plane analysis — technique used to analyse two-equation systems by plotting the respective trajectories on a two-dimensional plane with axes as the two dependant variables [87].

Although simplified representation guarantees minimal computational complexity, model equations are described in generic form that can be applied for several excitable systems. As a result these models fail to capture some of the important quantitative properties of the cardiac action potential, such as shape and restitution properties. Several variants of FHN model have been developed to reproduce cardiac action potential with these properties [6, 92].

Phenomenological Models

Phenomenological models resolve the limitations of two-variable models by capturing the important features of cardiac cell dynamics by including the restitution properties. The simplified electrophysiological properties are incorporated using a minimum set of ionic currents and gating variables that are computationally easier to solve. Examples are Fenton-Karma model [47] and Mitchell-Schaeffer model [108]. Fenton-Karma model consists of three state variables and thirteen parameters. This model is obtained from the simplification of Luo-Rudy I model. On the other hand, Mitchell-Schaeffer model is simplified from the Fenton-Karma model, which consists of two state variables and five parameters. In both models, state variables are dynamic in nature and represented using a system of ODEs. The primary state variable is the transmembrane voltage v, formed by the total flow of ionic current across the cell membrane and is described by

$$\frac{dv}{dt} = i^{in}(v,h) + i^{out}(v,h) + i^{st}, \tag{2.10}$$

where $i^{in}(v,h)$ and $i^{out}(v,h)$ represents the inward and outward ionic currents to the cell that contributes to increase and decrease the transmembrane potential respectively. The other state variables are primarily used to represent the gating properties of ionic channels. In (2.10), gating variable is denoted by h . Moreover, the model also includes time constants as parameters to characterise the opening and closing of ionic channels.

2.2.2 Tissue-level Modelling

The fundamental aim of modelling the electrical activity at tissue level is to describe the action potential propagation by integrating the informations from cellular models. Cardiac tissue can be modelled using either discrete or continuum-based approaches. The discrete modelling approach involves representing the characteristics of individual cells and utilises separate variables to describe cell-to-cell connections. These variables of individual cell properties include cell size, regional characteristics, capacitance and conductance at gap junctions [130]. As a result discrete models of tissue level are computationally expensive, especially for the large scale simulation studies. On the other hand, continuum-based modelling approach considers cardiac tissue as a functional syncytium in which the cell functions as a unit to allow smooth action potential propagation [33]. Majority of the theoretical and computational studies to quantify the complex spatiotemporal cardiac activity use continuum-based mathematical models. These models are described using PDEs to incorporate the spatial diffusion of action potentials across the tissue. They are briefly introduced in this section below.

Bidomain Tissue Model

In bidomain modelling approach, cardiac tissue is considered as functional syncytium that consists of intracellular and extracellular domains [65]. The transmembrane potential can be determined using (2.1). The bidomain model has two equations [130]. The first equation describes the extracellular potential integrated (∇v^{ex}) when the transmembrane voltage distribution (∇v) is known

$$\nabla \cdot (\mathbf{G}_{in} \nabla v) = -\nabla \cdot ((\mathbf{G}_{in} + \mathbf{G}_{ex}) \nabla v^{ex}), \tag{2.11}$$

where $\mathbf{G}_{in}$ and $\mathbf{G}_{ex}$ are the conductivity tensors are intracellular and extracellular spaces, respectively.

The second equation of the bidomain model is used to calculate the transmembrane potential at each step

$$\nabla \cdot \mathbf{G}_{in} (\nabla v + \nabla v^{ex}) = -q_m (\kappa_m \frac{dv}{dt} + i^{ion} + i^{st}), \tag{2.12}$$

where q_m is the surface-to-volume ratio (cm^{-1}) of the membrane. The values of surface to volume ratio and specific capacitance used in simulation studies ranges between 1000 to 5000 Cm^{-1} and 1 μ F cm^{-2} [33], respectively.

The intracellular and extracellular conductivity tensors in (2.11) and (2.12), are generally determined based on the anisotropic properties along the microstructural directions in the cardiac tissue [34, 131]. The microstructural directions are represented using a orthogonal coordinate system in three main axes along the cardiac tissue. The orientation and end-to-end coupling of cardiac cells are defined to follow along the first principal axis called fibre axis. These fibres are then arranged into laminar structures called as sheets. The plane perpendicular to both sheet and fibre is the cross-sheet plane [131]. Typical range for the magnitude of intracellular conductivity is 0.17 - 0.45 Sm^{-1} in longitudinal direction (along the fibre axis) and 0.019 - 0.06 Sm^{-1} in traverse direction (along the sheet axis). The extracellular conductivity lies between 0.12 - 0.62 Sm^{-1} in longitudinal direction and 0.08 - 1.74 Sm^{-1} in traverse direction. Moreover, it should be noted that the external stimulus current i^{st} is applied at both intracellular and extracellular domains [32].

Monodomain Tissue Model

Monodomain model formulation is based on the assumption that conductivity tensor in extracellular space is proportional to the conductivity tensor in intracellular space ($\mathbf{G}_{in} = b\mathbf{G}_{ex}$) [33]. This assumption results in a simplified model in which the anisotropy of both domains are same and deduce to a simplified representation of bidomain models [32]. The monodomain equation is given by

$$\frac{\partial v}{\partial t} = \nabla \cdot (\mathbf{\Theta}_g \nabla v) - \left(\frac{i^{ion} + i^{st}}{\kappa_m} \right), \tag{2.13}$$

where $\mathbf{\Theta}_g$ ($cm^2 ms^{-1}$) is the diffusion tensor and depends on the anisotropy in fibre, sheet and cross-sheet directions [33]. For an isotropic tissue, diffusion is assumed to be same in all directions and is given by [34]

$$\theta_g = \frac{G_i}{q_m \ \kappa_m} \tag{2.14}$$

where the typical value of isotropic longitudinal diffusion coefficient is 0.001 cm^2 ms^{-1} and 0.0005 cm^2 ms^{-1} and transverse diffusion coefficient is 0.001 cm^2 ms^{-1} and 0.00025 cm^2 ms^{-1} [32, 34].

2.2.3 Extracellular Electrograms Modelling

The modelling of cardiac electrograms involves quantifying the extracellular potentials generated from the currents at discrete cell positions and emerges to extracellular space. Thus the cell positions are considered to be point sources located in a conducting medium. The derivations of extracellular potentials for different types of point source conditions are given in [126]. One expression for unipolar extracellular electrogram is derived using the dipole source density of the transmembrane potential at locations in a spatial field. This approach has been implemented in simulation studies for understanding the dynamics of normal and arrhythmic cardiac activity [22, 35, 56, 126].

For a spatial field $\mathbf{s} = (s_x, s_y, s_z)$ with varying transmembrane voltage, the electrogram recorded at time t at a point sensor $\mathbf{s}' = (s'_x, s'_y, s'_z)$ can be modelled as follows

$$v^{ex}(\mathbf{s}', t) = \tilde{\kappa} \iiint (-\nabla v_t(\mathbf{s})) \cdot \nabla \left[\frac{1}{r} \right] ds_x ds_y ds_z, \tag{2.15}$$

where $\tilde{\kappa}$ is a constant that relates the cross-sectional area of the fiber and ratio of intracellular and extracellular conductivities. The Euclidean distance r is calculated between each location in the spatial field and the point sensor by

$$r = \sqrt{(s_x - s_x{}')^2 + (s_y - s_y{}')^2 + (s_z - s_z{}')^2}. \tag{2.16}$$

2.3 Estimation of the Cardiac Electrical Dynamics

Section 2.1 illustrated the limitations of available experimental techniques that hinders the dynamics at cellular and tissue levels during normal and arrhythmic conditions. Therefore, reconstruction of the underlying electrical dynamics of the tissue from the observed measurements is crucial, as it enables to elucidate the unobserved spatiotemporal behaviour of the complex electric dynamics. As described in Section 1.1, estimation methods can be used to infer the required quantities from the indirect, inaccurate and noisy measurements [11]. The estimation methodology based on the physiologically relevant cardiac models is important, as the models provide meaningful descriptions of state variables and parameters of the cardiac electrical dynamics at unobserved spatial scales. Systems theory provides model-based estimations, which can be used to infer the state variables or parameters from the electrophysiology data.

In statistical estimation theory, standard estimation techniques are generally based on finite-dimensional model representations. Stochastic state-space model are a class of widely used finite dimensional model structures, instrumental in the field of modelling and estimating of complex biological systems [9, 82]. In particular to cardiac modelling, a recent study [141] has demonstrated that the stochastic state-space representation of biophysically-detailed cell-level model can be used to investigate the repolarisation variability. The additive state disturbances are incorporated to account for the intrinsic or beat-to-beat variability within a cell. In this thesis, model-based estimation of cardiac electrical dynamics is presented in a state-space modelling framework, where the state variables and parameters of the cardiac models describe the spatiotemporal characteristics of electrical activity.

This thesis focusses on the estimation of dynamically changing state-variables described in the cardiac models, which is a state estimation problem. In order to provide better understanding of the model-based estimation methodology, the following subsections details the fundamental concepts of state-space models and briefly review the state estimation methods, which are more relevant to the methodologies proposed in Chapter 4 and Chapter 5.

2.3.1 State-space Models

In systems that are dynamic in nature, the states are defined as a collection of dynamic variables that enable to capture the important properties of a system. The evolution of changes in the dynamics of states is mathematically described using state evolution equation, which is coupled with a certain level of state disturbances. This disturbance is usually included to accommodate the uncertainties and errors in the modelling of system dynamics. The state evolution equation of a discrete time system can be written as

$$\mathbf{x}_{k+1} = \mathbf{f}_k(\mathbf{x}_k, \boldsymbol{\epsilon}_k^x), \tag{2.17}$$

where $\mathbf{x}_k \in \mathbb{R}^{n_x}$ and $\boldsymbol{\epsilon}_k^x \in \mathbb{R}^{n_x}$ are the vectors of n_x state variables and the state disturbances, respectively. System model dynamics is given by $\mathbf{f}_k(.)$ that maps the system state dynamics from the current time instant (k) to the next time instant ($k+1$). Depending on the nature of system, the $\mathbf{f}_k(.)$ linear or non-linear, time-varying or time-invariant. It is noteworthy that the state evolution equation follows the Markovian property. This implies that the future state of the state-space model only depends on the present state and conditionally independent of all the other past states.

States are generally hidden variables and observed through the noisy measurements. The dynamics of measurement process is mathematically described using observation equation, coupled with noise sequences is given by

$$\mathbf{y}_k = \mathbf{m}_k(\mathbf{x}_k, \boldsymbol{\epsilon}_k^y), \tag{2.18}$$

where $\mathbf{y}_k \in \mathbb{R}^{n_y}$ and $\boldsymbol{\epsilon}_k^y \in \mathbb{R}^{n_y}$ are the observation vector from n_y measurements and the measurement noise respectively. $\mathbf{m}_k(.)$ is the measurement model used to describe the relationship between the states of system to the measurements.

The inclusion of both state disturbances and measurement noises into the model equations forms the stochastic state-space models. More specifically, the disturbances can be assumed as random sequences sampled from a distribution with mean and covariance. In this thesis, they are considered to be $\mathcal{N}(\mathbf{0}, \Sigma)$, implying independent Gaussian distribution with zero mean and known covariance (Σ).

2.3.2 State Estimation Methods

One of the important problems in state-space modelling framework is to estimate the hidden states of the system. In systems theory, the process of computing the optimal estimate of states from the noisy observations is known as state estimation. The state estimation methods can be broadly classified into optimal filtering and smoothing. Filtering is the process of estimating the current states of system $\hat{\mathbf{x}}_k^f$ given all the previous and current measurement sequences as $\mathbf{y}_{1:k} = \{\mathbf{y}_1, \mathbf{y}_2, .., \mathbf{y}_k\}$. In Bayesian filtering context, it is the process of computing the filtering distributions $p(\hat{\mathbf{x}}_k^f | \mathbf{y}_{1:k})$ with $\mathbf{y}_{1:k} = \{\mathbf{y}_1, \mathbf{y}_2, .., \mathbf{y}_k\}$. The second state estimation method is the optimal smoothing, concerned with computing the estimate of states at time instant k as $\hat{\mathbf{x}}_k^s$, given the measurements up to a time instant T as $\mathbf{y}_{1:T} = \{\mathbf{y}_1, \mathbf{y}_2, .., \mathbf{y}_T\}, T > k$. In a similar way, bayesian smoothing computes the smoothing distributions $p(\hat{\mathbf{x}}_k^s | \mathbf{y}_{1:T})$, with $\mathbf{y}_{1:T} = \{\mathbf{y}_1, \mathbf{y}_2, .., \mathbf{y}_T\}$ [145].

Filtering Methods for State Estimation

In 1960, R.E.Kalman developed the well known Kalman filter to obtain the closed form solution for the linear Guassian filtering problem [84]. The derivation and algorithm of the Kalman Filter is presented in Appendix A. However, most of the real world systems are nonlinear in nature, where the state evolution and measurement models are nonlinear and the resulting distributions of the unknown states are non-Gaussian. Non-Gaussian models are not considered in this thesis. Since the Kalman Filter (KF) is tailored for specifically linear models, it cannot be applied directly to nonlinear filtering problems. Moreover, the state variables in the models of tissue and cell follow nonlinear characteristics. This illustrates the importance of nonlinear state estimation problem in the cardiac modelling domain.

The general form of a nonlinear state-space model is given by

$$\mathbf{x}_{k+1} = \mathbf{f}_k(\mathbf{x}_k) + \boldsymbol{\epsilon}_k^x, \tag{2.19}$$

$$\mathbf{y}_k = \mathbf{m}_k(\mathbf{x}_k) + \boldsymbol{\epsilon}_k^y, \tag{2.20}$$

where $\mathbf{f}_k(.)$ and $\mathbf{m}_k(.)$ are nonlinear functions. The state disturbances $\boldsymbol{\epsilon}_k^x$ and measurement noise $\boldsymbol{\epsilon}_k^y$ follows Gaussian distribution with covariance described as above.

Over the years, several extensions of the Kalman Filter have been developed to solve the nonlinear filtering problem. The state estimation in a nonlinear state space model form requires the implementation of Gaussian approximation methods to the filtering distribution. One of the commonly used approximation methods is the linearisation of nonlinear model functions at the most recent state estimate value. This forms the fundamental basis of Extended Kalman Filter (EKF), where the linearisation is employed based on first order Taylor series expansion.

Due to the local linearisation procedure, the implementation of EKF effects the estimation accuracy in systems with higher order nonlinearities. Other disadvantages of EKF are the actual computation involved in the calculation of Jacobian matrix especially for higher order partial derivatives, and the requirement of state evolution and measurement models to be differentiable functions [145]. Another well-known approximation method used in nonlinear filtering is Unscented Transform (UT), which is based on a deterministic sampling method. In this method, a finite number of sampling points also known as sigma points, are selected to capture the mean and covariance of the original state distribution. The sigma points are then propagated through the nonlinear model functions, after which the mean and covariance of the posterior distributions are computed.

To illustrate the UT method, consider an example where a random variable $\mathbf{x} \sim \mathcal{N}(\bar{\mathbf{x}}, \mathbf{P})$ following a nonlinear model function $\mathbf{f}(\mathbf{x})$ [145]. Instead of linearising the nonlinear model function, UT directly approximate the mean and covariance of the target state density by a Gaussian distribution. For this sigma points are computed using mean and covariance estimates are computed as

$$\chi_0 = \bar{\mathbf{x}}, \tag{2.21}$$

$$\chi_j = \bar{\mathbf{x}} + \left(\sqrt{(n_x + \lambda)\mathbf{P}}\right)_j, \quad j = 1, ..., n_x \tag{2.22}$$

$$\chi_j = \bar{\mathbf{x}} + \left(\sqrt{(n_x + \lambda)\mathbf{P}}\right)_j, \quad j = n_x + 1, ..., 2n_x \tag{2.23}$$

where $\left(\sqrt{(n_x + \lambda)\mathbf{P}}\right)_j$ is defined to be j^{th} a column in the scaled matrix square root of covariance matrix $\mathbf{P}$. It can be seen that UT method generates $2n_x + 1$ sigma points in the approximation with a scaling parameter λ given by

$$\lambda = \alpha^2(n_x + \kappa) - n_x, \tag{2.24}$$

where α and κ are the algorithm parameters used to regulate the spread of the sigma points around the mean $\bar{\mathbf{x}}$. In this thesis, the magnitude of α is set to 10^{-3} and κ to be $3 - n_x$ [9, 77]. The sigma points are then propagated through the nonlinear model function to calculate the transformed sigma points as

$$\hat{\chi}_j = \mathbf{f}(\chi_j). \quad j = 0, ..., 2n_x \tag{2.25}$$

The mean and covariance estimates of the transformed nonlinear points are then computed as

$$\mathbb{E}\left[\mathbf{f}(\mathbf{x})\right] \approx \bar{\mathbf{x}}_s = \sum_{j=0}^{2n_x} W_j^{(m)} \hat{\mathcal{X}}_j, \tag{2.26}$$

$$Cov\left[\mathbf{f}(\mathbf{x})\right] = \mathbf{S}_s = \sum_{j=0}^{2n_x} W_j^{(c)} (\hat{\mathcal{X}}_j - \bar{\mathbf{x}}_s)(\hat{\mathcal{X}}_j - \bar{\mathbf{x}}_s)^\top, \tag{2.27}$$

where $W_i^{(m)}$ and $W_i^{(c)}$ are the constant weights of the mean and covariance, calculated using

$$W_0^{(m)} = \frac{\lambda}{n_x + \lambda}, \tag{2.28}$$

$$W_0^{(c)} = \frac{\lambda}{n_x + \lambda} + (1 - \alpha^2 + \beta), \tag{2.29}$$

$$W_j^{(m)} = W_j^{(c)} = \frac{1}{2(n_x + \lambda)}, \quad j = 1, ..., n_x \tag{2.30}$$

where the additional parameter β is used to include the prior information of the distribution of the random variable $\mathbf{x}$. For Gaussian random variables, β is set to two [64].

The unscented transform approach above described is used in UKF algorithm to approximate the filtering distribution of nonlinear model functions, which enables to estimate the state variables [77, 159]. This can be described in terms of conditional densities as following

$$p(\mathbf{x}_k | \mathbf{y}_k) \simeq \mathcal{N}(\mathbf{x}_k | \hat{\mathbf{x}}_k^f, \mathbf{P}^f), \tag{2.31}$$

where $\hat{\mathbf{x}}_k^f$ and $\mathbf{P}^f$ are the mean and covariance estimates calculated using the algorithm.

A recent study in [142] has employed UKF based joint estimation approach for studying the intrinsic variability in a single cardiac cell. To reconstruct the cellular dynamics, the study used the noise corrupted versions of transmembrane voltage as measurements. The augmented UKF algorithm was then employed to infer the state variables (filtered transmembrane voltage and gating variables) and model parameters (maximal ionic conductances) using a stochastic ionic model. This study highlights the importance to extend the estimation algorithm for reconstructing the tissue dynamics, where the resulting estimation problem is for the high-dimensional state-space models. The UKF algorithm that can be used to compute the filtered state estimates are given in Algorithm 2.1. As it can be seen that the UKF based filtering does not require the model functions to be differentiable. Also, the state estimation using UKF demonstrated superior performance over EKF as it can capture higher order moments by using several sampling points in the approximation [78].

Algorithm 2.1: *State Estimation using the Unscented Kalman filter.*

---

1. Initialise states $\hat{\mathbf{x}}_o^f$ and covariance matrix $\mathbf{P}_o^f$.
2. **Recursive estimation** for $k \in \{0, 1, 2, ..T-1\}$.

Prediction:

(a) Compute the sigma points for $\hat{\mathbf{x}}_k^f$

$$\begin{aligned} \chi_{k,j} &= \hat{\mathbf{x}}_k^f, \\ \chi_{k,j} &= \hat{\mathbf{x}}_k^f + \left(\sqrt{(n_x + \lambda)\mathbf{P}_k^f} \right)_j, \quad j = 1, ..., n_x \\ \chi_{k,j} &= \hat{\mathbf{x}}_k^f - \left(\sqrt{(n_x + \lambda)\mathbf{P}_k^f} \right)_j, \quad j = n_x + 1, ..., 2n_x \end{aligned} \tag{2.32}$$

where λ is given in (2.24).

(b) Propagate the sigma points through state evolution equation

$$\hat{\chi}_{k+1,j}^{-} = \mathbf{f}(\chi_k). \tag{2.33}$$

(c) Compute the predicted mean and covariance estimates $\hat{\mathbf{x}}_{k+1}^{f-}$ and covariance matrix $\mathbf{P}_{k+1}^{f-}$ as

$$\hat{\mathbf{x}}_{k+1}^{f-} = \sum_{j=0}^{2n_x} W_j^{(m)} \hat{\chi}_{k+1,j}^{-} \tag{2.34}$$

$$\mathbf{P}_{k+1}^{f-} = \sum_{j=0}^{2n_x} W_j^{(c)} (\hat{\chi}_{k+1,j}^{-} - \hat{\mathbf{x}}_{k+1}^{f-})(\hat{\chi}_{k+1,j}^{f-} - \hat{\mathbf{x}}_{k+1}^{f-})^\top + \Sigma_{\epsilon^x}, \tag{2.35}$$

where $W_i^{(m)}$ and $W_i^{(c)}$ are the weights given in equations (2.28), (2.29) and (2.30).

Correction:

(a) Compute the sigma points

$$\begin{aligned} \chi_{k+1,j}^{-} &= \hat{\mathbf{x}}_{k+1}^{f-}, \\ \chi_{k+1,j}^{-} &= \hat{\mathbf{x}}_{k+1}^{f-} + \left(\sqrt{(n_x + \lambda)\mathbf{P}_{k+1}^{f-}} \right)_j, \quad j = 1, ..., n_x \\ \chi_{k+1,j}^{-} &= \hat{\mathbf{x}}_{k+1}^{f-} - \left(\sqrt{(n_x + \lambda)\mathbf{P}_{k+1}^{f-}} \right)_j, \quad j = n_x + 1, ..., 2n_x \end{aligned} \tag{2.36}$$

(b) Propagate the sigma points through nonlinear observation model equation

$$\tilde{\chi}^{-}_{k+1,j} = \mathbf{g}(\chi_k), \quad j = 0, ..., 2n_x \tag{2.37}$$

(c) Compute the predicted mean and covariance estimates as

$$\bar{\mathbf{y}}^{f-}_{k+1} = \sum_{j=0}^{2n_x} W_j^{(m)} \tilde{\chi}^{-}_{k+1,j}, \tag{2.38}$$

$$\mathbf{P}^{yy}_{k+1} = \sum_{j=0}^{2n_x} W_j^{(c)} (\tilde{\chi}^{-}_{k+1,j} - \bar{\mathbf{y}}^{f-}_{k+1})(\tilde{\chi}^{-}_{k+1,j} - \bar{\mathbf{y}}^{f-}_{k+1})^{\top} + \Sigma_{\epsilon^x}, \tag{2.39}$$

$$\mathbf{P}^{xy}_{k+1} = \sum_{j=0}^{2n_x} W_j^{(c)} (\chi^{-}_{k,j} - \hat{\mathbf{x}}^{f-}_{k+1})(\tilde{\chi}^{-}_{k+1,j} - \bar{\mathbf{y}}^{f-}_{k+1})^{\top}, \tag{2.40}$$

where $W_i^{(m)}$ and $W_i^{(c)}$ are the weights given in equations (2.28), (2.29) and (2.30).

(d) Compute filter gain, $\mathbf{K}^{f}_{k+1} = \mathbf{P}^{xy}_{k+1} \left[\mathbf{P}^{yy}_{k+1}\right]^{-1}$.

(e) Correct the state estimate : $\hat{\mathbf{x}}^{f}_{k+1} = \mathbf{x}^{f-}_{k+1} + \mathbf{K}^{f}_{k+1}(\mathbf{y}_{k+1} - \bar{\mathbf{y}}^{f-}_{k+1})$.

(f) Correct the error covariance matrix, $\mathbf{P}^{f}_{k+1} = \mathbf{P}^{f-}_{k+1} - \mathbf{K}^{f}_{k+1}\mathbf{P}^{yy}_{k+1}\mathbf{K}^{\top}_{k+1}$.

Smoothing Methods for State Estimation

The main difference between filtering and smoothing is that the later method incorporates the future information within the measurement sequence. This allows to compute more accurate and less noisy state estimates. Smoothing methods are broadly classified into the following three categories

- Fixed-point smoothing: At every iteration of time instants, the goal is to estimate the smoothed state at a fixed time instant in the past with respect to the current measurement. This can be expressed as $\hat{\mathbf{x}}^{s}_{j|k}$, where j is fixed value with measurements are added at the time instants of $k = \{j+1, j+2, ..\}$ [19].
- Fixed-lag smoothing: At every iteration of time instants, the goal is to estimate the smoothed state at a fixed lag in the past with respect to the current

measurement. This can be expressed as $\hat{\mathbf{x}}^s_{k-k_\tau|k}$, where k_τ is fixed positive lag value with measurements are added as $k = \{0, 1, 2, ..\}$. This smoothing can be applied online but with a delayed value [19].

- Fixed-interval smoothing : At every iteration of time instants, the goal is to estimate the smoothed state in a fixed time interval given all the measurements within the observation interval. This can be expressed as $\hat{\mathbf{x}}^s_{k|T}$, where measurements are given in the time interval $k = \{0, 1, .., T\}$.

Similar to the linear filtering problem, one of the commonly used closed form solution for linear Gaussian state-space models is Rauch Tung Streibel (RTS) smoother developed in 1965 [133]. This is a fixed-interval smoother consisting of forward and backward iterations through the datasets. In the forward iteration, the Kalman filtering algorithm is implemented to estimate the filtered states which is then followed by a backward iteration to compute the smoothed state estimates. The nonlinear smoothing algorithms include Extended Rauch Tung Streibel Smoother (ERTSS) [145], Unscented Rauch Tung Streibel Smoother (URTSS) [144], etc.

To illustrate the smoothing method, the UKF algorithm shown in Algorithm 2.1 can be extended to URTSS algorithm. Similar to the RTS algorithm, the forward iterations employs UKF algorithm to compute the filtered states and covariance matrix. This is followed by backward iteration of prediction and correction recursions to compute the smoothed state estimates is given in Algorithm 2.3. Here, the main objective is to estimate the smoothed state estimates $\hat{\mathbf{x}}^s_k$ for time instants $k \in \{T-1, ..., 0\}$. For this states and covariances are initialised using the filter estimates $\hat{\mathbf{x}}^s_T = \hat{\mathbf{x}}^f_T$ and $\mathbf{P}^s_T = \mathbf{P}^f_T$. It should be noted that the approximation of nonlinearity is obtained using unscented transform, where sigma points of smoother is calculated using filtered states.

Algorithm 2.2: *Backward iteration in the Unscented Rauch-Tung Stribel Smoother Estimation*

1. Initialise backward state estimate $\hat{\mathbf{x}}^s_T = \hat{\mathbf{x}}^f_T$ and error covariance matrix $\mathbf{P}^s_T = \mathbf{P}^f_T$.
2. **Recursive estimation** for $k \in \{T-1, ..., 2, 1, 0\}$:

Prediction:

(a) Compute the sigma points of the smoother using filtered state and covariance estimates as

$$\chi^s_{k,j} = \hat{\mathbf{x}}^f_k, \tag{2.41}$$

$$\chi^s_{k,j} = \hat{\mathbf{x}}^f_k + \left(\sqrt{(n_x+\lambda)\mathbf{P}^f_k}\right)_j, \quad j = 1, ..., n_x \tag{2.42}$$

$$\chi^s_{k,j} = \hat{\mathbf{x}}^f_k - \left(\sqrt{(n_x+\lambda)\mathbf{P}^f_k}\right)_j, \quad j = n_x+1, ..., 2n_x \tag{2.43}$$

where λ is same as in the filtering step given in (2.24).

(b) Propagate the sigma points through the nonlinear state evolution equation

$$\hat{\chi}^{s-}_{k+1,j} = \mathbf{f}(\chi^s_k). \tag{2.44}$$

(c) Estimate the predicted states, $\hat{\mathbf{x}}^{s-}_{k+1}$, covariance matrix $\mathbf{P}^{s-}_{k+1}$ and the cross-covariance matrix $\mathbf{S}_{k+1}$ as follows

$$\hat{\mathbf{x}}^{s-}_{k+1} = \sum_{j=0}^{2n_x} W^{(m)}_j \hat{\chi}^{s-}_{k+1,j}, \tag{2.45}$$

$$\mathbf{P}^{s-}_{k+1} = \sum_{j=0}^{2n_x} W^{(c)}_j (\hat{\chi}^{s-}_{k+1,j} - \hat{\mathbf{x}}^{s-}_{k+1})(\hat{\chi}_{k+1,j},^{s-} - \hat{\mathbf{x}}^{s-}_{k+1})^\top + \Sigma_{\epsilon^x}, \tag{2.46}$$

$$\mathbf{S}_{k+1} = \sum_{j=0}^{2n_x} W^{(c)}_j (\chi^s_{k,j} - \hat{\mathbf{x}}^{s-}_{k+1})(\hat{\chi}^{s-}_{k+1,j} - \hat{\mathbf{x}}^{s-}_{k+1})^\top, \tag{2.47}$$

where $W^{(m)}_i$ and $W^{(c)}_i$ are the constant mean and covariance weights defined in filtering step given in (2.28), (2.29) and (2.30).

Correction:

(d) Compute the smoother gain $\mathbf{D}_k$

$$\mathbf{D}_k = \mathbf{S}_{k+1}(\mathbf{P}^{s-}_{k+1})^{-1}. \tag{2.48}$$

(e) Compute the smoothed estimates of state $\hat{\mathbf{x}}^s_k$ and covariance $\mathbf{P}^s_k$

$$\hat{\mathbf{x}}^s_k = \hat{\mathbf{x}}^f_k + \mathbf{D}_k(\hat{\mathbf{x}}^s_{k+1} - \hat{\mathbf{x}}^{s-}_{k+1}), \tag{2.49}$$

$$\mathbf{P}^s_k = \mathbf{P}^f_k + \mathbf{D}_k(\mathbf{P}^s_{k+1} - \mathbf{P}^{s-}_{k+1})\mathbf{D}^\top_k. \tag{2.50}$$

2.4 Conclusion

This chapter has provided a background to the integral components of the model-based estimation, which are essential for the proposed modelling and estimation framework of cardiac electrical activity presented in the later chapters. The key observations from this background chapter are the following:

- The heart is an electromechanical pump, where the synchronised patterns of cardiac action potentials are important to obtain normal cardiac rhythmic conditions. The cardiac electrical activity demonstrates multiscale characteristics as the action potentials initiated at pacemaker cell propagates through the tissue to form complex spatio-temporal activation patterns. Experimental techniques such as electrical mapping and optical mapping enable to measure the cardiac activity at the surface of the heart. The electrical activation within the heart muscles cannot be measured from experimental techniques resulting the advantage of computational models of cardiac electrophysiology.

- Cardiac models of electrophysiology offers a wide range of quantitative descriptions of the initiation and propagation of the cardiac electrical activity. An important advantage of the multi-scale cardiac models is their ability to provide quantitative descriptions of the state variables and electrophysiological parameters, which cannot be measured using the data acquisition techniques. This illustrates that an integrated model of cardiac-electrophysiology can be derived by carefully assembling the model equations at the spatial scales of the heart.

- To infer the hidden state variables in the cardiac models, suboptimal filtering or smoothing methods in the statistical estimation frameworks can be employed. The review of cardiac models have demonstrated that quantitative descriptions of action potential are described by nonlinear equations, which include both differential and integral terms. Therefore, prevalent nonlinear state estimation methods were briefly reviewed. However, particular emphasis was given for the UKF and URTSS methodologies, as they have been considered as the fundamental state estimation method in the later chapters.

Chapter 3

Modelling and Simulation of Cardiac Electrophysiology

As described in Introduction of Chapter 1, cardiac models are considered as an effective tool for studying the underlying mechanisms during normal and pathological cardiac conditions. Data driven modelling and estimation based on the cardiac models allow inferring the electrophysiological state variables and parameters that can be directly interpreted by computational scientists [39]. Thus, it is important to develop a physiologically meaningful model that can be used to understand the underlying mechanisms of complex cardiac electrical activity patterns [31].

The overall aim of this chapter is to describe an integrated model of cardiac electrophysiology, which can be used as a mathematical model for inverse problems of cardiac electrical activity. Here, the integrated model is derived by combining model equations at following spatial levels:

- Cell-level model to describe the initiation of action potential at the cardiac myocytes,
- Tissue-level model to describe the action potential propagation through the cardiac tissue,
- Extracellular electrogram model to describe the measured cardiac electrical activity at a particular spatial distance from the tissue.

The review of cardiac cell models given in Section 2.2.1 demonstrates that the cardiac activity at the cell level can be described using simplified two-variables model, the complex biophysically detailed model and phenomenological model. Among the available cell models, phenomenological models with two variables are widely used for the simulation studies of cardiac arrhythmia [22, 47] and patient-specific modelling [39, 41, 79]. This is because, these models have simplified structure to reproduce the action potential characteristics at different conditions [33]. Also these models are computationally inexpensive and easier to solve numerically. In this thesis, Mitchell-Schaeffer model is considered as a suitable candidate cell model as it has fewer number of parameters compared to the Fenton-Karma model. However, classical MS model exhibits unstable pacemaker cell behaviour for some sets of parameters. The pacemaker behaviour is defined as a condition when transmembrane potential depolarises and repolarises in a cyclic manner, even when no external stimulus current is applied [38]. To resolve the instability problems, a modified version of Mitchell-Schaeffer (mMS) model is presented in [38]. Similar to MS model, modified version of Mitchell-Schaeffer model consists of two state variables and five parameters (four time constants and a threshold voltage). However, this model guarantees no pacemaker behaviour and is considered to be suitable for parameter fitting [22, 39]. In recent years, this model has been used in patient-specific electrophysiology simulation studies for both forward and inverse problems [22, 37, 39–41].

The state variables of mMS model are transmembrane voltage and gating variable, where the dynamic behaviour of transmembrane voltage is a nonlinear function generated as a result of total ionic current. On the other hand, dynamic behaviour of the gating variable in both models is described using a discontinuous function. This allows to describe the abrupt switching between the activation and inactivation (gate-open and gate-close) of ion channels. However, this abrupt value change in the gating variable due to the discontinuous nonlinear function may lead to divergence in the estimation of nonlinear systems, especially in case for the parameter estimation [9]. Moreover, discontinuous estimations methodologies can be computationally expensive [54]. To avoid this, a continuous version of gating variable function can be adopted using commonly used activation functions such as sigmoid functions, radial basis functions, etc. In particular for sigmoid functions, the slope parameter can be used to regulate the level of steepness in the continuous function depending on the type of inference problem.

Therefore, in this chapter, a continuous version of modified Mitchell-Schaeffer model is derived, where sigmoid function is used to approximate the abrupt change from activation to inactivation of the ionic channels. The derived ionic model is then coupled with the monodomain model equations to describe the activation patterns in a cardiac tissue. A simulation-based analysis is then conducted based on the developed integrated model to demonstrate the initiation and propagation of activation patterns.

The rest of this chapter is structured as follows. Section 3.1 details the derivation of the integrated model of cardiac electrophysiology. In Section 3.2, a detailed simulation study of the integrated cardiac model in one-dimensional and two-dimensional spatial fields are presented. Finally, a comparison between the mMS and proposed continuous version of the mMS model is presented in Section 3.3 .

3.1 An Integrated Model of Cardiac Electrophysiology

This section details the derivation of integrated model of cardiac electrophysiology used in this thesis.

3.1.1 Continuous Version of Modified Mitchell-Schaeffer Model

As described earlier, the primary state variable in the mMS ionic model is transmembrane voltage produced as a result of total ionic current flow across the cell membrane and modelled using (2.10). The total ionic current comprises inward and outward currents along with the external stimulus current. The fast inward current to the cell is primarily from the sodium and calcium ionic currents, given by

$$i^{in}(v,h) = h\frac{v(v-v_g)(1-v)}{\tau_{in}} \tag{3.1}$$

The outward current is produced from the potassium current $i_{out}(v,h)$, given as

$$i^{out}(v,h) = -(1-h)\frac{v}{\tau_{out}} \tag{3.2}$$

Finally, the external stimulus current i^{st}, can be applied as a series of pulses with a magnitude (v^{st}) and duration (T^{st}). Substituting (3.1) and (3.2) into (2.10), the transmembrane voltage across the cell membrane is described as

$$\frac{dv}{dt} = h\frac{v(v-v_g)(1-v)}{\tau_{in}} - (1-h)\frac{v}{\tau_{out}} + i^{st}, \tag{3.3}$$

where τ_{in} and τ_{out} are time constants of depolarisation and repolarisation phases. The activation threshold potential v_g, controls the flow of ions across the cell-membrane using a gating variable described by

$$\frac{dh}{dt} = \begin{cases} \frac{1-h}{\tau_{open}} & \text{if } v \leq v_g \\ \frac{-h}{\tau_{close}} & \text{if } v > v_g \end{cases}, \tag{3.4}$$

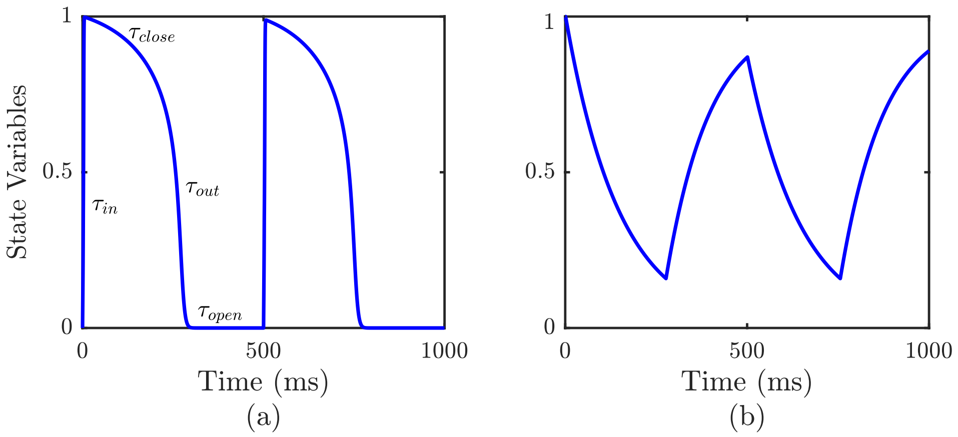

(a)

(b)

Figure 3.1. **State variables modelled using modified Mitchell-Schaeffer model**. An external stimulus is applied at every 500 ms with electrophysiology parameters: $\tau_{in} = 0.3, \tau_{out} = 6, \tau_{open} = 120, \tau_{close} = 150, v_g = 0.13, v^{st} = 0.15, T^{st} = 2ms$. (a) Normalised transmembrane voltage. (b) Gating variable.

where τ_{open} and τ_{close} are time constants of gate opening and closure.

An example of transmembrane voltage and gating variable simulated using (3.3) and (3.4) is given in Figure 3.1. The figure illustrates four major phases of the action potential within a cardiac cycle, where each phase is influenced by a time constant. At first, the cardiac myocyte is at rest ($v = 0$, $h = 1$). When an i^{st} of sufficient v^{st} and T^{st} is applied, the fast inward flow of sodium and calcium ions causes depolarisation phase ($v = 1$, $h = 1$), where i^{in} dominates the i^{out} with a rate of τ_{in}. It should be noted that the change in h during this phase is negligible [109]. Once the cell is fully depolarised, the ionic gates closes, balancing the inward and outward current at a time constant of τ_{close}. This is followed by repolarisation phase where v drops towards to zero with time constant of τ_{out}, when the gate variable $h = h_{min}$ [38]. Finally, the action potential goes to recovery phase where the gate reopens with time scale of τ_{open} and transmembrane voltage rapidly becomes zero and remains at this level until the next external stimulus current is applied.

It should be noted that both in classical and modified Mitchell-Schaeffer models time constant holds the assumption of $\tau_{in} << \tau_{out} << \tau_{open}, \tau_{close}$. This is because, action potential undergoes a much shorter depolarisation phase than the repolarisation phase, which also enables to describe the fast dynamics in the voltage compared to that of gating variable [38, 109].

As described earlier, the gating variable represents the activation, inactivation and recovery of the ionic channels. This switching between the activation (gate-open) and inactivation (gate-close) is based on the activation threshold potential and the transmembrane voltage. However, it can be seen that the dynamic behaviour of the gating variable in (3.4) is a discontinuous function.

To derive a continuous version of gating variable model, gating variable in (3.4) of the mMS model equations is first reformulated into a general form as given in [99, 109] as

$$\frac{dh}{dt} = \begin{cases} \frac{h_\infty(v)-h}{\tau(v)} & v \leq v_g \\ \frac{h_\infty(v)-h}{\tau(v)} & v > v_g \end{cases}, \tag{3.5}$$

where $h_\infty(v)$ is a transmembrane potential dependent function denoting the steady state conditions of a single gating variable with time constant $\tau(v)$ [109]. By comparing (3.4) and (3.5), steady state function $h_\infty(v)$ can be approximated as

$$h_\infty(v) \approx \begin{cases} 1 & v \leq v_g \\ 0 & v > v_g \end{cases}. \tag{3.6}$$

Equation (3.6) illustrates that the dynamic change is essentially a step function that depends on both v and v_g. A continuous approximation of $h_\infty(v)$ can be considered as a variant of unipolar sigmoid function that changes with $(v - vg)$. This allows to incorporate both negative and positive changes during the transmembrane voltage v crosses the activation threshold potential v_g

$$h_\infty(v) = 1 - \frac{1}{1 + e^{-\gamma(v-v_g)}}, \tag{3.7}$$

where γ is the slope of the sigmoid that quantifies the rate of change between the gate-open and gate-close condition.

To obtain a simplified analytical representation, the time constants of gating variable are further replaced as $\tau = max\{\tau_{open}, \tau_{close}\}$. This assumption is similar to that in [109], which was used to obtain simplified representation of gating variable for easier implementation of the asymptotic methods to capture the morphology of action potential and gating variable. Therefore, the continuous version of gating variable can be described as

$$\frac{dh}{dt} = \frac{h_\infty(v) - h}{\tau}, \tag{3.8}$$

where $h_\infty(v)$ is simplified as

$$h_\infty(v) = \frac{e^{-\gamma(v-v_g)}}{1 + e^{-\gamma(v-v_g)}}. \tag{3.9}$$

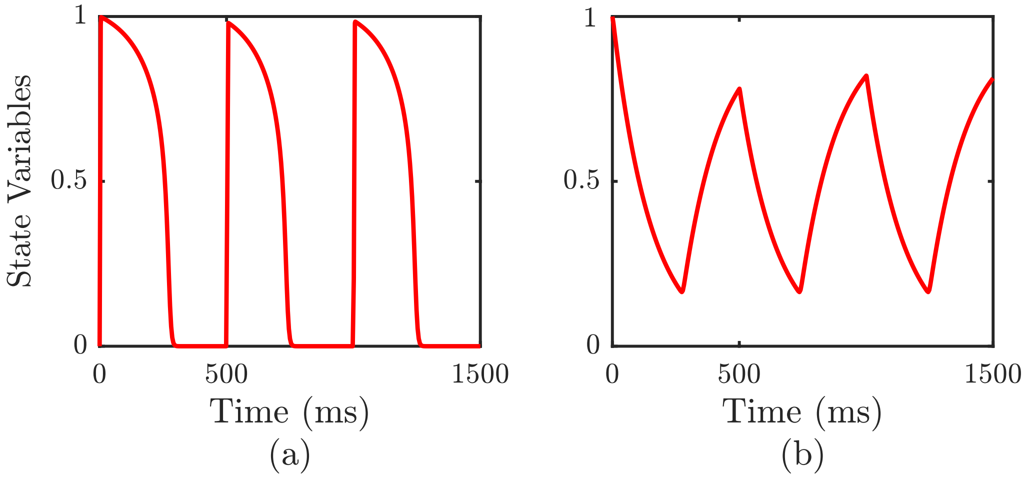

(a) (b)

Figure 3.2. **State variables simulated using the continuous version of modified Mitchell-Schaeffer model**. An external stimulus is applied at every 500ms with the electrophysiology parameters: $\tau_{in} = 0.3, \tau_{out} = 6, \tau_{open} = 120, \tau_{close} = 150, v_g = 0.13, v^{st} = 0.15, T^{st} = 2ms, \gamma = 25$. (a) Normalised transmembrane voltage. (b) Gating variable.

Figure 3.2 illustrates the evolution of state variables simulated using the continuous version of mMS model proposed in this chapter. It can be seen that the continuous model is able to capture the action potential characteristics with a simplified description of gating variable. A detailed comparison of activation patterns modelled by both models is presented in Section 3.3.

3.1.2 Monodomain Tissue Model

The generation of action potential at a cell level is modelled using a system of ODEs. This model can be coupled with PDEs to model the propagation of action potential across the tissue. Although bidomain model equations provide detailed descriptions of cardiac tissue electrophysiology, monodomain models are computationally easier to solve and thus widely used to study the cardiac electrical activity. Simulation studies have compared these models and shown that the patterns from both models result in similar dynamics. These include action potential propagation in the absence of external stimulus current [128] and trajectories of spiral wave tip in re-entrant waves [138]. Thus, propagation of the action potential through cardiac tissue is described using monodomain model equations given in (2.13). The monodomain model in (2.13) is essentially a reaction-diffusion equation, where the propagation of transmembrane voltage through the excitable cardiac tissue medium is described using the diffusion term gradient operator ∇

$$\nabla \cdot \mathbf{\Theta}_g \nabla v = \frac{\partial}{\partial \mathbf{s}} \cdot \left(\mathbf{\Theta}_g \frac{\partial v}{\partial \mathbf{s}} \right), \tag{3.10}$$

where $\mathbf{s}$ denotes space.

The reaction term in (2.13) represents the electrophysiological properties of a single cell, which is the sum of ionic currents and the external stimulus current. The relationship between transmembrane voltage from a single cell and the total ionic current is given by (2.2) [91]. By substituting continuous version of Mitchell-Schaeffer model equations given in (3.3) and (3.4), the monodomain tissue model can be written as

$$\frac{\partial v}{\partial t} = \nabla \cdot \mathbf{\Theta}_g \nabla v + h \frac{v(v - v_g)(1 - v)}{\tau_{in}} - (1 - h) \frac{v}{\tau_{out}} + i_{st}, \tag{3.11}$$

$$\frac{dh}{dt} = \frac{h_\infty(v) - h}{\tau}, \tag{3.12}$$

where $h_\infty(v)$ is simplified as

$$h_\infty(v) = \frac{e^{-\gamma(v - v_g)}}{1 + e^{-\gamma(v - v_g)}}. \tag{3.13}$$

In this thesis, the cardiac electrical activity in an isotropic tissue pattern is studied. For an isotropic tissue, spatial diffusion is assumed to be constant across the cardiac tissue, implying a scalar value $\mathbf{\Theta}_g = \theta_g$. The numerical value of diffusion coefficient is generally calculated using (2.14). Analytically, this enables to describe the diffusion term in a three-dimensional coordinate system ($\mathbf{s} = s_x, s_y, s_z$) as

$$\begin{aligned} \left(\frac{\partial}{\partial s_x} \bar{a}_x + \frac{\partial}{\partial s_y} \bar{a}_y + \frac{\partial}{\partial s_z} \bar{a}_z \right) \cdot \left(\theta_g \frac{\partial v}{\partial s_x} \bar{a}_x + \theta_g \frac{\partial v}{\partial s_y} \bar{a}_y + \theta_g \frac{\partial v}{\partial s_z} \bar{a}_z \right) = \\ \theta_g \left(\frac{\partial^2 v}{\partial s_x^2} + \frac{\partial^2 v}{\partial s_y^2} + \frac{\partial^2 v}{\partial s_z^2} \right), \end{aligned} \tag{3.14}$$

where $(\bar{a}_x, \bar{a}_y, \bar{a}_z)$ is the unit vector.

Thus, monodomain model equation of transmembrane voltage for an isotropic tissue can be written in an alternate form as

$$\frac{\partial v}{\partial t} = \theta_g \nabla^2 v + h \frac{v(v - v_g)(1 - v)}{\tau_{in}} - (1 - h) \frac{v}{\tau_{out}} + i^{st}. \tag{3.15}$$

3.1.3 Extracellular Electrogram Model

The action potentials from the tissue level can be then used to determine the extracellular unipolar electrograms. By placing the point sensors at $\mathbf{s}' = (s'_x, s'_y, s'_z)$ and at a particular distance from the tissue level, the electrogram measurements are described using the model given in (2.15). This is restated in this section for completeness.

$$v^{ex}(\mathbf{s}', t) = \tilde{\kappa} \iiint (-\nabla v_t(\mathbf{s})) \cdot \nabla \left[\frac{1}{r}\right] ds_x ds_y ds_z, \tag{3.16}$$

The above equation can be further simplified depending on the dimension and geometry of the spatial field [126]. For instance, the gradient measure for a three-dimensional spatial field can be expressed as

$$\nabla \left[\frac{1}{r}\right] = \frac{\partial}{\partial s_x}\left[\frac{1}{r}\right]\bar{a}_x + \frac{\partial}{\partial s_y}\left[\frac{1}{r}\right]\bar{a}_y + \frac{\partial}{\partial s_z}\left[\frac{1}{r}\right]\bar{a}_z, \tag{3.17}$$

$$\nabla \left[\frac{1}{r}\right] = \left[\frac{-(s_x - s_x{}')}{r^3}\right]\bar{a}_x + \left[\frac{-(s_y - s_y{}')}{r^3}\right]\bar{a}_y + \left[\frac{-(s_z - s_z{}')}{r^3}\right]\bar{a}_z. \tag{3.18}$$

Therefore, model equations given in (3.11), (3.12) and (3.16) constitute the generalised integrated model of cardiac electrical activity.

3.2 Simulation-based Study of Integrated Cardiac Model

In this section, evolutions of action potential propagation and the electrogram measurements are simulated using the integrated cardiac model.

As detailed in previous section, the tissue dynamics is described using the monodomain tissue equations coupled with the proposed continuous version of mMS model while the electrogram measurements are modelled using (3.16). A simulation-based study enables to study the formation and evolution of spatiotemporal cardiac activation patterns as an example of forward problem of cardiac electrophysiology [130].

Developing the simulations mainly involves obtaining the solutions of integrated cardiac model equations. These model equations are of continuum-based representations that consist of both differential and integral terms. To obtain the solutions, numerical techniques such as finite difference, finite element and finite volume methods are generally used in simulation studies [130]. Although finite element and volume approaches can be performed for irregular and complex spatial domains, these methods demand higher computational costs. Generally, cardiac modelling studies aimed to understand the cardiac electrical patterns are conducted on more regular spatial domains such as one-dimensional cable, two-dimensional and three-dimensional slabs, etc. These provide a low-dimensional representation which can also be used to simulate and quantify the complex activation patterns. In these studies, explicit finite difference methods are extensively used because of straightforward implementation [33]. However, it is important to perform the stability analysis for the chosen simulation parameters. For the explicit finite difference solution of the monodomain tissue model equations with isotropic diffusion, stability criterion is given by [32]

$$\frac{\theta_g \Delta_t}{\Delta_s} < \frac{1}{2n_d}, \tag{3.19}$$

where n_d is the dimension of the spatial field of the tissue model used in simulation. For instance, $n_d = 2$ in case of two-dimensional spatial field.

Therefore, in this section, normal and abnormal patterns of cardiac electrical activity in one-dimensional and two-dimensional space are developed using explicit finite difference methods.

3.2.1 One-dimensional Spatial Field

For an isotropic tissue in a one-dimensional space, monodomain equations can be written as

$$\frac{\partial v}{\partial t} = \theta_g \frac{\partial^2 v}{\partial s_x^2} + h\frac{v(v - v_g)(1 - v)}{\tau_{in}} - (1 - h)\frac{v}{\tau_{out}} + i^{st}, \tag{3.20}$$

where θ_g is the diffusion coefficient, assumed to be same in all directions.

The gradient operator of the diffusion term in (3.15) is simplified using the relationship given in (3.14). Additionally, it should be noted that the expression for gating variable in (3.12) and (3.13) remains unchanged for each cell in the spatial field.

Explicit finite difference approach is then employed to compute the state variables across space and time. In this method, the first step is to construct a gridded domain $[s_x = s_x^1, s_x^2, ..., s_x^{n_{s_x}}]$ with nodes separated at a distance. Here the nodes are placed at equidistant with an increment Δ_s in space, Δ_t in time. The next step is to approximate the differential operators (∇ and ∇^2) as finite differences expressions based on Taylor series expansions. Thus, Laplacian operator in (3.20) is approximated using a second order central difference operator. This finite difference operator determines the transmembrane potential at each point as difference in magnitude between its immediate left and right neighbouring points.

For a general point s_x^i, the second order central difference equation can be written as

$$\left.\frac{\partial^2 v}{\partial s_x^2}\right|_{s_x=s_x^i} \approx \frac{1}{\Delta_s}\left(\left.\frac{\partial v}{\partial s_x}\right|_{s_x=s_x^i+\frac{\Delta_s}{2}} - \left.\frac{\partial v}{\partial s_x}\right|_{s_x=s_x^i-\frac{\Delta_s}{2}} \right), \tag{3.21}$$

where the first-order derivative term for the neighbouring points in (3.21) is then approximated using central difference operators as following

$$\left.\frac{\partial v}{\partial s_x}\right|_{s_x=s_x^i+\frac{\Delta_s}{2}} \approx \frac{v(s_x^i+\Delta_s)-v(s_x^i)}{\Delta_s}, \tag{3.22}$$

$$\left.\frac{\partial v}{\partial s_x}\right|_{s_x=s_x^i-\frac{\Delta_s}{2}} \approx \frac{v(s_x^i)-v(s_x^i-\Delta_s)}{\Delta_s}. \tag{3.23}$$

The Laplacian operator can then be obtained by substituting (3.23) and (3.22) into (3.21)

$$\left.\frac{\partial^2 v}{\partial s_x^2}\right|_{s_x=s_x^i} \approx \frac{1}{\Delta_s}\left(\frac{v(s_x^i+\Delta_s)-v(s_x^i)}{\Delta_s} - \frac{v(s_x^i)-v(s_x^i-\Delta_s)}{\Delta_s} \right), \tag{3.24}$$

$$\left.\frac{\partial^2 v}{\partial s_x^2}\right|_{s_x=s_x^i} \approx \frac{v(s_x^i+\Delta_s)-2v(s_x^i)+v(s_x^i-\Delta_s)}{\Delta_s^2}. \tag{3.25}$$

Equation (3.25) illustrates that the weights associated with the node $v(s_x^i)$ in the explicit finite difference approach are related by $(1/\Delta_s^2, -2/\Delta_s^2, 1/\Delta_s^2)$. By considering only the magnitude of weights, the finite difference matrix can be precomputed and stored to reduce computational costs. For a gridded domain with n_{s_x} number of nodes, finite difference matrix $\mathcal{A}$ of the central difference method can be written as

$$\mathcal{A} = \begin{pmatrix} -2 & 1 & & & & & \\ 1 & -2 & 1 & & & & \\ & 1 & -2 & 1 & & & \\ & & \ddots & \ddots & \ddots & & \\ & & & 1 & -2 & 1 & \\ & & & & 1 & -2 & 1 \\ & & & & & 1 & -2 \end{pmatrix}_{[n_{s_x} \times n_{s_x}]} \tag{3.26}$$

where the magnitude of empty matrix entries is zero. It should be noted that the matrix comprises tridiagonal bands and could become highly sparse for larger number of nodes.

The final step is to incorporate the boundary conditions into the finite difference matrix. This process depends on the nature of spatial domain and is detailed in the next section. Similarly, transmembrane potential can be evaluated across time instants using first order forward difference equation given by

$$\frac{\partial v}{\partial t} = \frac{v_{t+\Delta_t}(s_x^i) - v_t(s_x^i)}{\Delta_t}. \tag{3.27}$$

The above approach is then repeated for gating state variable as it is represented by ODE with dependency described over time. On the other hand, electrogram measurements in a one-dimensional field equation can be written as

$$v^{ex}(\mathbf{s}', t) = \tilde{\kappa} \int_L (-\nabla v_t(s_x)) \cdot \nabla \left[\frac{1}{r}\right] ds_x. \tag{3.28}$$

Similar to the Laplcian operator, a finite difference matrix can be precomputed for the derivative operator in (3.28) as follows

$$\mathbf{M}_{s_x} = \begin{pmatrix} -1 & 1 & & & & & \\ & -1 & 1 & & & & \\ & & -1 & 1 & & & \\ & & & \ddots & \ddots & & \\ & & & & -1 & 1 & \\ & & & & & -1 & 1 \\ & & & & & & -1 \end{pmatrix}_{[n_{s_x} \times n_{s_x}]} \tag{3.29}$$

Normal Activation Patterns

In this example, the simulation of normal activation patterns in a one dimensional spatial domain is presented.

A one-dimensional cable with a length of 2 cm (L_x) is considered to represent both the tissue and electrodes field. A schematic illustration of the simulation setup is shown in Figure 3.3. It shows that the tissue field is placed at $(s_x, 0)$ axis while the electrograms are placed at an (s'_x, s'_y) axis parallel to this field.

The tissue field is assumed to be homogenous with the electrophysiology parameters given in Table 3.1, and isotropic with diffusion co-efficient of 0.001 cm^{2}ms^{-1}. Simulation studies based on explicit finite difference approach generally use space step value of 0.25 mm while time step size ranges between 0.05 ms and 0.1 ms [32]. Here, a space step is chosen to be 0.25 mm that results in a total of 81 cells in the tissue field. The model equations are then solved using the explicit finite difference method detailed in the previous section. However, no-flux boundary conditions are applied to calculate the transmembrane potential at the right and left boundary nodes in the tissue field. No-flux boundary conditions impose the assumption

Table 3.1. Electrophysiological parameters used in the simulations [38, 109].

Parameters	Values
Δ_s	0.025 cm
Δ_t	0.05 ms
τ_{in}	0.3 ms
τ_{out}	6 ms
τ_{open}	120 ms
τ_{close}	150 ms
τ	150 ms
$slope, \gamma$	25
vg	0.13

that there is no current flow into or out of the membrane by assigning the gradient of transmembrane potential to be zero [32]. As a result, the node at the right end of the cable only considers the potential from its left neighbouring node, given by

$$\left.\frac{\partial^2 v}{\partial s_x^2}\right|_{s_x = s_x^1} \approx \left(\frac{v(s_x^i + \Delta_s) - v(s_x^i)}{\Delta_s^2}\right). \tag{3.30}$$

Similarly, the node at the left boundary only considers the potential from its right neighbouring point given by

$$\left.\frac{\partial^2 v}{\partial s_x^2}\right|_{s_x = s_x^{L^x}} \approx \left(-\frac{v(s_x^i) - v(s_x^i - \Delta_s)}{\Delta_s^2}\right). \tag{3.31}$$

The finite difference matrix $\mathcal{A}$ for the numerical integration of tissue model is

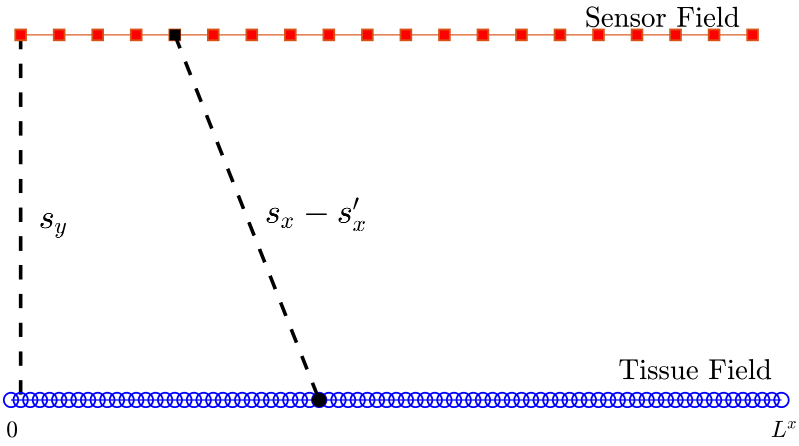

Figure 3.3. Schematic diagram of simulation setup for normal activation patterns in one-dimensional cable field model.

computed by including the dependency of nodes given in (3.30) and (3.31). The corresponding electrograms are measured at sensors placed at 1 mm from the tissue field. On the sensor field, the electrograms are placed 1 mm apart, resulting a total number of sensors to be 20. Similar to the tissue field, no-flux boundary condition is applied at the boundary nodes to obtain the corresponding difference matrix $\mathbf{M}_{s_x}$. The corresponding finite difference matrices from both tissue and sensor field are given by

$$\mathcal{A} = \begin{pmatrix} -1 & 1 & & & & \\ 1 & -2 & 1 & & & \\ & 1 & -2 & 1 & & \\ & & \ddots & \ddots & \ddots & \\ & & & 1 & -2 & 1 \\ & & & & 1 & -1 \end{pmatrix}_{[81\times 81]} \quad \mathbf{M}_{s_x} = \begin{pmatrix} -1 & 1 & & & & \\ & -1 & 1 & & & \\ & & -1 & 1 & & \\ & & & \ddots & \ddots & \\ & & & & -1 & 1 \\ & & & & & 0 \end{pmatrix}_{[81\times 81]} \tag{3.32}$$

Another important measure required in simulating the electrogram measurements is the distance between the tissue and sensor fields. The assumption that the sensors are placed on axis parallel to the tissue field implies $s_z{}' = 0$ and $s_y{}'$ to be a constant value (see Figure 3.3). Thus, Euclidean distance can be calculated as

$$r = \sqrt{(s_x - s_x{}')^2 + (s_y{}')^2}. \tag{3.33}$$

The gradient measure can be calculated as

$$\nabla\left[\frac{1}{r}\right] = \left[\frac{-(s_x - s_x{}')}{r^3}\right].\bar{a}_x \tag{3.34}$$

In order to initiate the normal action potential, an external stimulus current is applied at left edge of the tissue field from $s_x = 0$ mm to $s_x = 0.05$ cm, and at two different time instants, t = 0.05 ms and t = 500.05 ms. Simulation is performed for a total of 1000 ms with a time step of 0.05 ms. The resulting spatiotemporal activation patterns of the state variables at tissue level are depicted in Figure 3.4. Figure 3.4 (a) illustrates that the action potentials generated at external stimulus locations propagate along the cable over time. At every cell position, the action potential undergo depolarisation and repolarisation stages, followed by returning to the resting states. This forms one complete cycle of the action potential. The second stimulus applied at t = 500.05 ms creates another normal cycle of action potential propagation. The dynamics of state variables from individual cells are shown in Figure 3.5 under the normal cycles of action potential propagation. The electrograms measured at the electrodes are shown in Figure 3.6. The results

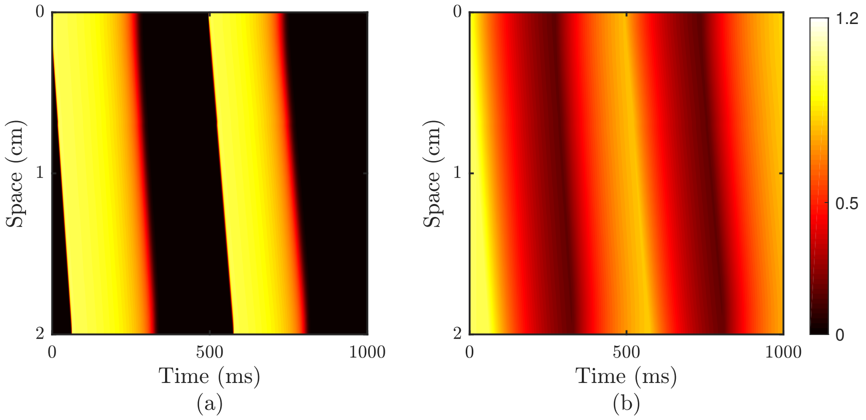

Figure 3.4. Example of the simulated spatiotemporal patterns during normal cardiac conditions in a one-dimensional cable field. The electrophysiology parameters are θ_g = 0.001 cm^{2}ms^{-1}, $v^{st} = 0.6, T^{st} = 2ms, \gamma = 25$. (a) Transmembrane voltage. (b) Gating variable.

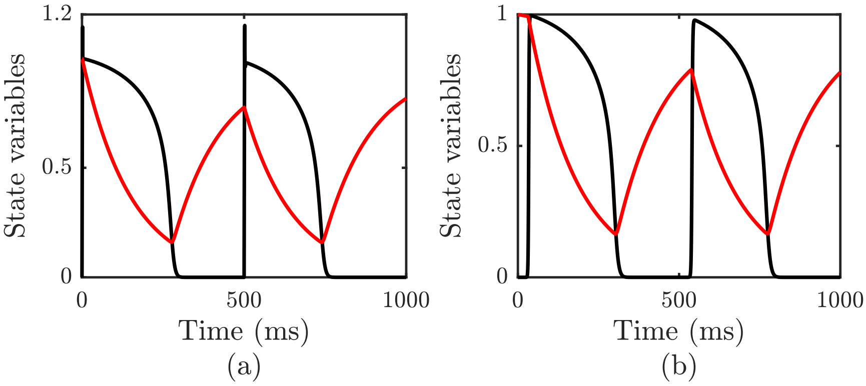

Figure 3.5. Examples of state variables from two different spatial locations along the cable tissue field. (a) At the stimulus location, s_x = 0.025 cm. (b) At s_x = 1 cm. State variables are transmembrane voltage (—), gating variable (—).

illustrate the monophasic characteristics of the electrograms at stimulus location and at the end of cable field, as detailed in Section 2.2.3. The biphasic electrogram characteristics is observed at the other electrodes. To illustrate this, an example of electrogram at 1.325 cm on cable is shown in Figure 3.6(b). The simulated electrograms follow a similar trend as that of clinical readings presented in [22].

Re-entrant Activation Patterns

In this example, re-entrant activation patterns in a one-dimensional spatial field are presented.

For the simulation, both the cardiac tissue and the sensor field are represented by a one-dimensional ring model. Similar to the studies based on re-entrant exci-

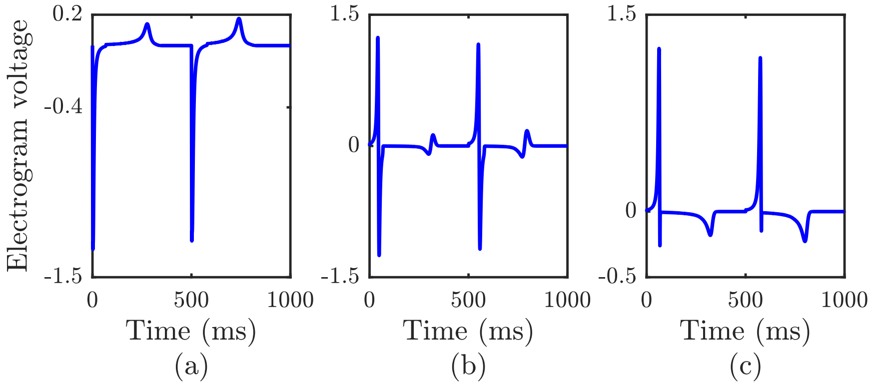

(a) (b) (c)

Figure 3.6. Examples of electrogram measurements at different spatial locations along the sensor field. (a) Monophasic at s'_x = 0 cm. (b) Biphasic at s'_x = 1.325 cm. (c) Monophasic at s'_x = 2 cm.

tations in [73, 132, 156], the ring models here are constructed as a closed loop of cable field shown in the previous section. This allows to reproduce the complex dynamics of re-entrant patterns in a simplified manner. A schematic representation of the ring models used for simulation is shown in Figure 3.7. The electrophysiological properties used here are same as for the normal activation patterns, that are given in Table 3.3. To compute the transmembrane voltage and gating variable over space and time, explicit finite difference method is then employed. In contrast to the cable fields, the finite difference matrices are formed here by incorporating the periodic boundary conditions. Thus, the finite difference matrices can be written as

$$\mathcal{A} = \begin{pmatrix} -2 & 1 & & & & 1 \\ 1 & -2 & 1 & & & \\ & 1 & -2 & 1 & & \\ & & \ddots & \ddots & \ddots & \\ & & & 1 & -2 & 1 \\ 1 & & & & 1 & -2 \end{pmatrix}_{[80\times 80]} \quad \mathbf{M}_{s_x} = \begin{pmatrix} -1 & 1 & & & & \\ & -1 & 1 & & & \\ & & -1 & 1 & & \\ & & & \ddots & \ddots & \\ & & & & -1 & 1 \\ 1 & & & & & -1 \end{pmatrix}_{[80\times 80]} \tag{3.35}$$

For the simulation of electrogram measurements, the distances between spatial locations in both tissue and sensor fields are then calculated. Here, a different approach is employed such that the symmetrical distance properties along the ring model are incorporated in the calculation. As shown in Figure 3.7, the distance from a spatial location in tissue field (s_x) to the sensor location (s'_x, s'_y) is calculated as

$$r = \sqrt{{c_x}^2 + {s'_y}^2}, \tag{3.36}$$

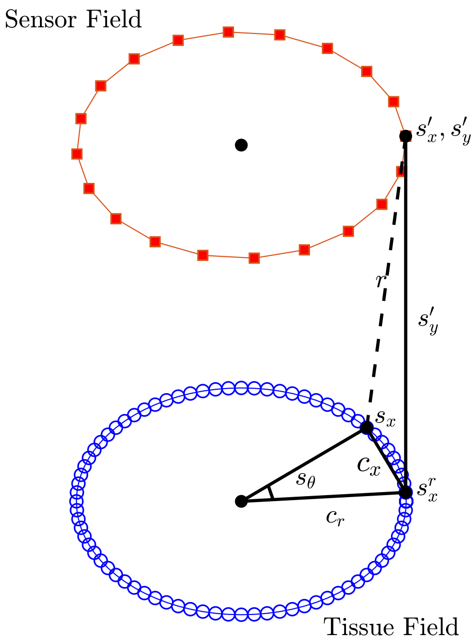

Figure 3.7. Schematic diagram of the simulation setup for modelling the re-entrant activation patterns in a one-dimensional ring domain.

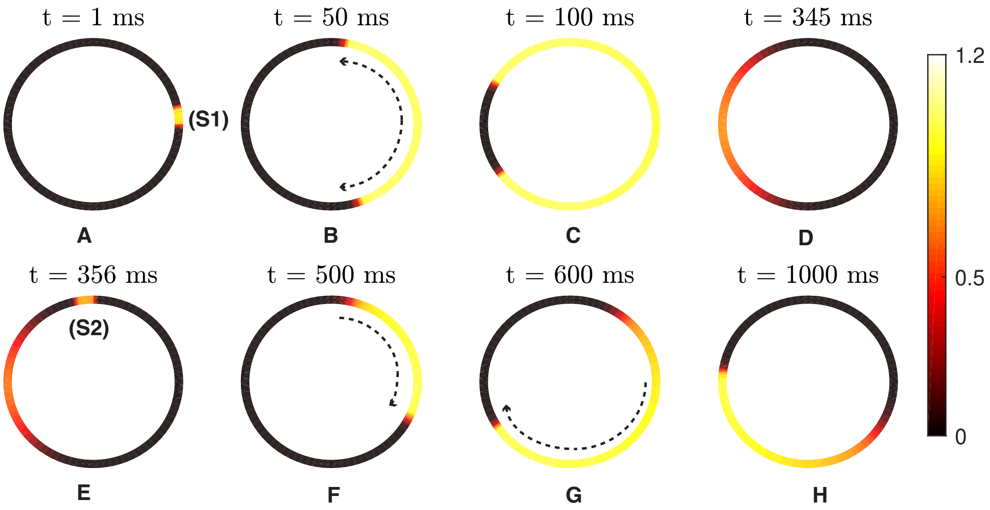

Figure 3.8. Example of the simulated spatiotemporal patterns of transmembrane voltage during re-entrant activity in an one-dimensional ring model. The electrophysiology parameters are θ_g = 0.001 cm^{2}ms^{-1}, $v^{st} = 0.6, T^{st} = 2ms, \gamma = 25$.

where c_x is the chord length between a reference point (s_x^r) and spatial location in tissue field (s_x) given by

$$c_x = 2c_r \sin\left(\frac{s_\theta}{2}\right), \tag{3.37}$$

where c_r is radius of the spatial fields and s_θ is the angle between s_x^r and s_x. The corresponding gradient measure can be calculated as

$$\nabla\left[\frac{1}{r}\right] = \left[c_r \cos\left(\frac{s_\theta}{2}\right)\right]\bar{a}_x. \tag{3.38}$$

To simulate re-entry, S1-S2 stimulation protocol is applied to one-dimensional ring [38]. Using this method, normal activation patterns are first generated by applying first stimulus (S1) from $s_x = 0$ cm to $s_x = 0.05$ cm (see Figure 3.8 A). Due to the closed loop structure of the ring, action potentials propagate in both directions as shown in Figure 3.8 B and 3.8 C. The patterns returns to its resting state and cancels out at the common point (see Figure 3.8 D). To generate the re-entrant circuit, the second stimulus (S2) is then applied during vulnerable window, when the tissue is partially refractory. As illustrated in Section 2.1, this time interval is within the action potential duration but after the absolute refractory period. Also, an external stimulus with a sufficient magnitude and duration can initiate the re-entrant wave. Here, S2 is applied from $s_x = 0.475$ cm to $s_x = 0.525$ cm at 350 ms, which initiates the re-entrant activation waves (see Figure 3.8 F). This activation wave travels along the direction, where the cells are recovered and can be re-excited (see Figure 3.8 (F-H)). As a result the symmetry of normal activation pathways is broken and creates a re-entry circuit by re-exciting the same tissue regions.

It should be noted that if S2 is applied before the vulnerable window, re-entrant waves cannot be generated as the cells are still refractory to external disturbance. On the other hand normal action potentials are generated and propagate along the tissue, when S2 is stimulated after the vulnerable window. Along with the stimulus parameters, the time at which S2 is applied plays a crucial part in the initiation of re-entrant activation wave.

Figures 3.9 and 3.10 show the evolution of state variables and electrogram measurements associated with the re-entrant excitation in one-dimensional ring. In Figure 3.9 (a) the normal action potential characteristics are observed followed by the first stimulus S1, which corresponds to monophasic electrogram in Figure 3.10 (a). This is similar to the trend shown in the previous section. The initiation of action potentials when the stimulus S2 is applied during vulnerable window is shown in Figure 3.9 (b). This causes an abrupt and negative deflection in elec-

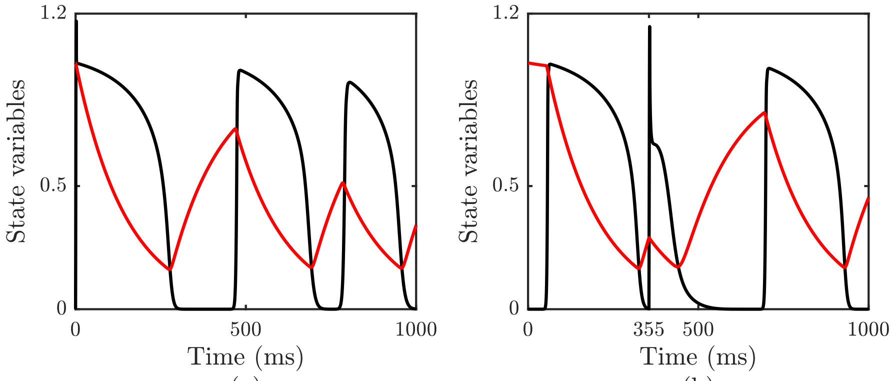

(a) (b)

Figure 3.9. Examples of state variables from two different spatial locations along the tissue field. (a) At the first stimulus location, $s_x = 0.025$ cm. (b) At the second stimulus location $s_x = 0.5$ cm. State variables are transmembrane voltage (—), gating variable (—).

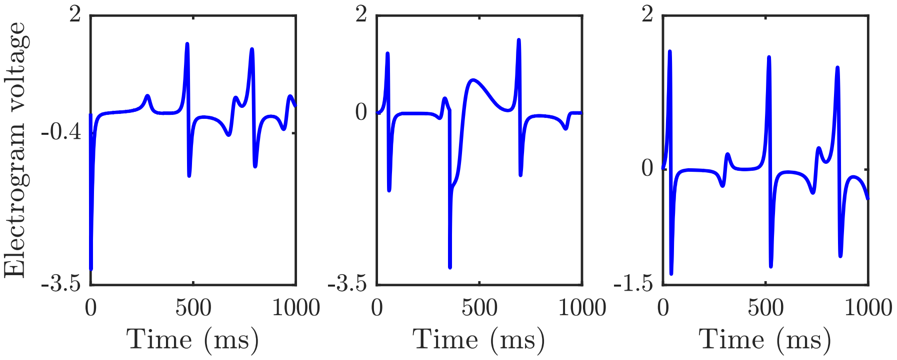

(a) (b) (c)

Figure 3.10. Examples of electrogram measurements at different spatial locations along the sensor field. (a) At first stimulus, $s'_x = 0$ cm . (b) At second stimulus, $s'_x = 0.525$ cm. (c) At $s'_x = 2$ cm.

trogram as illustrated in Figure 3.10 (b). The characteristics of activation patterns and electrogram caused by the re-excitation of cells can also be seen in Figure 3.10 (c). Moreover, the stability analysis shown in Table 3.2 shows that the selected simulation parameters in the one-dimensional spatial field are stable.

Table 3.2. Stability analysis for explicit finite difference method.

Diffusion value(cm^{2}ms^{-1})	Dimension of simulation (n_d)	Calculated stability criterion value	Stability Criterion limit	Stability Check
0.001	1	0.08	0.5	Yes
0.0001	2	0.008	0.25	Yes

3.2.2 Two-dimensional Spatial Field

In this section, simulation of normal and re-entrant activation patterns in a two-dimensional isotropic tissue slab is presented.

For a two-dimensional isotropic tissue field, the transmembrane voltage in monodomain equations can be described as

$$\frac{\partial v}{\partial t} = \theta_g \left(\frac{\partial^2 v}{\partial s_x^2} + \frac{\partial^2 v}{\partial s_y^2} \right) + h \frac{v(v - v_g)(1 - v)}{\tau_{in}} - (1 - h) \frac{v}{\tau_{out}} + i^{st}, \tag{3.39}$$

where the spatial field is expressed as ($\mathbf{s} = s_x, s_y$) and the simplification of diffusion term is obtained from

$$\nabla.(\theta_g \nabla v) = \frac{\partial}{\partial \mathbf{s}}. \left(\theta_g \frac{\partial v}{\partial \mathbf{s}} \right), \tag{3.40}$$

$$\left(\frac{\partial}{\partial s_x} \bar{a}_x + \frac{\partial}{\partial s_y} \bar{a}_y \right). \left(\theta_g \frac{\partial v}{\partial s_x} \bar{a}_x + \theta_g \frac{\partial v}{\partial s_y} \bar{a}_y \right) = \theta_g \left(\frac{\partial^2 v}{\partial s_x^2} + \frac{\partial^2 v}{\partial s_y^2} \right). \tag{3.41}$$

Similar to the one-dimensional field, an explicit finite difference method is used to obtain the solutions of the model equations. To begin with, a regular gridded domain with $[n_{s_x} \times n_{s_y}]$ nodes with a uniform space step of Δ_s ($\Delta_x = \Delta_y = \Delta_s$) is considered. The Laplacian operator can be then computed using the finite difference equations at each node as

$$\left. \frac{\partial^2 v}{\partial s_x^2} \right|_{s_x = s_x^i} \approx \frac{1}{\Delta_s} \left(\frac{v(s_x^i + \Delta_s, s_y^j) - v(s_x^i, s_y^j)}{\Delta_s} - \frac{v(s_x^i, s_y^j) - v(s_x^i - \Delta_s, s_y^j)}{\Delta_s} \right), \tag{3.42}$$

$$\left. \frac{\partial^2 v}{\partial s_y^2} \right|_{s_y = s_y^j} \approx \frac{1}{\Delta_s} \left(\frac{v(s_x^i, s_y^j + \Delta_s) - v(s_x^i, s_y^j)}{\Delta_s} - \frac{v(s_x^i, s_y^j) - v(s_x^i, s_y^j + \Delta_s)}{\Delta_s} \right), \tag{3.43}$$

$$\begin{aligned} \left(\frac{\partial^2 v}{\partial s_x^2} + \frac{\partial^2 v}{\partial s_y^2} \right) \approx & \left(\frac{v(s_x^i + \Delta_s, s_y^j) - v(s_x^i, s_y^j)}{\Delta_s^2} - \frac{v(s_x^i, s_y^j) - v(s_x^i - \Delta_s, s_y^j)}{\Delta_s} \right) + \\ & \left(\frac{v(s_x^i, s_y^j + \Delta_s) - v(s_x^i, s_y^j)}{\Delta_s^2} - \frac{v(s_x^i, s_y^j) - v(s_x^i, s_y^j + \Delta_s)}{\Delta_s^2} \right). \end{aligned} \tag{3.44}$$

The association of each node in the spatial field is then described using the finite difference matrix. Similar to one-dimensional scenario, this matrix is pre-computed and stored to reduce computational cost. However, coordinate system approach using (3.44) can lead to highly sparse three-dimensional matrix. To mitigate the use of high-dimensional matrix, the cartesian co-ordinate representations are converted to indices such that $s_l = [s_l^1, s_l^2, ..., s_l^{n_s}]$, with total number of nodes given by n_s. The index of each node is calculated using $s_l^i = (j-1)n_{s_x} + i$. As a result, the approximation of derivative operator in (3.44) can be rewritten as

$$\left(\frac{\partial^2 v}{\partial s_x^2} + \frac{\partial^2 v}{\partial s_y^2}\right) \approx \left(\frac{v(s_l^{i+1}) - v(s_l^i)}{\Delta_s^2} - \frac{v(s_l^i) - v(s_l^{i-1})}{\Delta_s^2}\right) + \left(\frac{v(s_l^{i+L_x}) - v(s_l^i)}{\Delta_s^2} - \frac{v(s_l^i) - v(s_l^{i-L_x})}{\Delta_s^2}\right). \tag{3.45}$$

Similar to the one-dimensional cable field, no-flux boundary conditions is then applied. Using this method, the nodes at the left boundary of the tissue slab (where $s_x = 0$) do not consider the voltage from its left neighbouring points

$$\left(\frac{\partial^2 v}{\partial s_x^2} + \frac{\partial^2 v}{\partial s_y^2}\right) \approx \left(\frac{v(s_l^{i+1}) - v(s_l)}{\Delta_s^2} + \frac{v(s_l^{i+n_{sx}}) - v(s_l^i)}{\Delta_s^2} - \frac{v(s_l^i) - v(s_l^{i-n_{sx}})}{\Delta_s^2}\right). \tag{3.46}$$

Similarly, the nodes at the right boundary of the tissue slab ($i = n_{s_x}$) do not consider the current from its right neighbouring points

$$\left(\frac{\partial^2 v}{\partial s_x^2} + \frac{\partial^2 v}{\partial s_y^2}\right) \approx \left(-\frac{v(s_l^i) - v(s_l^{i-1})}{\Delta_s^2} + \frac{v(s_l^{i+n_{sx}}) - v(s_l^i)}{\Delta_s^2} - \frac{v(s_l^i) - v(s_l^{i-n_{sx}})}{\Delta_s^2}\right). \tag{3.47}$$

The above boundary conditions are repeated for all the nodes at both $j = n_{s_y}$ (top) and $j = 0$ (bottom) of the tissue slab so that results in Laplacian operator approximation as

$$\left(\frac{\partial^2 v}{\partial s_x^2} + \frac{\partial^2 v}{\partial s_y^2}\right) \approx \left(\frac{v(s_l^{i+1}) - v(s_l^i)}{\Delta_s^2} - \frac{v(s_l^i) - v(s_l^{i-1})}{\Delta_s^2} - \frac{v(s_l^i) - v(s_l^{i-n_{sy}})}{\Delta_s^2}\right), \tag{3.48}$$

$$\left(\frac{\partial^2 v}{\partial s_x^2} + \frac{\partial^2 v}{\partial s_y^2}\right) \approx \left(\frac{v(s_l^{i+1}) - v(s_l^i)}{\Delta_s^2} - \frac{v(s_l^i) - v(s_l^{i-1})}{\Delta_s^2} + \frac{v(s_l^{i+n_{sy}}) - v(s_l^i)}{\Delta_s^2}\right). \tag{3.49}$$

In this approach, the resultant three-dimensional finite difference matrix can be approximated as two-dimensional matrix. For instance, the finite difference matrix for a 3 × 3 regular gridded domain can be written as

$$\mathcal{A} = \begin{pmatrix} -2 & 1 & 0 & 1 & 0 & 0 & 0 & 0 & 0 \\ 1 & -3 & 1 & 0 & 1 & 0 & 0 & 0 & 0 \\ 0 & 1 & -2 & 0 & 0 & 1 & 0 & 0 & 0 \\ 1 & 0 & 0 & -3 & 1 & 0 & 1 & 0 & 0 \\ 0 & 1 & 0 & 1 & -4 & 1 & 0 & 1 & 0 \\ 0 & 0 & 1 & 0 & 1 & -3 & 0 & 0 & 1 \\ 0 & 0 & 0 & 1 & 0 & 0 & -2 & 1 & 0 \\ 0 & 0 & 0 & 0 & 1 & 0 & 1 & -3 & 1 \\ 0 & 0 & 0 & 0 & 0 & 1 & 0 & 1 & -2 \end{pmatrix}_{[9\times 9]} \tag{3.50}$$

It should be also noted that corner node points of the tissue slab have two-node stencil point dependency. The time dependencies in the gating and transmembrane voltage variable is then approximated using the relationship given in (3.27).

The next step is to approximate the derivative operator in the extracellular electrogram model equation

$$\tilde{v}_{ex}(\mathbf{s}', t) = \tilde{\kappa} \iint (-\nabla v_t(\mathbf{s})) \cdot \nabla \left[\frac{1}{r}\right] ds_x ds_y. \tag{3.51}$$

Here, the tissue field is placed at plane with varying s_x, s_y and $s_z = 0$. The sensors are then placed on the axis parallel to the tissue field implying $s_z{}'$ is a constant value (height). Thus, Euclidean distance and the gradient measure can be calculated as

$$r = \sqrt{(s_x - s_x{}')^2 + (s_y - s_y{}')^2 + (s_z{}')^2}, \tag{3.52}$$

$$\nabla \left[\frac{1}{r}\right] = \left[\frac{-(s_x - s_x{}')}{r^3}\right] \bar{a}_x + \left[\frac{-(s_y - s_y{}')}{r^3}\right] \bar{a}_y. \tag{3.53}$$

Substituting the constituent gradient terms yields to

$$\tilde{v}_{ex}(\mathbf{s}', t) = \tilde{\kappa} \iint \left(\frac{\partial v}{\partial s_x} \frac{(s_x - s_x{}')}{r^3} + \frac{\partial v}{\partial s_y} \frac{(s_y - s_y{}')}{r^3} \right) ds_x ds_y. \tag{3.54}$$

To preserve the spatial information required in the above formulation, the finite difference matrix of the derivative operator is constructed for both s_x and s_y directions. By incorporating the no-flux boundary conditions, the forward finite difference matrices for s_x and s_y co-ordinates are formulated. Using the same example of 3 × 3 system, finite difference matrix for s_y direction can be written as

$$\mathbf{M}_{s_y} = \begin{pmatrix} -1 & 0 & 0 & 1 & 0 & 0 & 0 & 0 & 0 \\ 0 & -1 & 0 & 0 & 1 & 0 & 0 & 0 & 0 \\ 0 & 0 & -1 & 0 & 0 & 1 & 0 & 0 & 0 \\ 0 & 0 & 0 & -1 & 0 & 0 & 1 & 0 & 0 \\ 0 & 0 & 0 & 0 & -1 & 0 & 0 & 1 & 0 \\ 0 & 0 & 0 & 0 & 0 & -1 & 0 & 0 & 1 \\ 0 & 0 & 0 & 0 & 0 & 0 & 0 & 0 & 0 \\ 0 & 0 & 0 & 0 & 0 & 0 & 0 & 0 & 0 \\ 0 & 0 & 0 & 0 & 0 & 0 & 0 & 0 & 0 \end{pmatrix}_{[9\times9]} \tag{3.55}$$

On the other hand, the finite difference matrix $\mathbf{M}_{s_x}$ (s_x direction) follows a similar matrix structure as $\mathbf{M}_{s_x}$ in (3.32), which can be extended to two-dimensional field depending on the number of nodes.

Normal Activation Patterns

In this example, normal activation patterns in two-dimensional tissue slab of 1 × 1 cm are presented.

Similar to the one dimensional examples, discretisation is performed here using space and time steps of 0.025 cm and 0.05 ms respectively. This results in a 41×41 gridded domain and giving total number of cells as 1681. The electrodes are placed at a height of 1 mm on the plane parallel to the tissue field to measure the electrograms using model equation in (3.54). This gives the total number

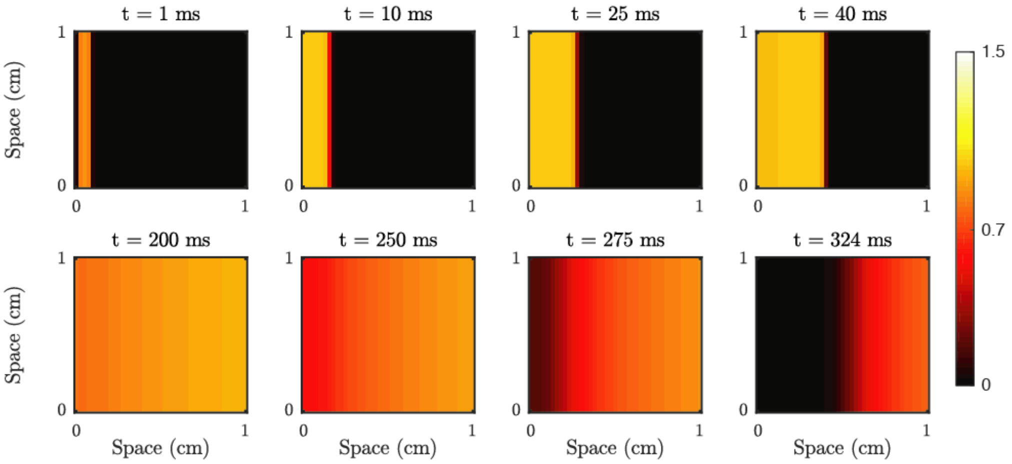

Figure 3.11. **Example of the simulated spatiotemporal patterns of transmembrane voltage as plane wave in a two-dimensional domain**. The electrophysiology parameters are θ_g = 0.0001 cm^{2}ms^{-1}, $v^{st} = 0.7, T^{st} = 2ms, \gamma = 25$.

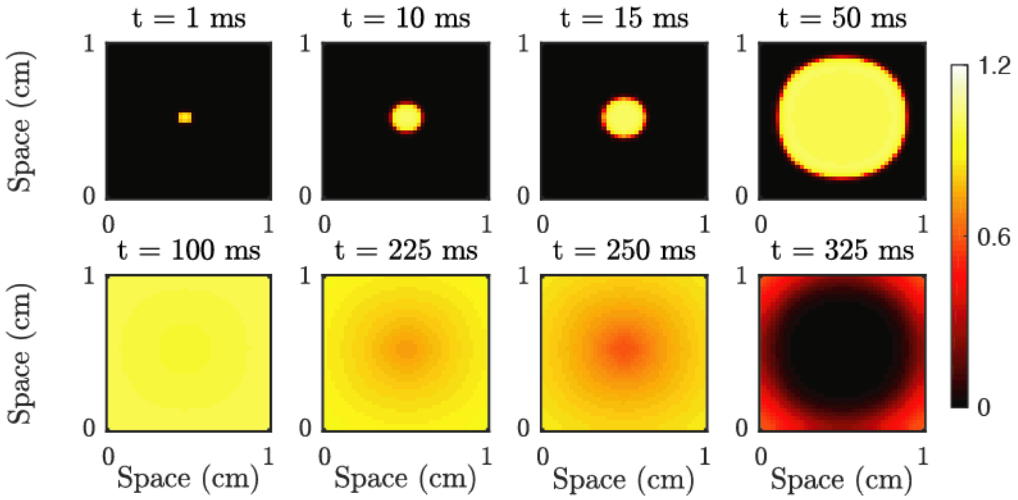

Figure 3.12. **Example of the simulated spatiotemporal patterns of transmembrane voltage as circular wave in a two-dimensional domain**. Here, the external stimulus is applied at the centre of the tissue field that resulted in circular activation patterns. The electrophysiology parameters are θ_g = 0.0001 cm^{2}ms^{-1}, $v^{st} = 0.7, T^{st} = 2ms, \gamma = 25$.

of electrodes to be 100. Simulation is performed for a total of 900 ms using the electrophysiology parameters given in Table 3.1.

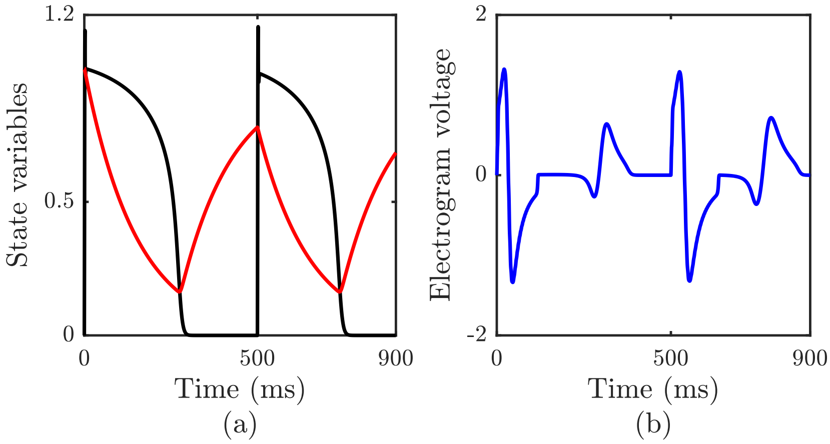

Figure 3.13. **Examples of state variables and electrogram measurements.** (a) State variable, s_x = 0.025 cm. (b) Electrogram measurements. State variables are transmembrane voltage (▬), gating variable (▬).

To illustrate the action potential propagation under normal cardiac conditions, two types of stimulations are considered. In the first example, external stimulus is applied from $s_x = 0.025$ cm to $s_x = 0.075$ cm (left edge of the slab) at two different times (0 ms and 500 ms). This results in two action potential cycles, and

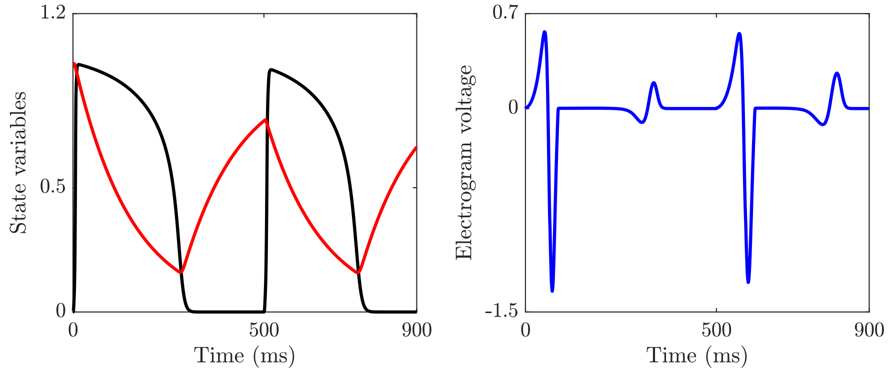

(a) (b)

Figure 3.14. Examples of state variables and electrogram measurements. (a) State variable, s_x = 0.025 cm. (b) Electrogram measurements. State variables are transmembrane voltage (—), gating variable (—).

the activation patterns during first cycle are shown in Figure 3.11. Within a cycle, action potentials are initiated at the left edge of the slab, travel along the space and terminate at the right boundary of the slab. This type of activation wave patterns is also known as planar wave [3].

In the second example, external stimulus is applied between $s_x, s_y = 0.475$ cm and $s_x, s_y = 0.525$ cm (3×3 grid), at two different times similar to that of plane wave simulation. As shown in Figure 3.12, action potentials are initiated from the stimuli location and propagate at all directions as a circular activation wave pattern [32]. After the repolarisation stage, cells return to their resting potential, beginning from the stimulus locations to the edges of tissue slab (See Figure 3.12). Examples of action potential and electrogram measurement from both simulations are shown in Figures 3.13 and 3.14, respectively.

Re-entrant Activation Patterns

In this example, re-entrant activation patterns in two-dimensional spatial field are presented.

To simulate the re-entrant activity, the cross-field stimulation protocol detailed in Section 3.2.1 is employed. Here, simulation is performed for a total of 2000 ms. Briefly, re-entry is generated by applying disturbance to the propagation of normal activation wave. Thus, the first stimulus S1 is applied to generate a planar wave that propagates along the tissue slab (see Figure 3.11). Once the wave-tail of this planar activation wave reaches the middle area of tissue slab, the second stimulus S2 is applied at the left bottom corner of slab (5 mm high × 2.5 mm wide) from 324 ms to 326 ms. Figure 3.16 illustrates the activation patterns corresponding to

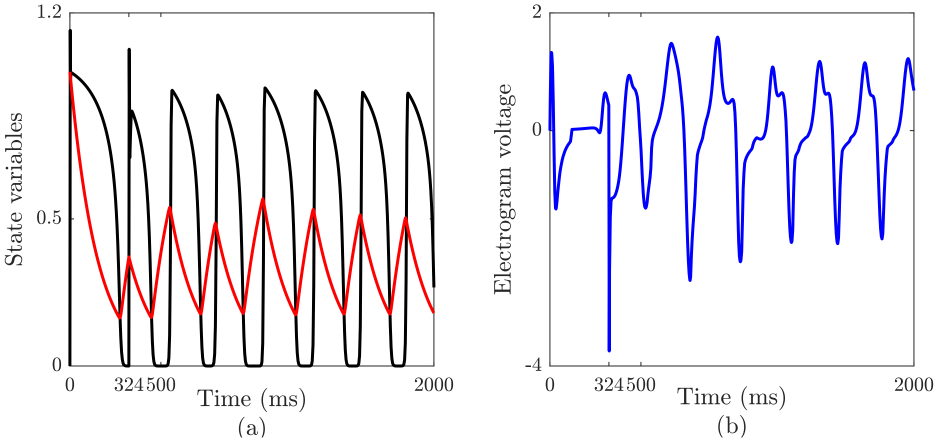

Figure 3.15. Examples of state variables and electrogram measurements from the continuous version of mMS model. (a) State variable, s_x, s_y = 0.025 cm. (b) Electrogram measurements. State variables are transmembrane voltage (—), gating variable (—).

the second stimulus S2 applied during the vulnerable window. As the symmetry of propagation is broken, the activation wave travels along the direction where the cells are being excitable. For instance at first activation waves travel towards the top edge of tissue slab due to the presence of travelling planar wave at the right side (see Figure 3.16 E-H). Once the planar wave has terminated and cells at the right side of tissue are excitable, activation wave propagates towards the right. This activity is then repeated and activation wave travels toward left side, where the tissue region has recovered. Thus, activation waves rotate by propagating into the recovering tissue and forms the spiral re-entrant activation patterns in a two-dimensional spatial field. The spiral re-entry patterns are persisted throughout the simulation as shown in Figure 3.16. Example of action potential in Figure 3.15 (a) shows the persisted excitation of action potential even without applying the external stimuli at a time interval. On the other hand, Figure 3.15(b) illustrates the characteristic difference in the electrogram during the spiral re-entry. Similar to the one-dimensional spatial field, the stability analysis shown in Table 3.2 shows that the selected simulation parameters satisfy the stability criterion.

3.3 Comparison with Modified Mitchell Schaeffer Model

In this section, the simulation results from the original Mitchell-Schaeffer model and the developed continuous version of modified Mitchell-Schaeffer models are compared.

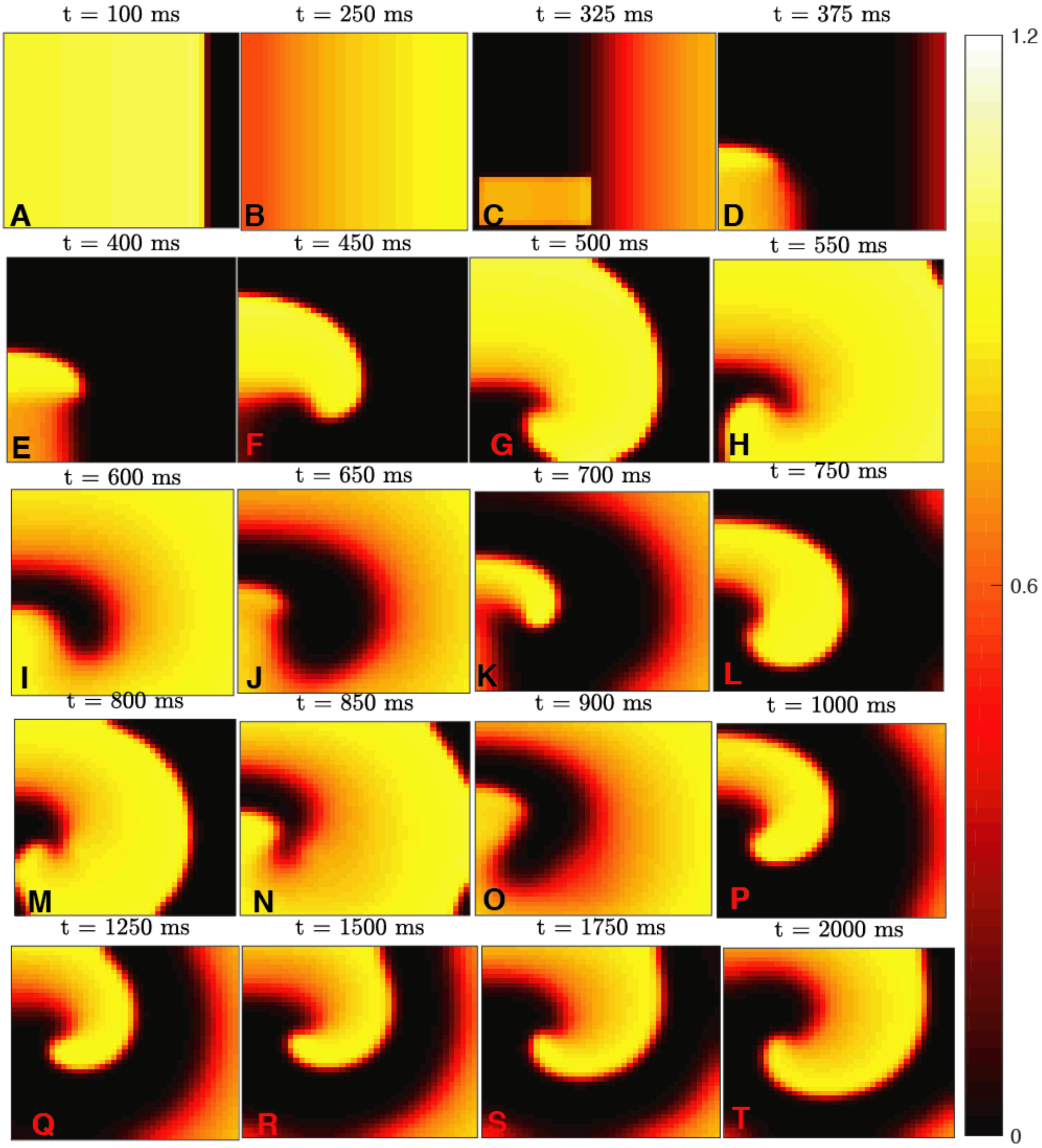

Figure 3.16. **Example of the simulated spatiotemporal patterns of transmembrane voltage during spiral re-entrant activity in an two-dimensional tissue model coupled with continuous version of mMS model.** The electrophysiology parameters are θ_g = 0.0001 cm^{2}ms^{-1}, $v^{st} = 0.7, T^{st} = 2ms, \gamma = 25$.

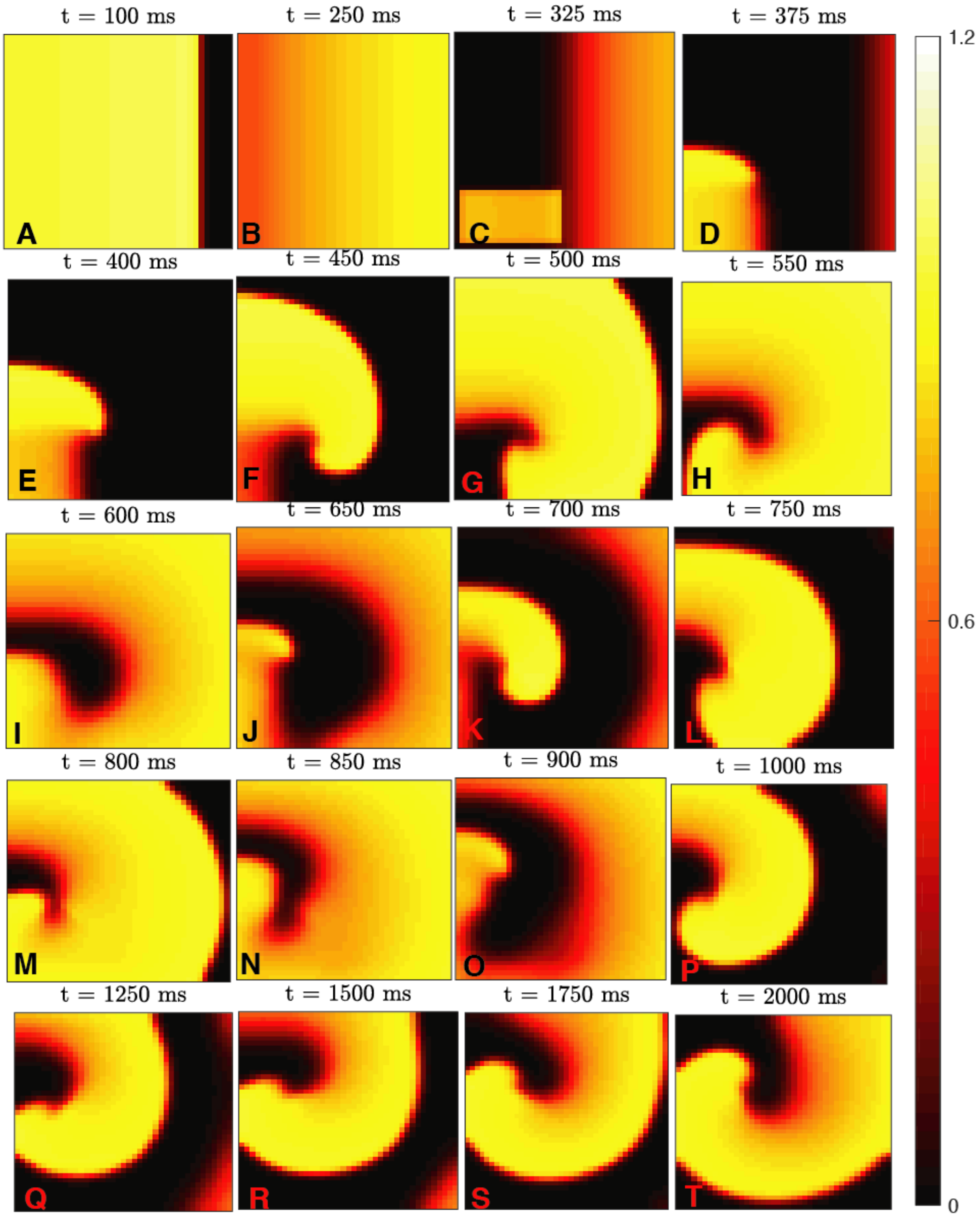

Figure 3.17. Example of the simulated spatiotemporal patterns of transmembrane voltage during spiral re-entrant activity in an two-dimensional tissue model coupled with the modified Mitchell-Schaeffer model. The electrophysiology parameters are θ_g = 0.0001 cm^{2}ms^{-1}, $v^{st} = 0.7, T^{st} = 2ms$.

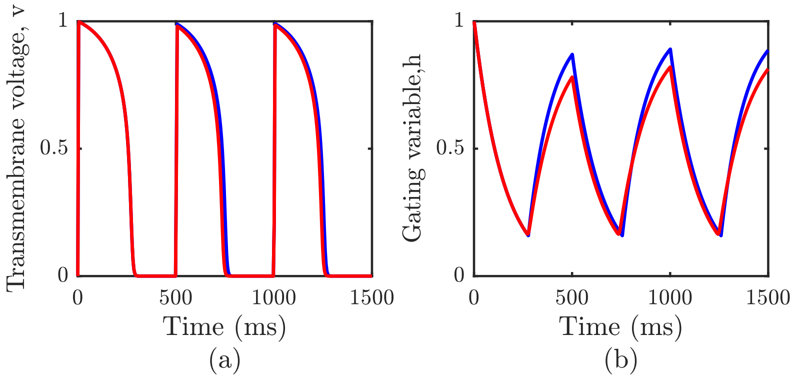

(a)

(b)

Figure 3.18. **State variables simulated using modified Mitchell-Schaeffer model (—) and the continuous version of mMS model (—).** An external stimulus is applied at every 500ms with electrophysiology parameters: $\tau_{in} = 0.3, \tau_{out} = 6, \tau_{open} = 120, \tau_{close} = 150, v_g = 0.13, v^{st} = 0.15, T^{st} = 2ms, \gamma = 25$. (a) Normalised transmembrane voltage. (b) Gating variable.

First the state variables simulated using the proposed continuous version of cell model given in equations (3.3) and (3.8) are compared with modified Mitchell-Schaeffer model (given in (3.3) and (3.4)). Here,the result from a single cell model using a slope value of 25 is shown in Figure 3.18. As described in section 3.1, action potential simulated from the proposed model follows the signal morphology of the modified Mitchell-Schaeffer model. It should be noted that the difference in the characteristics of action potential and gating variable can be decreased by increasing the slope value. However, the observed difference during repolarisation is the result of the approximation used to obtain a simplified representation of the time constants ($\tau = max\{\tau_{open}, \tau_{close}\}$).

To examine the performance of the proposed continuous model, state variables are computed from both models using three sets of electrophysiology parameters given in Table 3.3. These values are taken from the previous study [38] in which modified Mitchell-Schaeffer model was derived and compared with the classical Mitchell- Schaeffer model to test the pacemaker stability. The Root Mean Squared Error (RMSE) between the modified Mitchell- Schaeffer model and the proposed continuous version is calculated for corresponding values of slopes. For instance, RMSE of transmembrane voltage can be calculated as follows

$$\mathbf{RMSE}(v) = \sqrt{\frac{1}{T}\sum_{k=1}^{T}\left(v_k - \hat{v}_k\right)^2} \tag{3.56}$$

where v_k and $\hat{v}_k$ are the transmembrane voltages from modified Mitchell-Schaeffer and continuous version of Mitchell-Schaeffer models.

The results from this analysis is shown in Figure 3.19 demonstrate that the RMSE measure is higher for smaller slope values. This is because, switching dynamics in gating variable requires higher rate of change that can be achieved by increasing the slope measure. Consequently, the RMSE measure decreases with increase in slope value. Moreover, the smaller value of RMSE observed for higher slope values is due to the approximation used in the time constants.

Table 3.3. Time constant values used for comparing the state variables.

	τ_{in}	τ_{out}	τ_{open}	τ_{close}
1	0.3	6.0	120	150
2	0.1	9.0	100	120
3	0.15	6.5	90	85

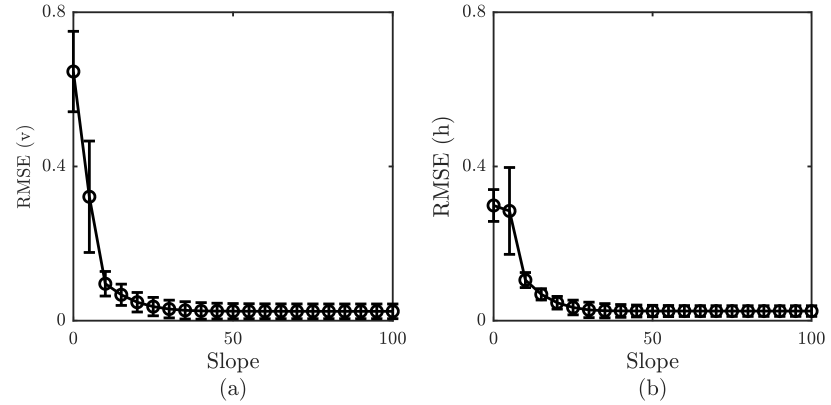

Figure 3.19. Error bar shows the averaged trend across three sets of electrophysiology parameters given in Table 3.3.

Finally, the differences in the tissue level characteristics were compared qualitatively by analysing the simulated activation patterns from both models. Here, spiral activations from the mMS model were simulated with the same simulation setup and electrophysiology parameters. The corresponding results are shown in Figure 3.17. It can be seen that the activation patterns follow similar trajectory and capture the basic structure of the activation patterns at the selected slope value ($\gamma = 25$). However, the above described approximations and the smaller slope value may cause a delay in the initiation of action potentials. This can be observed by comparing Figure 3.16 and Figure 3.17). This translational difference in the action potential morphology at the same node in the spatial field ($l = 43$) is then analysed for two slope values of 25 and 100, shown in Figure 3.20. The results show that increasing the slope value allows to capture the gating variable morphology more accurately, which reduces the differences in the transmembrane voltage.

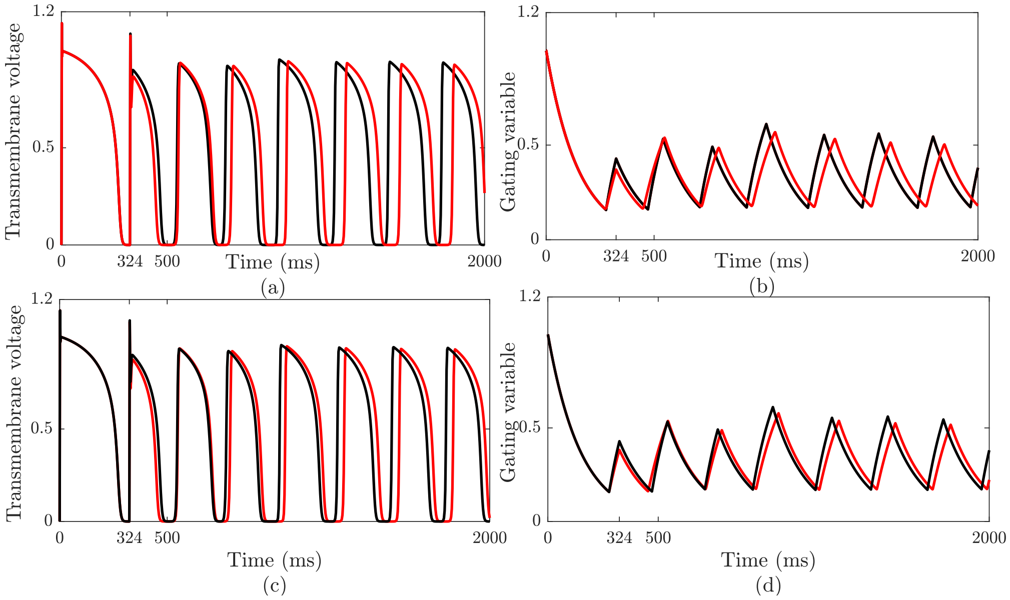

(a) (b) (c) (d)

Figure 3.20. **Example of state variables from the spiral re-entrant activation patterns from mMS model and continuous version of mMS model with two slope values.** (a)-(b) are modelled with a slope value of $\gamma = 25$, (c)-(d) are modelled with a slope value of $\gamma = 100$. Modified Mitchell-Schaeffer model (—) and the continuous version of modified Mitchell-Schaeffer model (—).

It should be noted that the proposed continuous version of mMS model has smaller approximation errors, which may lead to progressive delay and differences in the action potentials. However, this model allows the implementation of estimation frameworks, where state estimates and parameters are inferred from the measurements. The estimation frameworks include predictions and corrections steps, which are based on the observed measurements. Thus, the observed drifts are not of an issue in the estimation method as it can tackle with the small modelling errors.

3.4 Conclusion

This chapter has presented a modelling and simulation study of cardiac electrical activity patterns. From the literature of cardiac models, modified Mitchell-Schaeffer model is considered as a suitable candidate cell model as it has fewer number of parameters and two state variables. The nominal state variables are transmembrane voltage and gating variable.

The key contributions of this chapter are the following:

- A continuous version of modified Mitchell-Schaeffer model has been derived, by approximating the discontinuous gating variable formulation using a sigmoid function. By doing so, a slope parameter can be used to alter the rate of steepness in the gating variable dynamics. The proposed model allows straightforward implementation of state and parameter estimation frameworks, for otherwise abrupt changes in the gating variables may cause divergence in the estimation of nonlinear systems.

- An integrated model of cardiac electrophysiology has been derived by using incorporating the proposed cell model into the monodomain tissue equations. The resulting tissue level model is a coupled partial differential equation with spatial and temporal dynamics. An extracellular electrogram model equation was then added to the integrative model to capture the observed surface measurement characteristics. The derived integrated model equations can be used for inference framework to reconstruct the tissue dynamics from the electrogram measurements, proposed in Chapter 4 and Chapter 5.

- The cardiac electrical activity was further studied as a forward problem, by generating the normal and abnormal cardiac patterns in one and two dimensional spatial fields. The stimulation protocols that were used to generate the re-entrant activity aided to identify the spatiotemporal dynamics of stimulus variable in the tissue model equations. As a result, inference framework of tissue dynamics should incorporate an additional step for detecting and estimating the stimulus variable, along with estimation of the nominal state variables.

- The comparison of the action potentials modelled using mMS and continuous version of the mMS shows that the proposed model can reproduce the overall characteristics of the electrical activity patterns, especially the complex spiral dynamics. However, the proposed continuous version of mMS models illustrated differences in the action potentials, when using a smaller slope value in the sigmoid approximations of the gating variable. As the estimation frameworks include recursive predictions and corrections procedures, the modelling errors can be tackled by learning from the observations.

Chapter 4

Detection and Estimation Framework For One-dimensional Cardiac Model

As stated in Section 1.4, one of the important aims of this thesis is to develop a combined detection-estimation framework for reconstructing the tissue dynamics from electrogram measurements. This chapter establishes the proposed detection-estimation methodology for a one-dimension cardiac tissue model.

The proposed detection-estimation framework builds upon the integrated cardiac model derived in the previous chapter. However, the cardiac model equations with the continuous version of mMS ionic model given in (3.20), (3.12) and (3.28) are of deterministic nature. There are situations where uncertainties caused by un-modelled dynamics and inherent approximations should be considered in the modelling frameworks. This is mainly addressed by using stochastic models, which are derived after coupling the deterministic model equations with random forcing signals [75]. Stochastic models are of particular interest in cardiac modelling studies as they allow to incorporate the intrinsic and extrinsic variabilities observed in action potentials [106, 157, 158]. The intrinsic variability is associated with the temporal differences in action potentials within a cell. On the other hand, extrinsic variability characterises the differences in action potentials between cells at different spatial locations [158]. In order to account for the effects of above mentioned factors in the estimation framework, stochastic cardiac model equations are derived in this chapter.

The resulting stochastic version of the cardiac model can be represented as a finite-dimensional state space model, which allow the estimation of the state variables to be formulated as an filtering or smoothing problem. The resulting estimation problem can be solved using one of the nonlinear state estimation methods. Some studies have demonstrated the ability to infer the hidden gating variables, filtered transmembrane voltage variable, using the Kalman filter based estimation methods [69, 140]. However, the state of art highlights two important gaps in the current estimation approaches. Firstly, the estimation methods have been applied to optical mapping surface measurements, where the observations are predominantly noise corrupted versions of transmembrane voltage [69, 140]. However, the dynamics of extracellular electrograms detailed in Section 2.2.3 can be incorporated into estimation framework for reconstructing the tissue dynamics from unipolar cardiac electrograms, obtained from the electric mapping techniques [18, 22]. The inclusion of electrogram dynamics introduces an additional layer of latency into the modelling and estimation framework, where both transmembrane voltage and gating variable required to be estimated from the electrogram measurements. Secondly, the detection and estimation of stimulus variable can be incorporated into the estimation framework to improve the accuracy of the state estimates. This is also important as the stimulus variables can be considered as potential re-entrant activation sites within the tissue field, as evidenced by the simulation results in Chapter 3. For instance, it can be seen in Section 3.2.1 and Section 3.2.2 that the propagation of re-entrant activation patterns was initiated by stimulus current applied at particular spatial locations and time-instants. More specifically, re-entrant activity was caused from stimulus activation signals applied at recovering cell locations within the vulnerable window. Therefore, identifying the spatial locations and time instants that correspond to the initiation of the activation patterns, especially for the re-entrant activation patterns is important. In a clinical setting, detection of the re-entrant activation sites is particularly important, as it can be considered as the potential ablation targets for the treatment of the arrhythmic conditions. Moreover, the estimation of the stimulus variables can also be considered as a factor to obtain the accurate reconstruction of the underlying tissue dynamics field.

In signal estimation and detection theory, the class of estimation approaches that are used to infer the abrupt changes in the system dynamics are referred as detection-estimation approaches [154]. In general, detection-estimation problems play a vital role in signal estimation and detection theory [62] , which have been applied in several fields including cyber-physical systems [50] and biochemical systems [76] and radar systems [127], etc. However this type of model-based inference problems have not yet been reported in the literature of cardiac modelling.

Hence, in this chapter, a novel approach is proposed to estimate the state variables of tissue dynamics from electrogram measurements by incorporating the detection and estimation of stimulus variables. The estimation algorithm proposed includes the following steps:

- A model-based detection scheme is performed to determine if the cardiac activity is occurring with or without stimulus, where the model is formulated based on the nominal system behaviour.
- When a stimulus is detected and isolated, an augmented state space model is formed by incorporating the stimulus variables that corresponding to the sensor locations.
    - To capture the local support and interpolation properties introduced by the detected stimulus locations in the tissue field, linear combination of basis functions are used to represent the dynamics of stimulus variables. The basis functions are centered on the corresponding sensor locations in tissue field, which detected the presence of the stimulus.
    - The resulting basis functions are then incorporated into the augmented state-space model to estimate the stimulus variables at the detected sensor locations, and also to obtain accurate estimates of transmembrane voltage and gating variable across the tissue field.
- A nonlinear state estimation via URTS smoothing algorithm is employed for computing the state variables of the nominal or augmented state-space model.

To illustrate the performance of the proposed methodology, data of cardiac electrical activation patterns during normal and re-entrant cardiac conditions are modelled using the integrated model with mMS ionic model. This can also demonstrate the ability of the proposed model to capture the tissue dynamics.

The remainder of this chapter is organised as follows. Section 4.1 presents the derivation of stochastic models of cardiac electrophysiology. This is followed by the description of proposed detection-estimation methodology in Section 4.3. The simulation setup and data generation are then detailed in Section 4.4, and the results are presented and discussed in Section 4.5. Finally, important conclusions are summarised in Section 4.6.

4.1 Nonlinear State-space Representation of Stochastic Cardiac Models

In this section, the derivation of the stochastic cardiac model is presented. This is achieved by incorporating additive random disturbances into the deterministic model equations given in (3.20), (3.12) and (3.28).

The stochastic tissue model equations in one-dimensional tissue field can be written as

$$\begin{aligned}\frac{\partial v(s_x,t)}{\partial t} = \theta_g \frac{\partial^2 v(s_x,t)}{\partial s_x^2} + h(s_x,t)\frac{v(s_x,t)(v(s_x,t)-v_g)(1-v(s_x,t))}{\tau_{in}} \\ -(1-h(s_x,t))\frac{v(s_x,t)}{\tau_{out}} + i^{st}(s_x,t) + \sigma_v \frac{\partial \zeta^v(s_x,t)}{\partial t},\end{aligned} \tag{4.1}$$

$$\frac{\partial h(s_x,t)}{\partial t} = \frac{e^{-\gamma(v(s_x,t)-v_g)}}{\tau\left(1+e^{-\gamma(v(s_x,t)-v_g)}\right)} - \frac{h(s_x,t)}{\tau} + \sigma_h \frac{\partial \zeta^h(s_x,t)}{\partial t}, \tag{4.2}$$

where the additive disturbance term in each state variable ($\dot{\zeta}(s_x,t)$) is a space-time white noise, defined as a formal derivative of stochastic Weiner process or Brownian motion [75]. The additive disturbance term is further approximated to be spatially uncorrelated Weiner process.

The resulting tissue model is a system of nonlinear coupled stochastic partial differential equations (SPDE), which constitutes an infinite-dimensional spatiotemporal model. However, the standard signal processing and estimation techniques are generally developed for finite-dimensional model structures. Thus, a model reduction method is employed to convert the infinite-dimensional model to a finite-dimensional model structure. Similar to the simulation studies in Chapter 3, the method of finite difference is employed to form the finite dimensional state-space model. The resulting state-space formulation allows to describe the observed measurements and hidden state variables within a compact model structure for estimation.

To obtain the finite-dimensional state-space model, evolution of transmembrane voltage given in (4.1) is first rewritten as

$$\begin{aligned}\partial v(s_x,t) = \theta_g \frac{\partial^2 v(s_x,t)}{\partial s_x^2}\partial t - \theta_d\, v(s_x,t)\partial t + \theta_b\, h(s_x,t)\, v(s_x,t)\partial t + \theta_c\, h(s_x,t)\, v^2(s_x,t)\partial t \\ -\theta_a\, h(s_x,t)\, v^3(s_x,t)\partial t + i^{st}(s_x,t)\partial t + \sigma_v \partial \zeta^v(s_x,t),\end{aligned} \tag{4.3}$$

where the constant parameters are given by

$$\theta_a = \frac{1}{\tau_{in}},\ \ \theta_b = \left[\theta_d - \theta_a v_g\right],\ \ \theta_c = \left[\theta_a + \theta_a v_g\right],\ \ \theta_d = \frac{1}{\tau_{out}}.$$

Spatial discretisation is then implemented using finite difference method detailed in Section 3.2.1. It can be seen from (4.3) that the spatial dependency of nodes on their neighbouring nodes is described in the Laplacian operator of diffusion term. On the other hand, the spatial dependency of nodes in reaction terms is on the node itself. Therefore, Laplacian operator is approximated using finite difference approach to obtain the discrete representation of the spatial field. This approach also allows straightforward implementation compared to other model reduction techniques such as method of moments [63], basis function decompositions [102], spatial filters [124], etc. The finite difference matrix, $\mathcal{A}$, comprises difference quotients, that reflect the spatial dependency of each nodes on its neighbouring nodes. The resulting matrix $\mathcal{A}$ for one dimensional cable field and ring field domains is given in (3.32) and (3.35), respectively. Substituting the finite difference matrix $\mathcal{A}$ into (4.3) enables the formulation of the temporal evolution of transmembrane voltage as a Stochastic Differential Equation (SDE) given as

$$\begin{aligned} d\mathbf{v}(t) = \frac{\theta_g}{\Delta_s^2}\mathcal{A}\mathbf{v}(t)dt - \theta_d\, \mathbf{v}(t)dt + \theta_b\, \left(\mathbf{h}(t)\odot\mathbf{v}(t)\right)dt + \theta_c\, \left(\mathbf{h}(t)\odot\mathbf{v}(t)\odot\mathbf{v}(t)\right)dt - \\ \theta_a\, \left(\mathbf{h}(t)\odot\mathbf{v}(t)\odot\mathbf{v}(t)\odot\mathbf{v}(t)\right)dt + \mathbf{i}^{st}(t)dt + \sigma_v d\boldsymbol{\zeta}^v(t), \end{aligned} \tag{4.4}$$

where,

$$\begin{aligned} \mathbf{v}(t) &= \begin{pmatrix} v_1(t) & v_2(t) & \dots & v_{n_s}(t) \end{pmatrix}^\top, \\ \mathbf{h}(t) &= \begin{pmatrix} h_1(t) & h_2(t) & \dots & h_{n_s}(t) \end{pmatrix}^\top, \\ \boldsymbol{\zeta}^v(t) &= \begin{pmatrix} \zeta_1^v(t) & \zeta_2^v(t) & \dots & \zeta_{n_s}^v(t) \end{pmatrix}^\top, \\ \mathbf{i}^{st}(t) &= \begin{pmatrix} i_1^{st}(t) & i_2^{st}(t) & \dots & i_{n_s}^{st}(t) \end{pmatrix}^\top. \end{aligned}$$

The above expression also allows to represent the additive disturbance term as a function of time [21, 75]. Following the spatial discretisation, the temporal discretisation of transmembrane potential is then implemented using first order forward difference equation given in (3.27). To simplify the notations and for better clarity, descritised values are defined as $v_{\bar{s}_x,k} := v(s_x\Delta_s, k\Delta_t)$ and $h_{\bar{s}_x,k} := h(s_x\Delta_s, k\Delta_t)$ and the future time instant $(k+\Delta_t)$ is written as $(k+1)$. The first order forward difference in the time domain yields the following transmembrane voltage equation

$$\begin{aligned} \mathbf{v}_{k+1} - \mathbf{v}_k = \frac{\theta_g\Delta_t}{\Delta_s^2}\,\mathcal{A}\mathbf{v}_k - \theta_d\mathbf{v}_k\Delta_t + \theta_b\mathbf{H}_k\mathbf{v}_k\Delta_t + \theta_c\mathbf{H}_k\bar{\mathbf{v}}_{k2}\Delta_t - \theta_a\mathbf{H}_k\bar{\mathbf{v}}_{k3}\Delta_t \\ + \Delta t\mathbf{i}_k^{st} + \sigma_v\left(\boldsymbol{\zeta}_{k+1}^v - \boldsymbol{\zeta}_k^v\right), \end{aligned} \tag{4.5}$$

where $\mathbf{v}_k \in \mathbb{R}^{n_s}$, $\mathbf{H}_k \in \mathbb{R}^{n_s \times n_s}$, and stimulus variable $\mathbf{i}_t^{st} \in \mathbb{R}^{n_s}$,

$$\mathbf{H}_k = diag(h_{1,k} \quad h_{2,k} \quad ... \quad h_{n_s,k}),$$

$$\mathbf{v}_k = \left(v_{1,k} \quad v_{2,k} \quad ... \quad v_{n_s,k}\right)^\top,$$

$$\bar{\mathbf{v}}_{k2} = \left(v_{1,k}^2 \quad v_{2,k}^2 \quad ... \quad v_{n_s,k}^2\right)^\top,$$

$$\bar{\mathbf{v}}_{k3} = \left(v_{1,k}^3 \quad v_{2,k}^3 \quad ... \quad v_{n_s,k}^3\right)^\top,$$

$$\mathbf{i}_k^{st} = \left(i_{1,k}^{st} \quad i_{2,k}^{st} \quad ... \quad i_{n_s,k}^{st}\right)^\top.$$

The discretised form of additive disturbance term $\left(\zeta_{k+1}^v - \zeta_k^v\right) \in \mathbb{R}^{n_s}$ is the vector of stationary independent Weiner increment. A Weiner process is a stochastic process that follows a normal distribution with mean of 0 and covariance of $\sigma^2\Delta_t$ within the time interval $[k, k+1]$ [75]. Thus the additive disturbance follows a zero mean Gaussian noise process with covariance given by

$$\Sigma_v = \sigma_v^2 \mathbb{E}\left[\Delta\zeta_k^v \Delta\zeta_k^{v\top}\right], \tag{4.6}$$

$$\Sigma_v = \sigma_v^2 \Delta_t. \tag{4.7}$$

Simplifying the state evolution equation of transmembrane voltage gives

$$\mathbf{v}_{k+1} = \bar{\theta}_e \mathcal{A}\mathbf{v}_k + \bar{\mathbf{\Psi}}_k \bar{\boldsymbol{\theta}}^\top + \mathbf{i}_k^{st}\ \Delta_t + \boldsymbol{\epsilon}_k^v, \tag{4.8}$$

where

$$\bar{\theta}_e = \frac{\theta_g \Delta_t}{\Delta_s^2}, \quad \bar{\boldsymbol{\theta}} = \left[\theta_b\Delta_t \quad \theta_c\Delta_t \quad \theta_d\Delta_t\right], \quad \bar{\mathbf{\Psi}}_k = [\mathbf{v}_k \quad \mathbf{H}_k\mathbf{v}_k \quad \mathbf{H}_k\bar{\mathbf{v}}_{k2} \quad \mathbf{H}_k\bar{\mathbf{v}}_{k3}],$$

$$\boldsymbol{\epsilon}_k^v \sim \mathcal{N}(\mathbf{0}, \sigma_v^2\Delta_t\mathbf{I}).$$

Similarly, the stochastic model equation of the gating variable is descritised using first order forward difference temporal discretisation scheme. The resulting state evolution equation for the gating variable can be written as

$$\mathbf{h}_{k+1} = \bar{\theta}_f \mathbf{h}_k + \bar{\theta}_f \bar{\boldsymbol{\beta}}_k + \boldsymbol{\epsilon}_k^h, \tag{4.9}$$

where

$$\bar{\theta}_f = \frac{\Delta_t}{\tau}, \qquad \boldsymbol{\epsilon}_k^h \sim \mathcal{N}(\mathbf{0}, \sigma_h^2\Delta_t\mathbf{I}),$$

$$\bar{\boldsymbol{\beta}}_k = \left(\bar{\beta}_{1,k}, \bar{\beta}_{2,k}, \quad ... \quad \bar{\beta}_{n_s,k}\right)^\top, \quad \bar{\beta}_{n_s,k} = \frac{e^{-\gamma(v_{n_s,k}-v_g)}}{1 + e^{-\gamma(v_{n_s,k}-v_g)}}.$$

By combing the model equation of two state variables, evolution equation of the nonlinear state-space model can be summarised as

$$\mathbf{x}_{k+1} = \mathbf{f}(\mathbf{x}_k, \mathbf{i}_k^{st}) + \boldsymbol{\epsilon}_k^x, \tag{4.10}$$

where $\mathbf{x}_k \in \mathbb{R}^{n_x}$ is the vector of state variables that includes transmembrane voltage and gating variable $[\mathbf{v}_k \;\; \mathbf{h}_k]^\top$, n_x is the number of states, $\boldsymbol{\epsilon}_k^x = [\boldsymbol{\epsilon}_k^v, \boldsymbol{\epsilon}_k^h]^\top$ are Gaussian noise processes with zero mean and covariance $\boldsymbol{\Sigma}_v$ and $\boldsymbol{\Sigma}_h$, respectively. The nonlinear model function of state variables is given as

$$\mathbf{f}(\mathbf{x}_k, \mathbf{i}_k^{st}) = \begin{bmatrix} \bar{\theta}_e \mathcal{A}\mathbf{v}_k + \bar{\boldsymbol{\Psi}}_k \bar{\boldsymbol{\theta}}^\top + \mathbf{i}_k^{st}\Delta_t \\ \\ \bar{\theta}_f \mathbf{h}_k + \bar{\boldsymbol{\beta}}_k \bar{\theta}_f \end{bmatrix}.$$

The mapping of state variables to the extracellular electrograms measured at the discrete spatial locations in sensor field ($\mathbf{s}' = s_x', s_y'$) can be modelled using (3.28). The stochastic model equation for extracellular electrogram is given by

$$v_k^{ex}(\mathbf{s}') = \tilde{\kappa} \int_L \nabla v(s_x, t) \nabla(1/r) ds_x + \epsilon_k^y(\mathbf{s}'), \tag{4.11}$$

where $\epsilon_k^y(\mathbf{s}')$ is the independent Gaussian white noise sequences.

Equation (4.11) is temporally discrete and only the discretisation of differential operator in the temporal domain needs to be employed. The resulting finite dimensional matrix $\mathbf{M}_{s_x}$ derived in (3.32) and (3.35) can be chosen based on the type of sensor field. The gradient measure of distance between the tissue and sensor fields can be precomputed from the analytical expression given in (3.34). This allows to describe the observation equation of the state-space model as

$$\mathbf{y}_k = \mathbf{C}\mathbf{x}_k + \boldsymbol{\epsilon}_k^y, \tag{4.12}$$

where $\mathbf{y}_k \in \mathbb{R}^{n_y}$ is the extracellular potentials given by $\left\{v_{j,k}^{ex}\right\}_{j=1}^{n_y}$, n_y is the number of sensors, $\boldsymbol{\epsilon}_k^y \in \mathbb{R}^{n_y}$ is vector of normally distributed Gaussian white noise sequences with zero mean and covariance given by $\sigma_y^2\mathbf{I}$. It can be seen that the mapping between elctrograms and state variables is quantified using a linear observation equation, where mapping is given by observation matrix $\mathbf{C} \in \mathbb{R}^{n_y \times n_x}$. It is constructed as $\mathbf{C} = [\bar{\mathbf{C}} \;\; \mathbf{0}]$ such that current electrograms are mapped through the function of transmembrane voltage and corrupted by white noise. Thus each j^{th}row in $\bar{\mathbf{C}}$ matrix represents the dynamics of sensor at $\mathbf{s}_j'$ described by

$$\bar{\mathbf{C}}_j = \bar{\kappa} \left(\nabla 1/\mathbf{r}(\mathbf{s}_j', s_x)\right) \mathbf{M}_{s_x}. \tag{4.13}$$

By combining the dynamics described for all the n_y sensors, the observation matrix for transmembrane voltage can be written as

$$\bar{\mathbf{C}} = \bar{\kappa}\ \mathbf{R}_{s_x}^{\top}\ \mathbf{M}_{s_x}. \tag{4.14}$$

Hence, the final nonlinear state-space model equations of the stochastic cardiac model are given by (4.10) and (4.12).

4.2 Problem Statement

The overall aim is to reconstruct the tissue dynamics in the one-dimensional spatial field from the electrogram measurements. However, the tissue dynamics described in state evolution equation can take the following conditions as

$$\mathbf{x}_{k+1} = \begin{cases} \mathbf{f}(\mathbf{x}_k) + \boldsymbol{\epsilon}_k^x, & \text{under no stimulus condition} \\ \mathbf{f}(\mathbf{x}_k, \mathbf{i}_k^{st}) + \boldsymbol{\epsilon}_k^x, & \text{under stimulus condition} \end{cases} \tag{4.15}$$

Therefore, the aim is to estimate the state variables via nonlinear smoothing algorithm using one of the conditional models in (4.15).

4.3 Combined Detection-Estimation Framework

In this section, the methodology to estimate the states variables of the stochastic tissue model from the unipolar electrograms is established even in the presence or absence of the stimuli.

As described earlier, the URTS smoothing algorithm presented in Section 2.3.2 can be employed to infer the hidden states $\tilde{\mathbf{x}}_k = [\mathbf{v}_k, \mathbf{h}_k]$, from noisy observations based on the underlying stochastic cardiac model. However, changes in the cardiac electrical dynamics that are induced by the abrupt changes of stimuli need to be incorporated into the estimation framework. Although, stimulus drives the process as an input but it is not observed directly, and according to (4.15) the stimulus information can be considered as a system state in the stochastic cardiac model. It should be noted that when the stimulus is present, the unknown level of stimulus variable must also be estimated. This estimation problem can be tackled using state-augmentation approach. To solve this estimation problem by the augmentation of the full stimulus variables as an augmented vector $\mathbf{i}_k^{st}$, in the state vector $\mathbf{x}_k$, the estimation problem becomes high-dimensional in nature. This is because, the full state vector will be $\tilde{\mathbf{x}}_k = [\mathbf{v}_k, \mathbf{h}_k, \mathbf{i}_k^{st}]$ of size $3n_x$, which increases the computational load.

The simulation studies presented in Chapter 2 demonstrated that the occurrence of stimulus is a localised event in both spatial and temporal domains, and therefore a sparse event. It is not pragmatic to perform the full estimation of the sparse stimulus variable. Hence, the estimation problem can be modified into a detection-estimation problem by considering the hypothesis whether a stimulus is present at particular location or not, at a particular time instant. Although, this approach allows to reduce the high-dimensionality, it leads to a branching process with an hypotheses-tree structure, which is exponentially growing with time [68, 164]. The true electrical field sequence can only be one of the sequences associated with a stimulus sequence branch of the full hypothesis tree. Since the correct stimulus sequence is unknown, it becomes important to store the trajectories of all the possible stimulus sequences, and their associated probability of being the correct one. This is computationally prohibitive even after a few time instants, as the full-hypotheses estimation requires exponentially increasing memory and computations to incorporate every possible stimulus conditions [68].

In order to address this exponential growth of the state trajectories, suboptimal estimation methods consider one of the following approaches [164]: (1) By eliminating the insignificant state-trajectories (also known as pruning); (2) By merging different state trajectories. In the literature of statistical estimation theory, the most widely used such adaptive estimation approaches are the multiple-model (MM) algorithms, in which a finite number of possible system hypotheses (also known as system modes) are considered [11]. For this, a set of Kalman filters are employed in parallel, where each filter is based on a specific system mode. The suboptimal state estimates are then computed by combining the mode-conditioned state estimates from different filters, which are also assigned with probabilistic weights (specific to the MM-algorithm). Some of the MM-based estimation approaches include detection-estimation method [153, 154], interacting multiple model algorithm (IMM) [16], generalised pseudo-bayesian algorithm [11], autonomous multiple-model algorithm [11], etc.

In the estimation of cardiac field, the state-space models are of high dimensional in terms of both the spatial locations and time instants. Therefore, consideration beyond a single filter can be computationally costly. Therefore, the proposed approach in this thesis is confined to a single filter detection-estimation approach. This implies, state trajectories that do not satisfy the decision scheme are eliminated at every time instant. The system states of the selected model are then estimated via state-augmentation method. Therefore, a unified detection and estimation algorithm is proposed within the state-space modelling framework, using the following steps:

- Detect and isolate the locations of presence of stimuli using a filter-based detection method using the nominal systems model.
    - **If not detected**
        - Estimate the state variables $\mathbf{x}_k$, from the measurements $\mathbf{y}_k$.
    - **else**
        - Estimate the augmented state variables $\tilde{\mathbf{x}}_k$, from the measurements $\mathbf{y}_k$ via a state-augmentation method.
    - **end**

The following subsections detail the methods and formulations used within each step of the proposed estimation framework. It should be noted that the nonlinear state estimation procedure for computing the states of the nominal or augmented state-space model is formulated within URTSS algorithm detailed in Chapter 2.3.2.

4.3.1 Stimulus Detection

The state-space formulation proposed in (4.10) and (4.11) allows to implement a model-based detection approach. In this method, changes in system dynamics are detected by comparing actual system behaviour with a reconstructed behaviour under nominal conditions. The resulting differences in system behaviours are quantified using distance measure referred as residuals in literature [62]. A decision scheme based on this metric is then employed to identify if there is an anomalous behaviour.

Filter-based detection approaches enable to include the detection procedure in the state estimation process. In filter-based detection approach, the residual measure is derived from the innovation sequence, which is the difference between predicted output and actual measurement. This is because, when the system dynamics is accurately described by a model, innovation follows a Gaussian white noise characteristics. On the other hand, when there are changes in system dynamics that are not captured by the underlying system model, the resulting statistical characteristics of Gaussian white noise will be altered [62].

To detect the presence of stimulus behaviour, a similar filter-based detected approach is employed. By using the state-space model with state evolution equation without the stimulus variable and observation equation, the states are predicted using UKF as

$$\hat{\mathbf{x}}_{k+1}^{f-} = \sum_{i=0}^{2n_x} W_i^{(m)} \hat{\mathcal{X}}_{k+1,i}^{f-}, \tag{4.16}$$

$$\mathbf{P}^{f-}_{k+1} = \sum_{i=0}^{2n_x} W_i^{(c)} (\hat{\mathcal{X}}^{f-}_{k+1,i} - \hat{\mathbf{x}}^{f-}_{k+1})(\hat{\mathcal{X}}^{f-}_{k+1,i} - \hat{\mathbf{x}}^{f-}_{k+1})^\top + \Sigma_x. \tag{4.17}$$

where superscript f denotes the filtered estimates and minus (-) denotes the prediction step of the filter, respectively.

As described earlier, the measurement process is linear relationship in states and predicted model output can be calculated as

$$\mathbf{y}^{f-}_{k+1} = \mathbf{C}\hat{\mathbf{x}}^{f-}_{k+1}. \tag{4.18}$$

The innovation vector are then constructed as the differences between actual measurement and the predicted model output in (4.17) as

$$\mathbf{e}^{f-}_{k+1} = \mathbf{y}_{k+1} - \mathbf{y}^{f-}_{k+1}. \tag{4.19}$$

The corresponding covariance of the innovation vector is given by

$$\mathbf{Q}^{f-}_{k+1} = \mathbf{C}\mathbf{P}^{f-}_{k+1}\mathbf{C}^\top + \mathbf{\Sigma}_y. \tag{4.20}$$

To quantify the whiteness of the signal, a distance measure can be then computed based on the innovation vector. In literature several metrics have been proposed such as squared-residual [62, 101], normalised squared-residual [14, 42, 62], etc. It should be noted that the innovation constructed from a filter also capture the inherent statistics of disturbance, which may generate false alarm rates [14]. Hence a robust distance metric should be used as the distance measure to accurately identify the presence of stimulus. The detection performance is important for accurate initiation of activation patterns in tissue field. Here a distance measure based on the likelihood function presented in [80] is employed. Similar to [80], a distance metric is derived based on the likelihood function.

For this, consider the negative log-likelihood function of the model at the prediction step as

$$\tilde{L}_{k+1} = -\ln p(\mathbf{y}_{k+1}|\hat{\mathbf{x}}^{f-}_{k+1}), \tag{4.21}$$

where $p(\mathbf{y}_{k+1}|\hat{\mathbf{x}}^{f-}_{k+1}) \sim \mathcal{N}(\mathbf{e}^{f-}_{k+1}, \mathbf{Q}^{f-}_{k+1})$ given by

$$p(\mathbf{y}_{k+1}|\hat{\mathbf{x}}^{f-}_{k+1}) = \frac{1}{\sqrt{(2\pi)^{n_y}|\mathbf{Q}^{f-}_{k+1}|}} \exp\left(-\frac{1}{2}\left(\mathbf{e}^{f-}_{k+1}\right)\mathbf{Q}^{f-}_{k+1}\left(\mathbf{e}^{f-}_{k+1}\right)^\top\right). \tag{4.22}$$

Equation (4.21) is expanded by substituting (4.22) to give

$$\tilde{L}_{k+1} = \frac{1}{2}\left[n_y \ln(2\pi) + \ln|\mathbf{Q}^{f-}_{k+1}| + \left(\mathbf{e}^{f-}_{k+1}\right)\mathbf{Q}^{f-}_{k+1}\left(\mathbf{e}^{f-}_{k+1}\right)^\top\right]. \tag{4.23}$$

The above expression generates a scalar value at every time instant. This implies that it can only be used to detect the if a stimulus is present in the entire sensor field at a given time instant. However, the sensor locations corresponding to stimulus are required in state estimation to accurately map the stimulus variable along the tissue field. Thus a distance measure tailored to individual sensors needs to be determined. For this, let the sensor positions along the spatial field are represented by $\{\bar{s}_n\}_{n=1}^{n_y}$. A distance measure based on negative log-likelihood of individual sensor is employed. For an arbitrary sensor n, (4.22) can be written as

$$p(y_{n,k+1}|\hat{\mathbf{x}}_{k+1}^{f-}) = \frac{1}{\sqrt{(2\pi)q_{k+1}}} \exp\left(-\frac{1}{2}\frac{e_{k+1}^2}{q_{k+1}}\right), \tag{4.24}$$

where e_{k+1} is the innovation at the sensor location $\bar{s}_n$, q_{k+1} is the n^{th} diagonal element in covariance matrix $\mathbf{Q}_{k+1}^{f-}$ that quantifies the variance of innovation at $\bar{s}_n$. Subsequently, negative logarithm of this measure can be calculated as

$$\tilde{L}_{n,k+1}^{-} = \frac{1}{2}\left[\ln(2\pi) + \ln(q_{k+1}) + \frac{(e_{k+1}^2)}{q_{k+1}}\right]. \tag{4.25}$$

Once the distance measures for all sensor locations are calculated the stimulus detection is proceeded using a decision scheme. The sensors which detected the presence of stimuli are defined to be the sensors with negative log-likelihood values of individual component distribution greater than a predefined threshold value. The positions of these sensors can be described by

$$\bar{\mathbf{n}}_{k+1} := \left\{\bar{s}_n : \tilde{L}_{n,k+1}^{-} > \varpi\right\}, \tag{4.26}$$

where ϖ is the threshold value, which is selected such that required detection performance is achieved. The summary of the above proposed diagnosis approach is as follows : The predicted behaviour is calculated using nominal state-space model that does not include the stimulus characteristics. Under stimulus conditions, the inherent uncertainty from un-modelled dynamics is expected to cause relatively higher prediction error at the sensors around the stimulus. This also indicates that the negative log-likelihood measure at these sensors will be higher compared to the other sensor locations. On the other hand, when there is no stimulus present in the tissue field, the system dynamics is accurately modelled using the nominal state-space model. This results in the negative log-likelihood measure to be of smaller magnitude. Thus a decision scheme can be then employed to identify the the presence of stimuli.

4.3.2 State Augmentation

The stimulus detection scheme presented in the previous section returns the sensor locations where the presence of stimulus at the sensors has been detected. However, the sensors are placed at sparse locations in the sensor field. This means that there could be multiple stimuli present at the neighbouring locations of the sensor where stimulus has been detected, or also between the nearby detected sensor locations in the tissue field. For instance, if there is only one sensor location has detected the presence of stimulus, there could be multiple stimuli locations in the neighbourhood of this sensor. On the other hand, if the spatial regime of stimulus is wider, the two nearby sensor locations will be detected. In order to create a smooth stimulus function and estimate it from the sensor measurements, the dynamics of stimulus variables are represented the as a weighted sum of basis functions. The basis functions are selected so that they are centered at the detected sensor locations. The stimulus function can be thus decomposed as follows

$$\mathbf{i}_k^{st} = \mathbf{B}_k \mathbf{z}_k, \tag{4.27}$$

where $\mathbf{B}_k \in \mathbb{R}^{n_s \times n_z}$ are the set of linear B-spline functions(order of 2) [70], centered at the detected sensor locations. $\mathbf{z}_k \in \mathbb{R}^{n_z \times 1}$ is the associated estimates of the stimulus variables at sensor locations.

Based on the above described factors, the properties associated with the basis functions are the following:

- *Local support property*: If only one sensor is detected, stimulus is assumed not to be present at the locations of other sensors. Therefore, basis function should not span into the areas beyond the neighbourhood defined by the detected sensor (see Figure 4.1(a)).
- *Interpolation property*: If two nearby sensors detect the presence of stimulus, then the stimulus value is assumed to be the same at all the locations between the two sensors (see Figure 4.1(b)).

Subsequently, an augmented state-space model is formed by incorporating, a new state variable $\mathbf{z}_k \in R^{n_z}$ is added to the state vector $\mathbf{x}_k$. This results in

$$\widetilde{\mathbf{x}}_{k+1} = \widetilde{\mathbf{f}}(\mathbf{x}_k, \mathbf{z}_k) + \widetilde{\epsilon}_k^x, \tag{4.28}$$

where $\widetilde{\mathbf{x}}_{k+1} \in \mathbb{R}^{n'_x}$ is the vector of state variables that consists of transmembrane voltage, gating variable and the stimulus variables detected as $[\mathbf{v}_k \;\; \mathbf{h}_k \;\; \mathbf{z}_k]^\top$. n'_x is the number of states in the augmented state-space model, $\epsilon_k^x = [\epsilon_k^v, \; \epsilon_k^h, \epsilon_k^z]^\top$ are

Gaussian noise process with zero mean and covariance matrices as $\mathbf{\Sigma}_v$, $\mathbf{\Sigma}_h$ and $\mathbf{\Sigma}_z$, respectively. The number of stimulus locations in the sensor field is given by n_z.

The stimulus variable is formulated using Markovian property such that it is conditionally dependent only on the previous estimate of the stimulus variable. This is a reasonable assumption especially when the stimulus may persists from previous time instant to current time. Thus augmented model function $\widetilde{\mathbf{f}}(\mathbf{x}_k)$ is given by

$$\widetilde{\mathbf{f}}(\mathbf{x}_k, \mathbf{z}_k) = \begin{bmatrix} \bar{\theta}_e \mathcal{A}\mathbf{v}_k + \bar{\mathbf{\Psi}}_k \bar{\boldsymbol{\theta}}^\top + \mathbf{B}_k \mathbf{z}_k \; \Delta_t \\ \\ \bar{\theta}_f \mathbf{h}_k + \bar{\wp}_k \; \bar{\theta}_f \\ \\ \mathbf{z}_k \end{bmatrix}, \tag{4.29}$$

$$\mathbf{y}_k = \widetilde{\mathbf{C}}\tilde{\mathbf{x}}_k + \epsilon_k^y, \tag{4.30}$$

where $\widetilde{\mathbf{C}} \in \mathbb{R}^{n_y \times n'_x}$ is formed such that the current measurement is the noise corrupted signal of the transmembrane voltage $\mathbf{v}_k$.

Structure in Augmented State Vector and Covariance Matrix

As described in the previous section, stimulus behaviour may persists over a time interval, where changes in the same stimulus may continue from previous time

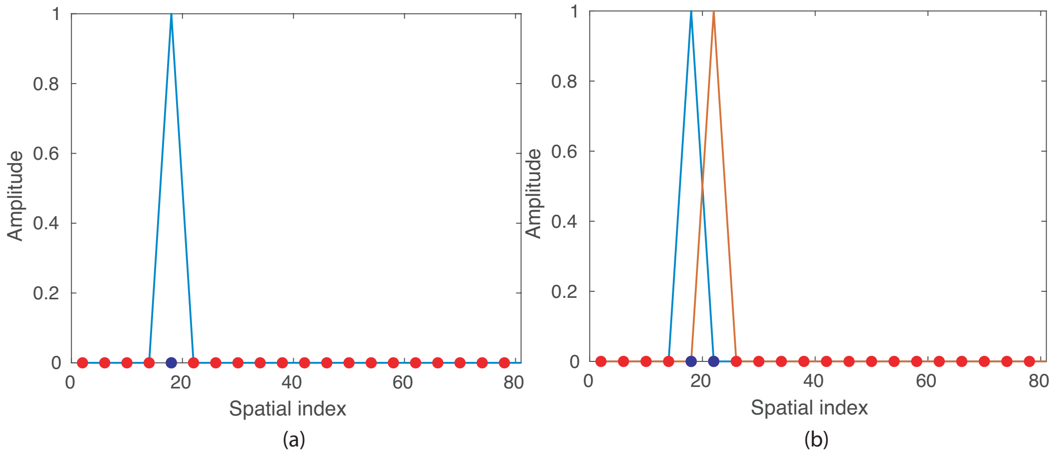

(a)

(b)

Figure 4.1. Examples of linear B-spline functions. (a) A single b-spline function to estimate the stimulus variables around the detected sensor. (b) Two overlapping b-spline functions to estimate the stimulus variables around the detected sensors. Here, red circles denote the sensors and the blue circles denote the sensors resulted from the detection scheme.

instant to the current instant. This dynamics of stimulus variables is quantified using Markovian property given in (4.28). On the other hand, there may be cases when new stimulus are detected at a time instant and required to be added to the augmented state vector. This requires initialisation of both prior state vector and prior covariance matrix associated with stimulus variables in the augmented state vector. Therefore, the dynamics of stimulus states are modelled as

$$\mathbf{z}_{k+1} = \begin{cases} \mathbf{z}_k + \boldsymbol{\epsilon}^z_k, & \text{when same stimulii detected} \\ \mathbf{z}^0_k + \boldsymbol{\epsilon}^z_k, & \text{when new stimulii detected} \end{cases} \tag{4.31}$$

where $\mathbf{z}^0_k$ is initialised as $\mathcal{N}(\mathbf{0}, \sigma_{z_0}\mathbf{I})$ [81]. The inclusion of above mentioned property introduces dynamic structure in both prior values of state vector and covariance matrix, which is then required for the prediction and correction steps based on the augmented state-space model. This can be explained as: At a time instant, the stimulus state variables in the prediction step may either depend on the previous time instant (same stimulus) or initialised to zero. This procedure is repeated for the covariance matrix, where a higher value of variance is assigned for the new stimulus. The state vector and covariance matrix are then updated in the correction step of the Kalman Filter. A similar estimation problem is presented in [81] for the sequential learning of neural network, where both state vector and covariance matrix were required to be initialised, when a new hidden unit was added into the neural network. To include the dynamic structure in both measures, a general mapping algorithm that can be applied for both forward and backward iterations in the URTS smoother is derived. Here, the implementation for the filtering states are shown below:

By following the filter-based formulations, the mapping in the stimulus state estimates is given by

$$\hat{\mathbf{z}}^f_k = \bar{\boldsymbol{\Phi}}^-_{k+1}\breve{\mathbf{z}}_k, \tag{4.32}$$

where $\breve{\mathbf{z}}^f_k \in \left\{0, \hat{z}^f_k\right\}^{n_y \times 1}$ and $\bar{\boldsymbol{\Phi}}_{k+1} \in \{0,1\}^{n_z \times n_y}$. $\breve{\mathbf{z}}^f_k$ is the vector of posterior states estimates positioned according to the stimulus sensor locations $\bar{\mathbf{n}}_k$. The entry of sensors those are not detected is assigned to zero. This can also be described as

$$\left[\breve{\mathbf{z}}^f_k\right]_n = \begin{cases} \left[\hat{\mathbf{z}}^f_k\right]_j, & \text{if } \left[\bar{\mathbf{n}}^-_k\right]_j = [\bar{\mathbf{s}}]_n \\ 0, & \text{otherwise} \end{cases} \tag{4.33}$$

where $\left(n = 1, 2, ..n_y\right)$ and j is the iteration variable that changes from $(1, 2, .., n)$ for every n value.

Subsequently, the stimulus state mapping matrix is constructed based on the stimulus detection from the prediction step, such that $\bar{\mathbf{\Phi}}^{-}_{k+1} = \left(\boldsymbol{\phi}_1, \boldsymbol{\phi}_2, ..., \boldsymbol{\phi}_{n_z}\right)^{\top}$, where $\boldsymbol{\phi}_j$ is a row vector used to represent a stimulus map vector. The element associated with the sensor location in stimulus map vector $\boldsymbol{\phi}_j$ is assigned to 1 and zero otherwise. This can also be described as

$$[\phi]_n = \begin{cases} 1, & [\bar{\mathbf{n}}^{-}_{k+1}]_n = [\bar{\mathbf{s}}]_n \\ 0, & \text{otherwise} \end{cases} . \tag{4.34}$$

To explain the above mentioned mapping, consider an example of sensor field with 4 sensors located at $\bar{\mathbf{s}} = (0, 0.1, 0.2, 0.3)$. The results of the posterior estimate are $n^{-}_{k} = 0$ and $z^{f}_{k} = z^{f}_{1,k}$. The detection scheme at the prediction step using the nominal model returned $n^{-}_{k+1} = (0, 0.1)$. Subsequently, the augmented state vector needs to be formed with the prior state estimate of stimulus variable. This newly formed augmented state-vector is then undergo prediction and correction steps. For this particular example, prior state estimate of stimulus variable in (4.31), is given by

$$\begin{bmatrix} 1 & 0 & 0 & 0 \\ 0 & 1 & 0 & 0 \end{bmatrix} \begin{bmatrix} z^{f}_{1,k} \\ 0 \\ 0 \\ 0 \end{bmatrix} = \begin{bmatrix} z^{f}_{1,k} \\ 0 \end{bmatrix}$$

The processing requires approximate set of states to be included in the estimation stages. In a similar way, this reflects in the dynamic structure of the augmented state covariance matrix $\widetilde{\mathbf{P}}^{f}_{k}$, which is formulated based on the stimuli locations obtained from (4.26). The augmented covariance matrix can be expressed as

$$\widetilde{\mathbf{P}}^{f}_{k} = \left[\begin{array}{cc|c} \mathbf{P}^{(vv)}_{k} & \mathbf{P}^{(vh)}_{k} & \mathbf{P}^{(vz)}_{k} \\ \mathbf{P}^{(hv)}_{k} & \mathbf{P}^{(hh)}_{k} & \mathbf{P}^{(hz)}_{k} \\ \hline \mathbf{P}^{(zv)}_{k} & \mathbf{P}^{(zh)}_{k} & \mathbf{P}^{(zz)}_{k} \end{array}\right]_{n'_x \times n'_x} \tag{4.35}$$

In the augmented state-covariance matrix, the covariance elements associated with (v and h) is same as the posterior estimates at k. On the other hand, covariances associated with stimulus variables require initialisation or mapping based on the results from the detection step. The covariance elements between the stimulus and transmembrane voltage in (4.35) can be obtained as

$$\mathbf{P}^{(zv)}_{k} = \ddot{\mathbf{\Phi}}^{-}_{k+1} \breve{\mathbf{P}}^{(zv)}_{k}, \tag{4.36}$$

where $\mathbf{P}_k^{(zv)} \in \mathbb{R}^{n_z \times n_s}$, $\ddot{\mathbf{\Phi}}_{k+1}^{-} \in \mathbb{R}^{n_z \times n_s}$ and $\breve{\mathbf{P}}_k^{(zv)} \in \mathbb{R}^{n_s \times n_s}$ constructed similar to (4.34) and (4.33), based on the sensor positions in the tissue field. Similarly, the covariance elements between the stimulus and gating variable in (4.35) can be constructed using

$$\mathbf{P}_k^{(zh)} = \ddot{\mathbf{\Phi}}_{k+1}^{-} \breve{\mathbf{P}}_k^{(zh)}, \tag{4.37}$$

where $\mathbf{P}_k^{(zh)} \in \mathbb{R}^{n_z \times n_s}$, $\ddot{\mathbf{\Phi}}_{k+1}^{-} \in \mathbb{R}^{n_z \times n_s}$ and $\breve{\mathbf{P}}_k^{(zh)} \in \mathbb{R}^{n_s \times n_s}$. Similarly, the covariance between the stimulus variables is achieved by

$$\mathbf{P}_k^{(zz)} = \bar{\mathbf{\Phi}}_{k+1}^{-} \breve{\mathbf{P}}_k^{(zz)} [\bar{\mathbf{\Phi}}_{k+1}^{-}]^{\top}, \tag{4.38}$$

where $\mathbf{P}_k^{(zz)} \in \mathbb{R}^{n_z \times n_z}$, $\bar{\mathbf{\Phi}}_{k+1}^{-} \in \mathbb{R}^{n_z \times n_y}$ and $\breve{\mathbf{P}}_k^{(zz)} \in \mathbb{R}^{n_y \times n_y}$. It should be noted that the variance value associated with the new stimulus is assumed to be 1, which is initialised as σ_{z_0}, explicitly in $\breve{\mathbf{P}}_k^{(zz)}$.

4.3.3 The Proposed Algorithm

The detection and estimation algorithm formulated using the above detailed methods is presented in this Algorithm 4.1. The nonlinear state estimation procedure for computing the states of the nominal or augmented state-space model is formulated within URTSS algorithm detailed in Chapter 2.5.

Algorithm 4.1: *The detection-estimation algorithm using Unscented Rauch-Tung Stribel Smoother.*

Forward Iteration

1. Initialise forward states $\hat{\mathbf{x}}_o^f$ and covariance matrix $\mathbf{P}_o^f$.

2. The recursive estimation procedure for time instants, $k \in \{0, 1, ..., T-1\}$:

Prediction using nominal state-space model :

(a) Compute the sigma points for $\hat{\mathbf{x}}_k^f$

$$\begin{aligned} \chi_{k,j}^f &= \hat{\mathbf{x}}_k^f, \\ \chi_{k,j}^f &= \hat{\mathbf{x}}_k^f + \left(\sqrt{(n_x + \lambda)\mathbf{P}_k^f} \right)_j, \quad j = 1, ..., n_x \\ \chi_{k,j}^f &= \hat{\mathbf{x}}_t^f - \left(\sqrt{(n_x + \lambda)\mathbf{P}_k^f} \right)_j, \quad j = n_x + 1, ..., 2n_x \end{aligned} \tag{4.39}$$

where λ is defined in (2.24).

(b) The sigma points are then propagated through the nonlinear state evolution equation

$$\hat{\mathcal{X}}^{f-}_{k+1,j} = \mathbf{f}(\chi^{f}_{k}). \tag{4.40}$$

(c) Compute the predicted states $\mathbf{x}^{f-}_{k+1}$ and covariance matrix $\mathbf{P}^{f-}_{k+1}$ as

$$\hat{\mathbf{x}}^{f-}_{k+1} = \sum_{j=0}^{2n_x} W^{(m)}_{j} \hat{\mathcal{X}}^{f-}_{k+1,j}, \tag{4.41}$$

$$\mathbf{P}^{f-}_{k+1} = \sum_{j=0}^{2n_x} W^{(c)}_{j} (\hat{\mathcal{X}}^{f-}_{k+1,j} - \hat{\mathbf{x}}^{f-}_{k+1})(\hat{\mathcal{X}}^{f-}_{k+1,j} - \hat{\mathbf{x}}^{f-}_{k+1})^{\top} + \Sigma_x, \tag{4.42}$$

where $W^{(m)}_{i}$ and $W^{(c)}_{i}$ are the constant mean and covariance weights defined in (2.28), (2.29) and (2.30).

Detection using nominal state-space model:

(a) Compute the innovation and the corresponding covariance of innovation

$$\mathbf{e}^{f-}_{k+1} = \mathbf{y}_{k+1} - \mathbf{y}^{f-}_{k+1}, \tag{4.43}$$

where $\mathbf{y}^{f-}_{k+1}$ is computed using (4.18)

$$\mathbf{Q}^{f-}_{k+1} = \mathbf{C}\mathbf{P}^{f-}_{k+1}\mathbf{C}^{\top} + \mathbf{\Sigma}_y. \tag{4.44}$$

(b) Calculate the distance measure, which is negative likelihood measure tailored for single sensor

$$L^{-}_{n,k+1} = \frac{1}{2}\left[\ln(2\pi) + \ln(q_{k+1}) + \frac{1}{2}\frac{(e^{2}_{k+1})}{q_{k+1}}\right]. \tag{4.45}$$

(c) Perform the detection scheme as

$$\bar{\mathbf{n}}_{k+1} := \left\{\bar{s}_n : L^{-}_{n,k+1} > \varpi\right\}, \tag{4.46}$$

where ϖ is the threshold value.

if stimulus sensors are not detected:

Correction using the nominal state-space model:

(a) Compute the Kalman gain, the corrected state estimates and covariance matrix

$$\mathbf{K}_{k+1} = \mathbf{P}^{f-}_{k+1}\mathbf{C}^{\top}(\mathbf{C}\mathbf{P}^{f-}_{k+1}\mathbf{C}^{\top}_{k+1} + \mathbf{\Sigma}_y)^{-1}, \tag{4.47}$$

$$\hat{\mathbf{x}}^{f}_{k+1} = \hat{\mathbf{x}}^{f-}_{k+1} + \mathbf{K}_{k+1}\mathbf{e}^{f-}_{k+1}, \tag{4.48}$$

$$\mathbf{P}^{f}_{k+1} = \mathbf{P}^{f-}_{k+1} - \mathbf{P}^{f-}_{k+1}\mathbf{C}(\mathbf{C}\mathbf{P}^{f-}_{k+1}\mathbf{C}^{\top} + \mathbf{\Sigma}_y)^{-1}\mathbf{C}. \tag{4.49}$$

else

Prediction using augmented state-space model:

(a) Form the augmented state vector $\tilde{\hat{\mathbf{x}}}^{f}_{k} = [\hat{\mathbf{x}}^{f} \;\; \hat{\mathbf{z}}^{f}_{k}]^{\top}$, where stimulus state variables are computed using (4.32), and covariance matrix $\widetilde{\mathbf{P}}^{f}_{k}$ of structure in (4.35) are computed using (4.36), (4.37) and (4.38).

(b) Compute the sigma points $\widetilde{\chi}_k$ using (4.39) for the augmented state vector $\tilde{\hat{\mathbf{x}}}^{f}_{k}$. For this, $\hat{\mathbf{x}}^{f}_{k}$, $\mathbf{P}^{f}_{k}$, λ and n_x are replaced by $\tilde{\hat{\mathbf{x}}}^{f}_{k}$, $\widetilde{\mathbf{P}}^{f}_{k}$, λ' and n'_x, respectively.

(c) Calculate the unscented transform values $\tilde{\hat{\chi}}^{f-}_{k+1}$ by propagating the sigma points through the augmented non-linear state evolution equation $\widetilde{\mathbf{f}}(\widetilde{\chi}_k)$. The nonlinear state evolution equation is given in (5.16), which includes the linear B-spline functions $\mathbf{B}_k$ at the detected sensor locations.

(d) Compute the predicted states $\tilde{\hat{\mathbf{x}}}^{f-}_{k+1}$ and covariance matrix $\widetilde{\mathbf{P}}^{f-}_{k+1}$

$$\tilde{\hat{\mathbf{x}}}^{f-}_{k+1} = \sum_{j=0}^{2n'_x} W'^{(m)}_{j}\bar{\chi}^{-}_{k+1,j}, \tag{4.50}$$

$$\widetilde{\mathbf{P}}^{f-}_{k+1} = \sum_{j=0}^{2n'_x} W'^{(c)}_{j}(\tilde{\hat{\chi}}^{f-}_{k+1,j} - \tilde{\hat{\mathbf{x}}}^{f-}_{k+1})(\tilde{\hat{\chi}}^{f-}_{k+1,j} - \tilde{\hat{\mathbf{x}}}^{f-}_{k+1})^{\top} + \Sigma_{\widetilde{x}}. \tag{4.51}$$

Correction using augmented state-space model:

(e) Compute the corrected state estimates $\tilde{\hat{\mathbf{x}}}^{f}_{k+1}$ and covariance matrix $\widetilde{\mathbf{P}}^{f}_{k+1}$ by recomputing Kalman gain $\widetilde{\mathbf{K}}_{k+1}$using augmented observation matrix $\widetilde{\mathbf{C}}$

$$\widetilde{\mathbf{K}}_{k+1} = \mathbf{P}^{f-}_{k+1}\widetilde{\mathbf{C}}^{\top}(\widetilde{\mathbf{C}}\mathbf{P}^{f-}_{k+1}\widetilde{\mathbf{C}}^{\top} + \mathbf{\Sigma}_y)^{-1}, \tag{4.52}$$

$$\tilde{\hat{\mathbf{x}}}^{f}_{k+1} = \tilde{\hat{\mathbf{x}}}^{f-}_{k+1} + \widetilde{\mathbf{K}}_{k+1}(\mathbf{y}_{k+1} - \widetilde{\mathbf{C}}\tilde{\hat{\mathbf{x}}}^{f-}_{k+1}), \tag{4.53}$$

$$\widetilde{\mathbf{P}}^{f}_{k+1} = \widetilde{\mathbf{P}}^{f-}_{k+1} - \widetilde{\mathbf{P}}^{f-}_{k+1}\widetilde{\mathbf{C}}(\widetilde{\mathbf{C}}\widetilde{\mathbf{P}}^{f-}_{k+1}\widetilde{\mathbf{C}}^{\top} + \mathbf{\Sigma}_y)^{-1}\widetilde{\mathbf{C}}. \tag{4.54}$$

end

Backward Iteration

---

1. Initialise backward states and covariances using the filter estimates $\hat{\mathbf{x}}^s_T = \hat{\mathbf{x}}^f_T$ and $\mathbf{P}^s_T = \mathbf{P}^f_T$.

2. Recursive backward iteration to estimate the smoothed state estimates $\hat{\mathbf{x}}^s_k$ for time instants $k \in \{T-1, ..., 0\}$:

if stimulus sensors are not detected in the filtering step:

Prediction using nominal state-space model :

(a) Compute the sigma points of the smoother $\chi^s_{k,j}$ are computed using filtered state and covariance estimates as

$$\chi^s_{k,j} = \hat{\mathbf{x}}^f_k, \tag{4.55}$$

$$\chi^s_{k,j} = \hat{\mathbf{x}}^f_k + \left(\sqrt{(n_x+\lambda)\mathbf{P}^f_k}\right)_j, \quad j = 1, ..., n_x \tag{4.56}$$

$$\chi^s_{k,j} = \hat{\mathbf{x}}^f_k - \left(\sqrt{(n_x+\lambda)\mathbf{P}^f_k}\right)_j, \quad j = n_x+1, ..., 2n_x \tag{4.57}$$

where λ is defined in (2.24).

(b) The sigma points are then propagated through the nonlinear state evolution equation

$$\hat{\chi}^{s-}_{k+1,j} = \mathbf{f}(\chi^s_k). \tag{4.58}$$

(c) The estimates of the predicted states, $\hat{\mathbf{x}}^{s-}_{k+1}$ and covariance matrix $\mathbf{P}^{s-}_{k+1}$ are computed as

$$\hat{\mathbf{x}}^{s-}_{k+1} = \sum_{j=0}^{2n_x} W^{(m)}_j \hat{\chi}^{s-}_{k+1,j}, \tag{4.59}$$

$$\mathbf{P}^{s-}_{k+1} = \sum_{j=0}^{2n_x} W^{(c)}_j (\hat{\chi}^{s-}_{k+1,j} - \hat{\mathbf{x}}^{s-}_{k+1})(\hat{\chi}^{s-}_{k+1,j} - \hat{\mathbf{x}}^{s-}_{k+1})^\top + \Sigma_x, \tag{4.60}$$

$$\mathbf{S}_{k+1} = \sum_{j=0}^{2n_x} W^{(c)}_j (\chi^s_{k,j} - \hat{\mathbf{x}}^{s-}_{t+1})(\hat{\chi}^{s-}_{k+1,j} - \hat{\mathbf{x}}^{s-}_{k+1})^\top, \tag{4.61}$$

where $W^{(m)}_i$ and $W^{(c)}_i$ are the constant mean and covariance weights defined in (2.28), (2.29) and (2.30).

Correction using nominal state-space model :

(a) Calculate the smoother gain to correct the state estimates and covariance matrix upon the measurements by

$$\mathbf{D}_k = \mathbf{S}_{k+1}(\mathbf{P}^{s-}_{k+1})^{-1}, \tag{4.62}$$

(b) Compute the resulting smoothed state $\hat{\mathbf{x}}^s_k$ and covariance $\mathbf{P}^s_k$ using

$$\hat{\mathbf{x}}^s_k = \hat{\mathbf{x}}^f_k + \mathbf{D}_k(\hat{\mathbf{x}}^s_{k+1} - \mathbf{x}^{s-}_{t+1}), \tag{4.63}$$

$$\mathbf{P}^s_k = \mathbf{P}^f_k + \mathbf{D}_k(\mathbf{P}^s_{k+1} - \mathbf{P}^{s-}_{k+1})\mathbf{D}^\top_k, \tag{4.64}$$

else

Prediction using augmented state-space model:

(a) Compute the sigma points $\tilde{\chi}_k$ using (4.39) by replacing $\hat{\mathbf{x}}^f_k$, $\mathbf{P}^f_k$, λ and n_x are replaced by $\widetilde{\hat{\mathbf{x}}}^f_k$, $\widetilde{\mathbf{P}}^f_k$, λ' and n'_x, respectively.

(b) Calculate the unscented transform values $\widetilde{\hat{\chi}}^{s-}_{k+1}$ by propagating the sigma points through the augmented non-linear state evolution equation $\widetilde{\mathbf{f}}(\tilde{\chi}_k)$, with the linear B-spline functions $\mathbf{B}_k$ at the detected sensor locations.

(c) Compute the predicted states $\widetilde{\hat{\mathbf{x}}}^{s-}_{k+1}$ and covariance matrix $\widetilde{\mathbf{P}}^-_{k+1}$

$$\widetilde{\hat{\mathbf{x}}}^{s-}_{k+1} = \sum_{j=0}^{2n'_x} W'^{(m)}_j \bar{\chi}^{s-}_{k+1,j}, \tag{4.65}$$

$$\widetilde{\mathbf{P}}^{s-}_{k+1} = \sum_{j=0}^{2n'_x} W'^{(c)}_j (\bar{\chi}^{s-}_{k+1,j} - \widetilde{\hat{\mathbf{x}}}^{s-}_{k+1})(\bar{\chi}^{s-}_{k+1,j} - \widetilde{\hat{\mathbf{x}}}^{s-}_{k+1})^\top + \Sigma_{\tilde{x}}, \tag{4.66}$$

$$\widetilde{\mathbf{S}}_{k+1} = \sum_{j=0}^{2n_x} W'^{(c)}_j (\tilde{\chi}^s_{k,j} - \widetilde{\hat{\mathbf{x}}}^{s-}_{k+1})(\hat{\chi}^{s-}_{k+1,j} - \widetilde{\hat{\mathbf{x}}}^{s-}_{k+1})^\top. \tag{4.67}$$

Correction using augmented state-space model:

(d) Form the augmented state vector $\widetilde{\hat{\mathbf{x}}}^s_{k+1} = [\hat{\mathbf{x}}^s_{k+1} \quad \hat{\mathbf{z}}^s_{k+1}]^\top$, where stimulus state variables $\hat{\mathbf{z}}^s_{k+1}$ and covariance matrix $\widetilde{\mathbf{P}}^s_{k+1}$ are re-evaluated to include the dynamic structure in the augmented form.

(e) Compute the corrected state estimates $\widetilde{\hat{\mathbf{x}}}^s_k$ and covariance matrix $\widetilde{\mathbf{P}}^s_k$ as

$$\widetilde{\mathbf{D}}_k = \widetilde{\mathbf{S}}_{k+1}(\widetilde{\mathbf{P}}^{s-}_{k+1})^{-1}, \tag{4.68}$$

$$\widetilde{\hat{\mathbf{x}}}^{s}_{k} = \widetilde{\hat{\mathbf{x}}}^{f}_{k} + \widetilde{\mathbf{D}}_{k}(\widetilde{\hat{\mathbf{x}}}^{s}_{k+1} - \widetilde{\hat{\mathbf{x}}}^{s-}_{k+1}), \tag{4.69}$$

$$\widetilde{\mathbf{P}}^{s}_{k} = \tilde{\mathbf{P}}^{f}_{k} + \widetilde{\mathbf{D}}_{k}(\widetilde{\mathbf{P}}^{s}_{k+1} - \widetilde{\mathbf{P}}^{s-}_{k+1})\widetilde{\mathbf{D}}^{\top}_{k}. \tag{4.70}$$

end

4.3.4 Performance Metrics

In this section, the performance metrics used to quantify the accuracy of the results in both detection and state estimation stages are briefly explained.

Detection Accuracy

To analyse the detection performance, a set of performance metrics can be computed by comparing with the ground truth given in the simulation datasets. Here the detection performance metrics considered are detection rate and false alarm rate at a particular threshold. They are defined as follows:

- Detection Rate: This measure can be used to determine the proportion of stimulus locations that are correctly identified by the algorithm. It is also known as the True Positive Rate (TPR) in the literature, and can be computed as

  $$\text{Detection Rate} = \frac{TP}{TP + FN}, \tag{4.71}$$

  where TP and FN denote the number of true positives and false negatives respectively.

- False Alarm Rate: This measure quantifies the proportion of normal locations that were incorrectly identified as stimulus locations, and calculated as

  $$\text{False Alarm Rate} = \frac{FP}{TN + FP}, \tag{4.72}$$

  where FP and TN are the number of false positives and true negatives respectively.

Estimation Accuracy

The state estimation accuracy can be evaluated by comparing the estimated state variables using the simulated state variables. For a single realisation the accuracy is quantified using RMSE measure. RMSE measure for a particular time instant k

can be given as

$$\mathbf{RMSE}_k(v) = \sqrt{\frac{1}{n_v}\sum_{j=1}^{n_v}\left(v_{k,j} - \hat{v}_{k,j}\right)^2}, \qquad k = 0, 1, 2, ...n_t \tag{4.73}$$

where $v_{k,j}$ and $\hat{v}_{k,j}$ are the true transmembrane voltage from modified Mitchell-Schaeffer model and the estimated variable at spatial location j. It should be noted that the above equation is also given in (3.19), and restated here for completeness. To compare estimation accuracy over several realisations, a global measure can be computed as

$$\mathbf{MRMSE}_k(v) = \frac{1}{n_o}\sum_{o=1}^{n_o}\sqrt{\frac{1}{n_v}\sum_{j=1}^{n_v}\left(v_{k,j}^{(o)} - \hat{v}_{k,j}^{(o)}\right)^2} \tag{4.74}$$

where n_o is the number of realisations and $v_{k,j}^{(o)}$ denotes the actual transmembrane voltage at o^{th} realisation.

4.4 Data Generation

A detailed description of the simulation setup and data generation is provided in Chapter 3. Briefly, activation patterns in an one dimensional tissue field of 2 cm were modelled using stochastic monodomain equations, coupled with the modified Mitchell-Schaeffer cell model from the literature [38]. The unipolar electrograms were then acquired from sensors located at a distance of 1 mm from the tissue field. Both models were solved using explicit finite differences methods with a no-flux boundary conditions. Both patterns were simulated for total duration of 1000 ms, which results in 20001 time instants to be estimated. The electrophysiology parameters used for data generation are shown in Table 3.1, unless explicitly stated otherwise.

Two action potential cycles of normal activation patterns were simulated by applying external stimulus from $s_x = 0.025$ cm to $s_x = 0.075$ cm in one-dimensional cable field, at time instants $k = 0.05$ ms and $k = 500.05$ ms. In addition to this, the state disturbance variances were set to $\sigma_v^2 = 10^{-4}$ and $\sigma_h^2 = 10^{-5}$, along with observation noise variance was assigned to $\sigma_y^2 = 10^{-4}$. The total number of spatial points in the tissue field denoted by n_s is 81, while the number of sensors n_y is 20. An example of noise corrupted true state variables and an electrogram measurement obtained at a specific location are shown in Figure 4.2.

In a similar way, the re-entrant activation patterns were generated in an one-dimensional ring model. The first stimulus (S1) was applied from $s_x = 0$ cm

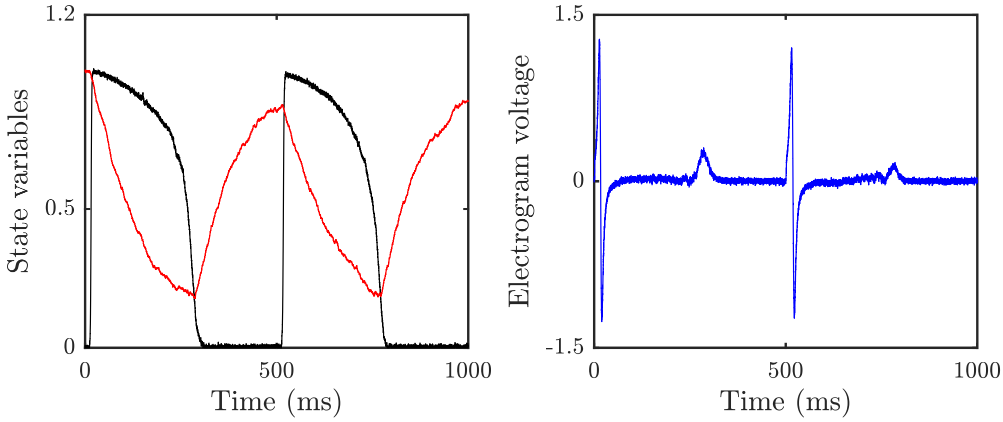

(a)

(b)

Figure 4.2. **Examples of state variables and electrogram measurements in a one-dimensional cable field**. (a) State variables at spatial location, $s_x = 0.025$ cm. (b) Electrogram measurements at spatial location, $s'_x = 1.325$ cm. State variables are transmembrane voltage (—), gating variable (—).

to $s_x = 0.05$ cm at $k = 0.05$ ms to generate the normal activation pattern. To simulate the re-entry, the second stimulus S2 was then applied from $s_x = 0.475$ cm to $s_x = 0.525$ cm at $k = 350$ ms (during the vulnerable window). The closed loop structure of the ring model gives n_s and n_y to be 80 and 20 respectively. The same values of state disturbance variances and the observation noises from normal activation patterns were used. Figure 4.3 shows the examples of noise corrupted true state variables and electrogram measurement.

4.5 Results and Discussion

This section presents the results obtained from the proposed combined detection-estimation algorithm, which allows to reconstruct the tissue level dynamics from the sparse electrogram measurements. It should be noted that the state-space model for the estimation is employed using the proposed continuous version of mMS model, where the gating variable approximation using the slope value of 25. Several experiments were employed to demonstrate the performance of the proposed framework. Experiment I illustrates the approach used to obtain the threshold value in the detection scheme, along with the estimation procedures and results from normal and re-entrant activation patterns. Experiment II illustrates the model mismatch by considering the effects of slope parameter on the estimation performance. Experiment III details the effectiveness of estimation algorithm in estimating transmembrane voltage and gating variable using the nominal state-space model, along with the importance of incorporating the stimulus detection.

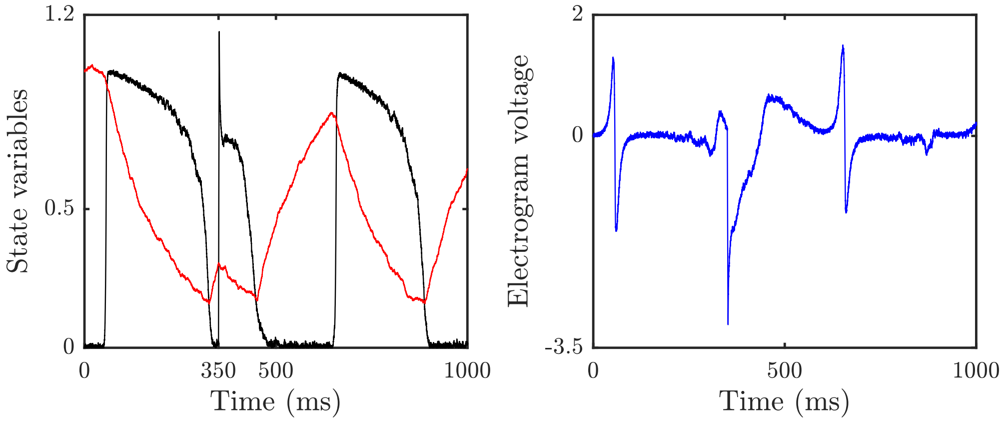

(a) (b)

Figure 4.3. **Examples of state variables and electrogram measurements in a one-dimensional ring field**. (a) State variables at spatial location, $s_x = 0.50$ cm. (b) Electrogram measurements at spatial location, $s'_x = 0.525$ cm. State variables are transmembrane voltage (—), gating variable (—).

This is followed by analysing the sensitivity of the proposed detection-estimation algorithm with respect to the observation noise variances, presented in Experiment IV. Finally, an analysis on different stimulus locations with respect to the sensor locations is presented in Experiment V.

4.5.1 Experiment I: Detection and Estimation Performance using Monte Carlo Simulations

The combined detection-estimation methodology given in Algorithm 4.1 was employed to estimate the hidden state variables from the electrogram measurements. Throughout the estimation, it was assumed that the disturbance covariances were known to the estimator. The initial states of $\mathbf{v}_0$ and $\mathbf{h}_0$ were drawn from the $\mathcal{N}\left(0, 10^{-4}\right)$ and $\mathcal{N}\left(1, 10^{-4}\right)$, where the mean value corresponds to the resting conditions of the state variables given in [38, 108].

In order to implement the detection scheme within the filtering step, a suitable threshold value needed to be determined. This step ensures that stimulus locations are accurately detected and incorporated into the state estimation framework. It can be seen from the state-space model formulation in (4.10) that the stimulus information is incorporated into the tissue level dynamics. This implies that the detection analysis needs to be employed based on the stimulus locations in the tissue field. In the proposed algorithm, detected stimulus locations are estimated in the tissue field using B-spline weighting functions.

To determine a suitable threshold value, detection performance metrics were

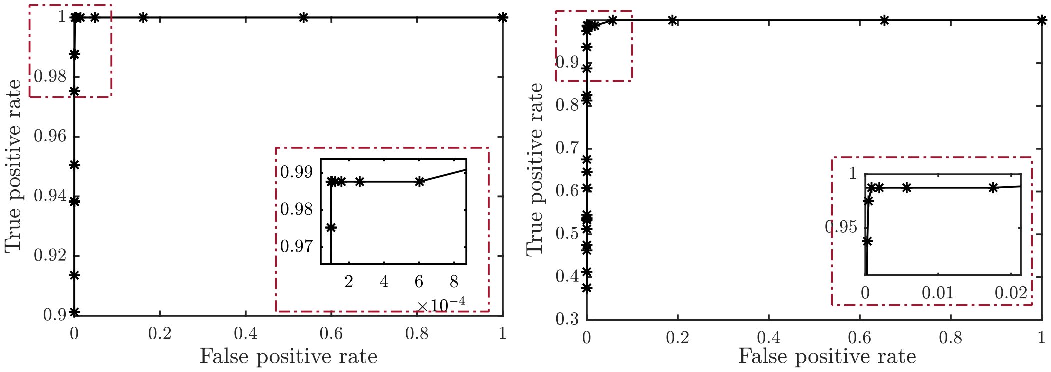

(a) (b)

Figure 4.4. ROC graphs from the detection scheme calculated using threshold values ranges between -5 to 20. (a) Normal activation pattern. (b) Re-entrant activation pattern. Red box within each sub-figure illustrates the ROC segment of optimal detection performance.

Table 4.1. Averaged detection metrics from 20 Monte Carlo realisations.

Normal Pattern			Reentrant Pattern		
Threshold	TPR	FPR	Threshold	TPR	FPR
6	0.985	1.22×10^{-4}	2	0.982	2.00×10^{-3}
7	0.984	1.06×10^{-4}	3	0.980	8.36×10^{-4}
8	0.983	1.04×10^{-4}	4	0.973	4.18×10^{-4}
9	0.981	1.00×10^{-4}	5	0.945	2.70×10^{-4}

first evaluated over a set of threshold values ranging from -5 to 20, in a single realisation of the activation patterns. Following Section 4.3.4, detection rate (also TPR) and the false alarm rate (also FPR) were calculated across the entire dataset. To analyse the detection performance, Receiver Operating Characteristics (ROC) curves for normal and re-entrant activation patterns were then plotted as shown in Figure 4.4. The ROC curves illustrate that a subset of threshold values is present within the selected range, where high level stimulus detection rate with low level false alarm rate is observed. In order to validate the consistency of the detection performance, Monte Carlo simulations-based analysis was then performed across selected values (see Table 4.1). The averaged detection metrics were computed across the 20 Monte Carlo realisations of the cardiac field and summarised in Table 4.1. Therefore, the threshold values for normal and re-entrant activation patterns were assigned to be 9 and 5 as the values give higher detection rate with minimum false alarm rate.

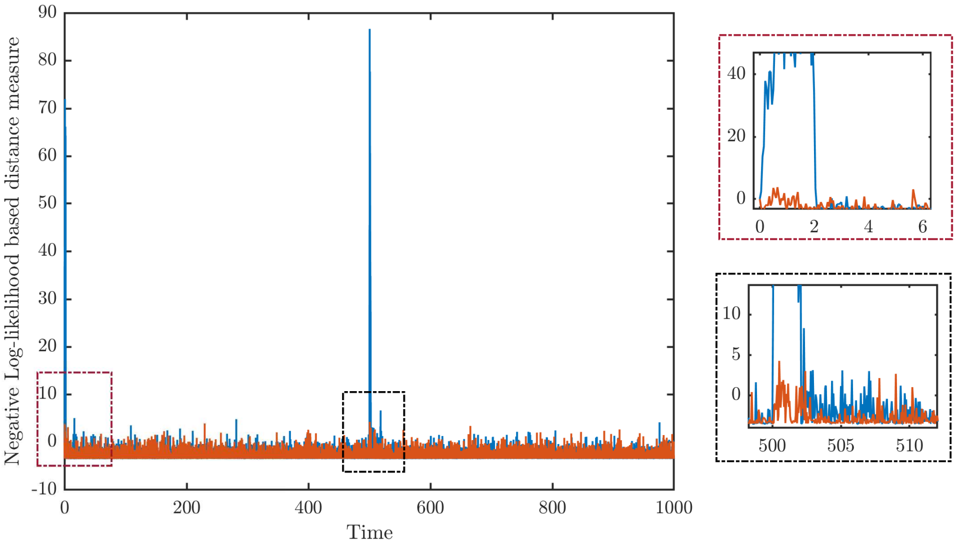

Figure 4.5. **Negative log-likelihood measure for normal activation patterns in one-dimensional cable field**. The distance measure within the stimulus intervals are illustrated within boxes for clarity.

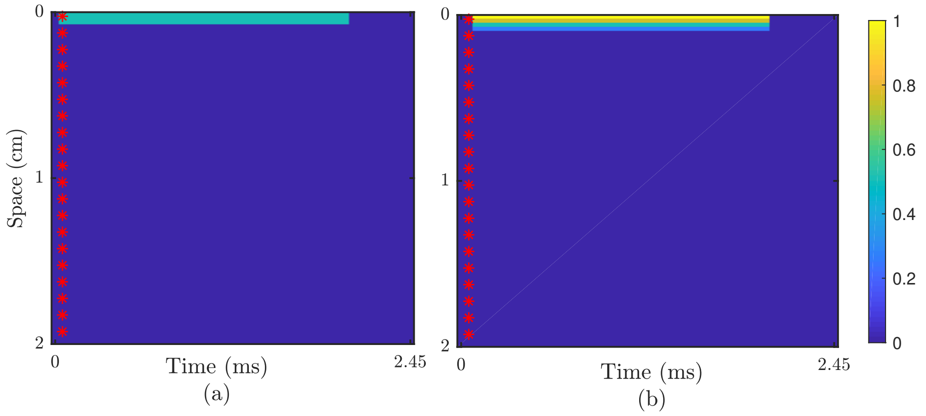

Figure 4.6. **Detection results from the normal activation patterns in the tissue field for the first stimulus applied at** $k = 0.05$ **for a time interval of 2 ms**. (a) Actual stimulus field. (b) Temporal evolution of the B-splines weighting function obtained from the detection step using a threshold value of 9.

State estimation results

In this subsection, the state estimation results during normal and re-entrant cardiac conditions are illustrated.

Firstly, the state estimation results of normal activation patterns in the cable

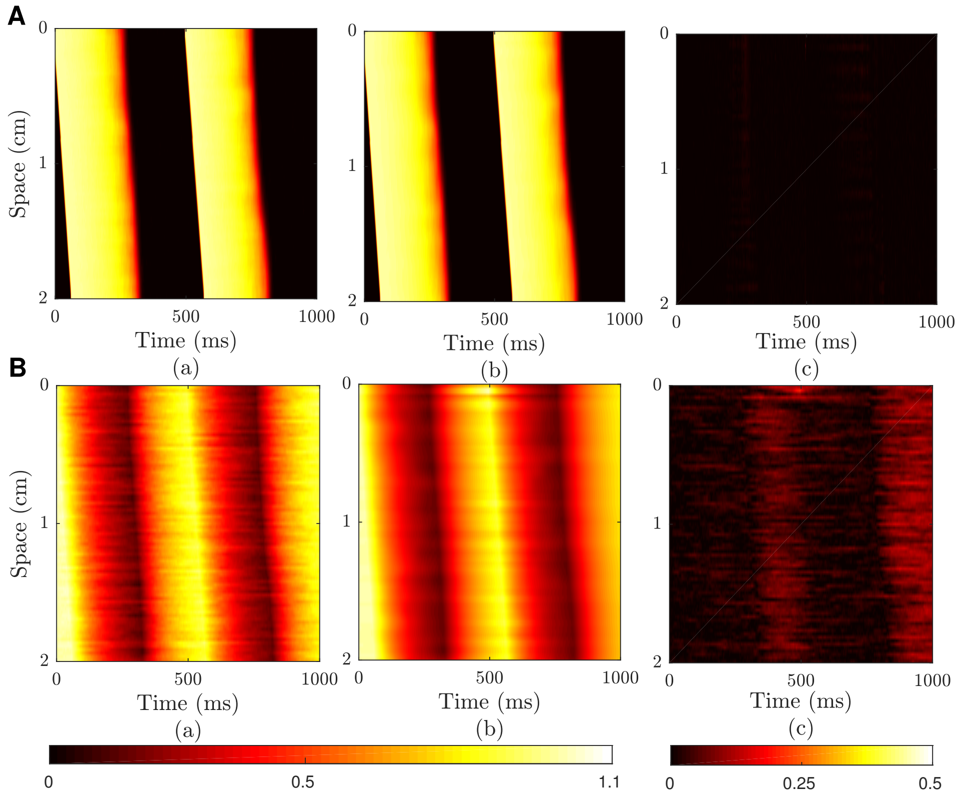

Figure 4.7. Estimation results from one-dimensional cable field. (A) Transmembrane voltage. (B) Gating variable. The sub-figures in each row are: (a) Actual pattern of state variable. (b) Estimated pattern of state variable. (c) Absolute difference in the actual and estimated patterns.

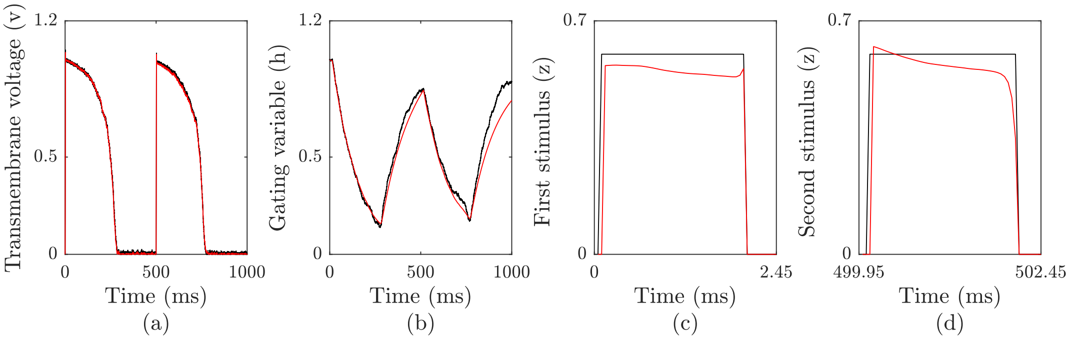

Figure 4.8. The state estimation results for normal activation patterns at spatial location, s_x = 0.525 cm. (a) Transmembrane voltage. (b) Gating variable. (c) First stimulus variable. (d) Second stimulus variable. Actual signal (▬), estimated signal (▬).

field are presented. As described in the previous analysis, the threshold value of 9 was used in the detection scheme to identify the stimulus locations. The distance

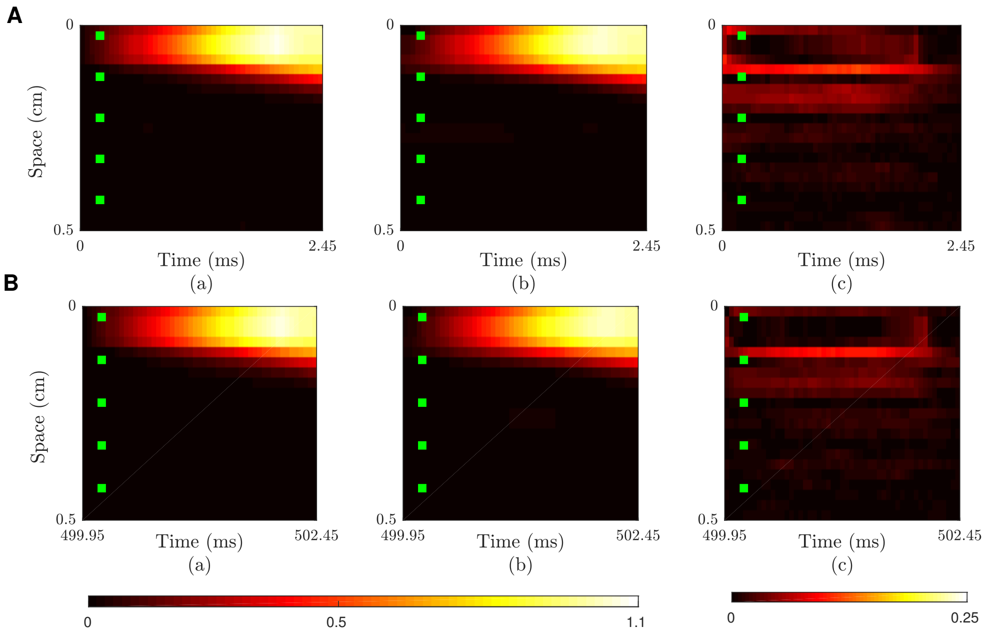

Figure 4.9. **Patterns of transmembrane voltage nearby the stimulus locations during normal conditions.** (A) Transmembrane voltage. (B) Gating variable. The sub-figures in each row are: (a) Actual pattern of state variable. (b) Estimated pattern of state variable. (c) Absolute difference in the actual and estimated patterns.

measure calculated using the nominal model is shown in Figure 4.5. The figure illustrates peak values in the model uncertainty during stimulus intervals at the sensor locations correspond to the stimulus locations. This also emphasises the need of incorporating the stimulus estimation, which is implemented using state-augmentation method. In Figure 4.6(a), actual stimulus pattern during the first stimulus interval is presented. On the other hand, the temporal evolution of B-spline functions constructed using the results from the detection step is shown in Figure 4.6(b). It can be seen that the detection scheme identified all the stimulus sensor locations except at the first time instant. By using the generated B-spline functions, state variables across the neighbourhood locations of detected sensor locations in the tissue field were then estimated.

The accuracy of the estimation algorithm was then evaluated by comparing the estimated patterns of state variables with the actual patterns. The modelled cardiac patterns and the estimated state variables from $s_x = 0.025$ cm, from the URTSS smoother are shown in Figure 4.7 and Figure 4.8, respectively. The differences in the activation patterns shown in Figure 4.7(c) indicate that the estimated state variables are in good agreement with that of actual cardiac activation patterns. In particular, the proposed continuous version of mMS model was able to

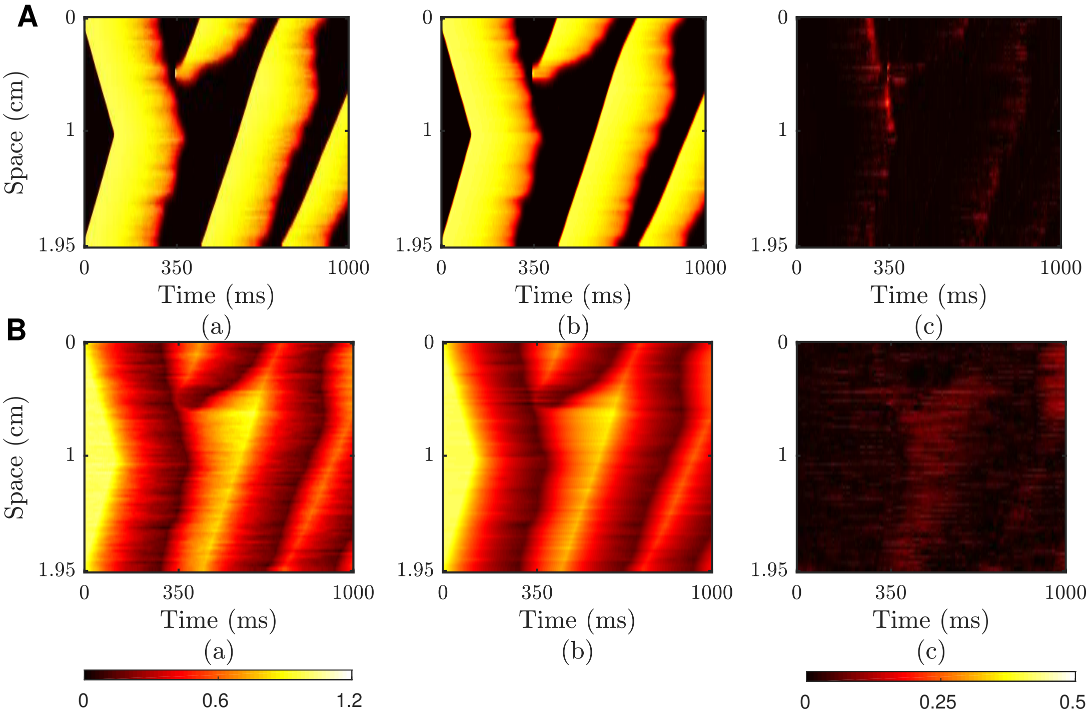

Figure 4.10. **Estimation results from one-dimensional ring field**. (A) Transmembrane voltage. (B) Gating variable. The sub-figures in each row are: (a) Actual pattern of state variable. (b) Estimated pattern of state variable. (c) Absolute difference in the actual and estimated patterns.

capture the dynamics of the gating variable by using a smaller slope value of 25. The estimated stimulus variable at the sensor location is shown Figure 4.8 (c)-(d). For completeness, transmembrane voltage around the stimulus (time instant and spatial location) in the tissue field is shown in Figure 4.9. The results show that B-spline functions enable to estimate the transmembrane voltage around the neighbourhood stimulus locations. However, it also illustrates the error contributed from the edges of the weighting function to neighbourhood locations.

In a similar way, the estimation algorithm was implemented for the re-entrant activation patterns in one-dimensional ring model. Here, the threshold value was then set to 5, based on the detection performance statistics summarised in Table 4.1. B-spline functions were then constructed by including the periodic boundary characteristics of the ring field. The estimation algorithm was then implemented to estimate the state variables from the electrogram measurements. The actual and estimated patterns of state variables are shown in Figure 4.10, along with the absolute error between the actual and estimated state variables. It can be seen that the estimation results are consistent with that in the normal activation patterns. An

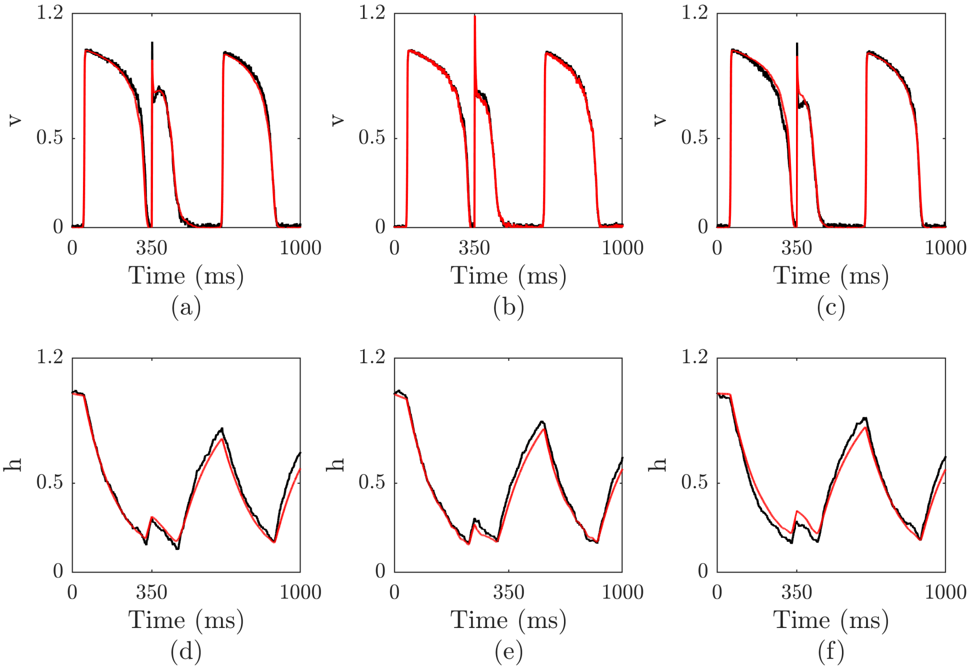

Figure 4.11. **The state estimation results of re-entrant activation patterns**. (a-c) Transmembrane voltage. (d-f) Gating variable. Actual signal (—), estimated signal (—).

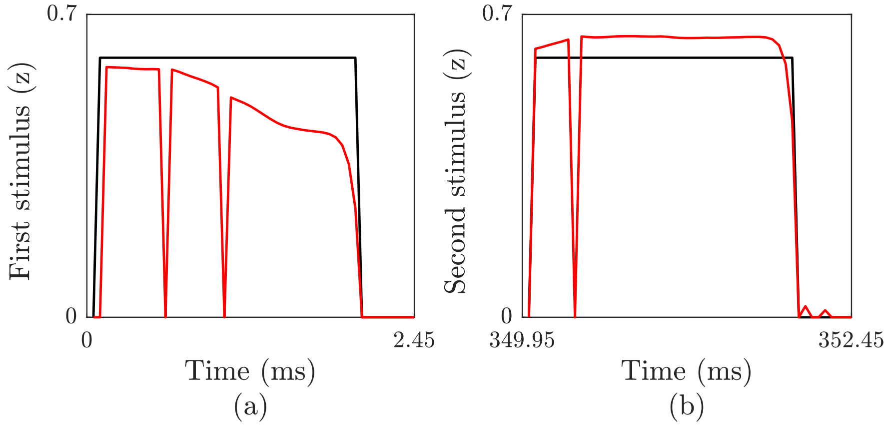

Figure 4.12. **The stimulus state estimation results of re-entrant activation patterns**. (a) First stimulus variable. (b) Second stimulus variable. Actual signal (—), estimated signal (—).

example of transmembrane voltage and gating variable estimates from the second stimulus (S2) locations are shown in Figure 4.11, while stimulus estimates at the (S1 and S2) sensor locations are shown in Figure 4.12. It can be seen that the state

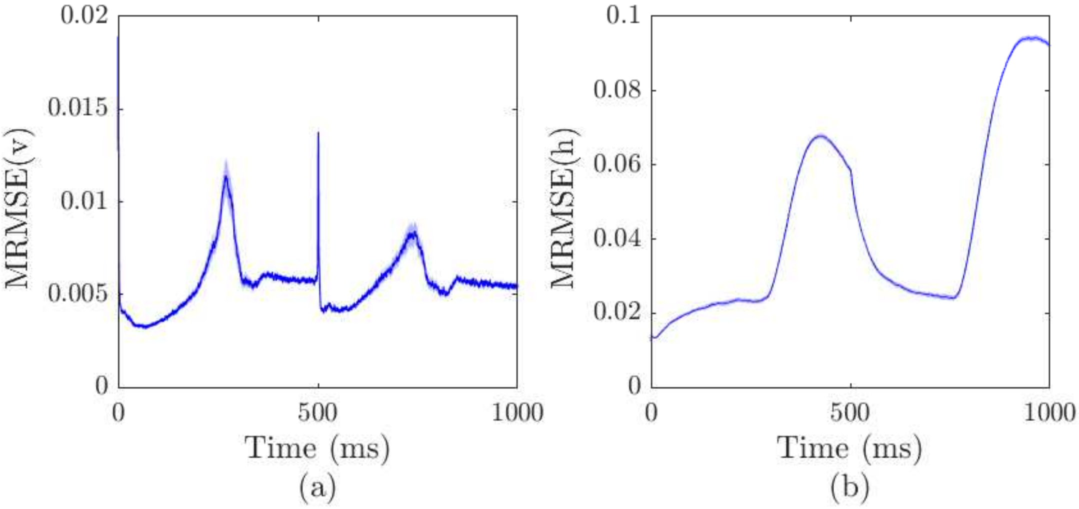

Figure 4.13. **MRMSE measure calculated over 50 realisations for the normal activation patterns**. The mean value is shown in blue colour along with 95% confidence interval (shaded region). (a) Transmembrane voltage. (b) Gating variable.

estimates at the sensor locations are corrected through the sensor measurement at the specific location. Since the detection step identifies a point stimulus in sensor field, the weights associated to the b-spline function at the neighbouring locations are smaller. This causes the discrepancies in the voltage estimates at those neighbourhood locations. Moreover, the results in Figure 4.12 also illustrate the effects of detection performance on the stimulus estimation. For instance, state estimation at the missed instants is based on the nominal state-space model, which caused higher magnitude of error at the particular time instants.

In order to validate the consistency of the estimation performance, a Monte-carlo based approach was then employed. Here, 50 realisations of the activation patterns in both one-dimensional tissue fields were first generated. Within each realisation of the activation pattern, the RMSE value (across space) were computed by comparing the actual and estimated state variables. The mean RMSE values (over realisations) were then computed for transmembrane voltage and gating variable using (4.74). The resulting MRMSE statistics from the normal and re-entrant activation patterns are shown in Figures 4.13 and 4.14, along with 95% confidence interval. Although the estimation algorithm can capture the tissue dynamics, state estimation error is observed during stimulus intervals in the transmembrane voltage estimates, especially in the re-entrant activation patterns (see Figure 4.14). As described in the simulation setup, the initial spatial location of the first stimulus (S1) was $s_x = 0$ cm, which coincided directly with the first sensor location. The inclusion of periodic weighting function at the closed curve

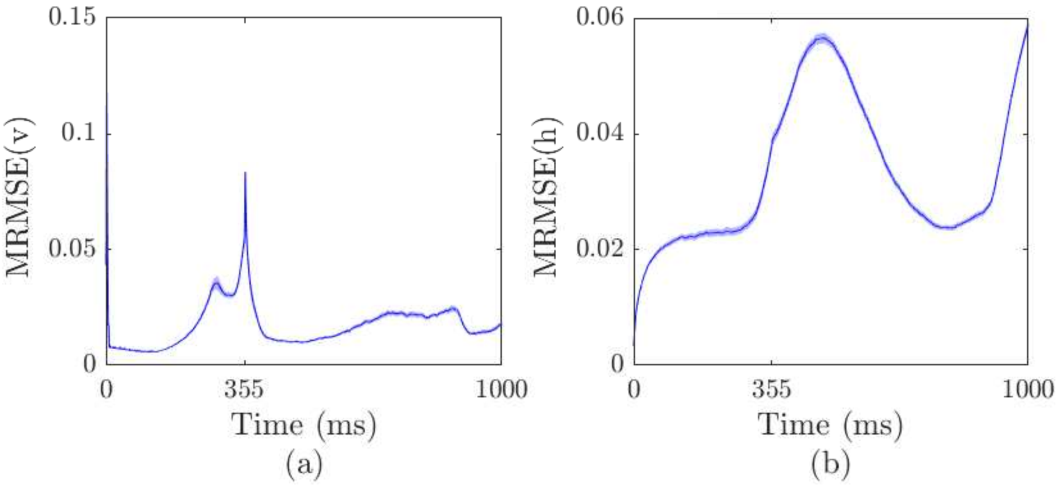

(a) (b)

Figure 4.14. MRMSE measure calculated over 50 realisations of the re-entrant activation patterns. The mean value is shown in blue colour along with 95% confidence interval (shaded region). (a) Transmembrane voltage. (b) Gating variable.

Table 4.2. MSE measure to analyse the effects of weighting function

Spatial location (cm)	Weights for states mapping	Mean squared error	Stimulus condition
0.450	0.5	0.0473	No
0.475	0.75	0.0144	Yes
0.5	1	0.0012	Yes
0.525	0.75	0.0120	Yes
0.550	0.5	0.0430	No

boundaries of the ring model caused initial state estimation error. This is illustrated in Figure 4.15 A, where the weights at non-stimulus locations caused state estimation error at the prior spatial locations. For instance, the estimation error at the second stimulus interval is examined using the mean squared errors at the stimulus and neighbouring locations during second interval (see Table 4.2). The MSE values and Figure 4.15 B show that estimation errors are caused from the weights, which were assigned to interpolate the state estimates into the neighbour locations. In addition to this, the model mismatch between proposed continuous version and modified Mitchell-Schaeffer model also contributed in the gating variable estimation error, illustrated in Section 3.3.

In summary, the results of this experiment shows that the proposed estimation algorithm can be employed to reconstruct the tissue dynamics during normal and abnormal activation patterns, by simultaneously detecting the stimuli locations. The estimation errors are predominantly caused from number of sources:

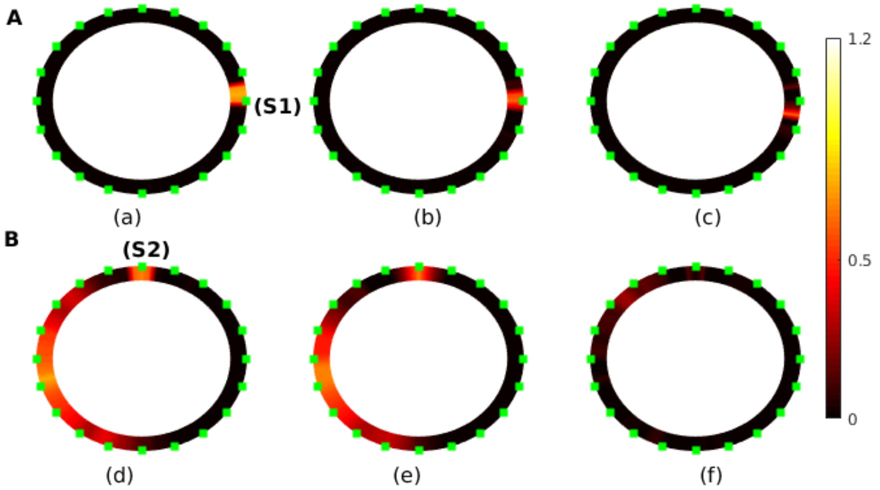

Figure 4.15. Patterns of transmembrane voltage nearby the stimulus locations during re-entrant conditions. (A) First stimulus interval. (B) Second stimulus interval. The sub-figures in each row are: (a) Actual pattern. (b) Estimated pattern. (c) Absolute difference in the actual and estimated patterns.

(a) model mismatch in the gating variable formulation, (b) missed stimulus in detection algorithm, (c) the edge effects and the weightings caused from mapping of the stimulus state variables using the weighting function, (d) the use of sparse measurements to estimate the tissue field dynamics. It must be also noted that the Gaussian approximation of the non-linear model used in the URTSS algorithm may also be a significant factor [104] .

4.5.2 Experiment II: Effects of Slope Value in Gating Variable Formulation

The previous analysis illustrated the error in gating variable state estimation, which caused from the inherent approximation of slope value in the gating model formulation. In this experiment, the effects of slope parameter on the estimation performance are examined. Recall the state-space model for the estimation is employed using the proposed continuous version of mMS model, where the gating variable approximation using the slope value of 25.

To examine the effects of slope parameter, the detection metrics and RMSE statistic of the transmembrane voltage and gating variable were calculated by varying the slope γ in (4.2). It should be noted that the other electrophysiological parameters were kept the same to that in Table 3.1. The results from this analysis are shown for the re-entrant activation patterns in Figure 4.16. Figure 4.16(a)

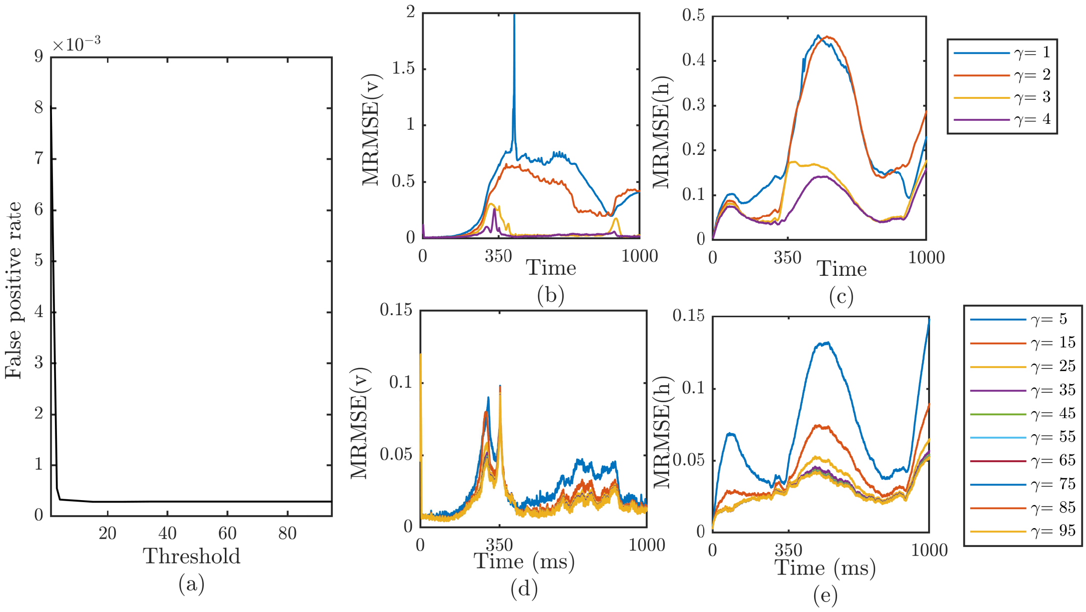

Figure 4.16. **Detection metrics and RMSE measures for different slope values.** (a) False positive rate. (b)-(d) RMSE measure of transmembrane voltage. (c)-(e) RMSE measure of gating variable.

shows that for selected slope values the false positives are higher for smaller slope values (γ) from 1 to 5 and remains constant. The increased false positives for the smaller slope values are reflected on the accuracy of the state estimation (see Figure 4.16 (b)-(c). Consequently, the RMSE measure of state estimates from the URTSS smoother decreases with increase in slope value. This is particularly evident in the RMSE measure of the gating variable shown in Figure 4.16 (b). This is because, as the slope value increases the underlying model approximation is becoming more accurate to the mMS model, which reduces the smoothing error.

In the previous analysis, the slope measure was kept to be a lower value of 25 for obtaining a crude representation of the real world situations, where the models are of imperfect nature. As a result, a lower value of slope may have to be used for reconstructing the tissue dynamics as a compromise between model accuracy and potential real life imperfections. It should be noted a higher slope value could also cause problems in the parameter estimation (beyond a particular value), due to the increased non-linearity from the sigmoid approximations [9].

4.5.3 Experiment III: Comparison with the Nominal Model

In this experiment the importance of the proposed combined detection-estimation algorithm is analysed. For this state estimates $\mathbf{x}_k = [\mathbf{v}_k, \mathbf{h}_k]^\top$ determined from the

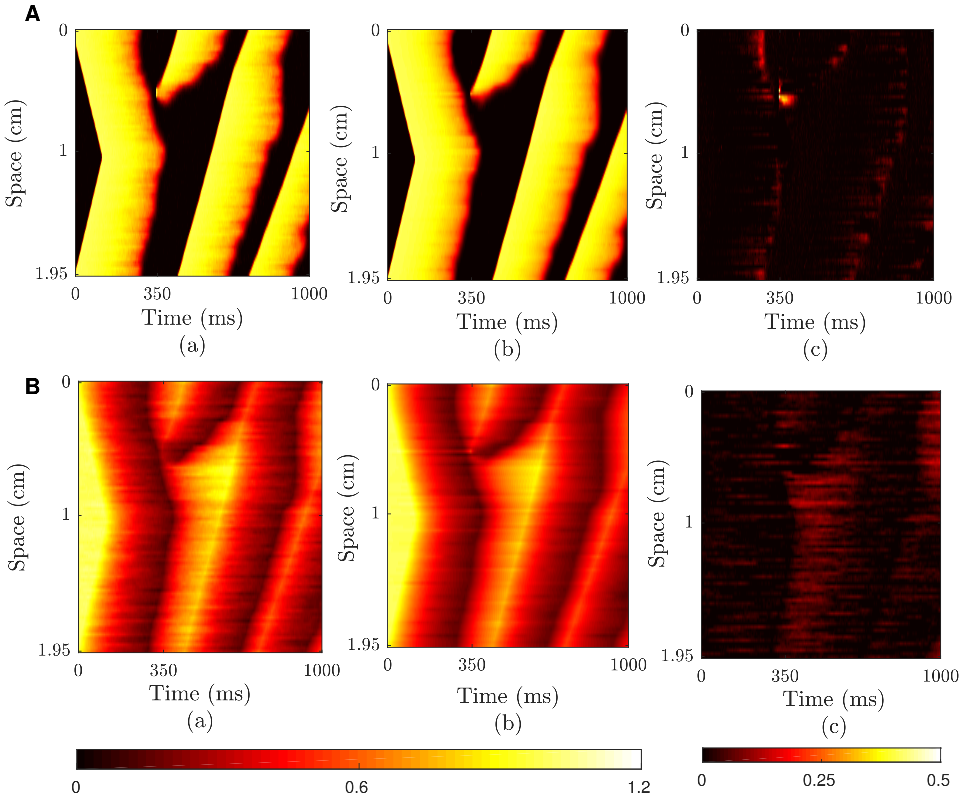

Figure 4.17. **Estimation results for re-entrant activation patterns using the nominal model conditions**. (A) Transmembrane voltage. (B) Gating variable. The sub-figures in each row are: (a) Actual pattern of state variable. (b) Estimated pattern of state variable. (c) Absolute difference in the actual and estimated patterns.

proposed method in Algorithm 4.1 were compared with the nominal state-space model estimates. The nominal state-space model can be defined by the following nominal state-evolution equation

$$\mathbf{x}_{k+1} = \mathbf{f}(\mathbf{x}_k) + \boldsymbol{\epsilon}_k^x, \tag{4.75}$$

where $\mathbf{f}(\mathbf{x}_k)$ is given by

$$\mathbf{f}(\mathbf{x}_k) = \begin{bmatrix} \bar{\theta}_e \mathcal{A} \mathbf{v}_k + \bar{\boldsymbol{\Psi}}_k \bar{\boldsymbol{\theta}}^\top \\ \\ \bar{\theta}_f \mathbf{h}_k + \bar{\boldsymbol{\beta}}_k \, \bar{\theta}_f \end{bmatrix},$$

where the observation equation remains the same as in (4.12).

The nominal state estimation was then employed with using the URTSS smoother without the detection and estimation of the stimulus variables. In this section, estimation results from the re-entrant activation patterns in one-dimensional ring

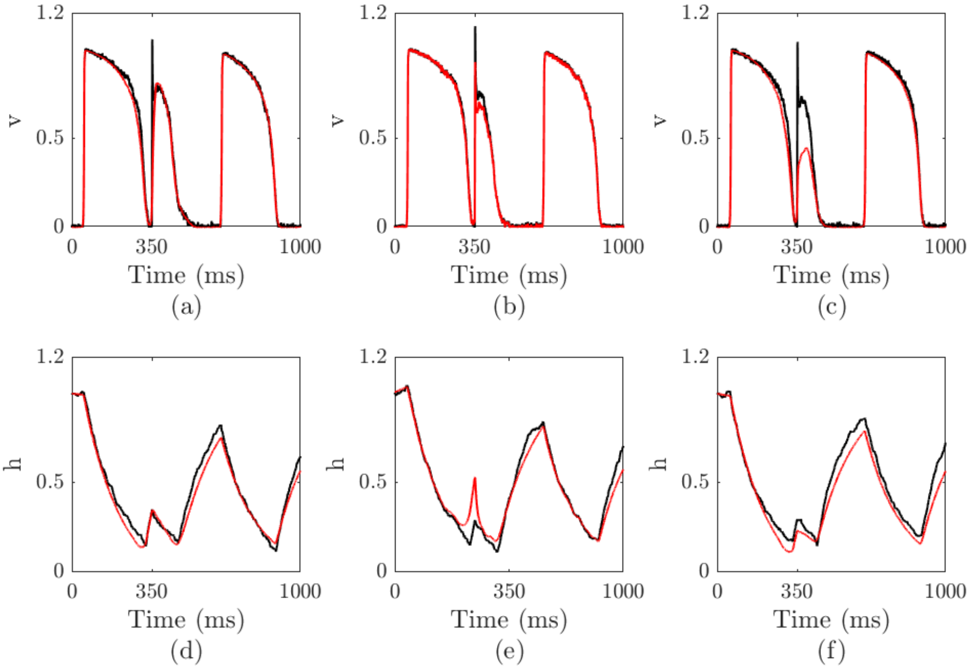

Figure 4.18. **The state estimation results for re-entrant activation patterns using the nominal model conditions**. (a-c) Transmembrane voltage. (d-f) Gating variable. Actual signal (▬), estimated signal (▬).

field are shown in Figure 4.17. The figure shows that the estimation using the nominal model of one-dimensional ring field can be used to reconstruct the basic structure of the tissue field by inferring from the sparse electrogram measurements. However the differences in the activation patterns at the stimulus locations (see Figure 4.17 A:(c)) are observed due to the absence of stimulus estimation. This can be further examined by analysing the state estimates at the second stimulus locations plotted in Figure 4.18. The transmembrane voltage estimate at the sensor location was corrected through the sensor measurement at the particular location. However, the characteristics of re-entrant activation were not estimated at neighbouring stimulus locations. Although the state estimates were then reconstructed in the following cardiac cycle from the sensor measurements, identifying the re-entrant drivers are important in the accurate reconstruction of the tissue field dynamics. The results from the proposed detection-estimation algorithm is shown in Figure 4.11 state estimates at all the stimulus locations were estimated accurately, after detecting the re-entrant drivers.

Although nominal estimation can capture the tissue dynamics by learning from the electrogram measurements, detection of the re-entrant drivers is important in

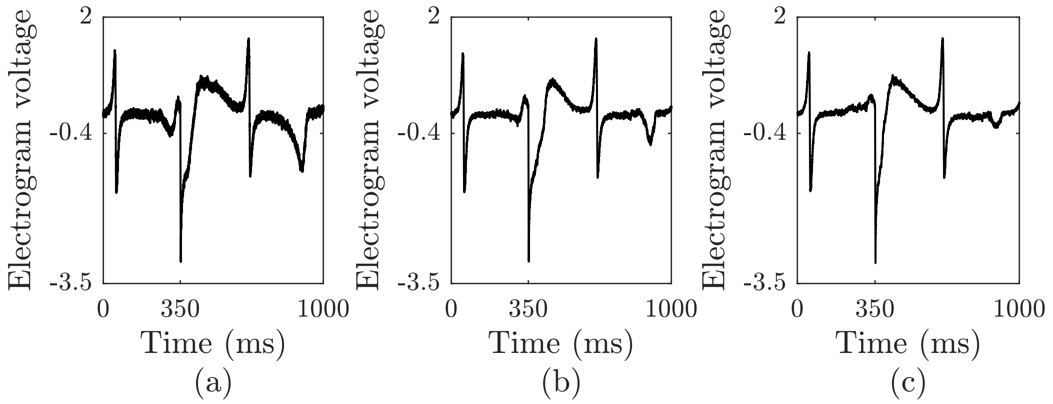

Figure 4.19. **Electrogram measurements with different SNR values.** (a) SNR = 21.61 dB (b) SNR = 31.64 dB (c) SNR = 41.53 dB

quantifying the spatio-temporal patterns. This is particularly significant in the complex abnormal conditions, where multiple stimulii are driving the re-entrant activity.

4.5.4 Experiment IV: Results for Different Observation Noise Levels

In this experiment, sensitivity of the proposed estimation algorithm with respect to the observation noise variance is analysed.

To demonstrate this, re-entrant activation patterns were generated with three different magnitude of observation noise variances. To calculate the corresponding Signal to Noise Ratio (SNR), the mean squared amplitude of a sensor measurement is first defined as

$$E_i = \frac{1}{T}\sum_{k=1}^{T}(y_k^i - [\epsilon_k^y]^i)^2 \tag{4.76}$$

Table 4.3. **Performance metrics for different level of observation noises.**

Performance Measure	$\sigma_y^2 = 10^{-3}$ ϖ=2	$\sigma_y^2 = 10^{-4}$ ϖ=5	$\sigma_y^2 = 10^{-5}$ ϖ=10
SNR (dB)	21.61	31.64	41.53
TPR (%)	65.02	96.35	98.6
FPR (%)	0.56	0.029	0.020
MRMSE (v) (%)	1.63	1.54	1.52
MRMSE (h) (%)	3.47	3.37	3.46
RMSE (z_1) (%)	77.04	34.11	23.65
RMSE (z_2) (%)	70.56	7.47	7.58

This measure can be then averaged across the sensor measurements as

$$\bar{E} = \frac{1}{n_y} \sum_{i=1}^{n_y} E_i \tag{4.77}$$

By using (4.76) and (4.77), SNR measure across the sensor measurements can be calculated as

$$SNR = 10 \log_{10} \frac{\bar{E}}{\sigma_y^2} \tag{4.78}$$

where σ_y^2 is the measurement noise variance.

Similar to the previous analysis, the estimation performance is quantified using Monte-Carlo based approach. Here 20 realisations of the re-entrant activation patterns were simulated. Examples of electrogram measurements used for this experiment are shown in Figure 4.19. The proposed detection-estimation methodology in Algorithm 4.1 was then implemented to estimate the state variables.

Table 4.3 summarises the detection performance metrics and average MRMSE

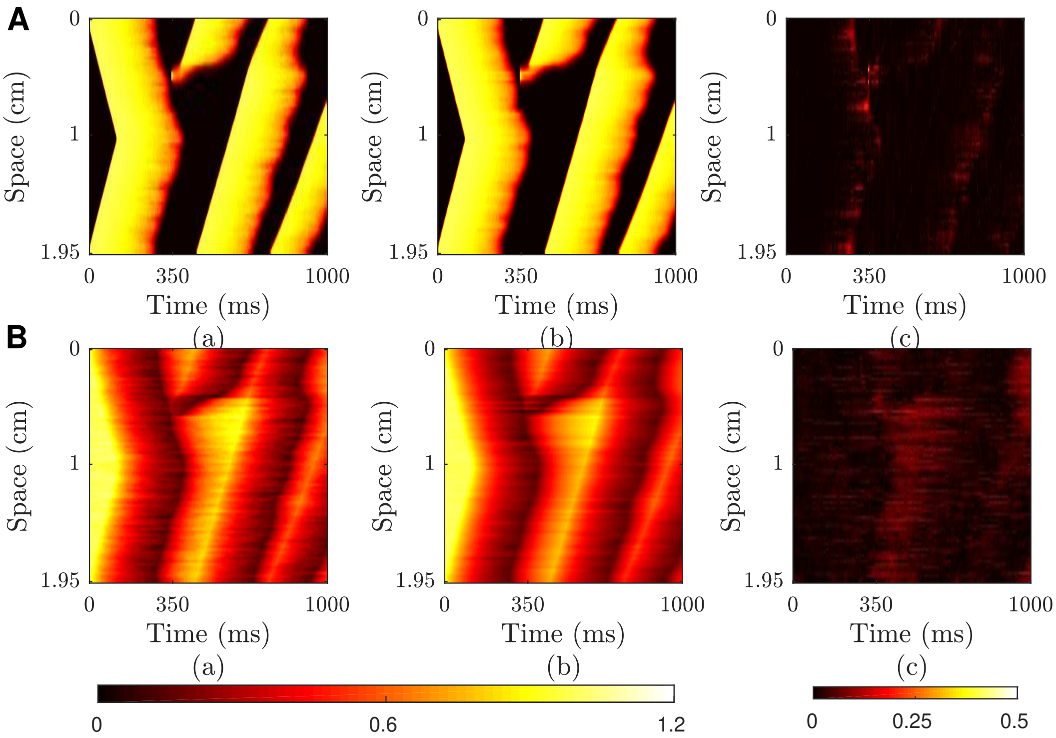

Figure 4.20. Estimation results from one-dimensional ring field with SNR = 21.61 dB. (A) Transmembrane voltage. (B) Gating variable. The sub-figures in each row are: (a) Actual pattern of state variable. (b) Estimated pattern of state variable. (c) Absolute difference in the actual and estimated patterns.

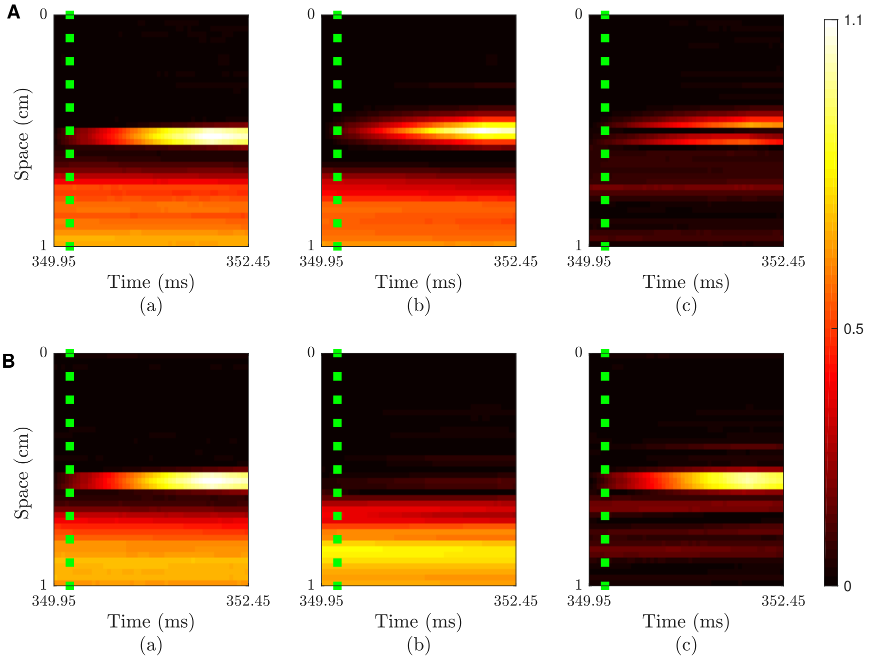

Figure 4.21. **Patterns of transmembrane voltage nearby the stimulus locations during normal conditions.** (A) First stimulus condition, where one of the stimulus coincide with the sensor. (B) Second stimulus condition, where the stimulus locations are between the sensors. The sub-figures in each row are: (a) Actual pattern of state variable. (b) Estimated pattern of state variable. (c) Absolute difference in the actual and estimated patterns.

calculated across the 20 realisations. It can be seen in Figure 4.20 that the underlying tissue variables can be reconstructed for all the three measurement noise variance conditions, especially for $\sigma_y^2 = 10^{-3}$. However, the detection and estimation of the stimulus variables are significantly affected by the increased noise statistic, as shown in Table 4.3. This is because, filter-based detection approaches incorporates the noise statistics into the formulation as given in (4.25). The detection performance is affected when the contribution of the changes in disturbances are significant compared to the abnormality quantified by the distance measure [14]. One approach to improve the detection scheme is by employing adaptive thresholding mechanisms [27].

4.5.5 Experiment V: Results for different Stimulus Locations with respect to the Sensor Locations

The previous analyses demonstrated the effectiveness of the proposed detection-estimation algorithm in reconstructing the tissue dynamics, along with the external stimulus variables. However it is particularly important to examine the limitations of the proposed algorithm, especially with the detection of the external stimulus in the tissue field from the sparse electrogram measurements.

In this experiment, the estimation performance is evaluated by varying the stimulus locations of re-entrant activity. For this two possible re-entrant stimulus conditions were considered other than in the previous analyses. They are : 1) The edge of stimuli coincide with one of the sensor location as shown in Figure 4.21 A:(a) 2) Stimulus locations are between two the sensors as shown in Figure 4.21 B:(a). The results from this analysis are shown in Figure 4.21, where the detection and estimation of stimulus variables are captured in the first stimulus condition but not in the second stimulus condition. This indicate that the detection scheme can be further improved to incorporate the information of tissue locations between the sensor locations.

4.6 Conclusion

This chapter presents a model-based statistical inference framework to reconstruct the tissue dynamics from cardiac electrogram measurements. More importantly, this chapter focussed on the estimation of both normal and the re-entrant cardiac activity generated in one-dimensional cable and ring fields, respectively.

The key contributions of this chapter are the following:

- A stochastic version of the integrated model of cardiac electrophysiology is presented by adding random disturbances into the deterministic model equations. Based on these model equations, finite-dimensional state-space model of the cardiac models are then derived to employ standard statistical inference frameworks.

- To obtain a computationally efficient algorithm for discrete-space and discrete-time state-space model, a single stage detection-estimation approach is proposed in this chapter. At every time instant, a filter-based detection approach is implemented to identify the stimulus conditions. Based on the results from the diagnosis scheme, the state variables of the corresponding state-space models are then estimated accordingly.

- The performances of the proposed method are evaluated using Monte-Carlo simulations and experiments with different slope values, noise conditions and stimulus locations, etc.

- The findings from this chapter demonstrate that the proposed detection-estimation algorithm can be used to estimate the state variables in a one-dimensional spatial field, by simultaneously detecting the external stimulus events.

- An important extension of the proposed approach is to employ the inference framework for quantifying the complex spiral wave dynamics. This is illustrated in the next chapter.

Chapter 5

Detection and Estimation Framework For Two-dimensional Cardiac Model

In the previous chapter, reconstruction of the one-dimensional cardiac tissue dynamics from the cardiac electrogram measurements was presented. The methodology used to reconstruct the tissue dynamics was established by estimating the state variables of the monodomain tissue model, along with the detection and estimation of stimulus variables.

A natural extension of the proposed inference problem is the reconstruction of electrical dynamics in a two-dimensional tissue field. By introducing another spatial dimension, the underlying cardiac electrical activity may exhibit more complex dynamics. This is because, the complex spatiotemporal patterns are formed because of the multiple interactions between the different spatial regimes in the two-dimensional tissue field with temporal dependencies.

The overall aim of this chapter is to establish a model-based inference framework for the reconstruction of the two-dimensional tissue dynamics, including the detection and estimation of stimulus variables. The chapter proceeds by detailing the stochastic integrated cardiac model in the two-dimensional cardiac field. The next stage is to represent the infinite-dimensional model as a finite-dimensional state space model to implement the standard signal processing and estimation techniques. The inference methodology is then proposed, which follows similar procedures to that of one-dimensional cardiac field. However, the inference methodology of two-dimensional cardiac field is essentially a detection and estimation for high-dimensional systems, because of the higher number of state variables (spatial nodes). This restricts the direct implementation of the proposed detection-estimation framework presented in Algorithm 4.1. The additional challenges caused by the high-dimensionality and the corresponding proposed solutions are given below.

1. For a state-space model with n_x states, the unscented transform in the proposed estimation algorithm requires the number of sigma points to be $2n_x + 1$ at every time instant [78]. These sigma points are then propagated through the nonlinear model to compute the state estimates and error covariance matrix. For a high-dimensional system of two-dimensional tissue field with $n_x \simeq 3362$, this requirement is computationally infeasible to employ the state estimation approach [7, 29, 45].
    - To address this, Reduced-Rank Unscented Kalman Filter (RRUKF) presented in [98, 149] is incorporated into the detection-estimation framework in Algorithm 4.1. The principle idea of this approach is to choose the reduced number of most significant sigma points, which captures the statistical properties of the actual sigma points. For this, a Truncated Singular Value Decomposition (TSVD) on the error-covariance matrix is first performed with a truncation index of n_r. The resulting reduced number of sigma points ($2n_r + 1$; $n_r << n_x$) is then used to compute the state and covariance estimates. This method is explained in Section 5.3.1.
2. For the implementation of fixed-interval smoothing algorithm, the error covariance matrices from the filtering step (forward iteration) are stored during the entire time interval. The stored estimates are then used to compute the smoothed error covariance matrix (2.50) and the smoothed state estimates in the smoothing step (backward recursion). For high-dimensional systems, storage and manipulation of error covariance matrices for higher values of n_x are computationally prohibitive [98]. For instance, in the forward recursion of URTS smoothing algorithm for two-dimensional spatial field, filtering error-covariance matrices are of size (3362×3362) which needs to be stored for $T = 20001$ time instants. In the backward recursion, the smoothed estimates are then computed based on these stored values. This recursive estimation process with both forward and backward recursions using a fixed interval setting imposes higher computational storage and time requirements for the estimation.
    - To address this, a fixed lag URTS smoother [148] is implemented, where the smoothing step is embedded into the filtering step [4**?**]. This

enables to obtain the smoothed estimates without storing the error-covariance matrices during the entire time interval in the filtering recursion. This method is briefly explained in Section 5.3.3.

To illustrate the performance of the proposed algorithm, complex spiral wave patterns presented in Section 3.2.2 are considered. This is because, the re-entrant arrhythmic conditions are widely studied by quantifying the spiral wave dynamics using cardiac models [25, 47] and experimental techniques [18, 55]. The important components of spiral wave dynamics include initiation process within the vulnerable window, the core around which the spiral waves rotate, and the spiral waves trajectories. It should be noted that the propagation of spiral wave is formed as a result of initiation process, during which the stimuli is applied at a particular locations and time instants within the vulnerable window. Since the stimulus conditions are unobserved, it is important to include the detection and estimation of stimulus events into the framework. Therefore, reconstruction of the tissue dynamics from the cardiac electrograms can be used to quantify the spiral wave dynamics.

The rest of this chapter is organised as follows. Section 5.1 presents the stochastic models of cardiac electrophysiology in two-dimensional spatial field. Section 5.2 provides the problem statement of this chapter. This is followed by the description of proposed detection-estimation methodology in Section 5.3. Following this, the simulation setup and data generation of spiral waves are detailed in Section 5.4. The results are presented in Section 5.5. Finally, conclusions are provided in Section 5.6.

5.1 Nonlinear State-space Model Representation

The stochastic tissue model in a one-dimensional tissue field given in (4.1) can be extended to the two-dimensional field as follows

$$\begin{aligned}\frac{\partial v(\mathbf{s},t)}{\partial t} = \theta_g\left(\frac{\partial^2 v(\mathbf{s},t)}{\partial s_x^2} + \frac{\partial^2 v(\mathbf{s},t)}{\partial s_y^2}\right) + h(\mathbf{s},t)\frac{v(\mathbf{s},t)(v(\mathbf{s},t)-v_g)(1-v(\mathbf{s},t))}{\tau_{in}} \\ -(1-h(\mathbf{s},t))\frac{v(\mathbf{s},t)}{\tau_{out}} + i^{st}(\mathbf{s},t) + \sigma_v\frac{\partial \zeta^v(\mathbf{s},t)}{\partial t},\end{aligned} \tag{5.1}$$

$$\frac{\partial h(\mathbf{s},t)}{\partial t} = \frac{e^{-\gamma(v(\mathbf{s},t)-v_g)}}{1+e^{-\gamma(v(\mathbf{s},t)-v_g)}}\theta_f - h(\mathbf{s},t)\theta_f + \sigma_h\frac{\partial \zeta^h(\mathbf{s},t)}{\partial t}, \tag{5.2}$$

where tissue spatial field is represented by $\mathbf{s} = \left(s_x, s_y\right)$.

Similarly, stochastic model of extracellular electrogram measurements at discrete spatial locations in sensor field ($\mathbf{s}' = s_x', s_y', s_z'$) is given by

$$y_k(\mathbf{s}') = \bar{\kappa} \iint \left(\frac{\partial v}{\partial s_x} \frac{(s_x - s_x{}')}{r^3} + \frac{\partial v}{\partial s_y} \frac{(s_y - s_y{}')}{r^3} \right) ds_x ds_y + \epsilon_k^y(\mathbf{s}'). \tag{5.3}$$

It should be noted that additive disturbance terms in above model equations are approximated to be spatially uncorrelated white noise processes [75]. The infinite-dimensional model equations are then converted to finite-dimensional state-space model using the procedures similar to that in Section 4.1. For completeness, the procedures are briefly explained in this section. To derive a discrete-space and discrete-time state evolution equation, spatial discretisation of the Laplacian operator in the diffusion term is first performed using finite difference method. The spatial discretisation of the Laplacian operator yields two-dimensional finite difference matrix after incorporating the no-flux boundary conditions. The resulting difference matrix $\mathcal{A}$ is given in (3.50). This procedure is followed by temporal discretisation of the model equations using explicit finite difference method. The resulting state evolution equation is given by

$$\mathbf{x}_{k+1} = \mathbf{f}(\mathbf{x}_k, \mathbf{i}_k^{st}) + \epsilon_k^x, \tag{5.4}$$

where $\mathbf{f}(\mathbf{x}_k)$ denotes the nonlinear model function of state variables given by

$$\mathbf{f}(\mathbf{x}_k, \mathbf{i}_k^{st}) = \begin{bmatrix} \bar{\theta}_e \mathcal{A} \mathbf{v}_k + \bar{\mathbf{\Psi}}_k \bar{\boldsymbol{\theta}}^\top + \mathbf{i}_k^{st} \Delta_t \\ \\ \bar{\theta}_f \mathbf{h}_k + \bar{\boldsymbol{\beta}}_k \bar{\theta}_f \end{bmatrix},$$

where $\mathbf{x}_k \in \mathbb{R}^{n_x}$ is the vector of state variables that comprises of transmembrane voltage and gating variable $[\mathbf{v}_k \;\; \mathbf{h}_k]^\top$, n_x is the number of states, $\epsilon_k^x = [\epsilon_k^v, \, \epsilon_t^h]^\top$ are the Gaussian noise sequences with zero mean and covariance $\mathbf{\Sigma}_v$ and $\mathbf{\Sigma}_h$, respectively. It should be noted that the state variables and the explicit finite difference matrix are arranged with respect to the vectorised spatial index number $l = [1, ..., n_s]$ as described in Section 3.2.2. The other electrophysiological parameters and the variables in (5.4) remain the same as in Section 4.1.

In a similar way, spatial discretisation of the gradient operator is employed for the extracellular electrograms model equation as it is temporally discrete. The linear observation equation is given by

$$\mathbf{y}_k = \mathbf{C}\mathbf{x}_k + \epsilon_k^y, \tag{5.5}$$

where $\mathbf{y}_k \in \mathbb{R}^{n_y}$ is the vector of n_y electrogram recordings, $\epsilon_k^y \in \mathbb{R}^{n_y}$ is vector of normally distributed Gaussian white noise sequences with zero mean and covariance given by $\sigma_y^2 \mathbf{I}$.

The observation matrix $\mathbf{C} = [\bar{\mathbf{C}} \;\; \mathbf{0}]$ maps the transmembrane voltage and gating variables to the electrogram measurements, where $\bar{\mathbf{C}} = \bar{\kappa}\mathbf{R}\mathbf{M}$. Following (3.53) and (3.54), the finite difference matrices $\mathbf{M} = [\mathbf{M}_{s_x} \;\; \mathbf{M}_{s_y}]^{\top}_{n_x \times n_s}$ are derived to preserve the spatial locations, and given in (3.55). In a similar way, the gradient of distance measures between the tissue and sensor fields in s_x and s_y directions, are constructed as $\mathbf{R} = [\mathbf{R}_{s_x} \;\; \mathbf{R}_{s_y}]_{n_y \times n_x}$.

5.2 Problem statement

The overall aim is to reconstruct the tissue dynamics in the two-dimensional spatial field from the extracellular electrogram measurements. The tissue dynamics is described using monodomain equation with continuous version of mMS ionic model. However, the tissue dynamics described in state evolution equation may take the following model structure as

$$\mathbf{x}_{k+1} = \begin{cases} \mathbf{f}(\mathbf{x}_k) + \epsilon_k^x, & \text{under no stimulus condition} \\ \mathbf{f}(\mathbf{x}_k, \mathbf{i}_k^{st}) + \epsilon_k^x, & \text{under stimulus condition} \end{cases} \tag{5.6}$$

5.3 Combined Detection-Estimation Framework

In this section, the detection and estimation algorithm tailored for the high-dimensional systems is presented.

The detection-estimation problem is formulated within the state-space modelling framework consisting of the following steps:

- Detect and isolate the locations of stimulus in the sensor field using a filter-based detection-scheme.
  - **If not detected**
    - Estimate the state variables as $\mathbf{x}_k = [\mathbf{v}_k, \mathbf{h}_k]$ from measurements $\mathbf{y}_k$ via RRUKF state estimation method.
  - **else**
    - Estimate the state variables and the stimulus variables $\tilde{\mathbf{x}}_k = [\mathbf{x}_k, \mathbf{z}_k]$ from measurements $\mathbf{y}_k$ via state-augmentation method.
      - Similar to the one-dimensional model, the new state vector $\mathbf{z}_k$ is used to denote the stimulus variables, at the sensors locations where the presence of stimulus has been detected.

    - Form a linear combination of basis functions to represent the dynamics of stimulus variables, where the basis function themselves are centered at the locations of sensors that detected the presence of the stimulus.

- **end**

The fundamental structure of the proposed solution to the above inference problem remains the same as that of Algorithm 4.1. However, the high-dimensional state estimation requires amendments to this framework as explained earlier. The following subsections are structured to introduce the additional methods, which are incorporated in the proposed methodology as discussed earlier.

5.3.1 Reduced-Rank Unscented Kalman Filter

In order to compute the filtering state estimates $\hat{\mathbf{x}}_k^f$ with smaller number of sigma points, RRUKF method first decomposes the $\mathbf{P}_k^f$ using the Singular Value Decomposition (SVD) method as follows [98]

$$\mathbf{P}_k^f = \mathbf{U}_k \bar{\boldsymbol{\pi}}_k \mathbf{U}_k^\top, \tag{5.7}$$

where the diagonal matrix $\bar{\boldsymbol{\pi}}_k$ comprises eigenvalues $\sigma_{k,j}^2$, which are arranged in the descending order $\bar{\boldsymbol{\pi}}_k = diag\left(\left[\sigma_{k,1}^2, \sigma_{k,2}^2, ..., \sigma_{k,n_x}^2\right]\right)$ with $\sigma_{k,\tilde{a}}^2 > \sigma_{k,\tilde{b}}^2, \forall \tilde{a}, \tilde{b}$. The matrix $\mathbf{U}_k = [\mathbf{u}_{k,1}, \mathbf{u}_{k,2}, ...\mathbf{u}_{k,n_x}]$ consists of the eigenvectors $\mathbf{u}_{k,j}$, corresponds to $\bar{\boldsymbol{\pi}}_k$.

A truncation index number, n_r, is then used to determine a smaller number of sigma points, which captures the statistical properties of the original sigma points. The sigma points are computed as

$$\begin{aligned} \overline{\chi}_{k,j} &= \hat{\mathbf{x}}_k^f, \\ \overline{\chi}_{k,j} &= \hat{\mathbf{x}}_k^f + \sqrt{(n_r + \overline{\lambda})}\ \sigma_{k,j}\mathbf{u}_{k,j}, \quad j = 1, ..., n_r \\ \overline{\chi}_{k,j} &= \hat{\mathbf{x}}_k^f - \sqrt{(n_r + \overline{\lambda}}\ \sigma_{k,j}\mathbf{u}_{k,j} \quad j = n_r + 1, ..., 2n_r \end{aligned} \tag{5.8}$$

where $\overline{\lambda}$ is given by $\alpha^2(n_r + \kappa) - n_r$ with $\kappa = 3 - n_r$.

Subsequently the computed sigma points are propagated through the nonlinear state evolution equation from which the states and error covariance matrix can be calculated as

$$\hat{\chi}_{k+1,j}^{f-} = \mathbf{f}(\overline{\chi}_k). \tag{5.9}$$

The predicted states $\hat{\mathbf{x}}^{f-}_{k+1}$ and covariance matrix $\mathbf{P}^{f-}_{k+1}$ are estimated as

$$\hat{\mathbf{x}}^{f-}_{k+1} = \sum_{j=0}^{2n_r} \overline{W}_j^{(m)} \hat{\mathcal{X}}^{f-}_{k+1,j} \tag{5.10}$$

$$\mathbf{P}^{f-}_{k+1} = \sum_{j=0}^{2n_r} \overline{W}_j^{(c)} (\hat{\mathcal{X}}^{f-}_{k+1,j} - \hat{\mathbf{x}}^{f-}_{k+1})(\hat{\mathcal{X}}^{f-}_{t+1,j} - \hat{\mathbf{x}}^{f-}_{k+1})^{\top} + \Sigma_x \tag{5.11}$$

where the corresponding weights for the estimation are $\overline{W}_j^{(m)}$ and $\overline{W}_j^{(c)}$ calculated in the RRUKF as

$$\overline{W}_0^{(m)} = \frac{\overline{\lambda}}{n_r + \overline{\lambda}} \tag{5.12}$$

$$\overline{W}_0^{(c)} = \frac{\overline{\lambda}}{n_r + \overline{\lambda}} + (1 - \alpha^2 + \beta) \tag{5.13}$$

$$\overline{W}_{k,j}^{(m)} = \overline{W}_j^{(c)} = \frac{1}{2(n_r + \overline{\lambda})}, \quad j = 1, ..., 2n_r \tag{5.14}$$

5.3.2 State Augmentation Method

Similar to the one-dimensional tissue field scenario given in Section 4.3.1, the stimulus detection is performed using the filter-based approach. Briefly, the distance measure is calculated as the negative log-likelihood measure associated with a single sensor measurements as given in (4.25). Following this, a suitable threshold value can be used to detect the sensors locations corresponding to the presence of stimulus. Subsequently, a new vector of stimulus variable $\mathbf{z}_k \in R^{n_z}$ is added to the state vector $\mathbf{x}_k$ to form the augmented state-space model as

$$\widetilde{\mathbf{x}}_{k+1} = \widetilde{\mathbf{f}}(\mathbf{x}_k, \mathbf{z}_k) + \widetilde{\epsilon}^x_k. \tag{5.15}$$

The augmented model function $\widetilde{\mathbf{f}}(\mathbf{x}_k)$ is given by

$$\widetilde{\mathbf{f}}(\mathbf{x}_k, \mathbf{z}_k) = \begin{bmatrix} \bar{\theta}_e \mathcal{A} \mathbf{v}_k + \bar{\mathbf{\Psi}}_k \bar{\boldsymbol{\theta}}^{\top} + \mathbf{B}_k \mathbf{z}_k \ \Delta_t \\ \\ \bar{\theta}_f \mathbf{h}_k + \bar{\wp}_k \ \bar{\theta}_f \\ \\ \mathbf{z}_k \end{bmatrix}, \tag{5.16}$$

The corresponding linear observation equation is given by

$$\mathbf{y}_k = \widetilde{\mathbf{C}} \tilde{\mathbf{x}}_k + \epsilon^y_k, \tag{5.17}$$

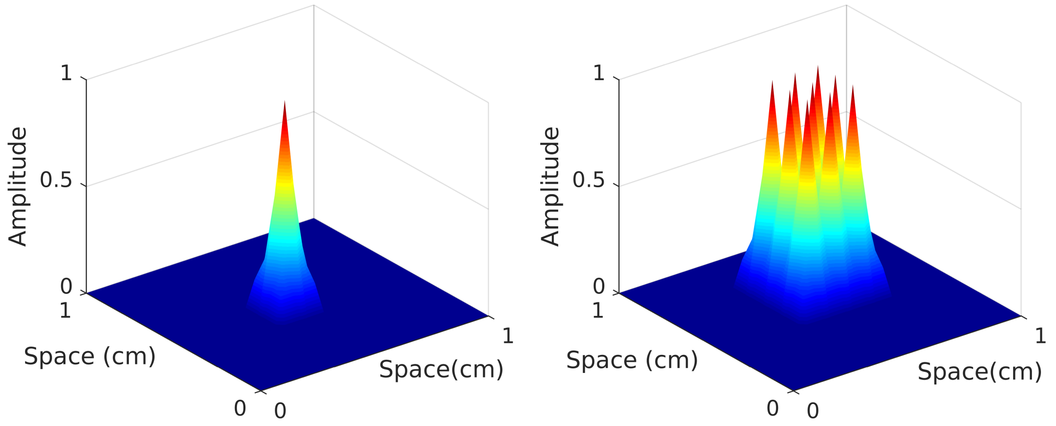

Figure 5.1. **Examples of tensor-field B-spline basis functions, order of 2.** (a) A single b-spline function to estimate the stimulus variables around the detected sensor. (b) Overlapping B-spline functions to estimate the stimulus variables around the detected sensors, illustrating the interpolation property.

where the $\tilde{\mathbf{x}}_k$ is the augmented state vector comprises of the stimulii variables $[\mathbf{x}_k, \mathbf{z}_k]^\top$.

Since the sensors are located at sparse locations in the sensor field, the linear combination of basis functions $\mathbf{B}_k$ are used to smoothly approximate the stimulus function. The basis functions themselves are centered at the sensor locations, and interpolate the stimulus variables for accurate estimation of transmembrane voltage v_k and gating variable h_k in the neighbourhood locations. The properties associated with the basis functions are similar to that in Section 4.3.2, including the local support and interpolation properties. Here, tensor-field B-spline basis functions were constructed, with order of 2 [70]. Examples of the resulting tensor product B-spline functions are shown in Figure 5.1. It is noteworthy that the inclusion of basis function method enables to reduce the number of additional state variables added to the augmented state vector, especially in the high-dimensional systems.

5.3.3 Fixed Lag URTS Smoother

As described in Section 2.3.2 fixed lag smoother enables to obtain the smoothed state estimates at $k - k_\tau$, given the measurements and filtered estimates upto the current time instant k. Here, the fixed-lag URTS smoothing is employed by modifying the fixed interval URTS smoothing method presented in Algorithm 5.1. This also implies that the smoothing step is embedded into filtering step instead of forward and backward recursions as a separate process [145**?**]. The smoother estimates at current time instant k are first initialised using the filtered estimates as $\hat{\mathbf{x}}_k^s = \hat{\mathbf{x}}_k^f$ and error covariance matrix $\mathbf{P}_k^s = \mathbf{P}_k^f$. This is followed by performing the backward recursions given $\{k-1, k-2, ..., k-k_\tau\}$ as same in Algorithm 5.1-Backward iterations.

5.3.4 The Proposed Algorithm

The detection and estimation algorithm tailored for the high-dimensional systems is presented in this section. It should be noted that the basic structure of the proposed method is similar to Algorithm 4.1. However, it is restated in Algorithm 5.1 along with the further changes for completeness. It can be seen that the detection and followed by the reduced-rank UKF state estimation. In order to obtain a computationally efficient smoothing algorithm for high dimensional systems, a pragmatic approach is to regulate the implementation of smoothing method to limited time frames. For instance, more accurate estimates of state variables are essential followed by the stimulus detection for a fixed length, where the filtered estimates can be considered as optimal afterwards. This approximation is significant to obtain a computationally efficient combined detection-estimation algorithm. Thus the fixed lag URTS smoother algorithm is employed only for a fixed time length after the stimuli are detected. The filtered estimates are considered as optimal state estimates at other time instants.

Algorithm 5.1: *The proposed detection-estimation algorithm using Reduced-order Unscented Rauch-Tung Stribel Smoother.*

Forward Iteration

---

1. Initialise forward states $\hat{\mathbf{x}}_0^f$ and covariance matrix $\mathbf{P}_0^f$.

2. The recursive estimation procedure for time instants, $k \in \{0, 1, ..., T-1\}$:

Prediction using nominal state-space model :

(a) Perform truncated singular value decomposition of the $\mathbf{P}_k^f$ using (5.7) and reduced rank of n_r.

(b) Form the sigma points χ_k for $\hat{\mathbf{x}}_k^f$ as

$$\begin{aligned}\overline{\chi}_{k,j} &= \hat{\mathbf{x}}_k^f,\\ \overline{\chi}_{k,j} &= \hat{\mathbf{x}}_k^f + \sqrt{(n_r + \overline{\lambda})}\,\sigma_{k,j}\mathbf{u}_{k,j}, \quad j = 1, ..., n_r \\ \overline{\chi}_{k,j} &= \hat{\mathbf{x}}_k^f - \sqrt{(n_r + \overline{\lambda}}\,\sigma_{k,j}\mathbf{u}_{k,j} \quad j = n_r + 1, ..., 2n_r\end{aligned} \tag{5.18}$$

where $\overline{\lambda}$ is given by $\alpha^2(n_r + \kappa) - n_r$ with $\kappa = 3 - n_r$.

(c) Propagate the sigma-points through the nominal state evolution equation

$$\hat{\chi}_{k+1,j}^{f-} = \mathbf{f}(\bar{\chi}_k). \tag{5.19}$$

(d) Compute the predicted states $\hat{\mathbf{x}}_{k+1}^{f-}$ and covariance matrix $\mathbf{P}_{k+1}^{f-}$ as follows

$$\hat{\mathbf{x}}_{k+1}^{f-} = \sum_{j=0}^{2n_r} \overline{W}_j^{(m)} \hat{\chi}_{k+1,j}^{f-}, \tag{5.20}$$

$$\mathbf{P}_{k+1}^{f-} = \sum_{j=0}^{2n_r} \overline{W}_j^{(c)} (\hat{\chi}_{k+1,j}^{f-} - \hat{\mathbf{x}}_{k+1}^{f-})(\hat{\chi}_{k+1,j}^{f-} - \hat{\mathbf{x}}_{k+1}^{f-})^\top + \Sigma_x, \tag{5.21}$$

where $\overline{W}_i^{(m)}$ and $\overline{W}_i^{(c)}$ are the constant mean and covariance weights defined in (5.12), (5.13) and (5.14).

Detection using nominal state-space model:

(a) Form the innovation sequences and the covariance of innovation sequences

$$\mathbf{e}_{k+1}^{f-} = \mathbf{y}_{k+1} - \mathbf{y}_{k+1}^{f-}, \tag{5.22}$$

where $\mathbf{y}_{k+1}^{f-}$ is computed using (4.18)

$$\mathbf{Q}_{k+1}^{f-} = \mathbf{C}\mathbf{P}_{k+1}^{f-}\mathbf{C}^\top + \boldsymbol{\Sigma}_y. \tag{5.23}$$

(b) Calculate the distance measure, which is negative likelihood measure tailored to single sensor measurements

$$L_{n,k+1}^{-} = \frac{1}{2}\left[\ln(2\pi) + \ln(q_{k+1}) + \frac{1}{2}\frac{(e_{k+1}^2)}{q_{k+1}}\right]. \tag{5.24}$$

(c) Perform the detection scheme as

$$\bar{\mathbf{n}}_{k+1} := \left\{ \bar{s}_n : L^{-}_{n,k+1} > \varpi \right\}, \tag{5.25}$$

where ϖ is the threshold value.

if stimulus sensors are not detected:

Correction using the nominal state-space model:

(a) Compute the Kalman gain, the corrected state estimates and covariance matrix

$$\mathbf{K}_{k+1} = \mathbf{P}^{f-}_{k+1}\mathbf{C}^{\top}(\mathbf{C}\mathbf{P}^{f-}_{k+1}\mathbf{C}^{\top}_{k+1} + \mathbf{\Sigma}_y)^{-1}, \tag{5.26}$$

$$\hat{\mathbf{x}}^{f}_{k+1} = \hat{\mathbf{x}}^{f-}_{k+1} + \mathbf{K}_{k+1}\mathbf{e}^{f-}_{k+1}, \tag{5.27}$$

$$\mathbf{P}^{f}_{k+1} = \mathbf{P}^{f-}_{k+1} - \mathbf{P}^{f-}_{k+1}\mathbf{C}(\mathbf{C}\mathbf{P}^{f-}_{k+1}\mathbf{C}^{\top} + \mathbf{\Sigma}_y)^{-1}\mathbf{C}. \tag{5.28}$$

else

Prediction using augmented state-space model:

(a) Form the augmented state vector $\hat{\widetilde{\mathbf{x}}}^{f}_{k} = [\hat{\mathbf{x}}^{f} \;\; \hat{\mathbf{z}}^{f}_{k}]^{\top}$, where stimulus state variables are computed using (4.32), and covariance matrix $\widetilde{\mathbf{P}}^{f}_{k}$ of structure in (4.35) are computed using (4.36), (4.37) and (4.38).

(b) Compute the sigma points $\bar{\chi}'_k$ using (4.39) for the augmented state vector $\hat{\widetilde{\mathbf{x}}}^{f}_{k}$, using the truncated SVD results of $\widetilde{\bar{\mathbf{P}}}^{f}_{k}$ with an order n_r, $\hat{\widetilde{\mathbf{x}}}^{f}_{k}$, λ' and n'_x, respectively.

(c) Calculate the unscented transform values $\hat{\widetilde{\chi}}^{f-}_{k+1}$ by propagating the sigma points through the augmented non-linear state evolution equation $\widetilde{\mathbf{f}}(\widetilde{\chi}_k)$. The nonlinear state evolution equation is given in (5.16), which includes the linear tensor field B-spline functions $\mathbf{B}_k$ at the detected sensor locations.

(d) Compute the predicted states $\hat{\widetilde{\mathbf{x}}}^{f-}_{k+1}$ and covariance matrix $\widetilde{\mathbf{P}}^{f-}_{k+1}$

$$\hat{\widetilde{\mathbf{x}}}^{f-}_{k+1} = \sum_{j=0}^{2n_r} \overline{W}^{(m)}_j \bar{\chi}^{-}_{k+1,j}, \tag{5.29}$$

$$\widetilde{\mathbf{P}}^{f-}_{k+1} = \sum_{j=0}^{2n_r} \overline{W}^{(c)}_j (\hat{\widetilde{\chi}}^{f-}_{k+1,j} - \hat{\widetilde{\mathbf{x}}}^{f-}_{k+1})(\hat{\widetilde{\chi}}^{f-}_{k+1,j} - \hat{\widetilde{\mathbf{x}}}^{f-}_{k+1})^{\top} + \Sigma_{\widetilde{x}}. \tag{5.30}$$

(e) Compute the corrected state estimates and covariance matrix as

$$\widetilde{\mathbf{K}}_{k+1} = \bar{\mathbf{P}}^{f-}_{k+1}\widetilde{\mathbf{C}}^{\top}(\widetilde{\mathbf{C}}\bar{\mathbf{P}}^{f-}_{k+1}\widetilde{\mathbf{C}}^{\top} + \mathbf{\Sigma}_y)^{-1}, \tag{5.31}$$

$$\tilde{\hat{\mathbf{x}}}^{f}_{k+1} = \tilde{\hat{\mathbf{x}}}^{f-}_{k+1} + \widetilde{\mathbf{K}}_{k+1}(\mathbf{y}_{k+1} - \widetilde{\mathbf{C}}\tilde{\hat{\mathbf{x}}}^{f-}_{k+1}), \tag{5.32}$$

$$\widetilde{\mathbf{P}}^{f}_{k+1} = \widetilde{\mathbf{P}}^{f-}_{k+1} - \widetilde{\mathbf{P}}^{f-}_{k+1}\widetilde{\mathbf{C}}(\widetilde{\mathbf{C}}\widetilde{\mathbf{P}}^{f-}_{k+1}\widetilde{\mathbf{C}}^{\top} + \mathbf{\Sigma}_y)^{-1}\widetilde{\mathbf{C}}. \tag{5.33}$$

end

Backward Iteration

Perform backward iterations with a fixed lag of k_τ, for a time sample length T_s after stimulus locations are detected.

1. Initialise backward states and covariances using the filter estimates $\hat{\mathbf{x}}^s_k = \hat{\mathbf{x}}^f_k$ and $\mathbf{P}^s_k = \mathbf{P}^f_k$.
2. Recursive backward iteration to estimate the smoothed state estimates $\hat{\mathbf{x}}^s_k$ for time instants $k \in \{k-1, ..., k-k_\tau\}$:

if stimulus sensors are not detected in the filtering step:

Prediction using nominal state-space model:

(a) Form the sigma points of the smoother $\chi^s_{k,j}$ using filtered state and covariance estimates using the filtered values of σ_k and $\mathbf{u}_k$

$$\begin{aligned}\overline{\boldsymbol{\chi}}^s_{k,j} &= \hat{\mathbf{x}}^f_k,\\ \overline{\boldsymbol{\chi}}^s_{k,j} &= \hat{\mathbf{x}}^f_k + \sqrt{(n_r + \overline{\lambda})}\ \sigma_{k,j}\mathbf{u}_{k,j}, \quad j = 1, ..., n_r\\ \overline{\boldsymbol{\chi}}^s_{k,j} &= \hat{\mathbf{x}}^f_k - \sqrt{(n_r + \overline{\lambda}}\ \sigma_{k,j}\mathbf{u}_{k,j} \quad j = n_r + 1, ..., 2n_r\end{aligned} \tag{5.34}$$

where $\overline{\lambda}$ is given by $\alpha^2(n_r + \kappa) - n_r$ with $\kappa = 3 - n_r$.

(b) Propagate the sigma points through the nonlinear state evolution equation

$$\hat{\boldsymbol{\chi}}^{s-}_{k+1,j} = \mathbf{f}(\bar{\boldsymbol{\chi}}^s_k). \tag{5.35}$$

(c) Compute the estimates of the predicted states, $\hat{\mathbf{x}}^{s-}_{k+1}$ and covariance matrix $\mathbf{P}^{s-}_{k+1}$, and the cross-covariance $\mathbf{S}_{k+1}$ as

$$\hat{\mathbf{x}}^{s-}_{k+1} = \sum_{j=0}^{2n_r} \overline{W}^{(m)}_j \hat{\boldsymbol{\chi}}^{s-}_{k+1,j}, \tag{5.36}$$

$$\mathbf{P}^{s-}_{k+1} = \sum_{j=0}^{2n_r} \overline{W}_j^{(c)} (\hat{\mathcal{X}}^{s-}_{k+1,j} - \hat{\mathbf{x}}^{s-}_{k+1})(\hat{\mathcal{X}}^{s-}_{k+1,j} - \hat{\mathbf{x}}^{s-}_{k+1})^{\top} + \Sigma_x, \tag{5.37}$$

$$\mathbf{S}_{k+1} = \sum_{j=0}^{2n_r} \overline{W}_j^{(c)} (\chi^{s}_{k,j} - \hat{\mathbf{x}}^{s-}_{t+1})(\hat{\mathcal{X}}^{s-}_{k+1,j} - \hat{\mathbf{x}}^{s-}_{k+1})^{\top}, \tag{5.38}$$

Correction using nominal state-space model:

(a) The state estimates and covariance matrix are then corrected upon the measurements by calculating the Smoother gain

$$\mathbf{D}_k = \mathbf{S}_{k+1}(\mathbf{P}^{s-}_{k+1})^{-1}. \tag{5.39}$$

(b) The resulting smoothed state $\hat{\mathbf{x}}^s_k$ is calculated as

$$\hat{\mathbf{x}}^s_k = \hat{\mathbf{x}}^f_k + \mathbf{D}_k(\hat{\mathbf{x}}^s_{k+1} - \mathbf{x}^{s-}_{t+1}). \tag{5.40}$$

(c) The smoothed covariance $\mathbf{P}^s_k$ is then given by

$$\mathbf{P}^s_k = \mathbf{P}^f_k + \mathbf{D}_k(\mathbf{P}^s_{k+1} - \mathbf{P}^{s-}_{k+1})\mathbf{D}_k^{\top}. \tag{5.41}$$

Note: The storage of filtered covariance matrix for high-dimensional may result in high computational load. When using higher fixed-lag order, $\mathbf{P}^f_k$ can be approximated by reconstructed covariance matrix,

$$\overline{\mathbf{P}}^f_k = \mathbf{U}_{k,n_r} \bar{\boldsymbol{\pi}}_k \mathbf{U}^{\top}_{k,n_r}. \tag{5.42}$$

where $\mathbf{U}_{k,n_r}$ and $\bar{\boldsymbol{\pi}}_k$ consists of stored Eigen vectors and values, respectively.

else

Prediction using augmented state-space model:

(a) Form the sigma points $\widetilde{\chi}_k$ using (4.39) with $\hat{\tilde{\mathbf{x}}}^f_k$, σ_k, $\mathbf{u}_k$ and n_r.

(b) Calculate the unscented transform values $\hat{\tilde{\mathcal{X}}}^{s-}_{k+1}$ by propagating the sigma points through the augmented non-linear state evolution equation $\widetilde{\mathbf{f}}(\widetilde{\chi}_k)$, with the tensor field B-spline functions $\mathbf{B}_k$ at the detected sensor locations.

(c) Compute the predicted states $\hat{\tilde{\mathbf{x}}}^{s-}_{k+1}$ and covariance matrix $\widetilde{\mathbf{P}}^{-}_{k+1}$

$$\hat{\tilde{\mathbf{x}}}^{s-}_{k+1} = \sum_{j=0}^{2n_r} \overline{W}_j^{(m)} \bar{\mathcal{X}}^{s-}_{k+1,j}, \tag{5.43}$$

$$\widetilde{\mathbf{P}}^{s-}_{k+1} = \sum_{j=0}^{2n_r} \overline{W}^{(c)}_j (\bar{\chi}^{s-}_{k+1,j} - \widetilde{\hat{\mathbf{x}}}^{s-}_{k+1})(\bar{\chi}^{s-}_{k+1,j} - \widetilde{\hat{\mathbf{x}}}^{s-}_{k+1})^\top + \Sigma_{\widetilde{x}}, \tag{5.44}$$

$$\widetilde{\mathbf{S}}_{k+1} = \sum_{j=0}^{2n_r} \overline{W}^{(c)}_j (\widetilde{\chi}^{s}_{k,j} - \widetilde{\hat{\mathbf{x}}}^{s-}_{k+1})(\hat{\chi}^{s-}_{k+1,j} - \widetilde{\hat{\mathbf{x}}}^{s-}_{k+1})^\top. \tag{5.45}$$

(d) Form the augmented state vector $\widetilde{\hat{\mathbf{x}}}^{s}_{k+1} = [\hat{\mathbf{x}}^{s}_{k+1} \;\; \hat{\mathbf{z}}^{s}_{k+1}]^\top$, where stimulus state variables $\hat{\mathbf{z}}^{s}_{k+1}$ and covariance matrix $\widetilde{\mathbf{P}}^{s}_{k+1}$ are re-evaluated to include the dynamic structure in the augmented form.

Correction using augmented state-space model:

(e) Compute the corrected state estimates $\widetilde{\hat{\mathbf{x}}}^{s}_{k}$ and covariance matrix $\widetilde{\mathbf{P}}^{s}_{k}$ as

$$\widetilde{\mathbf{D}}_k = \widetilde{\mathbf{S}}_{k+1}(\widetilde{\mathbf{P}}^{s-}_{k+1})^{-1}, \tag{5.46}$$

$$\widetilde{\hat{\mathbf{x}}}^{s}_{k} = \widetilde{\hat{\mathbf{x}}}^{f}_{k} + \widetilde{\mathbf{D}}_k(\widetilde{\hat{\mathbf{x}}}^{s}_{k+1} - \widetilde{\hat{\mathbf{x}}}^{s-}_{k+1}), \tag{5.47}$$

$$\widetilde{\mathbf{P}}^{s}_{k} = \tilde{\mathbf{P}}^{f}_{k} + \widetilde{\mathbf{D}}_k(\widetilde{\mathbf{P}}^{s}_{k+1} - \widetilde{\mathbf{P}}^{s-}_{k+1})\widetilde{\mathbf{D}}^\top_k. \tag{5.48}$$

end

5.4 Data Generation

The performance of algorithm is demonstrated using the complex spiral re-entrant activation patterns, which involves both normal (plane wave) and re-entrant propagation of cardiac electrical activity. The detailed descriptions of the simulation setup and procedures of activation patterns generation are given in Section 3.2.2. Briefly, data was generated in a two-dimensional tissue slab of 1 × 1 cm using the monodomain tissue equations with modified Mitchell-Schaeffer ionic model. Similar to the one-dimensional simulations, the unipolar electrograms were then calculated by placing the sensors along a at distance of 1 mm from the tissue field. Simulation was performed for total duration of 1000 ms, solved using explicit finite differences methods with no-flux boundary conditions. The spiral re-entry was simulated by applying the first stimulus (S1) at the left edge of the tissue field, s_x = 0.025 cm to s_x = 0.075 cm in tissue field at time instants k = 0.05 ms, followed by second stimulus (S2) at the left-bottom edge of the slab at k = 324 ms (see Figure 5.2(A). The stochasticity was added into the simulation using the state disturbance variances $\sigma_v^2 = 10^{-4}$ and $\sigma_h^2 = 10^{-5}$. For the results shown in Section 5.5, observation noise variance was assigned to $\sigma_y^2 = 10^{-5}$, where the SNR value was obtained as 42.61 dB using (4.78). The tissue field was descritised to a gridded domain with dimension of 41 × 41 while sensors are placed in a gridded domain of 10 × 10. An example of the electrogram is shown in Figure 5.2(B). The electrophysiology parameters used for data generation are shown in Table3.1 unless explicitly stated. The resulting spatiotemporal patterns of transmembrane voltage in tissue field are shown in Figure 5.6(a). The figure illustrates that the planar wave resulting from normal activation was disrupted and formed into a spiral re-entry, that was persistent throughout the simulation period.

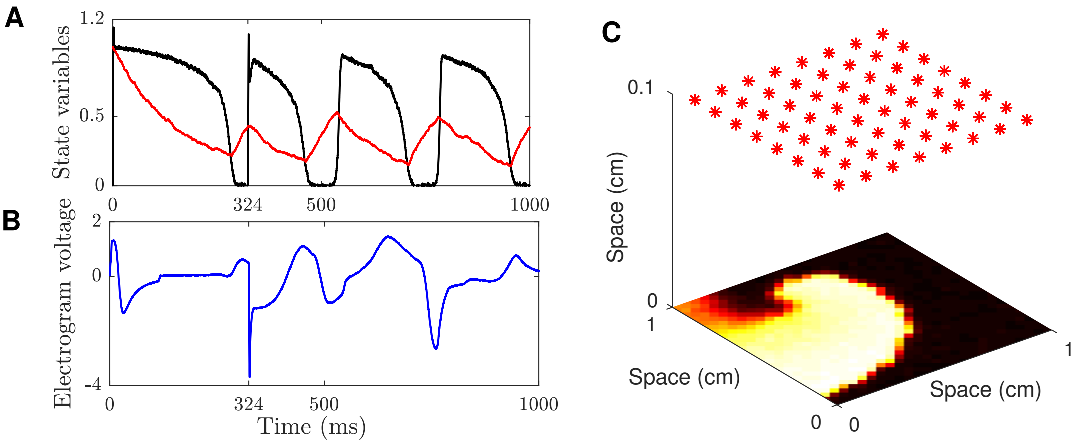

Figure 5.2. Examples of spiral re-entrant data in two-dimensional cable field. The subfigures are : (A) State variables at spatial index l = 43. (B) Electrogram measurements with SNR = 42.61 dB. (C) Snapshot of transmembrane voltage patterns at 500 ms, where the sensors as shown in red asterisks. State variables are transmembrane voltage (—), gating variable (—).

5.5 Results and Discussion

In this section, results of the proposed detection-estimation algorithm to the simulated spiral wave data is presented.

The combined detection-state estimation method presented in Algorithm 5.1 was employed to estimate the state variables from the electrogram measurements. The procedures used for the estimation is similar to that in Section 4.5. It is restated in this section for completeness. The initial state vector, $\mathbf{v}_0$ and $\mathbf{h}_0$, were drawn from the normal distributions of $\mathcal{N}\left(\mathbf{0}, 10^{-6}\mathbf{I}\right)$ and $\mathcal{N}\left(\mathbf{1}, 10^{-6}\mathbf{I}\right)$, where the mean values are selected as the resting conditions given in [38, 108]. It was assumed that the disturbance covariances were known to the estimator. By using the simulation setup presented in previous section, at every time instant, the to-

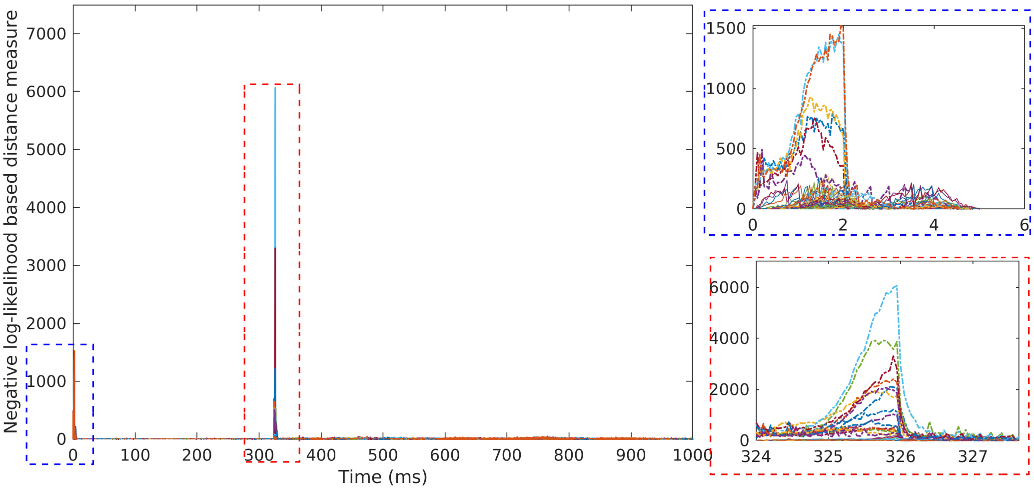

Figure 5.3. Negative log-likelihood measure for spiral activation patterns in two-dimensional cable field. The distance measure from first 50 sensors are shown. The stimulus intervals are illustrated within boxes for clarity, where the dashed lines denote the sensors correspond to stimulus locations.

tal number of states variables (n_x) to be estimated from the nominal state-space model is 3362 ($n_v = n_h = 1681$). The total simulation interval is 1000 ms, which results in the total number of time instants (n_t) with $\Delta_t = 0.05$ ms to be 20001. The algorithm was implemented on MATLAB R2019a, installed on a computer with Intel Xeon (R) CPU E5-2623 v3@ 3.00 GHz and 32 GB RAM.

In order to implement the algorithm presented in Algorithm 5.1, truncation index (n_r), threshold value (ϖ) and a fixed-lag order (k_τ) need to be assigned. However, computational complexities caused from the large number of state variables, and the storage and manipulation of resulting high-dimensional covariance matrices, restrict the implementation of rigorous analysis to determine the optimal number of n_r, ϖ and k_τ. A pragmatic approach is to use a truncation index with considerable level of computational complexity and estimation accuracy. In the LETKF based cardiac-field estimation algorithm presented in [69], an ensemble

Table 5.1. Averaged detection performance metrics

Threshold	TPR (S1)	TPR (S2)	FPR
100	0.995	0.946	0.076
150	0.990	0.941	0.059
180	0.977	0.923	0.056
200	0.946	0.891	0.049

size of 20 was used to estimate the state variables in three-dimensional scroll-waves. This study has also shown that the ensemble sizes of 10 and 20 yield a similar result, where the latter value was selected in estimation for extra dimensionality. In order to determine a suitable threshold value, the truncation index number was assigned to 10 in the initial analysis. Subsequently, the detection performance metrics detailed in Section 4.3.4 were then computed over a selected range of threshold values, in a single realisation of the simulated data. Contrary to the estimation of one-dimensional cardiac field, the detection metrics were computed in two-dimensional tissue field at every time instant, by comparing with the ground truth. The averaged detection rates during the first and second stimulus intervals (over number of time instants in each interval) and averaged false positive rate (over total number of false positives) are shown in Table 5.1 respectively. Based on this analysis, the threshold value for detection scheme was set to 180, as it yields higher detection rate with minimum false alarm rate. The distance measure calculated using the nominal state-space model is shown in Figure 5.3, which illustrates a clear distinction of the model uncertainty between the sensors, nearby the stimulus and non-stimulus locations. The results show that the estimation of stimulus variable should be incorporated, and also illustrate that a threshold value can be selected across a range of values.

Table 5.2. Averaged computational complexity measure expressed in seconds

Truncation index (n_r)	Forward and backward recursions (Stimulus detected conditions) (s)	Forward iterations (Normal conditions) (s)
500	241.4	196.6
30	28.5	4.37
20	28.2	2.80
10	28.0	2.20

In order to further validate the effectiveness of the selected truncation index number, performance metrics were computed over a range of values with the threshold value of 180. Firstly, the computational complexities during the normal and stimulus time intervals are calculated as the average time of iterations in a first 200 time points, where total samples for estimation was 20001. As demonstrated in Section 5.3.4, computational complexity was further reduced by tailoring the implementation of fixed lag backward iterations. For this, fixed lag smoother with a lag of 2 was employed for a 100 samples time-frame, following the the presence of stimulus locations have been detected. The result from this analysis is summarised in Table 5.2. Although computational complexity increases with the

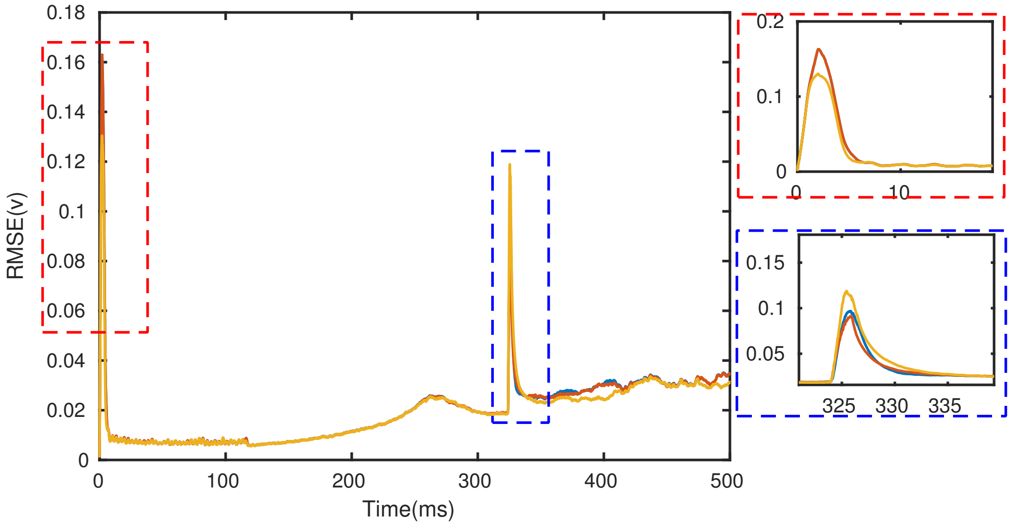

Figure 5.4. RMSE measure calculated for different values of reduced-rank values. $n_r = 10$ (—), $n_r = 20$ (—), $n_r = 30$ (—).

truncation index, time complexity measure for n_r of 10 and 20 produce similar results. Secondly, the estimation accuracy was analysed for a set of n_r values, by computing the RMSE measure between the actual and estimated field of transmembrane voltage. The results from this analysis is shown in Figure 5.4, illustrate that accuracy measure are comparable from the three n_r values. Hence, this analysis demonstrates that the choice of $n_r = 10$ provide acceptable level of computational complexity and estimation accuracy, where estimation results are explained in detail below.

The threshold value of 180 and truncation index of 10 were then selected for the detection and state estimation, respectively. Algorithm 5.1 was implemented to detect the stimulus locations and followed by estimating the state variables, which are transmembrane voltage, gating variable and stimulus variable. The true and estimated patterns of transmembrane voltage and gating variables at selected time instants are shown in Figure 5.5, while the evolutions of actual and estimated state variables at $l = 84, 85, 86$ are shown in Figure 5.6. Both results show that the proposed method can capture the underlying tissue dynamics, by accurately estimating the state variables from the electrogram measurements. However, differences in the actual and estimated patterns are observed along the trajectory of the spiral wave as shown in Figure 5.5B-(c). Recall, the simulated data is based on the mMS model where the estimation was employed using the proposed continuous version of mMs model, with a slope value of 25 . Therefore, the errors along the trajectory may be contributed from the sigmoid approximation of the gating

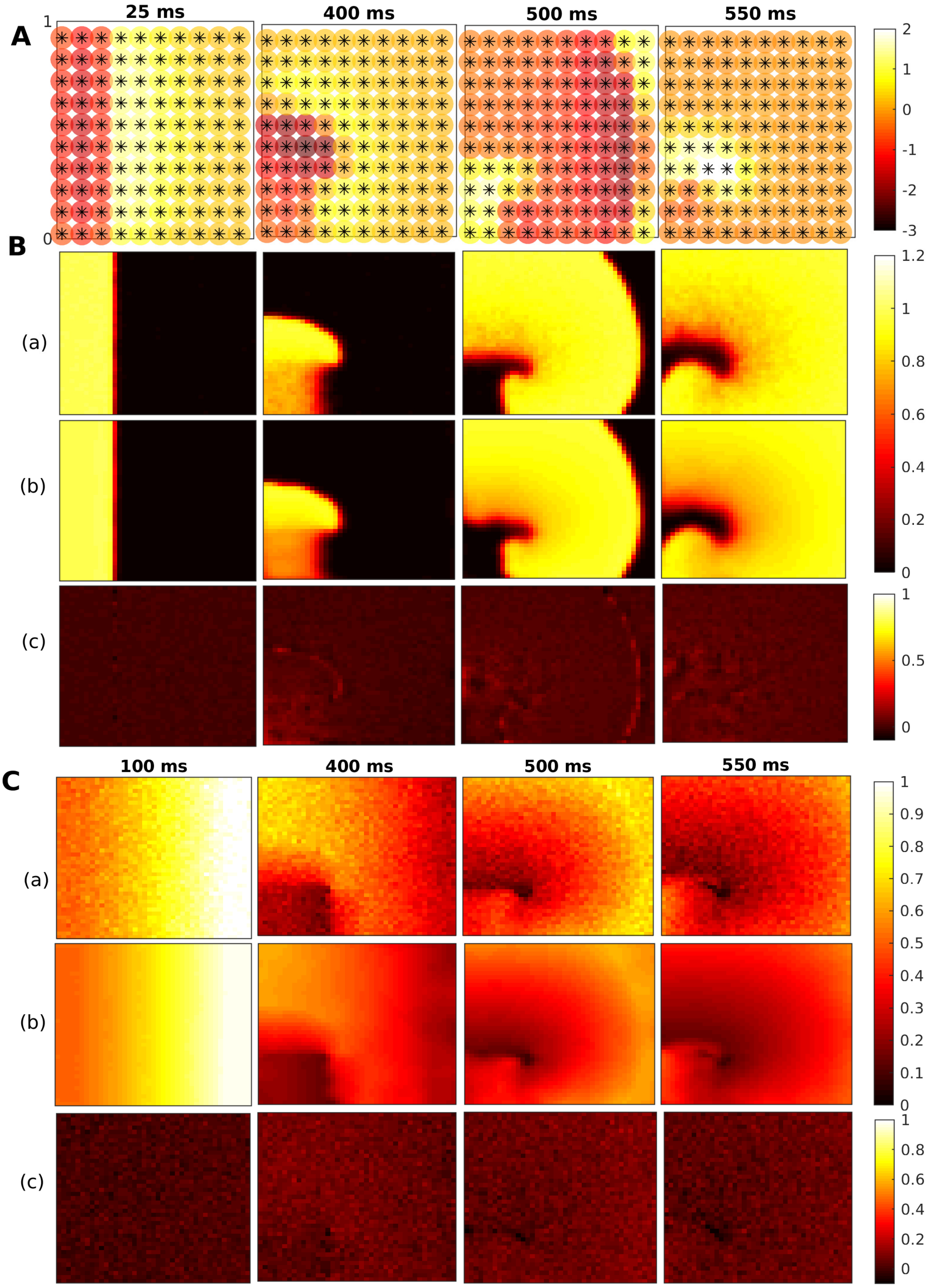

Figure 5.5. Estimation results of state variables during spiral re-entry in two-dimensional tissue field. (A) Electrogram measurements; Here, the electrogram potential at a sensor is shown in coloured circles, while the asterisks shows the sensor location. (B) Transmembrane voltage. (C) Gating variable. The sub-figures in (A) and (B) are: (a) Actual pattern of state variable. (b) Estimated pattern of state variable. (c) Difference in the actual and estimated patterns.

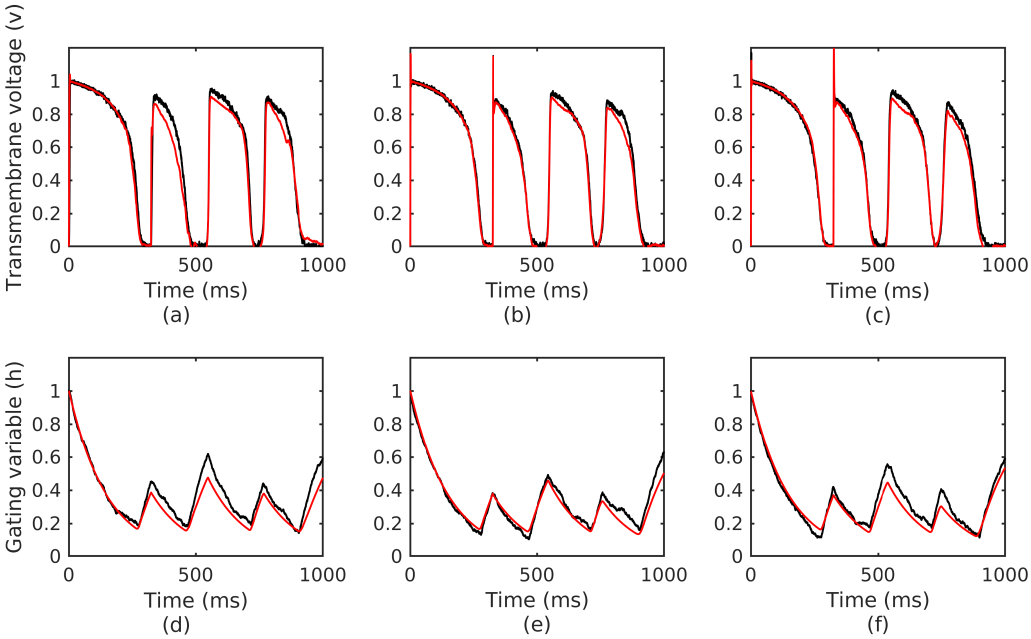

Figure 5.6. The state estimation results for re-entrant activation patterns. (a-c) Transmembrane voltage. (d-f) Gating variable. Actual signal (—), estimated signal(—).

variable using a smaller value of 25.

The state estimation results of transmembrane voltage during the S1 and S2 stimulus intervals are shown in Figure 5.7. The errors shown in both Figure 5.7 A and B -(c) indicate that the proposed method allows to improve the estimates of the transmembrane voltage across the stimulus regime, by interpolating the stimulus variables between the detected sensor locations. However, it also introduced error along the edges for this particular stimulus configurations as shown in Figure 5.7 A and B - (c).

The results can be further explained as follows: At every time instant during stimulus intervals, the detection scheme returned the sensors with distance measure above the pre-defined threshold value. State estimation was then employed using the augmented state-space model, with additional stimulus states ($\mathbf{z}_k$) at detected sensors locations and the corresponding basis functions ($\mathbf{B}_k$) centered at the stimulus locations. For example, the actual pattern of the stimulus variables at a particular time instant in S1 and S2 intervals are shown in Figure 5.8A-(a) and Figure 5.8B-(a), respectively. In this figure, red asterisks denote the sensor configurations, while the black circles denote the sensor locations returned by the detection-scheme. Based on the results from the detection-scheme, a set of linear tensor field B-spline functions are then constructed, centered at the detected sen-

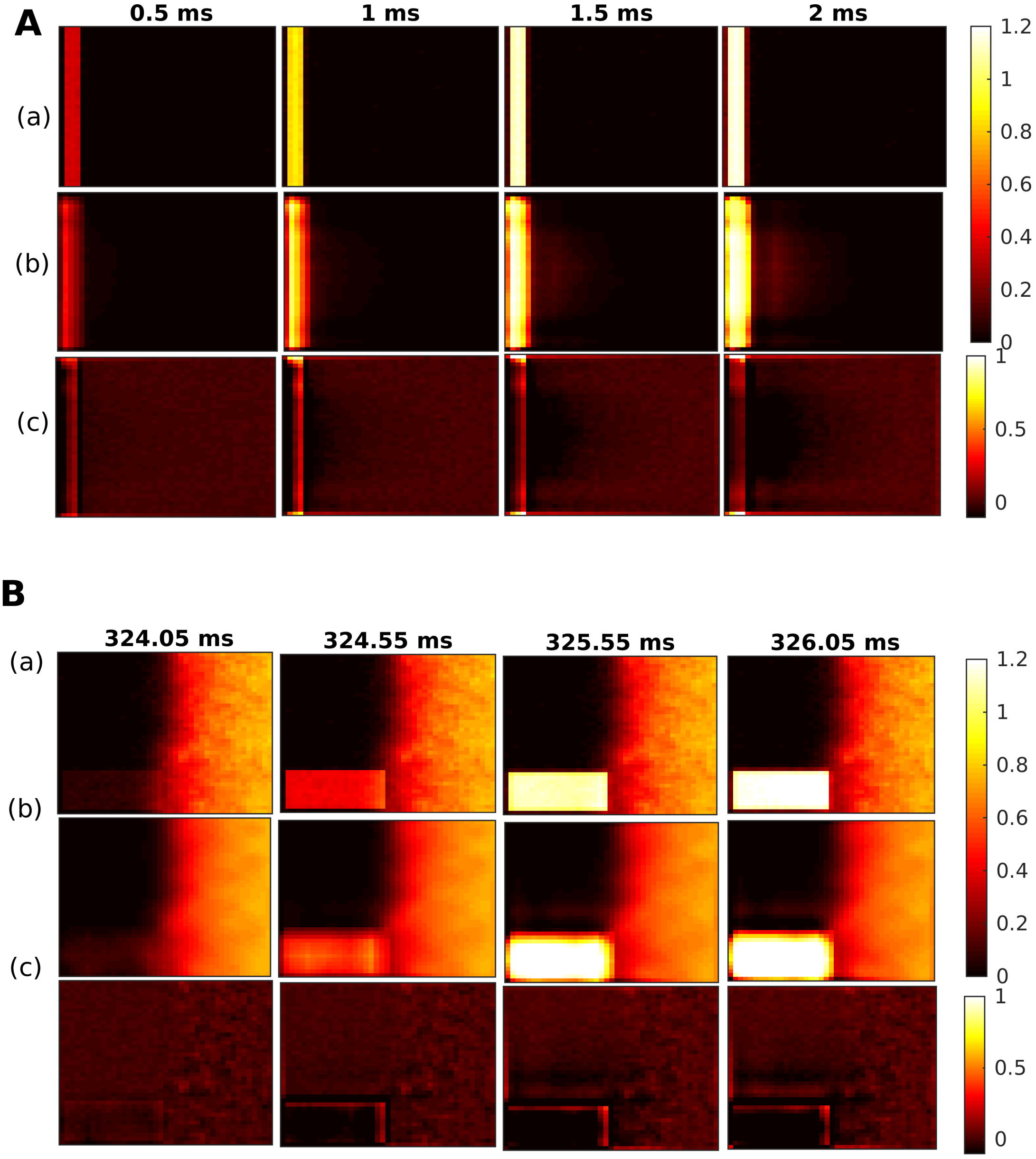

Figure 5.7. Estimation results of transmembrane voltage during stimulus intervals of spiral re-entry in two-dimensional tissue field. (A) First stimulus interval. (B). Second stimuls interval. The sub-figures are shown as: (a) Actual pattern. (b) Estimated pattern. (c) Error between the actual and estimated patterns

sor locations. Examples of basis functions are shown in Figure 5.8A-(b) and Figure 5.8B-(b). The resulting weighted sum of the basis functions during these intervals are shown in Figure 5.8A-(c) and Figure 5.8B-(c). It can be seen that the weighted sum of B-spline functions allow to create a smooth function of stimulus variables between the sensors. However, it causes errors due to the edge effects of basis functions as shown in Figure 5.7(c) and (f).

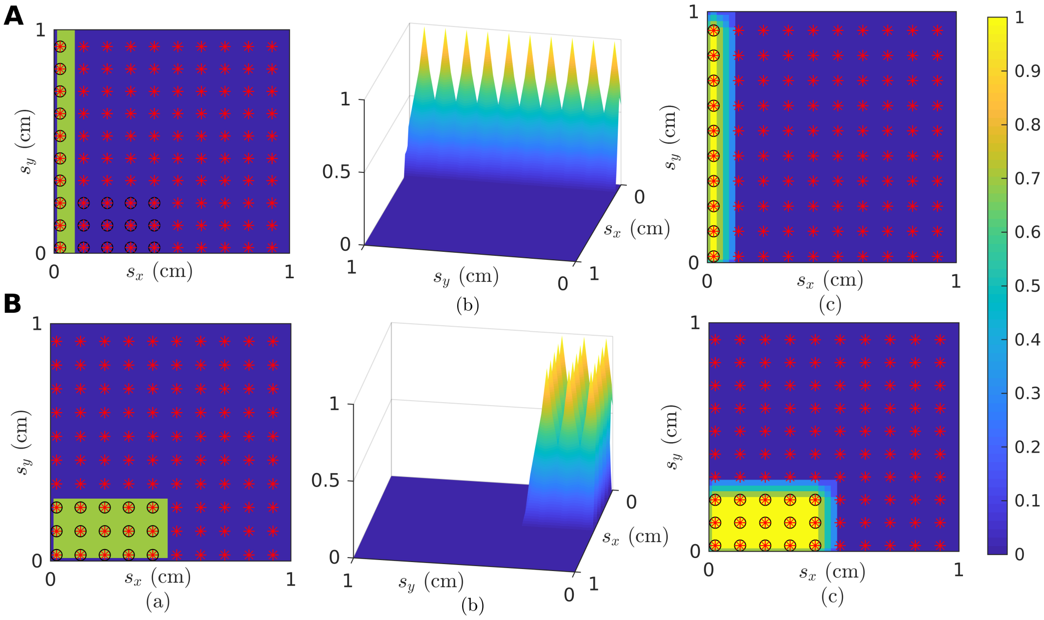

Figure 5.8. **Examples of the decomposition using B-spline functions**. (A) First stimulus interval (S1). (B) Second stimulus interval (S2). The subfigures in each row are: (a)The actual pattern of stimulus variable . (b) The overlapping B-spline functions centered at the sensors, which detected the presence of stimuli. (c) The resulting linear weighting in the tissue field. Here, red asterisks show the sensor locations while black circles show the sensors that detected the presence of stimuli.

In order to further validate the performance of the proposed detection and state estimation algorithm, a Monte-carlo based approach was then employed. For this, 5 realisations of the spiral activation patterns were first generated. The accuracies of the detection and state estimation results were then quantified by computing mean detection metrics and MRMSE measure, respectively. The resulting mean detection metrics are shown in Table 5.3, whereas the MRMSE statistics are shown in Figure 5.9, along with 95% confidence interval. Although the estimation algorithm can capture the tissue dynamics, state estimation error is observed during stimulus intervals in the transmembrane voltage estimates. This can be contributed from the edge effects. To investigate the source of error during the stimulus intervals, RMSE measures across the spatial locations were then com-

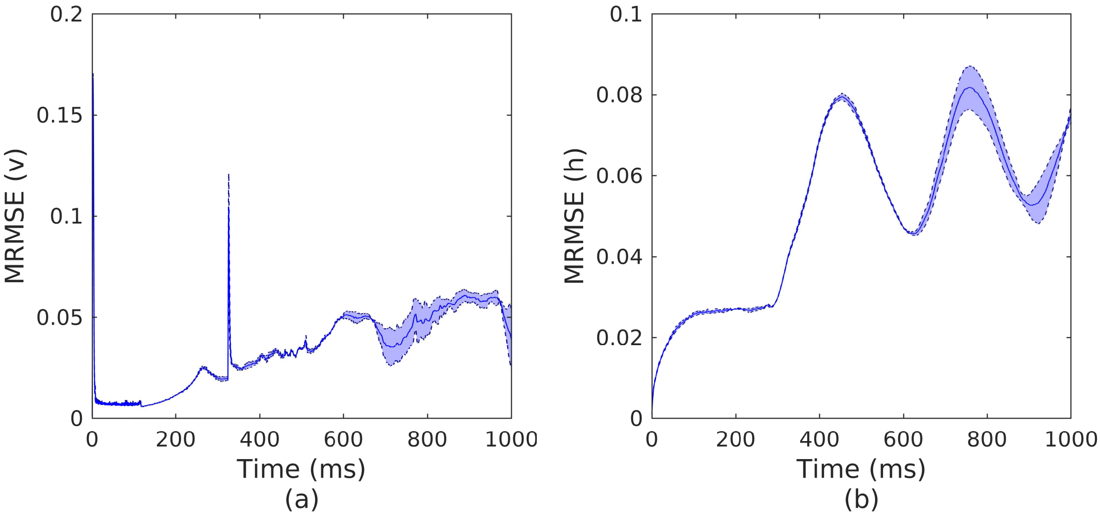

Figure 5.9. **MRMSE measure calculated over 5 realisations of the re-entrant activation patterns**. The mean value is shown in blue colour along with 95% confidence interval (shaded region). (a) Transmembrane voltage. (b) Gating variable.

Table 5.3. **Averaged detection performance metrics over 5 realisations**

Threshold	TPR (S1)	TPR (S2)	FPR
180	0.966	0.919	0.054

puted, by averaging across 1 ms duration of stimulus intervals. The results across the two stimulus intervals are shown in Figure 5.10. By comparing Figure 5.8 with Figure 5.9, the results show that the error in the state-estimation is predominantly contributed from the edges of B-spline functions. On the other hand, the error in gating variable is caused from the employed approximation in the continuous version of mMS model as illustrated in Section 4.5.2.

5.6 Conclusion

This chapter presents a model-based statistical inference framework to reconstruct the tissue dynamics from cardiac electrogram measurements. More specifically, the proposed framework provides a suboptimal solution for detection-estimation problems in high-dimensional state-space models of cardiac electrical activity.

The key contributions of this chapter are the following:

- Similar to the one-dimensional spatial field, finite dimensional stochastic state-space model in the two-dimensional spatial field has been derived

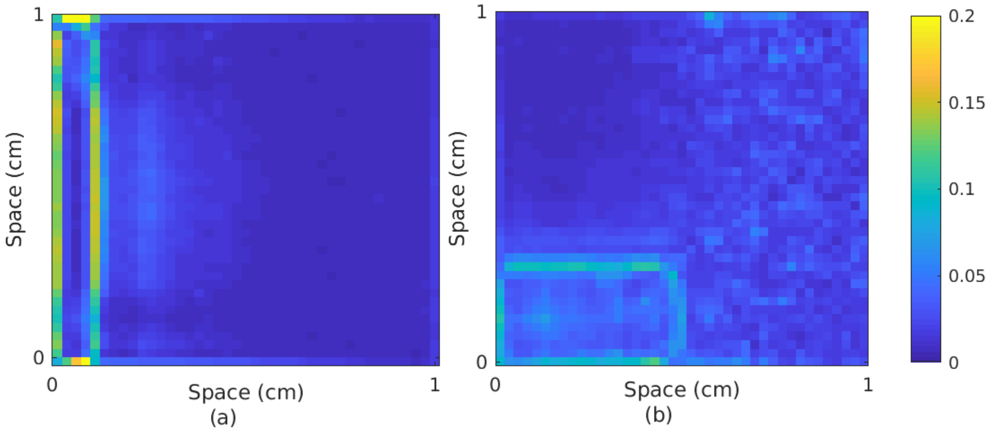

Figure 5.10. **RMSE measure computed across the two-dimensional tissue field**. (a) First stimulus interval (S1). (b) Second stimulus interval (S2).

based on the infinite-dimensional cardiac model.

- Although the proposed detection algorithm follows similar procedures to that in Chapter 4, the state estimation procedure is tailored for the high-dimensional state-space models, by using fixed lag, reduced rank UKF algorithm.
- The performance of the proposed algorithm has been illustrated using the complex spiral wave dynamics, where multiple stimuli initiate the spiral re-entry within the vulnerable window.
- The findings from this chapter illustrate that the proposed algorithm can be used for model-based inference of tissue dynamics from electrogram recordings in the simulation datasets of cardiac field.

Chapter 6

Complex Network Modelling of Spatiotemporal Organisation during Human Ventricular Fibrillation

As detailed in Section 1.2, the second aim of this project is to develop an approach to quantify the level of organisation in spatiotemporal activation patterns of human VF. This chapter presents a complex network modelling approach to quantify the spatiotemporal organisation in the clinical electrograms of VF.

A key tool in the analysis of activation patterns on the surface of the heart during VF has been phase analysis, which can identify both activation wavefronts and the phase singularities around which they rotate [36]. Although the complexity of re-entrant activation patterns can be assessed from the numbers and lifetimes of phase singularities [151], this approach does not allow any underlying connectivity structure to be identified.

The spatial characteristic length based on coherence and correlation functions has been used to quantify the extent of spatial organisation in both animal and human VF [46]. Correlation and coherence functions quantify the degree of functional association between electrical activation waves at different spatial locations in time and frequency domain respectively. These algorithms have shown promise in characterizing the extent of spatial organisation in both atrial and ventricular activation sequences particularly in differentiating between normal sinus rhythm and cardiac arrhythmias [46, 137]. However, quantifying and monitoring the level of organisation during different stages of ischaemic VF in the human heart has not to our knowledge been reported in the literature.

The level of spatial organisation within each episode of VF is quantified by determining patterns of connectivity underlying electrical activation recorded at different spatial locations. In theoretical neuroscience, analysis of cortical connectivity network, structural, functional and effective, has a long and rich history. Structural connectivity is built upon the anatomy of the brain while the functional and effective connectivity are based on analysing neuroimaging data [52, 139]. In functional connectivity networks, network connections are derived based on correlation or coherence between different regions, whereas network connections in effective connectivity are obtained via causal modelling such as Granger causality [59], partial directed coherence (PDC) [134] and more recently model-based frameworks which integrate anatomical information with multi-electrode electrophysiological recordings [9]. Another important approach is graph theory analysis which explores properties of complex networks and has been extensively applied to brain connectivity data [139].

Clustering techniques have been also applied to time series data or its corresponding functional network to group regions with similar functional activities [94]. These techniques can be adopted to study the spatial and temporal activation patterns in the human heart. For example, the effective connectivity network based on the PDC approach has been used to analyse intracardiac signals recorded during atrial fibrillation [134]. However, many of these methods have not yet been applied to human VF, and there is a sufficient volume of interesting results from theoretical neuroscience studies that warrants further investigation in this domain.

Therefore, the overall aim of this chapter is to evaluate techniques to quantify the level of spatial and temporal organisation in electrical activation sequences during human VF. First, a cross-correlation function based method is proposed for quantifying functional association between recordings from each epicardial electrode and hence to compute the global level of spatio-temporal organisation. Second, the spatiotemporal network structure obtained based on cross-correlation coefficients was then exploited to study the organisation of electrical activation sequences as spatio-temporal functional networks. Graph-theoretical measures were then applied to further quantify the properties of network-based representation. To examine and visualise the spatio-temporal patterns of similar functional association over different regions of the epicardial surface, a hierarchical clustering method based on the cross-correlation matrix was also employed. Temporal progressions of the underlying connectivity structures obtained from these methods were then quantified and monitored using a sliding window-based analysis.

The rest of this chapter is organised as follows. Section 6.1 presents the data acquisition techniques and preprocessing steps of epicardial electrograms. Section

6.2 explains the spatiotemporal organisation observed in the VF electrograms. Section 6.3 details the complex network modelling methods. The results are presented and discussed in Section 6.4. Following this, conclusions are provided in Section 6.5.

6.1 Mapping of Epicardial VF Electrograms

In this section, the data acquisition techniques and preprocessing steps of epicardial electrograms are detailed.

6.1.1 Data Acquisition

The clinical recordings used in this chapter are from a previous study of human VF [18], where the patient details and the methods used for data acquisition are covered in detail. The VF electrograms were collected from a group of ten patients (labelled as H055, H057-H060, H062-H066) undergoing routine cardiac surgery. This study was approved by the local hospital ethics committee (REC 01/0130).

Briefly, epicardial unipolar electrograms were recorded using an elasticated sock consisting of 256 electrodes with an electrode spacing of approximately 10 mm (see Figure 6.1 (a)). This sock was placed over the epicardial surface of the ventricles following cannulation for cardiopulmonary bypass (CPB). CPB is a commonly used technique in cardiac surgeries to replace functions of the circulatory and respiratory system. The CPB circuit comprises of pump and oxygenator to act as artificial heart and lungs, which allow to maintain the smooth blood and oxygen circulations in the body [143]. This technique ensures that the data acquisition procedures are conducted in a safe and controlled environment [111]. The unipolar

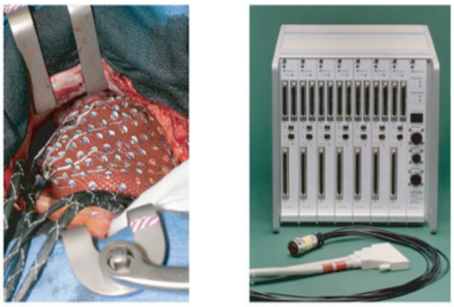
(a) (b)

Figure 6.1. **Materials used for epicardial mapping of VF electrograms.** (a) Elasticated electrode sock. (b) UnEmap system.

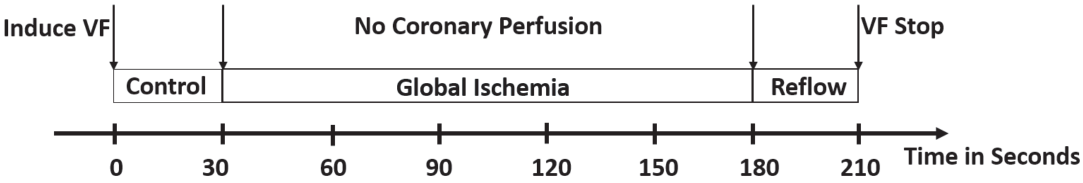

Figure 6.2. Example of experimental procedure used to record the electrograms during the three episodes of VF.

electrograms were collected at a sampling rate of 1 kHz using a UnEmap system (Auckland UniServices Ltd, New Zealand) with the reference electrode placed on the chest retractors (see Figure 6.1 (b)).

Following the institution of CPB, VF was induced by 50 Hz AC burst pacing and the recordings were continuously recorded for a total duration of 3.5 minutes. There are three main episodes in this process along which the electrograms were continuously recorded as shown in Figure 6.2. The first 30 s phase is controlled VF (referred to as control VF), where the coronary perfusion was maintained. Subsequently, aorta was cross-clamped between the coronary sinus and the CPB cannula interrupting the coronary perfusion and induces global myocardial ischaemia. The ischaemic recordings were collected for 150 s (referred to as ischaemic VF). The cross-clamp was then removed to enable coronary reperfusion (referred to as reflow VF), and a further 30 s of VF electrograms were recorded. Finally, ventricular defibrillation was applied after removing the electrode sock.

6.1.2 Electrogram Preprocessing

Epicardial electrograms are preprocessed using two major steps performed as a part of epicardial mapping procedure [18, 117]. First, slow variations due to respiratory artefacts are removed from each electrogram using piecewise linear trending. This step also ensured that the mean of each preprocessed electrogram was approximately zero. The second step is to identify and exclude electrodes with electrogram amplitude close to zero. This could be caused due to the poor contacts of channels with ventricular tissue and electrical interferences. Consequently, these electrograms can act as outliers and affect the accuracy of analyses based on the activation sequences. To avoid this, only electrograms with dominant frequency (DF) between 2 and 20 Hz is included in the analysis [18]. Following this, a visual examination is performed to exclude electrograms with amplitudes close to zero. As a result, an average of 219 electrodes (range 186 – 240) are used for the analysis.

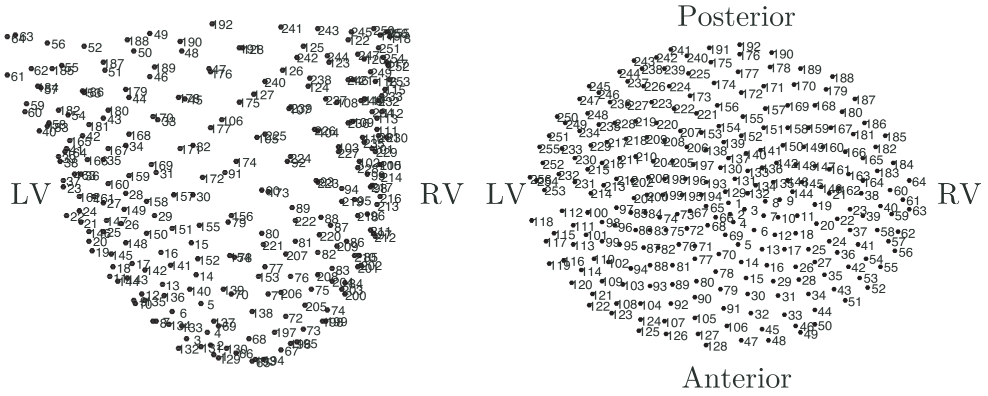

(a) (b)

Figure 6.3. **Representation of epicardial sock with the spatial coordinates of the epicardial electrodes (black circles) with respect to left and right ventricles (LV and RV).** (a) Three-dimensional view of electrodes. (b) Projection of electrodes onto flat two-dimensional surface.

6.1.3 Mapping of Electrode Positions

Prior to the data acquisition, the positions of epicardial electrodes in three-dimensional space are obtained by fitting the electrode sock over a heart model. The three-dimensional epicardial electrode positions are shown in Figure 6.3 (a). To obtain the two-dimensional coordinates used for the analysis, three-dimensional electrode positions are first projected onto a cone-shaped surface enclosing both ventricles. This is then projected onto a two-dimensional flat disc and the resulting two-dimensional coordinates of the electrodes are shown in Figure 6.3 (b).

6.2 Spatiotemporal Organisation of VF Electrograms

In this section, spatiotemporal activation patterns during three VF episodes (control VF, ischaemic and reflow VF) from a single patient (H055) are presented.

The changes in VF complexity can be qualitatively analysed by visualising the spatiotemporal patterns during different VF episodes. Firstly, the VF electrograms from control, ischaemic and relow VF is plotted in Figure 6.4 (a-c). It illustrates the temporal changes of cardiac activity in the electrograms of different episodes. For example, electrograms are more temporally organised with less changes during ischaemic VF compared to other two VF episodes. However, it is difficult to generalise here since this measurement is only from one single electrode.

To analyse the spatial organisation in the electrograms, spatial patterns are then obtained by interpolating the electrogram potentials on to two dimensional

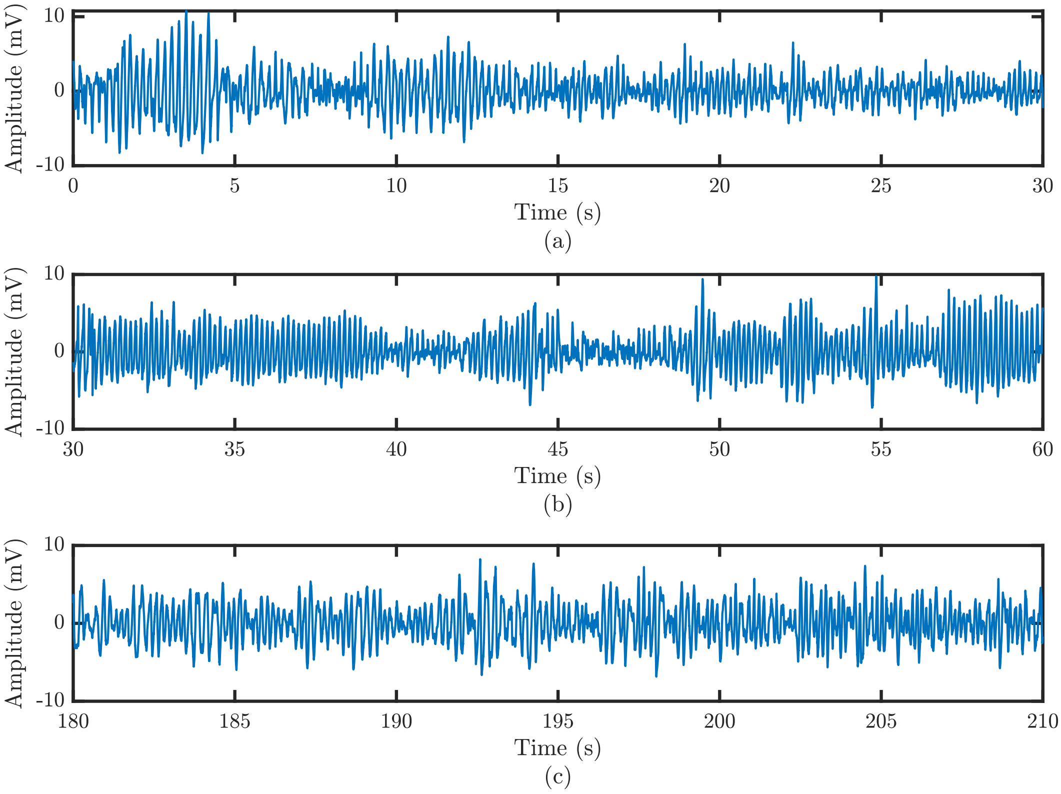

Figure 6.4. Examples of fibrillation electrograms obtained from an electrode during VF episodes. (a) Control VF. (b) First episode of ischaemic VF (isch1). (c) Reflow VF.

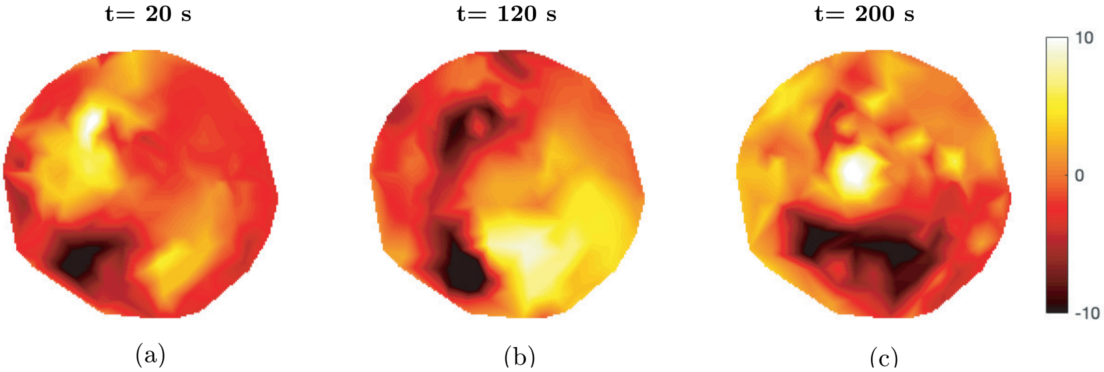

Figure 6.5. Examples of spatial fields across the epicardium surface at a time instant in VF episodes. (a) Control VF. (b) Fourth episode of ischaemic VF (isch4). (c) Reflow VF.

projection of epicardial surface. For this, a fine uniform grid of 150 × 150 points is first created based on the electrode positions (see Figure 6.3 (b)). The preprocessed electrogram potentials are then interpolated on this gridded domain at a particular time instant. The spatial fields shown in Figure 6.5 also indicate the difference in inherent complexity of the activation patterns at different regions of epicardium across VF episodes. At the given time instant, activation patterns of reflow VF is disorganised compared to the other two VF episodes. However, a systematic method to quantify the spatiotemporal organisation in activation patterns is important to characterise the level of complexity in VF episodes.

6.3 Complex Network Modelling

In this section, the complex network modelling methodology used to quantify the level of spatial and temporal organisation in electrical activation patterns of human VF are described.

6.3.1 Linear Coupling Measure

In order to quantify the level of functional association between fibrillation electrograms, a linear coupling measure based on cross-correlation functions is employed. Cross-correlation coefficients are calculated from a pre-defined set of time lags and used to determine the peak magnitude of linear dependency. The range of time lags is derived from the average of local activation cycle lengths over all electrodes. The normalised cross-correlation coefficient between a pair of preprocessed electrograms $y_l(k)$ and $y_j(k)$ can be calculated by

$$\rho_{l,j}(\omega) = \frac{\sum_{k=1}^{T-\omega} y_l(k) y_j(k+\omega)}{\sqrt{\sum_{k=1}^{T} y_l(k)^2}\sqrt{\sum_{k=1}^{T} y_j(k)^2}}, \tag{6.1}$$

where T is the number of samples and $\omega \in \{-\omega_d, ..0.., \omega_d\}$ is the time lag. The total time lag is set to the maximum value of the average activation cycle which is estimated from the average DF of epicardial recordings. The DF of an electrode is defined as the modal frequency in its spectrum and calculated using Welch's power spectral density method with a window length of 3000 samples and 1500 samples overlap.

In order to characterise the overall linear organisation a correlation matrix, $\mathbf{\Lambda}$, is defined such that

$$\mathbf{\Lambda}_{l,j} = \rho_{l,j}(\arg\max_{\omega} |\rho_{l,j}(\omega)|), \tag{6.2}$$

A single measure of linear organisation is then obtained to quantify the overall level of organisation using

$$\eta = \frac{||\mathbf{\Lambda}||_F}{n_y} \tag{6.3}$$

where n_y was the total number of sensors or electrodes and $|| \cdot ||_F$ denotes the Frobenius norm.

6.3.2 Functional Network Structures

In complex network analysis, a network is defined as a collection of interrelated elements that can be represented by a graph. The abstract mathematical formulation of a graph is defined as $\mathcal{G} = (\boldsymbol{\nu}_v, \boldsymbol{\nu}_e)$ where $\boldsymbol{\nu}_v = \{\nu_v^l\}$ is a set of nodes or vertices and $\boldsymbol{\nu}_e = \left\{\nu_v^l, \nu_v^j\right\}$ is a set of edges representing the connections between the nodes. The edges of a graph structure can be undirected or directed and binary or weighted.

To represent the functional network structure, a weighted undirected graph with no self or multiple connections is used. The nodes of the network are defined as epicardial electrodes and the weighted edges are the pairwise correlations obtained from the correlation matrix defined in (6.2). The edges can be interpreted as functional connectivity, i.e., a symmetrical association between regions of epicardial surface. For further analysis, the network structure of weighted graph is then represented by its connectivity matrix where rows and columns indicate nodes and matrix elements indicate weights. This is equivalent to the correlation matrix, $\mathbf{\Lambda}$, with its main diagonal set to zero to exclude self-connections.

In order to explore the connectivity matrix quantitatively, a set of graph theoretical measures is calculated for all nodes (electrodes) using adjacency and weights matrices. The weights matrix is obtained by thresholding the connectivity matrix where entries under a certain value were set to zero. The adjacency matrix is then obtained by replacing non-zero values with one in the weights matrix. It should be noted that thresholding is performed based on the absolute value of correlation coefficient.

Graph theoretical measures provide a powerful tool for a systematic study of the epicardial functional network, providing a quantitative connectivity structure which characterises the level of organisation of fibrillation electrograms over VF episodes. There are several graph-theoretical measures for analysis of complex networks in the literature. In this chapter connection density, node strength and strength distribution, and mean clustering coefficient are chosen and calculated using the Brain Connectivity toolbox in Matlab[139]. A brief description of each measure based on adjacency and weights matrices (undirected and weighted) is provided below.

Connection Density

Connection density is defined as the ratio of total number of edges in a network (non-zero entries of adjacency matrix) to the maximum possible number of connections [139]

$$\delta_{cd} = \frac{2n_{v_e}}{n_{v_v}(n_{v_v} - 1)}, \quad 0 \leq \delta_{cd} \leq 1 \tag{6.4}$$

where n_{v_v} is the total number of nodes and n_{v_e} is the total number of edges in the network.

Connection density can be calculated for a set of adjacency matrices obtained from different threshold values ranging from 0 and 1. A plot of connection density versus threshold values can be then produced. To calculate the overall level of sparseness or interconnectedness in a network, area under the curve (AUC) measure is computed which is independent of correlation-threshold value. This measure can be then used to monitor the changes in the overall level of organisation across different VF episodes.

Node Strength

In a weighted graph, node strength incorporates information about the total number of connections (degree) and the magnitude of functional association of individual nodes[139]. The node strength is defined as the sum of weights of all edges incident on a node which can be calculated by

$$\delta_s^l = \sum_{j \in n_{v_v}} \iota_{lj} \vartheta_{lj}, \tag{6.5}$$

where ι_{lj} and ϑ_{lj} are elements of adjacency and weights matrices respectively.

Clustering Coefficient

Clustering coefficient can be used to examine densely interconnected groups or clusters with similar functional association. For an undirected and binary graph, the local clustering coefficient of a node was defined as the number of triangles within its neighbourhood (its immediately connected neighbours) to the maximum possible number of edges between them [139].

In this work, the algorithm in [120] is used, which generalises the clustering coefficient for weighted networks by replacing the number of triangles with the sum of triangle intensities in the neighbourhood of a node. In this method, the local clustering coefficient of a node, l, is calculated by

$$\delta_{cc}^{l} = \frac{2\delta_t^l}{\delta_d^l(\delta_d^l - 1)}, \tag{6.6}$$

where δ_d^l is the degree of node, l and δ_t^l is the total intensity of triangles attached to node, l.

The intensity of each triangle is defined as geometric mean of its connection weights giving

$$\delta_t^l = \vartheta_{jk}(\vartheta_{lj}\vartheta_{jk}\vartheta_{kl})^{\frac{1}{3}}, \tag{6.7}$$

Note that weights are normalised by the largest weight in the network. The local clustering coefficients, δ_{cc}^l , can be then averaged across all nodes to quantify the average clustering coefficient of the whole network, i.e.,

$$\delta_c = \frac{1}{n_{\nu_v}} \sum_l \delta_{cc}^l \quad 0 \leq \delta_c \leq 1. \tag{6.8}$$

Similar to connection density, the average clustering coefficients can be calculated for different threshold values. In a plot of average clustering coefficients against threshold values, the AUC measure can be used to quantify the overall interconnectedness in the network.

6.3.3 Hierarchical Clustering based on Correlation Matrix

In order to characterise patterns with similar functional association and to quantify the level of spatial organisation over the epicardium surface, a hierarchical clustering method based on the correlation coefficients is implemented [94].

Hierarchical clustering is an agglomerative clustering approach which is initialized by considering each epicardial electrode as a cluster of its own. The first step is to quantify a measure of similarity or dissimilarity based on which clusters of closest functional association are merged to form larger clusters. Here, a distance or dissimilarity matrix calculated using the correlation matrix, $\mathbf{\Lambda}$ given in (6.2) as

$$\Gamma_{l,j} = 1 - |\mathbf{\Lambda}_{l,j}|. \tag{6.9}$$

From (6.9), it can be seen that a pair of electrodes with highest correlation coefficient forms a cluster with a distance or dissimilarity close to zero. Once larger clusters are formed the distance matrix should be updated using inter-cluster distances or linkage matrix as newly formed clusters consist of more than one electrode. The most commonly used linkage methods are single, complete and average

Algorithm 6.1 Algorithm to perform hierarchical clustering

```
1. Assign each electrode to a cluster,
2. Compute the distance matrix using (6.9),
3. Set $n_c$ to the number of clusters,
4. while $n_c > 1$
      - From the distance matrix find the closest pair of clusters and merge them to a single cluster,
      -Compute the inter-cluster distance using (6.10),
      -Update the distance matrix,
      -Update $n_c$.
   end
```

linkage. Single and complete linkage methods respectively adopt the distance between the closest and farthest neighbouring electrodes to evaluate the inter-cluster distances. These methods do not account for the cluster structure and could be sensitive to outliers. On the other hand, average linkage method calculates the average distance between all electrode pairs which makes the method more robust to outliers and hence more accurate compared with single and complete approaches [2]. Here, hierarchical clustering based on average linkage is used that follows

$$\Gamma_{\mathcal{E}_a,\mathcal{E}_b} = \frac{\sum_{l\in\mathcal{E}_a}^{n_{\mathcal{E}_a}} \sum_{j\in\mathcal{E}_b}^{n_{\mathcal{E}_b}} \Gamma_{l,j}}{n_{\mathcal{E}_a} n_{\mathcal{E}_b}}, \tag{6.10}$$

where $n_{\mathcal{E}_a}$ and $n_{\mathcal{E}_b}$ are the total number of electrodes in cluster $\mathcal{E}_a$ and cluster $\mathcal{E}_b$ respectively.

The hierarchical clustering algorithm based on the correlation matrix is given in Algorithm 6.1. The result of hierarchical classification can be then represented as a dendrogram. In order to divide the dendrogram into different sub-clusters, a cut-off distance measure should be chosen. The resulting clusters below the selected cut-off distance represent spatial regions with similar functional properties. The total number of clusters at different cut-off distances are measured and then normalised with respect to the total number of electrodes. A plot of normalised number of clusters against cut-off distance can be then produced. From this, AUC measure is then calculated and used to monitor the changes in number of clusters over different VF episodes. This measure is closely related to the average clustering coefficient. Both methods can illustrate the presence of spatial organisation on the epicardium surface through different procedures. Therefore, the result from one method can be used to examine and validate the results obtained from the other approach. The advantage of the hierarchical clustering approach is its ability to detect and visualise the clusters of electrodes which share functional properties.

6.4 Results

6.4.1 Linear Coupling Measure

In order to define the total number of lags in correlation analysis, the maximum activation cycle length for control VF, global myocardial ischaemic VF and reflow VF was calculated separately. Within each VF episode the average value of activation cycle length was estimated as the inverse of mean DF across all electrodes. For each patient this gave a mean activation cycle length for each segment of the time series. The calculated mean activation cycle lengths for ten patients were then averaged for each VF episode. The resultant cycle length during control VF was 180 ± 19.9 ms (mean ± 99% confidence interval (CI)). For ischaemic VF, this increased from 165 ± 14.7 ms to 207 ± 24.9 ms and reduced rapidly to 161 ± 22.3 ms during reflow. Based on the maximum value of activation cycle length, the range of time delays was set to -116 to 116 ms, giving a cycle length of 232 ms. Using the calculated cycle length the correlation matrix for each 30 s VF epoch was computed.

Correlation matrices from the clinical recording of Patient H055 (Figure 6.6 (a)) show the presence of functional organisation among electrograms in different regions, which changes over the time-course of VF. To monitor temporal changes in the overall level of organisation a sliding window-based analysis was performed. The window size was set to 1000 samples (1 s) with an overlap of 500 samples. The overlap was used to reduce the losses in temporal resolution between the window segments. This resulted in 420 window segments for each patient. The overall organisation was then quantified by calculating the normalised Frobenius norm of the correlation matrix in each window segment using (6.3). The computed Frobenius norms for the clinical recordings are shown in Figure 6.7 (a).

In order to quantify the changes within each VF epoch, a piecewise linear model is fitted to the computed Frobenius norm from each recording. The break points between linear segments in the model were set as the onset time of 30 s VF epochs. For each patient the parameters of the model were given by an intercept and the change in slope between each VF epoch. Figure 6.7 (b) shows the piecewise linear fit to the norm in each of the ten patients where black line shows the average fit over ten patients. The corresponding parameters of the mean regression model are given in Table 1. The results from this analysis shows that the mean of Frobenius norm decreases over time-course of VF episodes. During control VF, the mean intercept of Frobenius norm fit was decreased from 0.667 ± 0.068

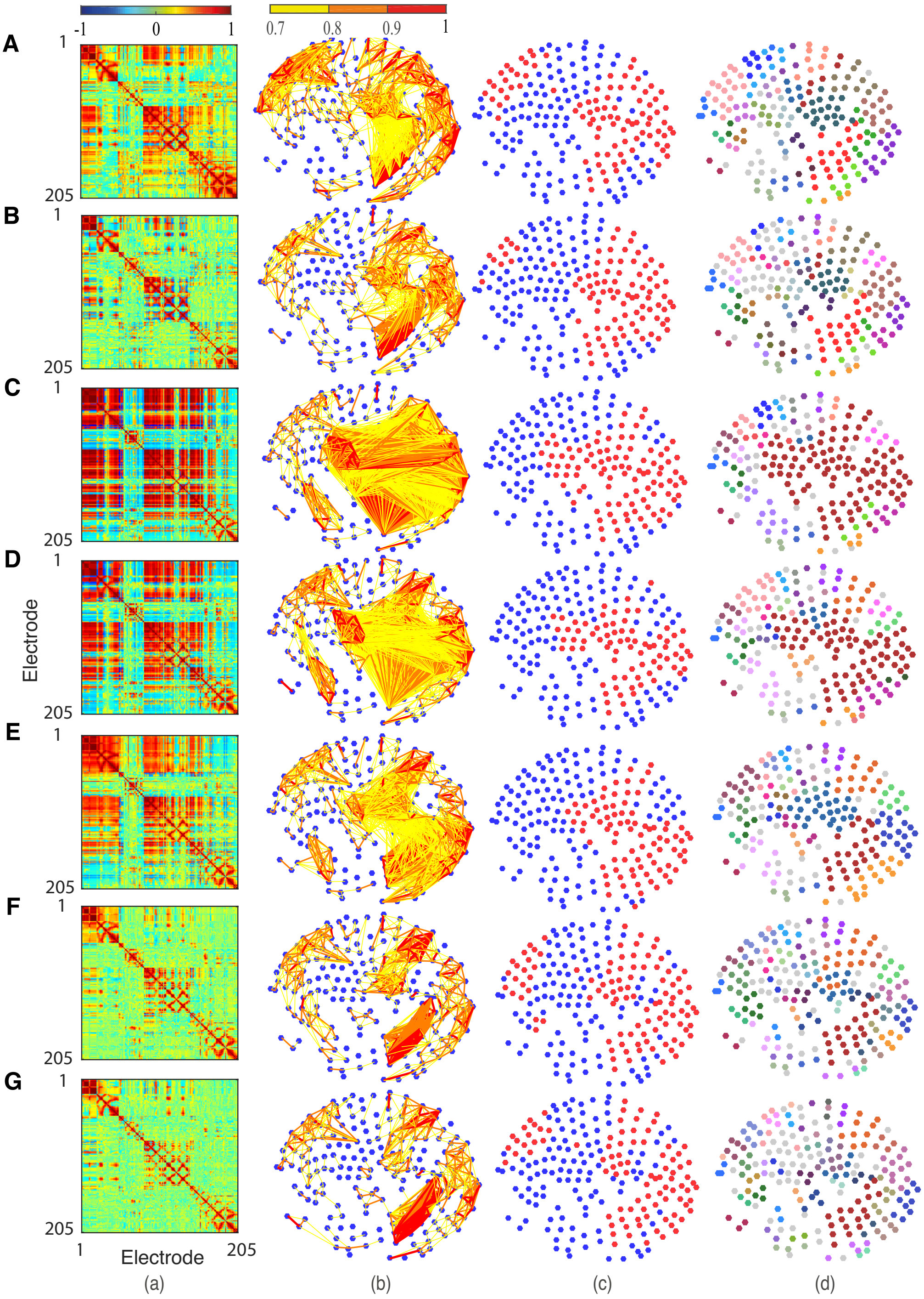

Figure 6.6. **Results from complex network analysis for Patient H055.** Each row shows a VF epoch of 30 seconds duration. (A) Controlled VF (Control). (B)-(F) Global myocardial ischaemia (Isch1-5). (G) Reflow. (a) Correlation matrices. (b) Network structure representation with network connections thresholded at value of 0.7. (c) Highly correlated nodes from node centrality measure (red circles). (d) Clusters from hierarchical clustering; electrodes in same clusters are shown with same colour. Electrodes which do not form a cluster are shown by white circles.

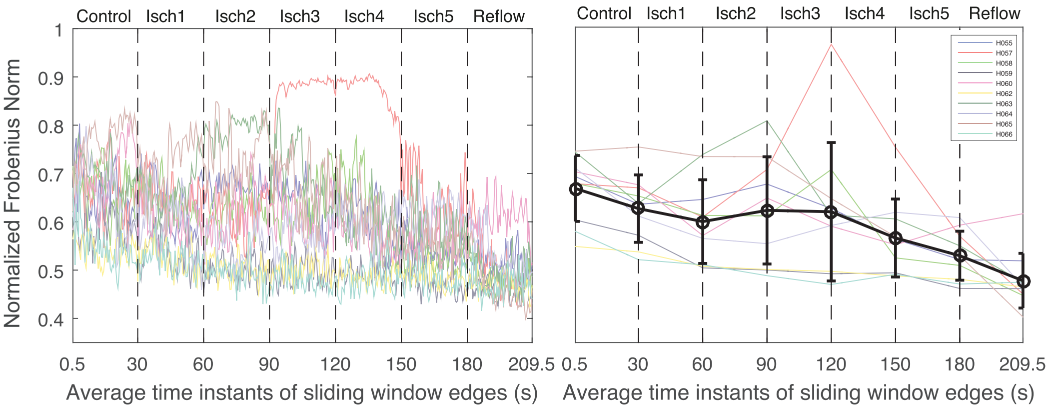

(a) (b)

Figure 6.7. **Results from correlation analysis.** (a) Temporal changes in the quantitative measure of overall organisation in correlation matrices during controlled ventricular fibrillation (Control), global myocardial ischaemia (Isch1-5) and reflow across recordings. (b) Piece-wise linear fit for the normalised Frobenius norm during VF episodes.

to 0.626 ± 0.069 (mean ± SD). During global ischaemia, this measure gradually decreased to 0.529 ± 0.050. However, there are distinct episodes during global ischaemia in each of the clinical recordings with higher level of organisation. In particular, Patient H057 shows a significant jump during the third and the fourth episodes of ischaemia. Highly organized ischaemic VF can be also observed in the second episode for Patient H063 and the beginning of the forth episode for Patient H058. After an increase in the level of organisation, VF follows a progressive decrease in the level of organisation, showing transition to an irregular activation sequence with increased complexity. This transition from higher level of organisation to the increased complexity during global ischaemia was observed in all the patients. Subsequently, the mean intercept of Frobenius norm significantly decreased to 0.477 ± 0.056 in reflow episode. In all the patients, Frobenius norm is lower during reflow compared to control, indicating that VF in the reperfused heart remains disorganised. The window based analysis is capable of capturing the fine changes at different VF epochs compared to correlation analysis. This is evident in Isch 5 and reflow as shown in Figure 6.6 (F) and (G).

6.4.2 Functional Network Analysis

Functional interactions between different regions of the epicardial surface can be represented as a network structure by calculating a measure of functional dependency between multi-electrode electrograms. The underlying functional network was constructed on the two dimensional projection of epicardial surface. The con-

Table 6.1. **Piecewise linear fit of organisation measures.** Presented are mean± SD.

Measures	**Mean Intercept**	**Mean Change in Slope (%)**						
		Control	Isch1	Isch2	Isch3	Isch4	Isch5	Reflow
Frobenius Norm	0.667 ± 0.06	−0.14 ± 0.13	0.051 ± 0.27	0.166 ± 0.22	−0.086 ± 0.40	−0.171 ± 0.61	0.058 ± 0.22	−0.53 ± 0.20
Connection density	0.646 ± 0.07	−0.15 ± 0.14	0.058 ± 0.30	0.184 ± 0.25	−0.097 ± 0.44	−0.182 ± 0.67	0.065 ± 0.23	−0.035 ± 0.21
Clustering Coeff	0.571 ± 0.08	−0.16 ± 0.14	0.069 ± 0.33	0.184 ± 0.26	−0.099 ± 0.45	−0.203 ± 0.69	0.072 ± 0.261	−0.068 ± 0.21
Number of clusters	0.133 ± 0.04	0.08 ± 0.08	−0.029 ± 0.15	−0.090 ± 0.12	0.037 ± 0.14	0.067 ± 0.23	−0.006 ± 0.11	0.068 ± 0.09

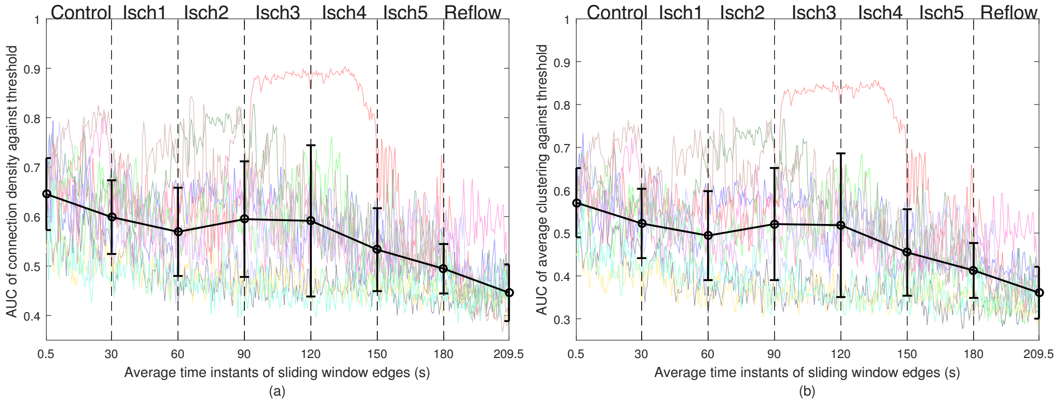

Figure 6.8. **Temporal changes in the quantitative measures from network analysis during controlled ventricular fibrillation (Control), global myocardial ischaemia (Isch1-5) and reflow across recordings.** (a) AUC measure of connection density. (b) AUC measure of average clustering coefficient. Error bar shows the averaged trend from piece-wise linear fit across patients.

nectivity matrix can be obtained by thresholding the correlation matrix using a threshold value between 0 and 1. In this section, a threshold value of 0.7 is used to examine the connectivity structures with higher level of functional association. For each VF epoch, the constructed connectivity network based on the connectivity matrix was then represented as a weighted undirected graph. This is shown for Patient H055 in Figure 6.6 (b). These graphs show the presence of both long and short range connectivities with a high level of organisation over the time-course of VF. There are a higher number of connections with a higher level of functional association in ischaemic VF episodes. Moreover, the number of connections in reflow is lower compared to control episode implying the irregular activation patterns in the reperfused heart. The network structures shown in Figure 6.6 (b) also highlight the presence of nodes with a high number of connectivities across the epicardium. These nodes can be identified using centrality measures such as node strength. Here the highly correlated nodes are defined as those with strength greater than the mean strength of the network. From Figure 6.6 (c), it can be seen that a relatively consistent spatial regions (across right ventricles) is observed that exhibit highly organised VF across epicardium.

The properties of functional network was further studied using a window-based graph-theoretical analysis. The window size and the overlap were chosen similar to the previous analysis. Within each window the connection density given in (6.4) and the average clustering coefficient in equations. (6.6)-(6.8) were calculated using different threshold values ranging from 0 to 1 with an increment of 0.05. It should be noted that connection density and average clustering co-efficient provide measures of the total number of connections and spatial connectivities in a network respectively. To quantify the overall level of organisation at all the threshold values, the AUC of connection density and average clustering coefficient versus threshold values was then computed. The temporal changes in the AUC of these measures over different VF episodes are shown in Figure 6.8. Similar to the correlation analysis, a piecewise linear model was then fitted to quantify the trend within each episode and the results from piecewise linear model are shown in Figure 6.8 and Table 6.1. These findings show that both connection density and average clustering coefficient show similar behaviour across VF epochs. During control VF, the mean intercept of connection density decreased from 0.646 ± 0.072 to 0.599 ± 0.074 whereas the mean of average clustering coefficient decreased from 0.571 ± 0.081 to 0.522 ± 0.080. In global ischaemia, the mean intercepts of the measures decreased to 0.494 ± 0.050 and 0.412 ± 0.64 respectively which was then significantly decreased to 0.44 ± 0.05 and 0.36 ± 0.06 during reflow. This shows that the level of organisation quantified using these two measures was low during reflow compared to control VF. This is in accordance with results based on correlation matrix analysis shown in Figure 6.7, indicating that both measures can be used to characterise the global level of organisation in VF episodes.

6.4.3 Hierarchical Clustering based on Correlation Matrix

In the previous sections, nodes with a similar level of functional organisation were identified at different locations on the epicardium. The hierarchical clustering approach based on cross-correlation matrix to group nodes into different clusters, to define regions that share similar characteristics. The hierarchical clustering in Algorithm 6.1 was applied to each of the seven segments VF recording. A cut-off distance of 0.3 was then used to split the parent cluster into different sub-clusters. The resulting clusters with 70% similarity in cross-correlation coefficients were mapped onto the two-dimensional epicardium surface shown in Figure 6.6 (d). This value was chosen to identify the clusters with higher level of functional organisation and also to compare with the network structures shown in Figure 6.6 (c). In Figure 6.6 (d) a high level of localised spatio-temporal organisation can be observed in different regions across VF epochs. As ischaemic VF progresses, larger clusters with a high level of spatial organisation were formed (Isch 2, 3 and 4). These clusters were then divided into smaller ones towards the end of the episode (Isch 5). One important observation is the higher number of electrodes which do not form a cluster (white circles) during reflow compared to control.

In order to monitor the changes in the number of clusters over space and time, sliding window-based approach was then employed. The quantity to calculate

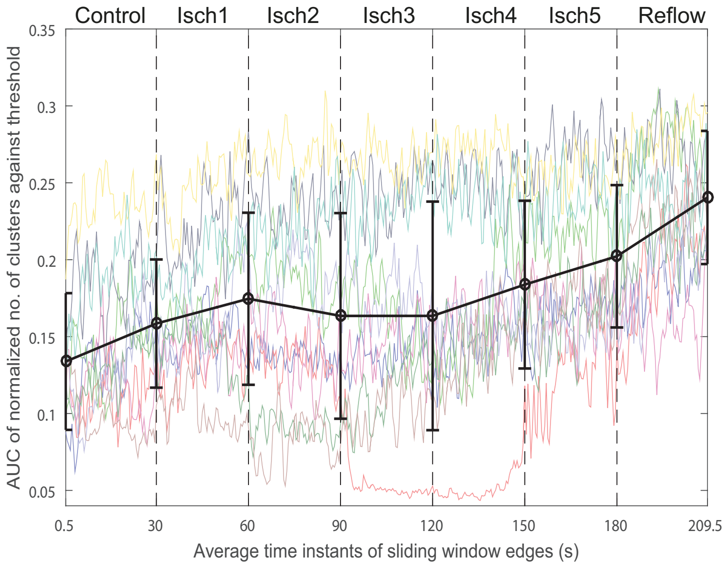

Figure 6.9. **Temporal changes in the AUC of normalised number of clusters during controlled ventricular fibrillation (Control), global myocardial ischaemia (Isch1-5) and reflow across recordings**. Error bar shows the averaged trend from piece-wise linear fit across patients.

over each window was the AUC of normalised number of clusters versus cut-off distances. Similarly, piecewise linear fit to this measure was applied for quantifying the trend within each VF epoch. The results from this analyses are shown in Figure 6.9 and Table 6.1, demonstrating a higher number of clusters in the reflow episode compared to the perfused one. This is consistent with our findings in previous sections as well as with a previous study, [18] which showed that the level of organisation during reflow did not recover to that observed during control. Hence, AUC measure of normalised number of clusters can be used to compare the level of complexity over different VF episodes. Notice, the expected opposite trend of this curve to the average clustering coefficient in Figure 6.8.

6.4.4 Comparison of Organisation Metrics

In this section, the organisation metrics obtained from correlation analysis, graph-theoretical method and hierarchical clustering are compared. This can be achieved by comparing the mean change in slope value shown in Table 6.1, computed from the piecewise linear fit to the organisation metrics. It should be noted that normalised AUC measure of number of clusters determined from hierarchical clustering is indeed a measure of disorganisation. To obtain the corresponding organisation metric for comparison, this measure was subtracted from 1, before the piecewise linear fit. It can be seen that the calculated mean change in slope val-

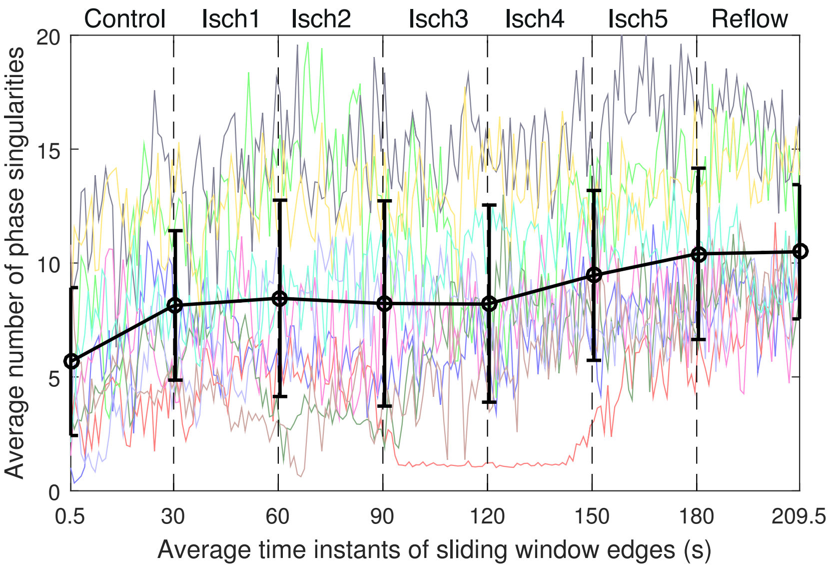

Figure 6.10. **Temporal changes in the average number of phase singularities during controlled ventricular fibrillation (Control), global myocardial ischaemia (Isch1-5) and reflow across recordings**. Error bar shows the averaged trend from piece-wise linear fit across patients.

ues across VF episodes follows a similar trend. This illustrates that the proposed methods provide consistent changes in the organisation across VF episodes.

Although the normalised Frobenius norm is an easier approach to estimate the global organisation level, an advantage of hierarchical clustering is its ability to detect and visualise clusters of electrodes which share functional properties (Figure 6.6 (d)) and to characterise the global complexity level in VF episodes. Moreover, the patterns obtained using clustering approach are more robust to outliers as it uses the average linkage method to calculate the inter-cluster distances [2]. It should be noted that the temporal information, i.e., time delays, between nodes were not investigated in correlation analysis. This is because, cross-correlation function can be sensitive to the inherent noise in the recordings, which significantly affect the estimation of time delays.

6.4.5 Comparison with Phase Analysis

Here, the AUC measure of normalised number of clusters is compared with the number of phase singularities obtained from phase analysis [18]. Both methods provide measures of the inherent complexity of electrical activation and so should provide consistent results. The temporal changes in the number of phase singularities are shown in Figure 6.10. The detailed description of the phase analy-

Table 6.2. Comparison of number of clusters and phase singularities

Patient Index	Coefficient Of Determination
H055	0.60
H057	0.89
H058	0.54
H059	0.62
H060	0.60
H062	0.53
H063	0.67
H064	0.76
H065	0.80
H066	0.60

sis approach used to compute the phase singularities is presented in a previous study [18]. Briefly, phase singularities are identified from the spatial distribution of phase, which requires robust estimation of phase angle from the phase plane trajectory of two state variables. For example, phase plane trajectory can be constructed using voltage and time-delayed voltage as state variables, where an appropriate delay parameter and a stable centre of rotation should be specified [61]. This method was extended by reconstructing the phase plane trajectory using voltage and its rate of change as state variables [121]. Although this method does not involve any additional parameters, the inherent differentiation of voltage has the tendency to amplify the noise in the signal. This can be addressed by considering the integral of voltage [136] or its Hilbert transform [116] as second state variable. However these approaches involve various pre-processing steps to obtain a stable center of rotation for the robust estimation of phase angle [36].

For each patient, a bivariate scatter plot of AUC measure of number of clusters versus number of phase singularities is first constructed as shown in Figure 6.11. In order to quantify the relationship between the two measures, linear correlation between the two was calculated using coefficient of determination, R-squared, from a linear regression model of this data using

$$\mathrm{R}^2 = 1 - \frac{\sum_{k=1}^{T}(n_{PS}(k) - \hat{n}_{PS}(k))^2}{\sum_{k=1}^{T}, (n_{PS}(k) - \bar{n}_{PS})^2}, \tag{6.11}$$

where n_{P_S} is the average number of phase singularities, $\hat{n}_{PS}$ is the corresponding mean value across time instants and $\bar{n}_{PS}$ are the predicted value using linear regression model.

The resulting R-squared values shown in Table 6.2 illustrate that the results

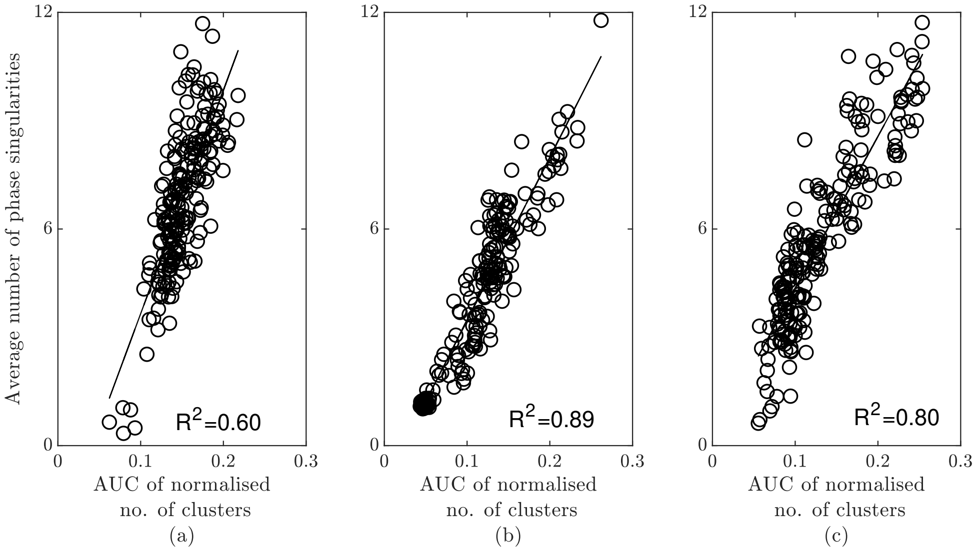

Figure 6.11. **Bivariate scatter plots of AUC measure of number of clusters versus number of phase singularities.** (a) Patient H055. (b) Patient H057. (c) Patient H065.

obtained from clustering approach is consistent with the phase analysis.

Temporal changes of the number of clusters and the average number of phase singularities shown in Figure 6.9 and Figure 6.10 also suggest that there are patterns of patients with similar and different complexity levels. The two complexity measures were compared by examining the clusters of patients determined from principal component analysis (PCA) [115]. PCA is a dimensionality reduction method that can used to identify the hidden patterns within complex dataset and enables analysis in low-dimensional feature space. The algebraic solution of PCA is commonly determined using eigen value or singular value decomposition. Within each 30s VF epoch PCA was applied to AUC measure of normalised number of clusters (Figure 6.9) and the average number of phase singularities (Figure 6.10). Here, the later method is used to identify the low-dimensional feature space. For instance, by using the first two principal components, PCA projects the time-varying complexity measures with a dimension of 30 × 10 samples to 2 × 10 components in each VF epoch. The resulting PCA feature spaces of the two complexity measures are shown in Figure 6.12. It can be seen from the result that the two quantities give identical groups of patients based on level of complexity, while preserving the spatial order.

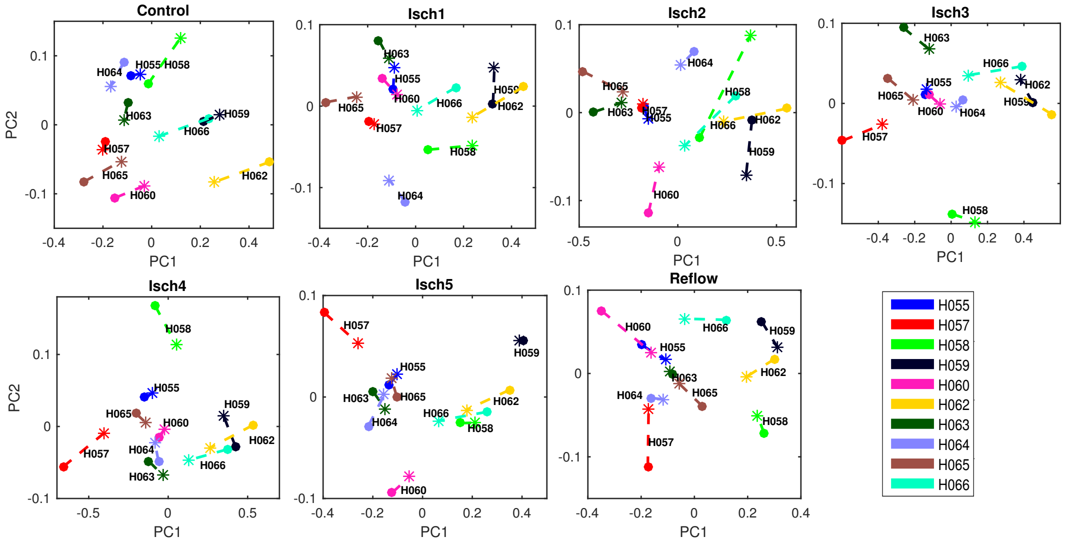

Figure 6.12. Principal component feature space of complexity measures during controlled VF (control),global myocardial ischaemia (Isch1-5) and reflow. Number of phase singularities (∗), number of clusters (•) and difference between the principal components of two quantities are shown in dashed lines.

6.5 Conclusion

This chapter demonstrates that it is possible to quantify trends in spatiotemporal organisation of epicardial electrograms during human VF that could be attributed to coronary perfusion, global myocardial ischaemia and reflow. The key findings from this study can be summarised as follows: 1) During control VF, there is a steady decrease in the level of organisation. 2) During global ischaemia, there were transient increases within distinct epochs followed by a progressive decrease in the level of organisation. 3) During reflow, the level of organisation was lower compared to that during perfusion. The results are in agreement with the findings presented in a previous study [18], where the changes in dynamics of complex electrical activation patterns were studied using traditional measures such as phase singularities and dominant frequency. It is also demonstrated that the proposed measures of organisation are consistent with the number of phase singularities from phase analysis. The proposed methods in this study do not require these additional pre-processing steps which makes it algorithmically straightforward to implement compared to the phase analysis. Therefore, the key contributions of this chapter can be summarised as following:

- The findings show that the complex spatiotemporal patterns can be studied using complex network modelling and hierarchical clustering.

- These analyses yield results that are consistent with more traditional measures such as the number of phase singularities and dominant frequency, and so provide new tools for quantifying and understanding the dynamics of complex electrical activation patterns in cardiac arrhythmias. One distinct advantage is their simple implementation which do not require additional pre-processing steps.
- This chapter also establishes that epicardial activity during human VF becomes progressively more disorganised and complex during a period of global myocardial ischaemia, and that a 30 s period of reperfusion does not reverse this decline.

Chapter 7

Conclusions and Future Work

Understanding the dynamics of complex cardiac electrical activity is important to advance the diagnosis and treatments for arrhythmia. By combining the cardiac electrophysiology concepts with the systems theoretic approaches, this thesis has presented the model-based estimation methods for quantifying the spatiotemporal cardiac electrical activity. Briefly, the proposed methods are the following:

- A statistical detection-estimation framework to reconstruct the underlying tissue dynamics in the simulated datasets of cardiac electrograms.

  The contributions of the proposed approach are the following:

  - The method introduces a modelling and estimation framework for cardiac surface measurements, which are acquired using electrical mapping techniques.
  - The method includes the stimulus dynamics into the estimation framework, which is particularly important for complex cardiac patterns that are formed from the multiple re-entrant stimuli.

- A complex network modelling approach to quantify the spatiotemporal organisation in the clinical electrograms of VF.

  The contributions of the proposed approach are the following:

  - The method proposes different complexity measures based on the correlation analysis, network analysis and hierarchical clustering algorithm.
  - The method quantifies the evolution of spatiotemporal organisation during different stages of VF.

The rest of this chapter is structured as follows. Section 7.1 summarises the important conclusions from each chapter in this thesis. Finally, some of the possible directions for further work are presented in Section 7.2.

7.1 Summary

The work presented in this thesis started by introducing the three integral components of model-based estimation approaches. As a result, Chapter 2 was subdivided into three major parts. The first part introduced the fundamental electrophysiology concepts of the cardiac electrical activity at the cell-level, tissue-level and the surface level. Most importantly, this part demonstrated that the electrical activation within the heart muscles cannot be measured from experimental techniques. Hence, the advantage of computational models of cardiac electrophysiology-based estimation method, which allows to reconstruct the underlying unobserved electrical dynamics of the tissue field from the cardiac electrograms. In order to obtain an integrated cardiac model, the following section reviewed some of the important classifications of the cardiac models at each spatial scale. This section illustrated that the cardiac modelling literature offers several candidate model structures with varying complexities and detailed descriptions. Based on the type of forward and inverse problem, a suitable model structure can be employed. Finally, stochastic state-space models and nonlinear state estimations were briefly introduced to provide a foundation to the estimation framework employed in this thesis.

In chapter 3, an integrated model of cardiac electrophysiology was derived based on the phenomenological models of cardiac action potential initiation and propagation. The phenomenological models are particularly suitable for the estimation frameworks because of their ability to reproduce the key features of the cardiac electrical activity, without describing the intricate electrophysiology relationships, such as ionic conductance, gating variables. The action potential characteristics are quantified using smaller number of parameters and state variables, and hence, phenomenological models are computationally less expensive to solve compared to the biophysical models. An important contribution of this chapter is the proposed continuous version of mMS model, which enables a straightforward implementation of statistical estimation methods. The continuous version of mMS model was then coupled with monodomain tissue model equation, which was extended to model the extracellular electrograms. The detailed simulation-based study of the proposed integrated model in one-dimensional and two-dimensional spatial fields enabled to identify the importance of state variables, the pattern formation and mechanisms of the re-entrant activity.

The reconstruction of the tissue dynamics from cardiac electrograms was presented in Chapter 4 and Chapter 5, for one-dimensional and two-dimensional tissue fields, respectively. The estimation problem was viewed as a statistical inference of the spatiotemporal data, which consists of the following important steps: (1) Deriving a stochastic versions of the cardiac models, (2) Model reduction step to form a finite dimensional state space model, (3) A single stage detection-state estimation step for simultaneously detecting the stimulus and estimating the state variables via URTS smoothing method. In the estimation framework, model-based detection scheme was employed to detect and isolate the sensor locations, nearby or at the stimulus conditions. The stimulus variables at the detected sensor locations were then augmented to the nominal state-space model, for improving the accuracy of the state estimates of the transmembrane voltage and gating variable. The dynamics of stimulus variables were further incorporated by representing as a weighted sum of b-splines functions in the spatial domain, followed by a temporal mapping scheme to capture the dynamic structure in the state estimates and covariance matrices. Although the above described procedures were similar for both one-dimensional and two-dimensional spatial field, the later spatial field introduced high-dimensional state estimation problems. In order to obtain a computationally efficient algorithm, a fixed lag-reduced rank URTS smoothing algorithm was then proposed. Therefore, the algorithm presented in Chapter 5 was tailored for high-dimensional state-space models. The performance of the proposed algorithms were evaluated for the normal and re-entrant conditions, where the data was modelled using mMS model. By doing so, certain level of model mismatch was incorporated into the estimation framework. The results from Chapter 4 and Chapter 5 show that the proposed method can be used to estimate the hidden state variables from the electrogram measurements, simultaneously by detecting the stimulus variables.

In Chapter 6, a complex network modelling approach was presented to study the spatiotemporal organisation in the complex spatiotemporal patterns of human VF. To quantify the level of organisation, different metrics from correlation-analysis, network analysis and hierarchical clustering are proposed. Correlation analysis quantified the linear coupling between the epicardial recordings, where the global level of organisation within VF episodes was characterised using the Frobenius norm. By representing the functional associations as network connections between the electrodes, the information extracted from network analysis can be used to identify the underlying network of highly interconnected fibrillation regions which drives complex spatiotemporal patterns of electrical activation. Similar to the Frobenius norm measure, connection density provided an overall measure of organisation while the spatial organisation within a network was characterised using average clustering coefficient. It can be seen that the degree of global clustering is dependent on the global functional organisation in electrograms, as the episodes with higher levels of organisation show higher levels of clustering and vice versa. On the other hand, the number of clusters measure from hierarchical analysis characterises the inherent complexity within VF episodes. Both clustering coefficient and the number of clusters illustrate the presence of localised spatial organisation on the epicardial surface through different procedures. Hence, the result from one method can be used to examine and validate results obtained from the other approach. The mean change in slope parameters obtained from the piecewise linear fit to proposed metrics show that the changes in organisation are consistent throughout the VF episodes. This illustrates that the proposed methods can be used to study the level of organisation in human VF.

7.2 Future Work

In this section, some of the further extensions from the work presented in this thesis are outlined.

Robust measures in network modelling

In the case of complex network modelling, the functional networks of the underlying spatiotemporal patterns were quantified using a correlation, which is a linear coupling measure. A natural extension of the proposed network modelling approach is to capture the nonlinear dependencies between the different spatial locations. For instance, information theory measures such as mutual information can be used [58]. In this way, weighted networks with nodes as the electrode positions and edges as the nonlinear dependencies can be constructed. Following this, the underlying properties of the functional networks with nonlinear dependencies can also be studied using different graph-theoretical measures from the literature [49].

Observability Analysis

The proposed detection-estimation framework has demonstrated that it is possible to reconstruct the tissue dynamics from the sensor configurations. However, an observability analysis can be performed to investigate the detection and estimation performance with different sensor configuration. A thorough observability analysis may also help to determine the minimum number of sensors, which are required for the accurate reconstruction of the tissue dynamics from the electrograms.

Joint estimation and identification problem

The proposed detection-estimation framework in Chapter 4 and Chapter 5 has shown the evidence for reconstructing the state variables of tissue dynamics. In addition to the state-estimation, other interesting extension is to include estimation of electrophysiology parameters described in the tissue model. The parameters such as diffusion coefficient, time constants within the cell-model can be considered into the estimation framework. The state and parameter estimation are collectively known as joint estimation in the literature, which has been recently implemented for estimating the both state variables and time constants of a single cardiac cell [140]. In this paper, the parameters were augmented into the state vector along with the state variables, and estimated using UKF algorithm. However, the development of a detection-joint estimation method can be used to fully reconstruct the spatial and temporal characteristics of the tissue dynamics from the observations.In particular to the reconstruction of tissue dynamics, one of the important parameter to be estimated is the diffusion co-efficient, which can be considered with homogenous or hetrogenous characteristics. In order to estimate this diffusion co-efficient, methods such as Expectation-Maximisation (EM) algorithm [112], variational inference [165] could be employed.

Implementation of the proposed detection-estimation algorithm on clinical recordings

In this thesis, the performance of the proposed algorithm was evaluated on the simulation data of cardiac electrical activity. An interesting and natural extension stems from this thesis is the implementation of algorithm in the clinical recordings of normal and arrhythmic conditions. By re-constructing the state variable dynamics in the clinical recordings, the underlying mechanisms of the cardiac activity can be elucidated. To achieve this, certain amendments should be incorporated among which some of them are the following: (1) The heart is essentially a heterogeneous tissue, where the dynamics changes from cell to cell. The variations can be observed with the thickness of muscles, ion channel densities and fiber orientations. Studies have shown that the tissue heterogeneities have played an important role in the breakups of activation wavefronts [152]. This implies that the assumptions of homogeneous and isotropic diffusion need to be changed for incorporating the heterogeneous and anisotropic dynamics. (2) Here, the integrated cardiac models were discretised using explicit finite difference method, which requires smaller value of sampling time to obtain stable and accurate patterns. However, this may not be the case in clinical recordings, especially in the electrical mapping. Depending on the type of data acquisition, an efficient discretisation method may be incorporated.

Appendix A

The Kalman Filter

In this section, the derivation of Kalman filter for linear Gaussian state-space models is presented [20]. For this consider a stationary linear state-space model form of (2.17) and (2.18) given by

$$\mathbf{x}_{k+1} = \mathbf{A}\mathbf{x}_k + \boldsymbol{\epsilon}_k^x, \tag{A.1a}$$

$$\mathbf{y}_k = \mathbf{C}\mathbf{x}_k + \boldsymbol{\epsilon}_k^y, \tag{A.1b}$$

where $\mathbf{A} \in \mathbb{R}^{n_x \times n_x}$ is the state transition matrix and $\mathbf{C} \in \mathbb{R}^{n_y \times n_x}$ is the observation matrix. As described earlier, both state disturbance and measurement noise are considered to be white noise sequences sampled from zero mean with covariance matrices given by Σ_{ϵ^x} and Σ_{ϵ^y}, respectively.

By assuming that initial state estimate and error covariance matrix are known, the estimation error can be defined as

$$\bar{\mathbf{e}}_{k+1}^- = \mathbf{x}_{k+1} - \hat{\mathbf{x}}_{k+1}^-, \tag{A.2}$$

where $\hat{\mathbf{x}}_{k+1}^-$ is the prior filtered state estimate, which is computed based on the observations.

The prior error covariance matrix associated with this prior state estimate is

$$\mathbf{P}_{k+1}^- = \mathbb{E}\left[\bar{\mathbf{e}}_{k+1}^- \bar{\mathbf{e}}_{k+1}^{-\top}\right] = \mathbb{E}\left[\left(\mathbf{x}_{k+1} - \hat{\mathbf{x}}_{k+1}^-\right)\left(\mathbf{x}_{k+1} - \hat{\mathbf{x}}_{k+1}^-\right)^\top\right]. \tag{A.3}$$

Now the objective is to correct the prior estimates by incorporating the observations. The expression for posterior state estimate is given by

$$\hat{\mathbf{x}}_{k+1} = \hat{\mathbf{x}}_{k+1}^- + \mathbf{K}_{k+1}(\mathbf{y}_{k+1} - \mathbf{C}\hat{\mathbf{x}}_{k+1}^-), \tag{A.4}$$

where $\mathbf{K}_{k+1}$ is the Kalman gain, which needs to be calculated for obtaining an optimal state estimate. One important measure in this formulation is the difference between measurement and predicted state estimate, which is often referred as residuals or innovation

$$\mathbf{e}_{k+1} = \mathbf{y}_{k+1} - \mathbf{C}\hat{\mathbf{x}}^{-}_{k+1}. \tag{A.5}$$

Similar to (A.3), the posterior state covariance can be written as

$$\mathbf{P}^{f}_{k+1} = \mathbb{E}\left[\mathbf{e}_{k+1}\hat{\mathbf{e}}^{\top}_{k+1}\right] = \mathbf{E}\left[\left(\mathbf{x}_{k+1} - \hat{\mathbf{x}}_{k+1}\right)\left(\mathbf{x}_{k+1} - \hat{\mathbf{x}}_{k+1}\right)^{\top}\right] \tag{A.6}$$

Substituting (A.4) and (A.1b) in (A.6) gives

$$\begin{aligned}\mathbf{P}_{k+1} = \mathbf{E}\Big[&\left[\left(\mathbf{x}_{k+1} - \mathbf{x}^{-}_{k+1}\right) - \mathbf{K}_{k+1}(\mathbf{C}\mathbf{x}_k + \epsilon^{y}_{k} - \mathbf{C}\mathbf{x}^{-}_{k+1})\right] \\ &\left[\left(\mathbf{x}_{k+1} - \mathbf{x}^{-}_{k+1}\right) - \mathbf{K}_{k+1}(\mathbf{C}\mathbf{x}_k + \epsilon^{y}_{k} - \mathbf{C}\mathbf{x}^{-}_{k+1})\right]^{\top}\Big]\end{aligned} \tag{A.7}$$

The above expression is then simplified to represent in terms of prior state covariance matrix as

$$\mathbf{P}_{k+1} = \left(\mathbf{I} - \mathbf{K}_{k+1}\mathbf{C}\right)\mathbf{P}^{-}_{k+1}\left(\mathbf{I} - \mathbf{K}_{k+1}\mathbf{C}\right)^{\top} + \mathbf{K}_{k+1}\mathbf{\Sigma}_{\epsilon^{y}}\mathbf{K}^{\top}_{k+1} \tag{A.8}$$

The diagonal elements of $\mathbf{P}_{k+1}$ represent the estimation error variance of each state. The Kalman gain is computed such that it minimises the estimation error variance of states following minimum mean-square error performance criterion. This can be calculated by evaluating the trace of $\mathbf{P}_{k+1}$ and then setting to zero. The resulting expression for Kalman gain is given by

$$\mathbf{K}_{k+1} = \mathbf{P}^{-}_{k+1}\mathbf{C}^{\top}(\mathbf{C}\mathbf{P}^{-}_{k+1}\mathbf{C}^{\top} + \mathbf{\Sigma}_{\epsilon^{y}})^{-1} \tag{A.9}$$

The expression for posterior state covariance $\mathbf{P}_{t+1}$ can expressed in few ways. For instance, (A.8) is often referred as "Joseph" form of covariance update equation while $\mathbf{K}_{k+1}$ can be substituted into (A.7) and re-arranged to give

$$\mathbf{P}_{k+1} = \mathbf{P}^{-}_{k+1} - \mathbf{P}^{-}_{k+1}\mathbf{C}(\mathbf{C}\mathbf{P}^{-}_{k+1}\mathbf{C}^{\top} + \mathbf{\Sigma}_{\epsilon^{y}})^{-1}\mathbf{C}\mathbf{P}^{-}_{k+1} \tag{A.10}$$

The final step is to formulate the update equations for prior state estimate and error covariance matrix. By using the state transition matrix and the previous state estimate, the prior state estimate is updated as

$$\mathbf{x}^{-}_{k+1} = \mathbf{A}\hat{\mathbf{x}}_{k} \tag{A.11}$$

To find the updated prior error covariance matrix, the estimation error is first

Algorithm A.1 Linear Kalman filter

```
1. Initialisation: Prior state estimate $\hat{\mathbf{x}}_0$ and error covariance matric $\mathbf{P}_0$
2. Recursive estimation for $k \in \{0, 1, ..., T-1\}$
    Prediction :
        Compute the predicted state estimate : $\hat{\mathbf{x}}_{k+1}^{-} = \mathbf{A}\hat{\mathbf{x}}_k$
        State estimate : $\hat{\mathbf{x}}_{k+1}^{-} = \mathbf{A}\hat{\mathbf{x}}_k$
        Error covariance matrix, $\mathbf{P}_{k+1}^{-} = \mathbf{A}\mathbf{P}_k\mathbf{A}^{\top} + \mathbf{\Sigma}_x$
    Correction :
        Compute Kalman gain, $\mathbf{K}_{k+1} = \mathbf{P}_{k+1}^{-}\mathbf{C}^{\top}(\mathbf{C}\mathbf{P}_{k+1}^{-}\mathbf{C}^{\top} + \mathbf{\Sigma}_y)^{-1}$
        State estimate : $\hat{\mathbf{x}}_{k+1} = \hat{\mathbf{x}}_{k+1}^{-} + \mathbf{K}_{k+1}(\mathbf{y}_{k+1} - \mathbf{C}\hat{\mathbf{x}}_{k+1}^{-})$
        Error covariance matrix, $\mathbf{P}_{k+1} = \mathbf{P}_{k+1}^{-} - \mathbf{P}_{k+1}^{-}\mathbf{C}(\mathbf{C}\mathbf{P}_{k+1}^{-}\mathbf{C}^{\top} + \mathbf{\Sigma}_y)^{-1}\mathbf{C}$
```

reformulated by substituting (A.1b)and (A.11) into (A.2)

$$\mathbf{e}_{k+1}^{-} = \mathbf{A}\left(\mathbf{x}_k - \hat{\mathbf{x}}_k\right) + \epsilon_k^x = \mathbf{A}\mathbf{e}_k + \mathbf{\Sigma}_{\epsilon^x} \tag{A.12}$$

Equation (A.12) is then substituted into (A.6)

$$\mathbf{P}_{k+1}^{-} = \mathbb{E}\left[\left(\mathbf{A}\mathbf{e}_k + \epsilon_k^x\right)\left(\mathbf{A}\mathbf{e}_k + \epsilon_k^x\right)^{\top}\right], \tag{A.13}$$

The above equation is expanded and then expectation is taken with respect to the $\mathbf{e}_k$ and ϵ_k^x to obtain

$$\mathbf{P}_{k+1}^{-} = \mathbf{A}\mathbf{P}_k\mathbf{A}^{\top} + \mathbf{\Sigma}_{\epsilon^x} \tag{A.14}$$

This completes the derivation of Kalman Filter. In summary, the recursive estimation procedure of Kalman Filter is given in Algorithm A.1, which comprises of two major steps : 1) prediction and 2) correction.

Bibliography

[1] Electrophysiology âĂŤ Physiome Model Repository. URL `https://models.physiomeproject.org/electrophysiology?b_start:int=0`.

[2] Hierarchical Clustering. In *Wiley Series in Probability and Statistics*, pages 71–110. John Wiley & Sons, Ltd, Chichester, UK, January 2011.

[3] R.A. Abbas, S.F. Lin, D. Mashburn, J. Xu, and J.P. Wikswo. A Phased-Array Stimulator System for Studying Planar and Curved Cardiac Activation Wave Fronts. *IEEE Transactions on Bio-medical Engineering*, 55(1):222–229, January 2008.

[4] W. Aftab, R. Hostettler, A. De Freitas, M. Arvaneh, and L. Mihaylova. Spatio-temporal gaussian process models for extended and group object tracking with irregular shapes. *IEEE Transactions on Vehicular Technology*, 68(3):2137–2151, 2019.

[5] N.E. Alaa, H. Lefraich, and I. El Malki. A second-generation computational modeling of cardiac electrophysiology: response of action potential to ionic concentration changes and metabolic inhibition. *Theoretical Biology & Medical Modelling*, 11, October 2014.

[6] R.R. Aliev and A.V. Panfilov. A simple two-variable model of cardiac excitation. *Chaos, Solitons & Fractals*, 7(3):293–301, March 1996.

[7] J.T. Ambadan and Y. Tang. Sigma-Point Kalman Filter Data Assimilation Methods for Strongly Nonlinear Systems. *Journal of the Atmospheric Sciences*, 66(2):261–285, February 2009.

[8] A. Arab. Spatial and Spatio-Temporal Models for Modeling Epidemiological Data with Excess Zeros. *International Journal of Environmental Research and Public Health*, 12(9):10536–10548, August 2015.

[9] P. Aram, D.R. Freestone, M.J. Cook, V. Kadirkamanathan, and D.B. Grayden. Model-based estimation of intra-cortical connectivity using electrophysiological data. *NeuroImage*, 118:563–575, 2015.

[10] A.L. Aro and S.S. Chugh. *Epidemiology and global burden of arrhythmias*, volume 1. Oxford University Press, July 2018.

[11] Y. Bar-Shalom and X.R. Li. Estimation and tracking- principles, techniques, and software. *Norwood, MA: Artech House, Inc, 1993.*, 1993.

[12] C.W. Barton, W.E. Cascio, D.N. Batson, C.L. Engle, and T.A. Johnson. Effect of rates of perfusion on dominant frequency and defibrillation energy in isolated fibrillating hearts. *Pacing and Clinical Electrophysiology*, 23(4):504–511, 2000.

[13] G.W. Beeler and H. Reuter. Reconstruction of the action potential of ventricular myocardial fibres. *The Journal of Physiology*, 268(1):177–210, June 1977.

[14] D. Bernal and Y. Bulut. A Modified Whiteness Test for Damage Detection Using Kalman Filter Innovations. pages 399–404. March 2011.

[15] S.A. Billings. Identification ofCoupled Map Lattice and Partial Differential Equations of Spatio-temporal Systems. In *Nonlinear system identification: NARMAX methods in the time, frequency, and spatio-temporal domains*, pages 431–472. Wiley, Chichester, West Sussex, United Kingdom, 2013.

[16] H. Blom and Y. Bar-Shalom. The interacting multiple model algorithm for systems with Markovian switching coefficients. *IEEE Transactions on Automatic Control*, 33(8):780–783, August 1988.

[17] P.M. Boyle, S. Zahid, and N.A. Trayanova. Using personalized computer models to custom-tailor ablation procedures for atrial fibrillation patients: are we there yet? *Expert Review of Cardiovascular Therapy*, 15(5):339–341, 2017.

[18] C.P. Bradley, R.H. Clayton, M.P. Nash, A. Mourad, M. Hayward, D.J. Paterson, and P. Taggart. Human ventricular fibrillation during global ischemia and reperfusion: paradoxical changes in activation rate and wavefront complexity. *Circulation: Arrhythmia and Electrophysiology*, pages CIRCEP–110, 2011.

[19] M. Briers, A. Doucet, and S. Maskell. Smoothing algorithms for state–space models. *Annals of the Institute of Statistical Mathematics*, 62(1):61, 2010.

[20] R.G. Brown, P.Y. Hwang, et al. *Introduction to random signals and applied Kalman filtering*, volume 3. Wiley New York, 1992.

[21] C.E. BrÃľhier. A short introduction to Stochastic PDEs. page 25.

[22] R. Cabrera-Lozoya, B. Berte, H. Cochet, P. Jais, N. Ayache, and M. Sermesant. Image-Based Biophysical Simulation of Intracardiac Abnormal Ventricular Electrograms. *IEEE Transactions on Biomedical Engineering*, 64(7):1446–1454, July 2017.

[23] J.W. Cain and D.G. Schaeffer. Shortening of cardiac action potential duration near an insulating boundary. *Mathematical medicine and biology: a journal of the IMA*, 25(1):21–36, 2008.

[24] J. Caldwell, F.L. Burton, G.L. Smith, and S.M. Cobbe. Heterogeneity of Ventricular Fibrillation Dominant Frequency During Global Ischemia in Isolated Rabbit Hearts. *Journal of Cardiovascular Electrophysiology*, 18(8):854–861, August 2007.

[25] E.M. Cherry and F.H. Fenton. Visualization of spiral and scroll waves in simulated and experimental cardiac tissue. *New Journal of Physics*, 10(12): 125016, 2008.

[26] Choi Bum-Rak, Liu Tong, and Salama Guy. The Distribution of Refractory Periods Influences the Dynamics of Ventricular Fibrillation. *Circulation Research*, 88(5):e49–e58, March 2001.

[27] I.I. Christov. Real time electrocardiogram qrs detection using combined adaptive threshold. *Biomedical Engineering Online*, 3(1):28, 2004.

[28] S.S. Chugh, K. Reinier, C. Teodorescu, A. Evanado, E. Kehr, M. Al Samara, R. Mariani, K. Gunson, and J. Jui. Epidemiology of Sudden Cardiac Death: Clinical and Research Implications. *Progress in Cardiovascular Diseases*, 51(3): 213–228, November 2008.

[29] F. Chunshi and Z. You. Highly Efficient Sigma Point Filter for Spacecraft Attitude and Rate Estimation. *Mathematical Problems in Engineering*, 2009.

[30] R.H. Clayton and A. Murray. Linear and non-linear analysis of the surface electrocardiogram during human ventricular fibrillation shows evidence of order in the underlying mechanism. *Medical & biological engineering & computing*, 37(3):354–358, 1999.

[31] R. Clayton and M. Bishop. Computational models of ventricular arrhythmia mechanisms: recent developments and future prospects. *Drug Discovery Today: Disease Models*, 14:17–22, 2014.

[32] R. Clayton and A. Panfilov. A guide to modelling cardiac electrical activity in anatomically detailed ventricles. *Progress in Biophysics and Molecular Biology*, 96(1-3):19–43, January 2008.

[33] R. Clayton, O. Bernus, E. Cherry, H. Dierckx, F. Fenton, L. Mirabella, A. Panfilov, F. Sachse, G. Seemann, and H. Zhang. Models of cardiac tissue electrophysiology: Progress, challenges and open questions. *Progress in Biophysics and Molecular Biology*, 104(1-3):22–48, January 2011.

[34] R.H. Clayton and A.V. Holden. A method to quantify the dynamics and complexity of re-entry in computational models of ventricular fibrillation. *Physics in medicine and biology*, 47(2):225, 2002.

[35] R.H. Clayton and A.V. Holden. Propagation of normal beats and re-entry in a computational model of ventricular cardiac tissue with regional differences in action potential shape and duration. *Progress in Biophysics and Molecular Biology*, 85(2):473–499, June 2004.

[36] R.H. Clayton and M.P. Nash. Analysis of Cardiac Fibrillation Using Phase Mapping. *Cardiac Electrophysiology Clinics*, 7(1):49–58, March 2015.

[37] C. Corrado, J. Whitaker, H. Chubb, S. Williams, M. Wright, J. Gill, M. O'Neill, and S. Niederer. Predicting spiral wave stability by personalized electrophysiology models. In *2016 Computing in Cardiology Conference (CinC)*, pages 229–232, September 2016.

[38] C. Corrado and S.A. Niederer. A two-variable model robust to pacemaker behaviour for the dynamics of the cardiac action potential. *Mathematical Biosciences*, 281:46–54, November 2016.

[39] C. Corrado, J. Whitaker, H. Chubb, S. Williams, M. Wright, J. Gill, M. O'Neill, and S. Niederer. Personalized models of human atrial electrophysiology derived from endocardial electrograms. *IEEE Transactions on Biomedical Engineering*, pages 1–1, 2017.

[40] C. Corrado, S. Williams, G. Plank, M. O'Neill, and S. Niederer. A Predictive Personalised Model for the Left Atrium. September 2017.

[41] C. Corrado, S. Williams, R. Karim, G. Plank, M. OâĂŹNeill, and S. Niederer. A work flow to build and validate patient specific left atrium electrophysiology models from catheter measurements. *Medical Image Analysis*, 47:153–163, July 2018.

[42] M. Das, S. Sadhu, and T.K. Ghoshal. Fault Detection and Isolation using an Adaptive Unscented Kalman Filter. *IFAC Proceedings Volumes*, 47(1):326–332, January 2014.

[43] J.M.T. de Bakker and F.H.M. Wittkampf. The Pathophysiologic Basis of Fractionated and Complex Electrograms and the Impact of Recording Techniques on Their Detection and Interpretation. *Circulation: Arrhythmia and Electrophysiology*, 3(2):204–213, April 2010.

[44] V. DeCaprio, P. Hurzeler, and S. Furman. A comparison of unipolar and bipolar electrograms for cardiac pacemaker sensing. *Circulation*, 56(5):750–755, November 1977.

[45] C. Fan and Z. You. Highly Efficient Sigma Point Filter for Spacecraft Attitude and Rate Estimation. *Mathematical Problems in Engineering*, 2009:1–23, 2009.

[46] L. Fendelander, P.W. Hsia, and R.J. Damiano Jr. Spatial coherence: A new method of quantifying myocardial electrical organization using multichannel epicardial electrograms. *Journal of Electrocardiology*, 30(1):9–19, January 1997.

[47] F.H. Fenton, E.M. Cherry, H.M. Hastings, and S.J. Evans. Multiple mechanisms of spiral wave breakup in a model of cardiac electrical activity. *Chaos: An Interdisciplinary Journal of Nonlinear Science*, 12(3):852–892, August 2002.

[48] R. FitzHugh. Impulses and Physiological States in Theoretical Models of Nerve Membrane. *Biophysical Journal*, 1(6):445–466, July 1961.

[49] V. Fleischer, A. Radetz, D. Ciolac, M. Muthuraman, G. Gonzalez-Escamilla, F. Zipp, and S. Groppa. Graph Theoretical Framework of Brain Networks in Multiple Sclerosis: A Review of Concepts. *Neuroscience*, 403:35–53, April 2019.

[50] N. Forti, G. Battistelli, L. Chisci, and B. Sinopoli. Joint attack detection and secure state estimation of cyber-physical systems. *arXiv:1612.08478 [cs]*, December 2016. arXiv: 1612.08478.

[51] B.h. Foundation. *Implantable cardioverter defibrillator*, 2016. `https://www.bhf.org.uk/informationsupport/treatments/implantable-cardioverter-defibrillator`.

[52] D.R. Freestone, P.J. Karoly, D. Nešić, P. Aram, M.J. Cook, and D.B. Grayden. Estimation of effective connectivity via data-driven neural modeling. *Frontiers in neuroscience*, 8:383, 2014.

[53] D. Freestone, P. Aram, M. Dewar, K. Scerri, D. Grayden, and V. Kadirkamanathan. A data-driven framework for neural field modeling. *NeuroImage*, 56(3):1043–1058, June 2011.

[54] C.W. Gear and O. Osterby. Solving ordinary differential equations with discontinuities. Technical report, Illinois Univ., Urbana (USA). Dept. of Computer Science, 1981.

[55] D. Geberth and M.T. HÃijtt. Predicting the Distribution of Spiral Waves from Cell Properties in a Developmental-Path Model of Dictyostelium Pattern Formation. *PLoS Computational Biology*, 5(7):e1000422, July 2009.

[56] K. Gima and Y. Rudy. Ionic current basis of electrocardiographic waveforms: a model study. *Circulation Research*, 90(8):889–896, May 2002.

[57] A. Gizzi, E.M. Cherry, R.F. Gilmour, S. Luther, S. Filippi, and F.H. Fenton. Effects of pacing site and stimulation history on alternans dynamics and the development of complex spatiotemporal patterns in cardiac tissue. *Frontiers in Physiology*, 4:71, 2013.

[58] Y.K. Goh, H.M. Hasim, and C.G. Antonopoulos. Inference of financial networks using the normalised mutual information rate. *PLOS ONE*, 13(2): e0192160, February 2018.

[59] C.W. Granger. Investigating causal relations by econometric models and cross-spectral methods. *Econometrica: Journal of the Econometric Society*, pages 424–438, 1969.

[60] R.A. Gray and P. Pathmanathan. Patient-specific cardiovascular computational modeling: Diversity of personalization and challenges. *Journal of Cardiovascular Translational Research*, 11(2):80–88, Apr 2018.

[61] R.A. Gray, A.M. Pertsov, and J. Jalife. Spatial and temporal organization during cardiac fibrillation. *Nature*, 392(6671):75–78, March 1998.

[62] F. Gustafsson. *Adaptive Filtering and Change Detection: Gustafsson: Adaptive*. John Wiley & Sons, Ltd, Chichester, UK, October 2001.

[63] R.F. Harrington. *Field Computation by Moment Methods*. Wiley-IEEE Press, 1993.

[64] S. Haykin. *Kalman filtering and neural networks*, volume 47. John Wiley & Sons, 2004.

[65] C.S. Henriquez. A Brief History of Tissue Models For Cardiac Electrophysiology. *IEEE Transactions on Biomedical Engineering*, 61(5):1457–1465, May 2014.

[66] S. Herzog, F. WÃűrgÃűtter, and U. Parlitz. Data-Driven Modeling and Prediction of Complex Spatio-Temporal Dynamics in Excitable Media. *Frontiers in Applied Mathematics and Statistics*, 4, 2018.

[67] A.L. Hodgkin and A.F. Huxley. A quantitative description of membrane current and its application to conduction and excitation in nerve. *The Journal of Physiology*, 117(4):500–544, August 1952.

[68] M. Hofbaur and B. Williams. Hybrid Estimation of Complex Systems. *IEEE Transactions on Systems, Man and Cybernetics, Part B (Cybernetics)*, 34(5):2178–2191, October 2004.

[69] M.J. Hoffman, N.S. LaVigne, S.T. Scorse, F.H. Fenton, and E.M. Cherry. Reconstructing three-dimensional reentrant cardiac electrical wave dynamics using data assimilation. *Chaos: An Interdisciplinary Journal of Nonlinear Science*, 26(1):013107, January 2016.

[70] K. Hollig and J. Horner. *Approximation and modeling with B-splines*, volume 132. SIAM, 2013.

[71] H.C. Huang and N. Cressie. Spatio-temporal prediction of snow water equivalent using the Kalman filter. *Computational Statistics & Data Analysis*, 22(2):159–175, July 1996.

[72] J.F. Huizar, M.D. Warren, A.G. Shvedko, J. Kalifa, J. Moreno, S. Mironov, J. Jalife, and A.V. Zaitsev. Three distinct phases of VF during global ischemia in the isolated blood-perfused pig heart. *AJP: Heart and Circulatory Physiology*, 293(3):H1617–H1628, June 2007.

[73] H. Ito and L. Glass. Theory of reentrant excitation in a ring of cardiac tissue. *Physica D: Nonlinear Phenomena*, 56(1):84–106, April 1992.

[74] J. Jalife. Ventricular fibrillation: mechanisms of initiation and maintenance. *Annual review of physiology*, 62(1):25–50, 2000.

[75] A.H. Jazwinski. *Stochastic Processes and Filtering Theory*. Courier Corporation, January 2007.

[76] A. Jeremic and A. Nehorai. Detection and estimation of biochemical sources in arbitrary 2d environments. In *Proceedings. (ICASSP '05). IEEE International Conference on Acoustics, Speech, and Signal Processing, 2005.*, volume 4, pages iv/1013–iv/1016 Vol. 4, March 2005.

[77] S.J. Julier, J.K. Uhlmann, and H.F. Durrant-Whyte. A new approach for filtering nonlinear systems. In *Proceedings of 1995 American Control Conference - ACC'95*, volume 3, pages 1628–1632 vol.3, June 1995.

[78] S.J. Julier and J.K. Uhlmann. Unscented filtering and nonlinear estimation. *Proceedings of the IEEE*, 92(3):401–422, 2004.

[79] A. Kaboudian, E.M. Cherry, and F.H. Fenton. Real-time interactive simulations of large-scale systems on personal computers and cell phones: Toward patient-specific heart modeling and other applications. *Science Advances*, 5 (3):eaav6019, March 2019.

[80] V. Kadirkamanathan, P. Li, M.H. Jaward, and S.G. Fabri. Particle filtering-based fault detection in non-linear stochastic systems. *International Journal of Systems Science*, 33(4):259–265, January 2002.

[81] V. Kadirkamanathan and M. Niranjan. A function estimation approach to sequential learning with neural networks. *Neural computation*, 5(6):954–975, 1993.

[82] V. Kadirkamanathan, S.R. Anderson, S.A. Billings, X. Zhang, G.R. Holmes, C.C. Reyes-Aldasoro, P.M. Elks, and S.A. Renshaw. The neutrophil's eye-view: Inference and visualisation of the chemoattractant field driving cell chemotaxis in vivo. *PLOS ONE*, 7(4):1–11, 04 2012.

[83] V. Kadirkamanathan, S.R. Anderson, S.A. Billings, X. Zhang, G.R. Holmes, C.C. Reyes-Aldasoro, P.M. Elks, and S.A. Renshaw. The Neutrophil's Eye-View: Inference and Visualisation of the Chemoattractant Field Driving Cell Chemotaxis In Vivo. *PLoS ONE*, 7(4):e35182, April 2012.

[84] R.E. Kalman. A new approach to linear filtering and prediction problems. *Journal of basic Engineering*, 82(1):35–45, 1960.

[85] D.T. Kaplan and R.J. Cohen. Is fibrillation chaos? *Circulation Research*, 67(4): 886–892, October 1990.

[86] I.V. Kazbanov, R.H. Clayton, M.P. Nash, C.P. Bradley, D.J. Paterson, M.P. Hayward, P. Taggart, and A.V. Panfilov. Effect of Global Cardiac Ischemia on Human Ventricular Fibrillation: Insights from a Multi-scale Mechanistic Model of the Human Heart. *PLoS Computational Biology*, 10(11):e1003891, November 2014.

[87] J.P. Keener and J. Sneyd. *Mathematical physiology*. Number 8 in Interdisciplinary applied mathematics. Springer, New York, NY, 2nd ed edition, 2009. OCLC: ocn298595247.

[88] Khurshid Shaan, Choi Seung Hoan, Weng Lu-Chen, Wang Elizabeth Y., Trinquart Ludovic, Benjamin Emelia J., Ellinor Patrick T., and Lubitz Steven A. Frequency of Cardiac Rhythm Abnormalities in a Half Million Adults. *Circulation: Arrhythmia and Electrophysiology*, 11(7):e006273, July 2018.

[89] R.E. Klabunde. *Cardiovascular physiology concepts*. Lippincott Williams & Wilkins/Wolters Kluwer, Philadelphia, PA, 2nd ed edition, 2012. OCLC: ocn712765593.

[90] A.G. Kleber. Basic Mechanisms of Cardiac Impulse Propagation and Associated Arrhythmias. *Physiological Reviews*, 84(2):431–488, April 2004.

[91] A.G. KlÃl'ber and Y. Rudy. Basic Mechanisms of Cardiac Impulse Propagation and Associated Arrhythmias. *Physiological Reviews*, 84(2):431–488, April 2004.

[92] B.Y. Kogan, W.J. Karplus, B.S. Billett, A.T. Pang, H.S. Karagueuzian, and S.S. Khan. The simplified FitzHugh-Nagumo model with action potential duration restitution: Effects on 2d wave propagation. *Physica D: Nonlinear Phenomena*, 50(3):327–340, July 1991.

[93] J.I. Laughner, F.S. Ng, M.S. Sulkin, R.M. Arthur, and I.R. Efimov. Processing and analysis of cardiac optical mapping data obtained with potentiometric dyes. *American Journal of Physiology-Heart and Circulatory Physiology*, 303(7): H753–H765, July 2012.

[94] X. Liu, X.H. Zhu, P. Qiu, and W. Chen. A correlation-matrix-based hierarchical clustering method for functional connectivity analysis. *Journal of neuroscience methods*, 211(1):94–102, 2012.

[95] S.S. Lobodzinski and M.M. Laks. New devices for very long-term ECG monitoring. *Cardiology Journal*, 19(2):210–214, 2012.

[96] C.H. Luo and Y. Rudy. A model of the ventricular cardiac action potential. Depolarization, repolarization, and their interaction. *Circulation Research*, 68 (6):1501–1526, June 1991.

[97] C.h. Luo and Y. Rudy. A dynamic model of the cardiac ventricular action potential. I. Simulations of ionic currents and concentration changes. *Circulation research*, 74(6):1071–1096, 1994.

[98] K.K. Manoj, Y. Tang, Z. Deng, D. Chen, and Y. Cheng. Reduced-Rank Sigma-Point Kalman Filter and Its Application in ENSO Model. *Journal of Atmospheric and Oceanic Technology*, 31(10):2350–2366, October 2014.

[99] M.E. Marsh, S.T. Ziaratgahi, and R.J. Spiteri. The secrets to the success of the rushâĂŞlarsen method and its generalizations. *IEEE Transactions on Biomedical Engineering*, 59(9):2506–2515, Sep. 2012.

[100] S. Masse, T. Farid, P. Dorian, K. Umapathy, K. Nair, J. Asta, H. Ross, V. Rao, E. Sevaptsidis, and K. Nanthakumar. Effect of global ischemia and reperfusion during ventricular fibrillation in myopathic human hearts. *AJP: Heart and Circulatory Physiology*, 297(6):H1984–H1991, December 2009.

[101] R.K. Mehra and J. Peschon. An innovations approach to fault detection and diagnosis in dynamic systems. *Automatica*, 7(5):637–640, September 1971.

[102] J. Mercieca, P. Aram, B.L. Jones, and V. Kadirkamanathan. A Spatiotemporal Estimation Framework for Real-World LIDAR Wind Speed Measurements. *IEEE Transactions on Control Systems Technology*, pages 1–8, 2019.

[103] J. Mercieca, P. Aram, B.L. Jones, and V. Kadirkamanathan. A spatiotemporal estimation framework for real-world lidar wind speed measurements. *IEEE Transactions on Control Systems Technology*, 2019.

[104] J. Mercieca, P. Aram, B. Ll. Jones, and V. Kadirkamanathan. A spatiotemporal estimation framework for real-world lidar wind speed measurements. *IEEE Transactions on Control Systems Technology*, PP:1–8, 05 2019.

[105] G.R. Mirams, M.R. Davies, Y. Cui, P. Kohl, and D. Noble. Application of cardiac electrophysiology simulations to pro-arrhythmic safety testing. *British journal of pharmacology*, 167(5):932–945, 2012.

[106] G.R. Mirams, P. Pathmanathan, R.A. Gray, P. Challenor, and R.H. Clayton. Uncertainty and variability in computational and mathematical models of cardiac physiology. *The Journal of Physiology*, 594(23):6833–6847, 2016.

[107] S. Mironov, J. Jalife, and E.G. Tolkacheva. Role of Conduction Velocity Restitution and Short-Term Memory in the Development of Action Potential Duration Alternans in Isolated Rabbit Hearts. *Circulation*, 118(1):17–25, July 2008.

[108] C. Mitchell. A two-current model for the dynamics of cardiac membrane. *Bulletin of Mathematical Biology*, 65(5):767–793, September 2003.

[109] C.C. Mitchell and D.G. Schaeffer. A two-current model for the dynamics of cardiac membrane. *Bulletin of Mathematical Biology*, 65(5):767–793, Sep 2003.

[110] G.K. Moe, A.S. Harris, and C.J. Wiggers. Analysis of the initiation of fibrillation by electrographic studies. *American Journal of PhysiologyâĂŞLegacy Content*, 134(3):473–492, 1941.

[111] V. Molyneux and A.A. Klein. *Equipment and monitoring for cardiopulmonary bypass*, page 1âĂŞ23. Cambridge University Press, 2 edition, 2015.

[112] T.K. Moon. The expectation-maximization algorithm. *IEEE Signal processing magazine*, 13(6):47–60, 1996.

[113] J.D. Moreno, Z.I. Zhu, P.C. Yang, J.R. Bankston, M.T. Jeng, C. Kang, L. Wang, J.D. Bayer, D.J. Christini, N.A. Trayanova, et al. A computational model to predict the effects of class i anti-arrhythmic drugs on ventricular rhythms. *Science translational medicine*, 3(98):98ra83–98ra83, 2011.

[114] N. Murakoshi and K. Aonuma. Epidemiology of Arrhythmias and Sudden Cardiac Death in Asia. *Circulation Journal*, 77(10):2419–2431, 2013.

[115] K.P. Murphy. *Machine learning: a probabilistic perspective.* MIT press, 2012.

[116] M.P. Nash. Evidence for Multiple Mechanisms in Human Ventricular Fibrillation. *Circulation*, 114(6):536–542, August 2006.

[117] M.P. Nash, A. Mourad, R.H. Clayton, P.M. Sutton, C.P. Bradley, M. Hayward, D.J. Paterson, and P. Taggart. Evidence for multiple mechanisms in human ventricular fibrillation. *Circulation*, 114(6):536–542, 2006.

[118] D. Noble. Cardiac Action and Pacemaker Potentials based on the Hodgkin-Huxley Equations. *Nature*, 188(4749):495–497, November 1960.

[119] D. Noble. Electrical properties of cardiac muscle attributable to inward going (anomalous) rectification. *Journal of Cellular and Comparative Physiology*, 66 (S2):127–135, December 1965.

[120] J.P. Onnela, J. Saramäki, J. Kertész, and K. Kaski. Intensity and coherence of motifs in weighted complex networks. *Physical Review E*, 71(6):065103, 2005.

[121] N.H. Packard, J.P. Crutchfield, J.D. Farmer, and R.S. Shaw. Geometry from a time series. *Physical review letters*, 45(9):712, 1980.

[122] S.V. Pandit and J. Jalife. Rotors and the dynamics of cardiac fibrillation. *Circulation research*, 112(5):849–862, 2013.

[123] M. Papadakis, S. Sharma, S. Cox, M.N. Sheppard, V.F. Panoulas, and E.R. Behr. The magnitude of sudden cardiac death in the young: a death certificate-based review in England and Wales. *Europace*, 11(10):1353–1358, October 2009.

[124] M.M. Petrou and C. Petrou. *Image processing: the fundamentals*. John Wiley & Sons, 2010.

[125] G. Plank, L.J. Leon, S. Kimber, and E.J. Vigmond. Defibrillation depends on conductivity fluctuations and the degree of disorganization in reentry patterns. *Journal of Cardiovascular Electrophysiology*, 16(2):205–216, February 2005.

[126] R. Plonsey and R.C. Barr. *Bioelectricity: a quantitative approach*. Springer, New York, NY, 3rd ed edition, 2007.

[127] H.V. Poor. *An Introduction to Signal Detection and Estimation*. Springer Science & Business Media, 1998.

[128] M. Potse, B. Dube, J. Richer, A. Vinet, and R. Gulrajani. A Comparison of Monodomain and Bidomain Reaction-Diffusion Models for Action Potential Propagation in the Human Heart. *IEEE Transactions on Biomedical Engineering*, 53(12):2425–2435, December 2006.

[129] L. Priebe and D.J. Beuckelmann. Simulation Study of Cellular Electric Properties in Heart Failure. *Circulation Research*, 82(11):1206–1223, June 1998.

[130] A. Pullan, L. Cheng, and M. Buist. *Mathematically Modelling the Electrical Activity of the Heart: From Cell to Body Surface and Back Again*. World Scientific Publishing Company, 2005.

[131] A.J. Pullan, L.K. Cheng, and M.L. Buist. Tissue modelling. In *Mathematically Modelling the Electrical Activity of the Heart: From Cell to Body Surface and Back Again*, pages 151–166. World Scientific, 2005.

[132] W. Quan and Y. Rudy. Unidirectional block and reentry of cardiac excitation: a model study. *Circulation Research*, 66(2):367–382, February 1990.

[133] H.E. Rauch, C. Striebel, and F. Tung. Maximum likelihood estimates of linear dynamic systems. *AIAA journal*, 3(8):1445–1450, 1965.

[134] U. Richter, L. Faes, A. Cristoforetti, M. Masè, F. Ravelli, M. Stridh, and L. Sörnmo. A novel approach to propagation pattern analysis in intracardiac atrial fibrillation signals. *Annals of biomedical engineering*, 39(1):310–323, 2011.

[135] B.N. Roberts, P.C. Yang, S.B. Behrens, J.D. Moreno, and C.E. Clancy. Computational approaches to understand cardiac electrophysiology and arrhythmias. *American Journal of Physiology-Heart and Circulatory Physiology*, 303(7): H766–H783, 2012.

[136] J.M. Rogers. Combined phase singularity and wavefront analysis for optical maps of ventricular fibrillation. *IEEE transactions on biomedical engineering*, 51(1):56–65, 2004.

[137] K.M. Ropella, A.V. Sahakian, J.M. Baerman, and S. Swiryn. The coherence spectrum. A quantitative discriminator of fibrillatory and nonfibrillatory cardiac rhythms. *Circulation*, 80(1):112–119, July 1989.

[138] B.J. Roth. Meandering of spiral waves in anisotropic cardiac tissue. *Physica D: Nonlinear Phenomena*, 150(1-2):127–136, March 2001.

[139] M. Rubinov and O. Sporns. Complex network measures of brain connectivity: Uses and interpretations. *NeuroImage*, 52(3):1059 – 1069, 2010. Computational Models of the Brain.

[140] D.A. Sampedro-Puente, J. Fernandez-Bes, L. VirÃąg, A. VarrÃş, and E. Pueyo. Data-driven identification of stochastic model parameters and state variables: Application to the study of cardiac beat-to-beat variability. *IEEE Journal of Biomedical and Health Informatics*, pages 1–1, 2019.

[141] D.A. Sampedro-Puente, J. Fernandez-Bes, L. VirÃąg, A. VarrÃş, and E. Pueyo. Data-driven identification of stochastic model parameters and state variables: Application to the study of cardiac beat-to-beat variability. *IEEE Journal of Biomedical and Health Informatics*, pages 1–1, July 2019.

[142] D.A. Sampedro-Puente, J. Fernandez-Bes, L. Virág, A. Varró, and E. Pueyo. Data-driven identification of stochastic model parameters and state variables: Application to the study of cardiac beat-to-beat variability. *IEEE journal of biomedical and health informatics*, 2019.

[143] M. Sarkar and V. Prabhu. Basics of cardiopulmonary bypass. *Indian journal of anaesthesia*, 61(9):760, 2017.

[144] S. Särkkä. Unscented rauch–tung–striebel smoother. *IEEE Transactions on Automatic Control*, 53(3):845–849, 2008.

[145] S. Särkkä. *Bayesian filtering and smoothing*, volume 3. Cambridge University Press, 2013.

[146] N.H. Service. *Arrhythmia*, 2018 (accessed October 20, 2019). `https://www.nhs.uk/conditions/arrhythmia/`.

[147] M.S. Spach, R.C. Barr, E.A. Johnson, and J.M. Kootsey. Cardiac Extracellular Potentials: Analysis of Complex Wave Forms about the Purkinje Networks in Dogs. *Circulation Research*, 33(4):465–473, October 1973.

[148] S. SÃĎrkkÃĎ. Unscented Rauch–Tung–Striebel Smoother. *IEEE Transactions on Automatic Control*, 53(3):845–849, April 2008.

[149] Y. Tang, Z. Deng, K.K. Manoj, and D. Chen. A practical scheme of the sigma-point Kalman filter for high-dimensional systems. *Journal of Advances in Modeling Earth Systems*, 6(1):21–37, 2014.

[150] K.H.W.J. ten Tusscher, D. Noble, P.J. Noble, and A.V. Panfilov. A model for human ventricular tissue. *American Journal of Physiology. Heart and Circulatory Physiology*, 286(4):H1573–1589, April 2004.

[151] K.H.W.J. ten Tusscher, A. Mourad, M.P. Nash, R.H. Clayton, C.P. Bradley, D.J. Paterson, R. Hren, M. Hayward, A.V. Panfilov, and P. Taggart. Organization of ventricular fibrillation in the human heart: experiments and models. *Experimental Physiology*, 94(5):553–562, May 2009.

[152] K. Ten Tusscher and A.V. Panfilov. Reentry in heterogeneous cardiac tissue described by the luo-rudy ventricular action potential model. *American Journal of Physiology-Heart and Circulatory Physiology*, 284(2):H542–H548, 2003.

[153] J.K. Tugnait and A.H. Haddad. A detection-estimation scheme for state estimation in switching environments. *Automatica*, 15(4):477–481, July 1979.

[154] J.K. Tugnait. Detection and estimation for abruptly changing systems. *Automatica*, 18(5):607–615, 1982.

[155] Umapathy Karthikeyan, Nair Krishnakumar, Masse Stephane, Krishnan Sridhar, Rogers Jack, Nash Martyn P., and Nanthakumar Kumaraswamy. Phase Mapping of Cardiac Fibrillation. *Circulation: Arrhythmia and Electrophysiology*, 3(1):105–114, February 2010.

[156] A. Vinet and F.A. Roberge. The dynamics of sustained reentry in a ring model of cardiac tissue. *Annals of Biomedical Engineering*, 22(6):568–591, November 1994.

[157] J. Walmsley, G. Mirams, M. Bahoshy, C. Bollensdorff, B. Rodriguez, and K. Burrage. Phenomenological modeling of cell-to-cell and beat-to-beat variability in isolated Guinea Pig ventricular myocytes. In *2010 Annual International Conference of the IEEE Engineering in Medicine and Biology*, pages 1457–1460, August 2010.

[158] J. Walmsley, G.R. Mirams, J. Pitt-Francis, B. Rodriguez, and K. Burrage. Application of stochastic phenomenological modelling to cell-to-cell and beat-to-beat electrophysiological variability in cardiac tissue. *Journal of Theoretical Biology*, 365:325–336, January 2015.

[159] E.A. Wan and R. Van Der Merwe. The unscented kalman filter for nonlinear estimation. In *Proceedings of the IEEE 2000 Adaptive Systems for Signal Processing, Communications, and Control Symposium (Cat. No. 00EX373)*, pages 153–158. Ieee, 2000.

[160] C.J. Wiggers. The mechanism and nature of ventricular fibrillation. *American Heart Journal*, 20(4):399–412, October 1940.

[161] A.T. Winfree. Varieties of spiral wave behavior: An experimentalistâĂŹs approach to the theory of excitable media. *Chaos: An Interdisciplinary Journal of Nonlinear Science*, 1(3):303, 1991.

[162] R.L. Winslow, D.F. Scollan, A. Holmes, C.K. Yung, J. Zhang, and M.S. Jafri. Electrophysiological Modeling of Cardiac Ventricular Function: From Cell to Organ. *Annual Review of Biomedical Engineering*, 2(1):119–155, August 2000.

[163] R. Wu and A. Patwardhan. Restitution of Action Potential Duration During Sequential Changes in Diastolic Intervals Shows Multimodal Behavior. *Circulation Research*, 94(5):634–641, March 2004.

[164] X Rong Li, Xiaorong Zwi, and Youmin Zwang. Multiple-model estimation with variable structure. iii. model-group switching algorithm. *IEEE Transactions on Aerospace and Electronic Systems*, 35(1):225–241, Jan 1999.

[165] A. Zammit-Mangion, G. Sanguinetti, and V. Kadirkamanathan. Variational estimation in spatiotemporal systems from continuous and point-process observations. *IEEE Transactions on Signal Processing*, 60(7):3449–3459, July 2012.